Scale-Bridging Computational Modeling of Irradiation Effects in Alpha-Zirconium and its Alloys

A Dissertation Presented for the
Doctor of Philosophy
Degree
The University of Tennessee, Knoxville

Jose Francisco March-Rico
August 2022

Acknowledgements

Completing a dissertation would simply not be possible without the generous support of many people. First of all, I would like to thank my advisor, professor Brian D. Wirth, for five years of guidance over the course of this dissertation. During this time, our offices have moved between three buildings, and yet Brian has always been down the hall, enthusiastic to bounce off research ideas and provide invaluable direction. I would similarly like to thank my advisors Dr. Richard W. Smith and Dr. Jesse Carter for five years of guidance and advice during my summer practicum at Bettis and my time at the University of Tennessee, Knoxville. I'm already looking forward to future collaborations.

I would also like to pay my respects to Dr. Steven J. Zinkle and Dr. William J. Weber who have both provided invaluable insight inside and outside of the classroom.

The financial support of the Rickover Fellowship has been crucial throughout the course of this dissertation. The generous stipend, payment of tuition and fees, and allowance of a travel budget have all allowed me to focus entirely on my work and to reach as broad an audience as possible. I again want to thank the Rickover committee for awarding me this honor.

Of course, I also need to thank my friends and family for encouraging me to complete this dissertation and being there for me throughout the years. My mother, Emilia Rico-Munoz, and my father, Jose March-Leuba, were both inspirations to pursue a career in the sciences. My sister, Victoria March-Rico, has always supported my career and provided much needed relief. My closest friends, John Valenti, Ben Maxey, Drew Marlow, Jackson Harrington, and Zack McGhee, have always made my life easier and were there to support me every step of the way. I will also miss the incredible members of my research group; I hope to continue working with them throughout my career: Ryan Sweet, Danny Schapell, Jason Rizk, Zack Bergstrom, Wendy Garcia, Dave Martin, Congyi Li, Dwaipayan Dasgupta, Li Yang. In particular, I would like to thank Guiyang Huang for his training concerning DFT calculations, and Sophie Blondel for her invaluable assistance with the implementation of my model into Xolotl.

Finally, last but not certainly not least, I cannot express enough gratitude for my late dog, Tinker, who passed away in the final months of my dissertation. Her relentless optimism kept my spirits up throughout the COVID-19 pandemic and the mental challenges of this dissertation. While she cannot take these final steps across the finish line, her optimism continues to carry me through my defense.

Abstract

One of the issues concerning the long-term lifespan of Zr cladding tubes is an axial expansion and radial contraction that occurs in response to neutron irradiation. This volume-conservative response in the absence of an applied stress has been termed irradiation growth, a consequence of both the inherent anisotropy of alpha-Zr hexagonal close-packed crystal structure, and crystalline texture in tube fabrication. Irradiation growth strains generally saturate at low doses, but suddenly accelerate after an incubation dose. This growth breakaway has been correlated with the nucleation of faulted vacancy loops on basal planes (c-loops); at lower doses, the irradiated Zr microstructure is characterized by the co-existence of vacancy and interstitial dislocation loops on prismatic planes (a-loops). The goal of this dissertation is split into two categories: 1) to elucidate the mechanisms governing microstructure evolution and develop a computational database to describe such mechanisms; and 2) to incorporate this database into a mechanistically-based cluster dynamics (CD) model capable of describing interstitial and vacancy a-loop co-existence in addition to c-loop nucleation and growth.

This goal requires a computational multi-scale approach that bridges several orders of magnitude in length and time scales. Lower-length scale techniques such as density functional theory (DFT) and molecular dynamics (MD) have been used to simulate interactions at the atomic scale and provide essential parameters, including: 1) Interaction energies of solute and impurities with stacking faults and c-loop precursors; 2) defect production rates from displacement cascades; 3) preferred defect cluster configurations and mobilities; 4) defect binding energies; 5) dislocation loop stress states; and 6) defect capture radii. With these key physics incorporated into a CD model, it was found that an inherent bias exists between vacancy and interstitial a-loops for the capture of same-type defects. The resultant interaction rates drive the simultaneous growth of these loops in the microstructure. The growth of c-loops, on the other hand, is driven by the anisotropy difference of defect cluster diffusion, rather than that of point defects. The work presented in this dissertation marks the first time that these phenomenon have been successfully modeled in a purely mechanistic fashion, and highlights the importance of scale-bridging computational approaches to solve current and future issues of materials performance in extreme nuclear environments.

Table of Contents

List of Tables

List of Figures

Chapter One:

Introduction and Background

Zr alloys have historically been selected as cladding materials for nuclear applications primarily due to their low thermal neutron absorption cross section and good balance of strength and corrosion resistance [1]. At the intended operating conditions of conventional LWRs, these alloys crystalize in the low-temperature (T < 863 °C) hexagonal close-packed (hcp) α phase and undergo volume conservative irradiation growth strains when exposed to a neutron flux [2]. In Zr single crystals, these strains manifest as an expansion along the *a*-axis with a corresponding contraction along the *c*-axis [3, 4]. The growth behavior in single crystals is characterized by an initial transient followed by strain saturation at low-to-moderate fluences. This apparent saturation ends once a threshold, or incubation, dose is reached, at which point the growth strain exhibits a greatly accelerated "breakaway" with increasing neutron fluence. These three stages of irradiation growth are captured in Fig. 1-1 for Zr single crystals oriented along the a-axis (positive strain data) and c-axis (negative strain data).

In polycrystalline Zr the macroscopic growth response will depend upon the orientation of its grains. Due to the anisotropic response of Zr to cladding fabrication processes, the tubes will develop a preferred texture [5]. The fraction of basal poles, f^c, oriented along the radial, transverse, and axial directions following fabrication is approximately 0.60, 0.33, and 0.07 for the Zircaloy family of alloys. The macroscopic irradiation growth response in a given direction, D, is governed by the "growth anisotropy factor", G_D:

$$G_D = 1 - 3f_D^c \qquad (1\text{-}1)$$

A large fraction of basal poles oriented in a given direction will result in large negative strains, while positive growth strains will manifest perpendicular to those directions. For Zr cladding tubes, the consequence of texture is an overall shrinkage in the radial direction and expansion in the axial direction. Continued growth strains in the accelerated regime can cause significant bowing of Zr cladding rods and restriction of cooling channels [6]. Despite significant effort by various researchers over several decades, the mechanisms responsible

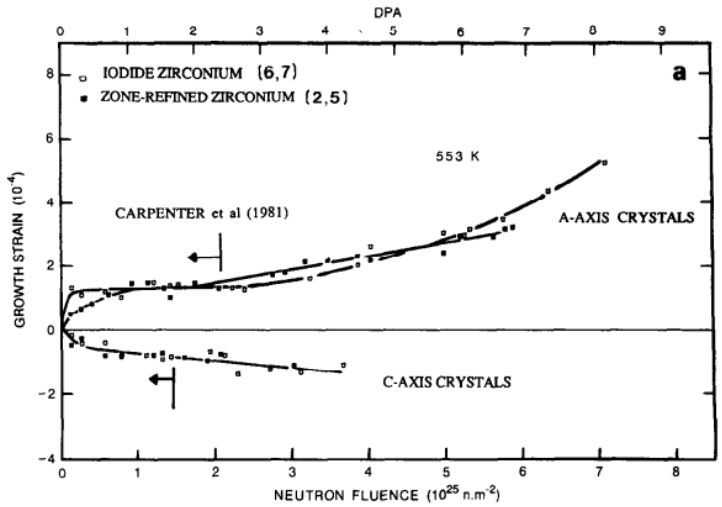

Fig. 1-1. Irradiation growth behavior in iodide and zone-refined Zr single crystals as a function of neutron fluence (T = 553 K), as reproduced from reference [4].

for breakaway irradiation growth are still largely ambiguous. Suggested controlling mechanisms including point defect diffusion anisotropy and the role of impurities are often contradictory in the existing literature. The goal of this dissertation is to further our understanding of the mechanisms responsible for breakaway irradiation growth through multi-scale modeling and simulation. This document will first present an overview of existing literature and attempt to highlight the most likely contributors to the phenomenon. Finally, the work performed towards the completion of this dissertation will be summarized and the organization of this document will be summarized for the reader.

1.1 Irradiated microstructure in α-zirconium

The irradiation growth strains of α-Zr in response to an incident particle flux are best understood by correlating the behavior with the evolution of irradiation damage over time. Damage is initially produced as a consequence of sequential atomic collisions that occur once a Zr atom is ejected from its lattice site by an incident energetic particle. A significant number of Frenkel pair defects are generated locally during the subsequent displacement cascade, and while a considerable fraction of these defects recombine athermally during the thermal spike period, residual damage remains in the form of single interstitials, monovacancies, and defect clusters [7-12]. Mobile defects will diffuse through the surrounding structure via random jumps between one low-energy site to another, resulting in long-range transport away from their origins. The eventual fate of these defects is to either recombine with defects of opposite type, cluster with defects of the same type, or be absorbed at various sinks (such as dislocation loops, voids, or grain boundaries). The microstructure that evolves in irradiated materials is the end result of continuous defect production, transport, and interaction. Understanding this microstructure evolution in irradiated α-Zr and correlating it with the observed growth strains is a key step in predicting irradiation growth behavior.

1.1.1 Prismatic a-loops

In Zr, the predominant extended defects are interstitial and vacancy dislocation loops that co-exist in the structure. At low fluence, dislocation loops are only found to form on $\{10\bar{1}0\}$ prismatic type I (PPI) habit planes with perfect $\vec{\boldsymbol{b}} = 1/3\langle 11\bar{2}0\rangle$ Burgers vector; because their Burgers vector lies in one of the three a-axis hcp directions, these loops have been termed "a-loops" [13-18]. A-loops are expected to be faulted at small sizes with a Burgers vector of $\vec{\boldsymbol{b}} = 1/2\langle 10\bar{1}0\rangle$ and only form perfect loops through a $1/6\langle 1\bar{2}10\rangle$ shearing of the fault plane [19]. While these loops initially form in a seemingly homogenous distribution throughout the matrix, a-loops tend to undergo significant ordering as the incident particle fluence is increased, as is evident in Fig. 1-2 [20]. In particular, vacancy a-

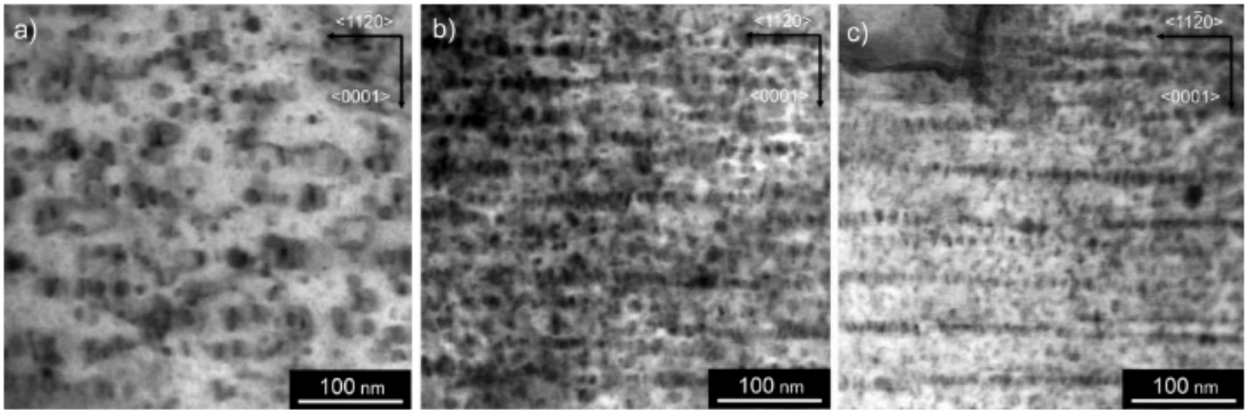

Fig. 1-2. Vacancy and interstitial dislocation a-loops co-exist in the structure, and order as a the incident particle fluence increases (2.3, 4.7, and 7.0 dpa proton fluence in a) – c) respectively), as reproduced from reference [20].

loops order onto parallel basal sheets while interstitial a-loops lie in between these rows [13, 16, 20]. Within these ordered sheets of vacancy a-loops, the loop faces are randomly oriented such that the tensile strain fields normal to the loop faces do not overlap [17, 21].

While a definite mechanism for a-loop ordering has not yet been agreed upon, it is interesting to note that a similar basal plane ordering has been reported for krypton bubble lattices in hcp Ti [22] and void lattices in hcp Al_2O_3 [23]. In an effort to explain void and bubble lattice formation, a model based on 2-D diffusion of self-interstitial (SIA) dumbbells was developed to simulate void movement when exposed to an imbalanced SIA flux [24]. Voids were found to order within parallel sheets in such a way that their SIA capture volumes overlap (i.e. neighboring voids self-shield against SIA capture). This scenario is analogous to a-loop banding in α-Zr and may explain why only vacancy loops undergo long-range ordering. While 2-D diffusion of SIAs in Zr have not yet been reported in literature, small basal-crowdion clusters are believed to migrate through a sequence of 1-D jumps along primary a-axis directions [25]. Due to the fact that all a-axes lie within the basal plane, the mass transport of SIA clusters is overall 2-D and may drive vacancy a-loop ordering. Solute atoms may additionally play some role in the ordering efficacy in Zr alloys. For example, a-loop ordering is evident in Zircaloy-2 alloys and may be related to the anti-correlation of Fe and Sn in alternating basal sheets [20]. Conversely, low-Sn ZIRLO, E635, and E110 alloys (which contain higher amounts of Nb and lower amounts of Sn), exhibit reduced a-loop banding [26-28].

There are three defining characteristics for a-loop microstructure: 1) number density; 2) size distribution (average size); and 3) relative fraction of interstitial to vacancy type a-loops. Each of these characteristics are heavily dependent on factors such as temperature, incident particle fluence, and alloying composition. In general, increasing irradiation temperature results in larger a-loops with lower number densities [16-18, 29]. Similarly, increasing particle fluence will result in larger a-loops [16, 29]. However, perhaps most interesting is the difference in a-loop microstructure between alloyed and pure Zr. It is consistent in literature that a-loops grow to much larger sizes with broader size distributions in pure Zr [18, 29]; for example, at 573K the average a-loop diameters in pure Zr and Zircaloy-2 alloy were 18.6 nm and 6.5 nm, respectively [29]. This particular observation is rarely discussed in literature, but it is clear that solute must have some effect on the interaction rates between defects and sinks such as dislocation loops. It is possible that solute interaction with mobile defects may reduce their overall diffusivity [30], or that solute segregation to dislocation loops may screen their strain fields [31] and, thus, reduce defect capture distances.

1.1.2 Faulted basal c-loops

Following some incubation dose, faulted loops of vacancy character begin to first form near amorphizing precipitates, and eventually develop with high number densities [13, 32-36]. The nucleation of these unique defects has been correlated with the onset of breakaway irradiation growth and has therefore been a subject of significant scrutiny in the literature.

These loops lie on basal planes with a Burgers vector of either **b** = 1/2 [0001] (corresponding to basal extrinsic faulting) or **b** = $1/6 < 20\bar{2}3 >$ (corresponding to basal I_1 intrinsic faulting) [37]; because these loops have components of their Burgers vectors along the hcp c-axis, these loops have been termed "c-loops". While a-loops are known to range in diameter from several nm to several tens of nm, c-loops often grow in excess of 100 nm in diameter and are rarely seen below 10 nm in diameter.

It is hypothesized that the initial growth transient of Zr under irradiation is due to the formation of small defect clusters and dislocation a-loops [38]. Interstitial a-loops apply a compressive strain along the a-direction and a weak tensile strain along the c-direction. As fluence increases, it is speculated that growth saturation occurs due to the compensating effect of vacancy a-loop formation (which exhibit the opposite strain field characteristics of interstitial a-loops). The breakaway regime, then, would be a consequence of the large c-axis tensile strains that emanate from c-loops. It is unclear why c-loop formation would also result in accelerating a-axis expansion unless their growth reduced the availability of vacancy a-loops in the structure. There is weak experimental evidence for this case [20], but there is certainly a need for future work to confirm or deny such a hypothesis. Regardless, it is evident that understanding c-loop formation is the key to predicting breakaway irradiation growth behavior. Despite decades of research, however, the mechanisms that drive c-loop nucleation and growth are still ambiguous. A summary of some potential key factors will be described in the preceding section.

1.2 Factors that affect breakaway irradiation growth

1.2.1 Temperature

The effect of temperature is clear in Fig. 1-3(a) and has been discussed in the framework of the production bias model (PBM) [39-41]. This model is an improvement over the conventional rate theory approach which assumes that defect generation occurs only in the form of Frenkel pair defects. A production bias arises due to the clustering of defects in-cascade; SIA clusters are mobile while small vacancy clusters are assumed to be immobile. Vacancy clusters may act as a source of mobile monovacancies by thermal evaporation at higher temperatures while SIA clusters are far more thermally stable. The thermal instability of vacancy clusters produced in-cascade are hypothesized to be the cause of the drastic increase of irradiation growth strains at higher temperatures [42]. Other theories for the temperature dependence include a direct decrease in stacking fault energies of c-loops at higher temperatures [34] and increased solute mobility [33].

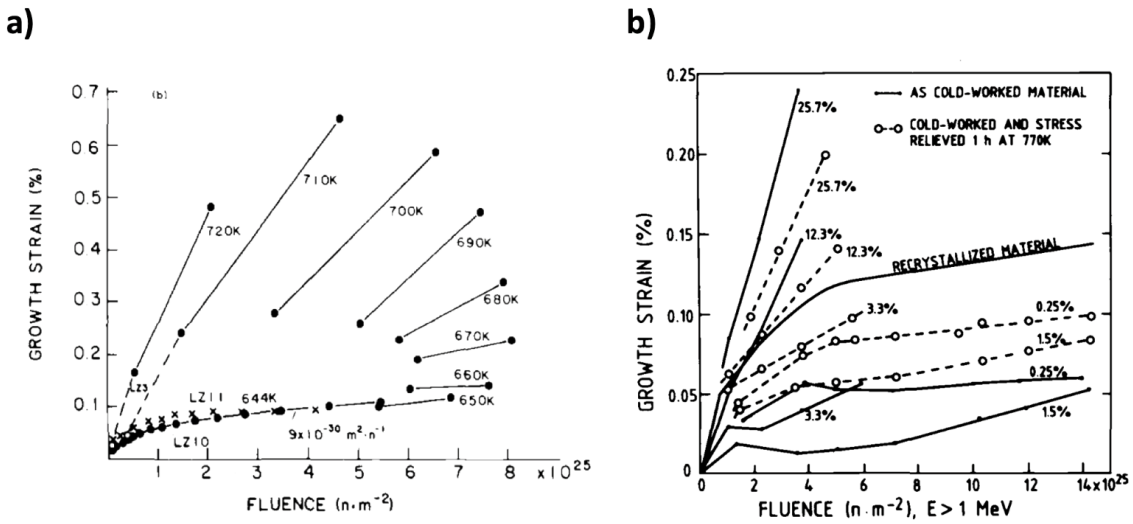

Fig. 1-3. Irradiation growth strains as a function of neutron fluence in Zircaloy-2 as a function of a) Temperature [42] and b) cold-work [44].

1.2.2 Cold-work

Similar to the impact of increasing temperature, Fig. 1-3(b) shows that a sharp increase in irradiation growth strain rates is noted for heavily cold-worked materials [32, 36, 43-45]. The microstructure of cold-worked Zr alloys prior to irradiation is characterized by a dense network of pre-existing c-component dislocations. The density of c-component network dislocations varies from grain-to-grain, with a higher density present in grains that contain their c-axis oriented near the radial direction of the tube; upon irradiation, these same grains contain a higher number density of basal faulted c-loops than other grains [32]. The formation and multiplication of c-loops by helical climb on pre-existing c-component dislocations has been noted several times in literature, as evidenced by screw <c+a> dislocation segments threading through faulted basal plane segments [36, 43, 44]. Irradiation causes the pre-existing c-component network dislocations to split by climb into partials, forming a stacking fault segment. The absorption of vacancies at these basal faulted segments could cause the nucleation of faulted c-loops and explain the almost instantaneous breakaway growth of cold-worked alloys [13, 44].

1.2.3 Difference in point defect diffusional anisotropy

The diffusional anisotropy difference (DAD) of point defect diffusion model was an early attempt to explain basal c-loop formation [46]. The basis for the model was the preferential diffusion of self-interstitial atoms within the basal plane and quasi-isotropic diffusion of vacancies; thus, any sink oriented along the prismatic plane would be exposed to a higher net flux of interstitials when compared to basal c-loops. This theory was supported by molecular dynamics (MD) work using older interatomic potentials [47, 48]. The migration energies for diffusion in-plane and out-of-plane were 0.06 eV and 0.15 eV for interstitials, respectively, but 0.91 eV and 0.96 eV for vacancies. SIA diffusion was found to change from 1-D to 2-D to 3-D mobility with increasing temperature while vacancies only slightly preferred in-plane diffusion to out-of-plane diffusion at lower temperatures [48]. On the contrary, recent density functional theory (DFT) work indicates that both vacancies and interstitials exhibit strong anisotropic diffusion with a preference for diffusion within the basal plane [49]. Anisotropic diffusion for vacancies has been noted experimentally at 1000 K ($D_a/D_c \sim 3$) [50], but near-isotropic diffusion ($D_a/D_c \sim 1$) is reported at 1100 K [51], which indicates a temperature dependence for anisotropy as predicted by Samolyuk et al. [49]. Anisotropic vacancy diffusion at low temperatures would invalidate the DAD model, but 1-D diffusion of SIA clusters (as strongly indicated by the directional dependence of the interstitial-denuded zone near grain boundaries imaged in Fig. 5 in Ref. [52]) would still explain low interstitial cluster fluxes towards basal c-loops. Additionally, Rouchette et al. argue that there is a shape anisotropy of SIAs that induces preferential absorption of interstitial defects on prismatic, rather than basal, planes due to elastic interactions [53].

1.2.4 a-loop banding

As was described in greater detail in Section 1.1.1, a-loops have a tendency to order with increasing particle fluence [17, 20, 21]. In particular, vacancy loops organize onto parallel basal sheets while interstitial loops lie in between these sheets. It has recently been hypothesized that there may be a correlation between this a-loop ordering and the nucleation of c-loops, which could explain why c-loops only form at higher fluences. This hypothesis is driven by transmission electron microscope (TEM) micrographs that demonstrate an anti-correlation between the positions of c-loops and a-loops within the ordered basal sheets (Fig. 1-4) [20]. This is an attractive hypothesis, as it provides a foundation to describe both the delayed onset of c-loop nucleation as well as the rapid a-axis expansion in Zr grains (due to an overall reduction in vacancy a-loops from the growth of c-loops). However, there is currently only weak experimental evidence that a-loop number densities decrease in correspondence with increasing c-loop densities [20]. Furthermore, the mechanism through which a-loop banding promotes c-loop nucleation is unclear. Harte et al. argue that a-loops may directly transform into c-loops, but a potential dislocation reaction for this transformation was not provided, nor does this explain why spatial organization of a-loops would be necessary for such a transformation. MD simulations of displacement cascades performed on existing a-loops have shown that c-loop precursors may nucleate in such events [21], but these pre-cursors were rapidly re-absorbed by the a-loops. Further work is required to sufficiently corroborate a potential link between a-loop banding and c-loop nucleation.

1.2.5 Solute and impurities

The factors presented in this section thus far have all been independent of the alloying or impurity content in Zr. However, it is generally observed that breakaway growth occurs at lower fluences and at accelerated rates in Zr alloys when compared to high-purity Zr, as demonstrated in Fig. 1-5 [13, 19, 33, 35, 36, 43, 45, 54, 55]. The sensitivity of irradiation microstructure to solute content is apparent through the comparison of neutron-irradiated sponge and high-purity crystal-bar Zr [33]. Due to the increased impurity content of the sponge Zr, a uniform distribution of Fe-rich precipitates form under irradiation with a corresponding increase in the number of *c*-loops when compared to high-purity crystal-bar Zr. A recurring observation in the microstructural evolution of irradiated Zr is the nucleation of a high number density of *c*-loops near dissolving precipitates [32, 33, 35] and hydrides [36]. Growth strains are particularly high for alloys rich in Sn and Fe content (Zircaloy-2, Zircaloy-4, and EXCEL) [33, 54]. Conversely, alloys rich in Nb content tend to exhibit mitigated growth behavior [26, 56].

The role of solute in catalyzing c-loop nucleation is not fully understood. It is possible that solute interaction with mobile defects could affect their transport in the

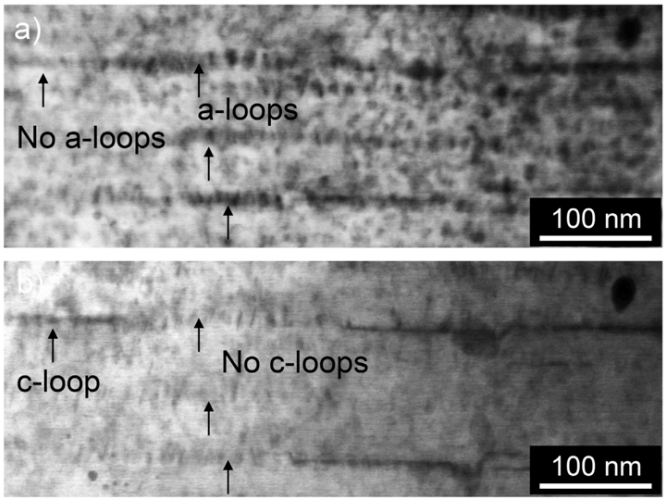

Fig. 1-4. Anti-correlation of c-loops and a-loops in proton-irradiated Zircaloy-2 (7 dpa) under different BF-STEM imaging conditions: a) taken on-axis parallel to $< 11\bar{2}0 >$ and b) 4° from $< 11\bar{2}0 >$ along the **g** = 0002 systematic row, as reproduced from [20].

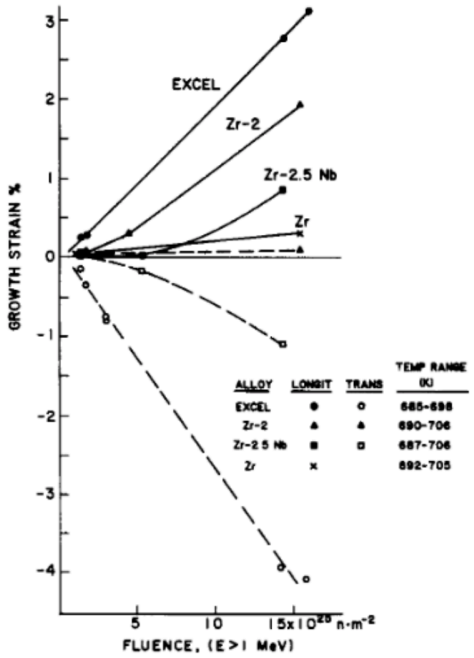

Fig. 1-5. Irradiation growth strains in pure Zr and Zr alloys at temperatures between 665K and 706K are contrasted, as reproduced from [54].

material, and thus, their interaction rates with sinks. For example, Fe is hypothesized to facilitate vacancy diffusion along the c-axis, and this may drive vacancy absorption at c-loops or c-loop precursors [57, 58]. Another potential effect of solute could be in either promoting or inhibiting the banding of vacancy a-loops. Fe and Sn are found to be anti-correlated in Zircaloy-2, segregating to alternating basal sheets [20]; a-loops band quite extensively in these alloys. In alloys with reduced Sn content, however, a-loop banding is less developed and c-loop densities are noticeably lower [26-28]. While these indirect effects of solute may contribute to c-loop growth, the major role of solute is expected to be a reduction in c-loop stacking fault energies (SFE) via solute segregation [13, 19, 33, 35].

This type of interaction was first reported by Suzuki et al. and the phenomenon is now known as the "Suzuki" effect [59]. Fe is often cited as the main contributor to this effect, although these observations are empirical in nature and have not been demonstrated by direct calculation for any of the common alloying solute. The effect of impurity segregation on SFE has only been investigated for H [19]. Fe, Cr, and Ni have negligible solubility in the hcp α-Zr matrix and are almost entirely contained within secondary phase precipitates (SPPs) prior to irradiation [60]. These elements are only expected to supersaturate within the matrix upon ballistic dissolution of these SPPs under irradiation. Increasing Fe content in pure Zr was shown to lead to increased c-loop number densities, where c-loops were seen to align with Fe precipitates in the basal plane [35]. X-ray linescans have demonstrated Cr and Fe segregation to ordered rows of c-loops in Zircaloy-2 [32]. However, significant clustering of Fe and Cr is also noted in parallel bands along the basal trace consistent with vacancy a-loop ordering [20]. Vacancy a-loops may offer a high number density of nucleation sites for Fe and Cr clusters that could inhibit their migration in the matrix to stabilize c-loops. C. Dai et al. investigated the segregation of Fe [61] and Ni [31] to dislocation loops and argue that, due to a change in the stress field and core energy of the loop by alloy segregation, the dislocation loops see enhanced stability in the presence of irradiation damage. Additionally, positive binding between small Fe-Fe, Cr-Cr, and Fe-Cr clusters has been demonstrated through DFT [62] that supports the clustering propensities seen in recent TEM and APT work [20, 63].

In binary Zr-Sn alloys, increasing Sn content appears to accelerate irradiation growth strains [56, 64]. The opposite is true of Nb-enriched alloys, which exhibit lower c-loop densities at equivalent doses when compared to Sn-enriched alloys [26]. In Zr-2.5Nb, the number densities of a-loops is an order of magnitude larger than in pure Zr at similar doses with much smaller diameters, which may indicate that Nb solute affects defect diffusion [65]. Atomistic studies by Christensen et al. highlight point defect mobility characteristics in addition to the interaction of H and alloying solute with irradiation defects [30, 66]. A strong tendency for substitutional Fe, Cr, and Ni to exchange positions (i.e. become interstitial) with migrating Zr SIAs was reported. This is hypothesized to assist in the recombination of vacancies and SIAs. Fe was

found to have the highest binding to single vacancies, with weak binding shown by Cr, Ni, Nb, and Sn (although Sn clusters may be more effective at trapping vacancies [50]). Nb is shown to have strong binding with SIAs while Sn is weakly repulsed.

Recent work has further demonstrated the complexity of solute impact on breakaway irradiation growth [56]. For example, while Zr-1Sn alloys show accelerated growth strains, the growth strains of Zr-1Sn-1Nb are greatly reduced in comparison. Furthermore, despite the fact that Fe is historically quoted as a significant contributor to c-loop nucleation and breakaway growth [33, 35], increasing Fe content in Zr-1Sn, Zr-1Nb, Zr-1Sn-1Nb, and E635 alloy (Zr-1Nb-1.3Sn-0.4Fe) appears to reduce growth strains instead [27, 28, 56]. A concrete explanation has not been supported for these experimental observations, although it appears that there must be some synergistic effect between Nb, Sn, and Fe that cause Fe and Sn to impact growth strains differently than in un-alloyed Zr. It has been noted that the positions of Fe and Sn are anticorrelated in the Zircaloy-2 matrix; Fe segregates to the parallel bands of vacancy a-loops while Sn is found in between these bands [20]. Additionally, Fe and Sn are found to segregate to c-loops, but both solute are never found to segregate to the same c-loops simultaneously [63]. The additions of Fe and Sn are reported to cause a-loop alignment on parallel basal sheets, while alloys with increasing amount of Nb have lowered a-loop alignment. While some reports argue that a-loop alignment facilitates the nucleation of c-loops in the Zircaloys [20, 21, 26], Shishov argues the opposite behavior for E110 and E635 Russian alloys [27, 28]. It is clear that a considerable amount of work is still necessary to fully comprehend the underlying mechanisms and factors responsible for breakaway irradiation growth in α-Zr and its alloys.

1.3 Defect production, configurations, and mobility

The experimental database of observations and micrographs concerning microstructure evolution in irradiated Zr is extensive; despite this, most of the mechanisms driving such evolution remain ambiguous. In order to further elucidate these mechanisms, lower-length scale techniques capable of probing the atomic scale are necessary. The most common computational tools used to quantify fundamental interactions are molecular dynamics (MD) and density functional theory (DFT), which will be discussed in greater depth in Section 1.5.2. For the case of microstructure evolution, there are a few key questions that must be answered (and parameterized) in order to effectively inform higher-order codes. These include, but are certainly not limited to: 1) At what rate are point defects and defect clusters produced from incident irradiation?; 2) What configurations do defect clusters assume?; 3) Which defects are mobile and what are their modes of transport through the structure?

1.3.1 Defect production from displacement cascades

Irradiation damage is produced on the nanometer and picosecond scale in the form of displacement cascades. These events initiate when a lattice atom is knocked off of its equilibrium site through elastic collision with an incident particle, such as a neutron. The number of defects that are produced from the subsequent atomic collisions has historically been calculated with the Norgett-Robinson-Torrens (NRT) model [67]:

$$N_F(NRT) = \frac{0.8 \cdot E_{dam}}{2 \cdot E_{disp}} \quad (1\text{-}2)$$

Using the NRT equation, the total number of defects produced in displacement cascade events can be estimated based on the PKA energy available for the displacement of target atoms (E_{dam}) and the energy necessary to eject another atom from its lattice site (E_{disp}). With MD simulations, the interaction between colliding atoms is determined by the interatomic potential of choice, and the resulting damage can be directly observed. The first displacement cascades in α-Zr considered PKA energies in the range of 0.3 – 5 keV [10], but these energies were later expanded to include up to 20 keV cascades [11]. The production of Frenkel pairs is found to obey a power-law dependence for PKA energy with an exponent less than unity; the production efficiency of defects is reduced as PKA energy is increased. This trend is true below a PKA energy of approximately 10 keV, above which cascades begin to develop sub-cascade structure and the number of produced defects becomes linear with energy [11, 12]. In general, the surviving defect fraction approaches 25% of the NRT-predicted value due to significant in-cascade athermal recombination of Frenkel pairs [10-12].

Defects are found to readily cluster within the cascade heat spike period, and this is particularly true for vacancies due to the vacancy-rich core structure of the cascades. The fraction of defects found in clusters increases with PKA energy (ranging between 20% and 60% of total defects clustered) [11]. Later work investigated the effect of temperature on defect production efficiencies, demonstrating that higher temperatures prolong the lifetime of the thermal spike period and, thus, reduce the surviving defect fraction [68]. Most of this early research utilized the 1995 Ackland, Wooding, and Bacon embedded-atom method (EAM) potential [69], although an updated EAM potential was published in 2007 that better predicted the *ab initio*-calculated properties of α-Zr [70]. Research implementing this updated potential have investigated the coupled effects of strain and temperature [71], higher-energy cascades up to 80 keV [12], as well as interaction with existing defects such as grain boundaries [72], dislocation lines [73], and dislocation loops [21, 74]. While one set of MD simulations has implemented electronic stopping [12], these effects are typically omitted and their impact on damage production remains unquantified.

1.3.2 Preferred defect cluster configurations

A considerable fraction of irradiation-induced defects are sub-nanometer in size, and are therefore unidentifiable in TEM micrographs. It is these defects, however, that are the primary drivers of microstructure evolution, and only computational tools allow us to probe the atomic scale to effectively assess their structures. Considering the configuration of single interstitials, Samolyuk et al. have demonstrated the preference for the basal octahedral (BO) site [49, 75] rather than the octahedral (O) site, which had been incorrectly predicted by prior DFT calculations that utilized small supercell sizes [76, 77]. The preference for the BO SIA configuration is similarly predicted by the recent BMD19 interatomic potential [78] while the older A95 and M07 #3 interatomic potentials predicted a preference for the basal-split (BS) and O configurations, respectively [69, 70]. N. de Diego et al. simulated SIA clusters containing up to 30 SIAs [25], and later up to 300 SIAs [79], using the A95 potential. It was reported that the preferred configuration consisted of parallel BS dumbbells on second-order prism planes (PPII) with rectangular cluster shapes. This is not consistent with experiments, for which interstitial a-loops are shown to be elliptical with habit planes near PPI [17, 18]. The M07 #3 potential similarly predicted the incorrect PPII habit plane for large basal crowdion (BC) SIA clusters [80]. Interestingly, it was reported that lowest energy configuration for small SIA clusters consisted of all SIAs occupying a single basal plane, similar to the BO single interstitial.

Considering vacancy clustering, both the A95 and M07 #3 potentials identified double-layer corrugated vacancy loops with PPI habit planes as the thermodynamically preferred dislocation loop structure (rather than faulted loops on basal planes), consistent with experimental observations of irradiated α-Zr at low fluences [13, 37, 80, 81]. Due to the unique spacing of prismatic planes in the hcp structure, a double-layered prismatic vacancy loop configuration is expected to be lower in energy than a single-layer configuration [82]. While the correct dislocation loop structure is identified by these interatomic potentials, both the A95 and M07 potentials overall predict that spherical cavities are the lowest energy configuration for large vacancy clusters [37, 81]. This is certainly inconsistent with experimental studies of irradiated microstructure. While cavities may form near grain boundaries or precipitates, the most common vacancy structures are dislocation loops [13, 83].

Expressions for the formation energy of vacancy clusters of differing geometry parameterized with *ab initio* calculations do correctly predict that prismatic vacancy a-loops should be lower in energy than either spherical cavities or faulted basal c-loops [37]. Although, recent analysis has begun to consider faulted basal pyramids as potential pre-cursors to c-loop formation [84]. These structures are reported to have either a basal intrinsic [84] or a basal extrinsic faulted base [85], with six pyramidal faulted sides. It was originally thought that c-loops would precipitate as a single-layer vacancy platelet, resulting in high energy B-B layer contact [66, 86]. This structure would certainly act as a nucleation barrier due to its high energy configuration [82], and as such it is feasible to assume that another structure may instead act as a c-loop pre-cursor. Faulted basal pyramids have been reported to form directly in displacement cascades [85] and there may be some experimental

evidence for these structures in He-irradiated pure Zr [87]. It is clear that there is still considerable room for improvement when simulating defect structures in Zr, and more recent interatomic potentials such as the BMD19 potential may offer more accurate tools to do so.

1.3.3 Defect cluster mobility

Simply identifying defect generation rates and the configurations that these defects will take is insufficient to model microstructure evolution. For example, MD simulations of displacement cascades in fcc copper and bcc iron have shown that the number and size distribution of defect clusters are strikingly similar [7, 8]. Despite this, the differences in damage accumulation behavior between these two metals are significant [88] and may be related to the ratio of sessile and glissile defect clusters [89]. Ultimately, it is the transport of mobile clusters and their interaction rates with existing defects that drives microstructure evolution. This is particularly true in the inherently anisotropic alpha phase of zirconium. Depending upon the degree of anisotropy of diffusion, mobile defects will be more or less likely to interact with sinks of varying geometry [46]. As such, the anisotropy of point defect migration has been a topic of interest in literature [30, 40, 47-49, 90].

Through a combination of DFT and kinetic Monte Carlo techniques, Samolyuk et al. concluded that monovacancy diffusion should be significantly more anisotropic than SIAs at temperature below 900K [49]. This conclusion is in contrast with previous MD and molecular statics calculations that predicted significant SIA anisotropy at low temperatures [47, 48, 90]. Strongly anisotropic SIA diffusion and quasi-isotropic monovacancy diffusion formed the basis for Woo's DAD model for the growth of c-loops; Samolyuk et al. instead hypothesize that highly anisotropic diffusion of larger SIA clusters may instead explain c-loop growth behavior in irradiated α-Zr [46, 49].

There is limited data concerning the mobility of such clusters in literature. The A95 potential predicts that small SIA clusters can migrate in 1-D, 2-D, or even remain entirely immobile depending on their particular configuration [25]. A similar correlation between cluster geometry and modes of transport was predicted by the M07 #3 potential [80]. Small SIA clusters were found to transform between basal-plane geometries and prismatic-plane geometries during migration. When SIA clusters are entirely contained within a single basal plane, diffusion is found to be 2-D; when SIA clusters take the form of parallel O configurations, diffusion is instead 3-D. The migration of larger clusters consisting of up to 24 parallel basal crowdions is instead described as synchronized jumps of individual crowdions along the Burgers vector direction. The thermally activated movement of such clusters are characterized by low activation energies on the order of those for an individual basal crowdion. The correlation factor of cluster jumps, a ratio of the number of backward and forward jumps, was found to be greater than unity [25]. In other words, the jump direction of large SIA clusters is biased towards the direction of its previous jump (rather than random motion). The migration behavior of these larger SIA clusters is similar to what has been reported for all crowdion-based SIA clusters in bcc Fe [91-93].

1.4 Microstructure evolution modeling in α-zirconium

1.4.1 EID, DAD, and production bias models

Attempts to model irradiation growth behavior in Zr date to 1975 [94]. Because basal c-loops had yet to be identified, Carpenter and Northwood based their model purely on elastic interaction distances (EID) with dislocation lines by interstitials and vacancies. Dislocations were assumed to climb by absorbing an excess of interstitials while an excess of vacancies were assumed to be absorbed at all grain boundaries. Unsurprisingly, this simple model did not have good agreement with growth strain data, and could not predict breakaway growth behavior [94]. Once reports in literature finally agreed upon the existence of faulted basal c-loops, it became clear that these dislocation loops may be the key to understanding the onset of breakaway irradiation growth. In an attempt to explain why c-loops are uniquely vacancy in character, it was postulated that a difference in the anisotropy of diffusion (DAD) of point defects may be the driving force [46]. Woo claimed that the zero-order DAD effect dominates the first-order and second-order EID effect such that sinks are no longer biased for defect capture in the traditional sense. Rather, it is the geometry of the sink which determines its bias for the capture of anisotropically diffusing defects. Considering the assumption that SIAs migrate anisotropically within the basal plane and monovacancies migrate quasi-isotropically, any sink oriented parallel to the c-axis will see a higher flux of SIAs than vacancies; the opposite is true for any sink oriented perpendicular to the c-axis [46]. Using the principles of the DAD model, Woo [40] and Holt [95] were later able to obtain good agreement with low temperature growth data, but was unable to describe a sharp increase in the high-temperature growth behavior.

At higher temperatures, the growth saturation regime is shortened and breakaway growth occurs at a higher rate [39-42]. These trends were hypothesized to be a result of a production bias of mobile defects [39, 41]. While point defects produced in displacement cascades are mobile, defect clusters are assumed to be entirely immobile in the production bias model (PBM). The difference in low temperature and high temperature growth could then be attributed to the thermal instability of vacancy clusters. Mobile vacancies are emitted from dissociating clusters and, thus, the production of mobile vacancies is enhanced at higher temperatures [39]. Combined modeling that incorporated the temperature-dependent DAD model in addition to the production bias model produced good agreement with growth data [40]. However, it is important to note that limited information was available at the time concerning defect mobility and dissociation rates and, as such, several assumptions were required to fit the data. For example, it is now known that defect clusters are in fact mobile [25, 80] and that monovacancy diffusion may be significantly more anisotropic than Woo assumed [49].

Golubov et al. later based an expanded model on the PBM to attempt to explain concepts such as breakaway growth, negative a-type strains, and the co-existence of vacancy and interstitial type a-loops [96]. The production of SIA clusters from displacement cascades was considered in addition to their 1-D migration tendencies; conversely, vacancies are

conveniently assumed to not cluster at all in displacement cascades (despite considerable evidence otherwise [10-12]). Additionally, the dislocation bias for absorption of SIA defects is ignored, all anisotropy effects were disregarded, and point defect recombination is neglected. The unique predictions of this model stemmed from the assumption that 1-D migrating SIA clusters do not interact with c-type loops or a-type loops with non-parallel Burgers vectors to that of the cluster [96]. Thus, c-loops are able to grow through vacancy absorption (the number of mobile monovacancies is much greater than single interstitials due to the assumed lack of vacancy clustering in-cascade). Simultaneous growth of interstitial and vacancy a-loops is only explained with this model if the authors assume there is an asymmetric distribution of a-type dislocations along the three primary a-axes. This model was later refined by Barashev et al., but all irradiation growth predictions were arbitrarily determined by manually adjusting the terminal density of a-loops, critical nucleation dose of c-loops, terminal dose of c-loops, and terminal density of c-loops [97]. As such, no mechanistic understanding could be gleamed from their approach.

1.4.2 Cluster dynamics models

In contrast to the early irradiation growth models (which were simpler low-order models based on single concepts), CD modeling aims to directly track the evolution of cluster concentrations through parameterized rates. The earliest cluster dynamics model developed by Christien and Barbu introduced SIA diffusion anisotropy to model the growth of electron-irradiated Zr thin foils [98]. Only Frenkel pairs were considered to be produced (electron irradiation), defect clusters were assumed to be immobile, and only two parallel surfaces were implemented (thin foil). SIA anisotropy was considered to modify SIA interaction rates with dislocation lines, dislocation loops, and the two parallel surfaces [98]. Under this framework, microstructure evolution was found to vary significantly based on the angle of the foil surface with the predominant SIA flux direction. When the foils were oriented such that the bias for surface absorption of SIAs was greater than dislocation loops, vacancy loops were capable of growing.

In an attempt to address the breakaway irradiation growth phenomenon, Christien and Barbu expanded their CD model to incorporate the nucleation of c-loop defects [99]. Their model was benchmarked against neutron-irradiated single-crystalline pure Zr growth data [4]. As such, surfaces are ignored in their calculations. Other assumptions include the fact that only point defects are mobile, that only Frenkel pairs are created from neutron irradiation (inconsistent with the wealth of displacement cascade data available at the time [7, 10, 11, 68]), and that pre-existing dislocation lines are ignored. The diffusivities of single interstitials and monovacancies are manually adjusted to fit to experimental data. Considering this model for single-crystalline Zr, only interstitial a-loops are found to form at low fluence; vacancy a-loops were unable to grow under their parameter set. In order to model breakaway irradiation growth, c-loops are assumed to nucleate at Fe clusters, which exist prior to irradiation and are assumed to not ballistically dissolve under irradiation [99]. The number density of c-loops, then, was arbitrarily set to the number density of Fe clusters.

Comparisons with experimental data relied on adjusting the Fe cluster density rather than implementing known densities from experiments. Once nucleated, the growth of the c-loops was driven by the difference in anisotropy of single interstitials and monovacancies.

In an attempt to reduce the number of assumptions, Li and Ghoniem recently developed a reduced set of cluster dynamics equations to model irradiation growth strains [100]. Unlike all previous models, the production of defect clusters was considered from displacement cascades. Unfortunately, only the production of di- and tri- defects were implemented, and the clustering fractions were considered to be $3.5x10^{-4}$ and $3.3x10^{-8}$ for interstitials and vacancies, respectively. It is well understood that these fractions should be in the range of 0.2 to 0.6, several orders of magnitude greater than the values assumed in this approach [10, 11]. The values of point defect diffusivities were set equal to the values that Christien and Barbu manually adjusted in their CD approach rather than basing the calculations on lower-length scale data. For this model, vacancy a-loops were entirely ignored (despite accounting for more than half of visible microstructure at low fluence [13, 17]). The growth of vacancy clusters via monovacancy absorption were the basis for c-loop nucleation. In order to delay their growth, c-loops below some critical radius were assigned a reduced capture efficiency for monovacancies (an arbitrary value of 20% efficiency) in order to fit experimental data.

1.4.3 Summary of issues with irradiation growth modeling

It is evident from the overview presented in the preceding sections that the current state of irradiation growth modeling is quite lacking. While many of these modern approaches are more complex than early models, and theoretically better equipped to incorporate fundamental mechanisms, there is a tendency to arbitrarily adjust the physics to best fit experimental data. Oftentimes parameters are adjusted well outside of reasonable ranges. Despite such a wide array of approaches and adjusted parameters, each of these models reports a near-perfect agreement with experimental data. The consequence of such practices is that it is impossible to gauge which of the underlying physics may be mechanistically responsible for microstructure evolution. Despite decades of modeling attempts, the driving force for the simultaneous growth of interstitial and vacancy a-loops, as well as the nucleation and growth of c-loops, is entirely ambiguous.

Common issues and assumptions with current irradiation growth modeling includes: 1) only point defects are assumed to be mobile; 2) defect cluster production from displacement cascades is largely ignored; 3) mobile defect diffusivities are based on manually adjusted parameters; 4) binding energies are based on manually adjusted parameters; 5) Vacancy a-loops are almost entirely ignored; 6) c-loop densities are arbitrarily forced into the models to fit breakaway growth strains; and 7) critical parameters are adjusted to unphysical values to match experimental data. Parameters such as defect diffusivity, defect generation rates, and interaction energies should be derived from lower-length scale techniques rather than manually adjusted. There is a significant need for scale-

bridging computational modeling to provide a truly mechanistic model capable of describing microstructural evolution.

1.5 Dissertation goals and outline

Irradiation growth of α-Zr and its alloys is a fascinating phenomenon that ultimately stems from the inherent anisotropy of the hcp crystal structure. This anisotropy leads to a multitude of microstructural and mechanistic responses to irradiation that are uniquely different than more common isotropic metals. Within this behavior, there are two broad observations that are the most critical for predicting irradiation growth behavior: 1) vacancy and interstitial dislocation a-loops co-exist and dominate the irradiated microstructure at low-to-moderate fluences; 2) faulted basal vacancy c-loops nucleate after some incubation dose in correlation with the onset of breakaway irradiation growth. Despite decades of experimental and computational research, neither of these observations can be satisfactorily explained or modeled from a mechanistic viewpoint. Most of the modeling attempts to date have either not been able to appropriately capture simultaneous vacancy and interstitial a-loop growth [99], or have out-right ignored vacancy a-loops in their models [94, 100-102]. Any modeling attempts that claim to sufficiently model all three stages of irradiation growth while ignoring half of the visible microstructure in irradiated Zr cannot provide any physically-relevant conclusions. Furthermore, c-loop nucleation and growth is traditionally either arbitrarily adjusted into the model [96, 97] or based on physically unreasonable mechanisms [99-101].

The goal of this dissertation is thus split into two categories: 1) to elucidate the mechanisms governing microstructure evolution and develop a database to describe such mechanisms; 2) to incorporate this database into a mechanistically-based cluster dynamics (CD) model capable of describing interstitial and vacancy a-loop co-existence in addition to c-loop nucleation and growth. This goal requires a multi-scale approach that bridges several orders of magnitude of length and time scales. Lower-length scale techniques such as density functional theory (DFT) and molecular dynamics (MD) have been used to simulate interactions at the atomic scale and provide essential parameters, including: 1) Interaction energies of solute and impurities with stacking faults and c-loop precursors; 2) defect production terms from displacement cascades; 3) preferred defect cluster configurations and mobilities; 4) defect binding energies; 5) dislocation loop stress states; and 6) defect capture radii. While some of these aspects have been investigated previously in Zr literature, the mechanisms are rarely reported in sufficient detail to incorporate into higher-order models.

1.5.1 Overview of scale-bridging computational modeling

For this dissertation, fundamental parameters will be derived using the lower-length scale techniques of DFT and MD; these parameters will directly inform a CD model such that extraneous assumptions are reduced to a minimum. Graphical representation of the length and time scales that these three techniques are capable of probing is provided in Fig. 1-6. A brief summary of these tools is provided along with a description of their capabilities and limitations:

- **Density Functional Theory (DFT):** DFT is a quantum mechanical modeling technique that simplifies the many-body Schrödinger equation by treating electrons with a density function [103]. The interactions between core electrons of an atom and its nucleus are treated based on user-defined pseudopotentials. Despite many useful approximations (such as the local density or generalized gradient approximation for the exchange-correlation functionals), DFT is capable of accurately investigating the electronic structure of many-body systems. Users provide the positions for atoms within a structure of interest, and upon determining the minimized energy of the system, several useful properties can be determined. This can include defect formation energies, interaction energies, lowest energy configurations, or even migration energies. Due to the computational cost involved, however, systems are typically restricted to a few hundred atoms.

- **Molecular Dynamics (MD):** MD codes implement user-defined interatomic potentials to describe the interactions between neighboring atoms and solve Newton's equations of motion to simulate their trajectories [104]. Interatomic potentials are informed by extensive DFT datasets, but the accuracy of MD simulations is generally considered to be lower than DFT. While *ab initio* MD is possible to implement, this technique has not been explored in this dissertation. In exchange for reduced accuracy, MD simulations are able to include up to millions of atoms and can reach times of up to tens or hundreds of nanoseconds. As such, MD can investigate large defect structures, defect cluster mobilities, displacement cascades, stress states, and interaction radii. It is critical to understand that the selection of interatomic potentials may significantly alter the values derived from these simulations. As such, any quantitative conclusions should be considered with caution, and the limitations of each selected potential must be adequately weighed.

- **Cluster Dynamics (CD):** CD modeling is built upon mean field rate theory (MFRT), which relied on point defect balance equations to predict SIA and monovacancy concentrations [105]. As an expansion of this fundamental approach, CD modeling additionally considers the concentrations of defect clusters and models their interaction with mobile defects through a system of reaction-diffusion equations. Rather than implementing the underlying lattice structure of materials, CD tracks

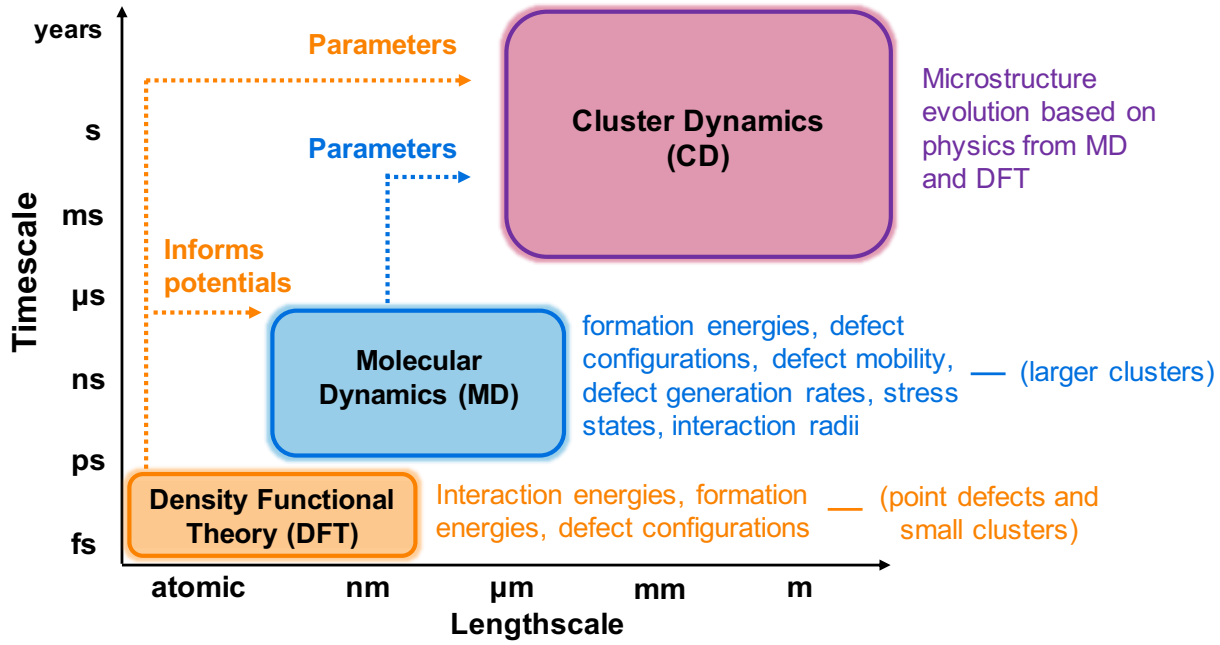

Fig. 1-6. Graphical representation of computational modeling spanning several orders of magnitude along the length and time scales. Lower-length scale techniques directly inform higher-order techniques.

the concentration of defects over long times (up to several years) and the equivalent of large length scales (up to several meters). The accuracy of CD models is entirely dependent on the parameter set that users define, and should be based on values calculated either experimentally or with lower-length scale techniques. If implemented correctly, CD models can provide a wealth of knowledge through the correlation of physical mechanisms with microstructural evolution.

1.5.2 Dissertation structure and chapter breakdown

The work involved in this dissertation has been approached under a "bottom-up" analysis pipeline: lower-length scale simulations were performed to provide the mechanistic parameters to inform a higher-order CD model. In order to put the lower-length scale simulations into proper perspective, an overview of the CD model and the necessary parameters will be provided first. Once the parameters of interest have been described, and it is made clear which areas are lacking in literature, individual chapters will detail the simulation work involved to provide an adequate database. Finally, it will be detailed how the various mechanisms were incorporated into the CD model, and the model predictions of microstructural evolution will be analyzed. Thus, the outline of this dissertation is as follows:

- **Chapter Two – Cluster Dynamics Model Overview:** Fundamental equations for defect concentration balance are provided, and each of the intended interactions is described in a high-level overview. The necessary parameters that are lacking in current literature are identified, and the recommended tools to determine are outlined.

- **Chapter Three – Effect of Solute and Impurity Segregation on Stacking Fault and Vacancy Platelet Energetics:** Common stacking faults pertaining to a-loop and c-loop structures, in addition to c-loop vacancy platelet precursors, are constructed. Interaction energies between common solute and impurities with these structures are calculated with DFT.

- **Chapter Four – Defect Production from Displacement Cascades: Quantifying the Effect of Electronic Stopping:** MD simulations of displacement cascades are performed to assess the generation rates of point defects and their clusters. The impact of a friction force proportional to electronic stopping powers on defect generation rates is quantified.

- **Chapter Five – Defect Cluster Configurations and Mobilities:** The preferred configurations for small and large defect clusters are determined via molecular statics calculations. Mean-squared displacement calculations are then performed with MD to tabulate diffusivities within the basal plane and along the c-axis.

- **Chapter Six - Dislocation Loop Stress States and Point Defect Capture Radii:** Interstitial a-loops, vacancy a-loops, and vacancy c-loops are constructed and MD calculations of stress states radial and perpendicular to these loops are performed. The binding energy maps of point defects are calculated and used to determine capture radii via spontaneous and thermal drift methods.

- **Chapter Seven – Cluster Dynamics Modeling of Interstitial and Vacancy a-Loop Co-Existence:** The database collected from lower-length scale simulations are incorporated into the CD model. It is then demonstrated that scale-bridging computational modeling can effectively predict the coexistence of interstitial and vacancy a-loops.

- **Chapter Eight – Cluster Dynamics Modeling of c-Loop Nucleation and Growth:** The CD framework described in Chapter Seven is extended to consider the nucleation and growth of c-loops. The key parameters relating to nucleation and growth rates are identified and discussed.

- **Chapter Nine – Conclusions and Recommended Future Work:** Critical observations derived from the CD model will be summarized and compared with earlier attempts in literature. Aspects of the model that would require future improvement are detailed to motivate additional work in the field.

Chapter Two:

Cluster Dynamics Model Overview

Initially based on the classical rate theory approach, CD modeling expands upon point defect balance equations to consider defect clusters and their interactions. The CD approach is at its essence a coupled set of reaction-diffusion equations that governs defect cluster concentrations as a function of time [105]. The change in any given cluster population is determined through a balance of gains and losses of that cluster:

$$\frac{dC_i}{dt} = g_i + \nabla(D_i \nabla C_i) - D_i k_i^2 C_i + \sum_{n+m \to i} k_{n,m}^{+} C_n C_m - \sum_j k_{i,j}^{+} C_i C_j + \sum_{n \to n-i,i} k_{n-i,i}^{-} C_n - \sum_j k_{i,j}^{-} C_i \quad (2\text{-}1)$$

Where C_i is the volumetric concentration of defect species *i*. The right-hand-side (RHS) terms of Eq. (2-1) correspond to the changes in cluster *i* concentration as a result of production from displacement cascades, spatial diffusion, loss at existing sinks, production of *i* from cluster interaction, loss of *i* from cluster interaction, production of *i* from cluster dissociation, and loss of *i* from *i* dissociation, respectively. For the work in this dissertation, defect clusters are assumed to be randomly and uniformly distributed; changes in defect concentrations from spatial diffusion (the second RHS term) are ignored. In this chapter, the general equations governing the key reactions will be derived, and the parameters necessary to perform the calculations will be identified. This overview is intended to motivate the work performed in Chapters Two through Six. In Chapter Seven, this model will be applied to the irradiated α-Zr system and specific details relating to the types of clusters and their behaviors (which depend upon insight from Chapters Three through Six) will be outlined there along with critical assumptions.

2.1 Descriptions of reactions and physical processes

2.1.1 Defect source term (g_i)

With the exception of the source term, all of the reactions involved in Eq. (2-1) conserve a mass balance of the species involved; interstitial and vacancy species are either mutually annihilated, or are evolved through interaction with mobile species. The source term provides the single method through which additional defects are introduced into the net system. Physically, any given cluster *i* can be produced as residual damage from a displacement cascade event. MD simulations provide insight into the number of defects of each cluster size that may be generated from cascades initiated by PKAs of any given energy [10-12, 68]. In order to convert this data into a meaningful parameter for CD modeling, one must consider the expected PKA energy spectrum for a specific neutron flux profile. In this dissertation, we have decided to simulate typical PWR operating conditions, for which an expected Zr PKA spectrum has been estimated with SPECTRA-PKA in Fig. 2-1[106]. The generation source term for any given cluster *i* can then be calculated as:

$$g_i = \sum_{40\ eV}^{E_{PKA,max}} N_i(E) * \phi(E) \qquad (2\text{-}2)$$

where $N_i(E)$ is the average number of cluster *i* produced from a PKA of energy *E* and $\phi(E)$ is the number of PKAs produced with energy *E* per s per volume. The total volumetric production of *i* is simply determined by summing along the spectrum of possible PKA energies per s per volume (Fig. 2-1). The energy range is considered from 40 eV, the recommended atomic displacement energy in α-Zr [107], up to the maximum PKA energy in the estimated spectrum, $E_{PKA,max}$. Many values for $N_i(E)$ have been reported in literature, but only one set of MD simulations has incorporated electronic stopping effects in their approach [12]. Unfortunately, $N_i(E)$ is reported in coarse bins, with no distinction between clusters of size 2 < n < 10, 11 < n < 40, and 41 < n < 80. This data resolution is too poor to provide an accurate defect source term. Thus, MD simulations of displacement cascades have been performed for this dissertation, and a full description of electronic stopping effects of defect production is provided in Chapter 4.

2.1.2 Defect diffusivity (D_i) and anisotropy

The transport of mobile defects within a material defines the rates at which they interact with pre-existing sinks, other mobile defects, and defects clusters; as such, defect diffusivity directly affects every RHS term in Eq. (2-1)with the exception of the source term. In isotropic materials, the determination of D_i depends only upon two parameters: the

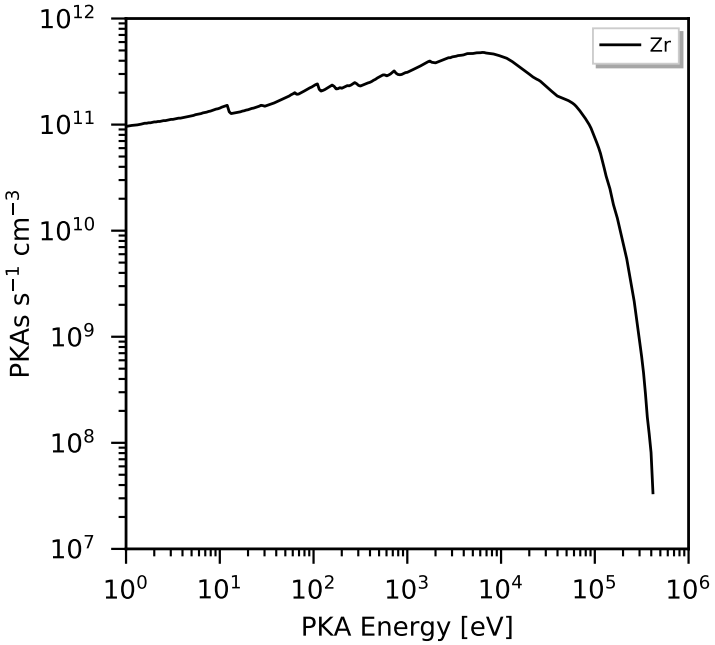

Fig. 2-1. Estimated Zr PKA spectrum from a typical PWR neutron flux profile (SPECTRA-PKA [106]).

diffusivity pre-factor, D_0, and the migration energy, E_m. A standard Arrhenius dependence relates these two parameters to the defect diffusivity at any given temperature, T:

$$D_i(T) = D_0 \exp \frac{-E_m}{k_b T} \quad (2\text{-}3)$$

For inherently anisotropic hcp materials such as α-Zr, mobile defects do not migrate equally in all directions, and the concept of an unbiased sink is no longer applicable. Defects tend to preferentially migrate within the basal plane along the primary a-axis directions rather than along the c-axis [49, 50, 66, 108, 109]. Furthermore, because all directions of 1-D glide are contained within the basal plane, 1-D SIA cluster glide can only contribute to a mass 2-D transport within the basal plane [25]. The consequence of this anisotropic migration behavior is that the capture efficiency of any sink now depends upon the geometry of the sink; sinks with capture volumes or surfaces parallel to the c-axis will preferentially capture basal-plane diffusers. The capture efficiency, $P(\lambda)$, itself will depend upon the angle between the sink surface (or line direction) and the c-axis, λ, as well as the anisotropy factor of the mobile defect diffusion, p [46]:

$$P(\lambda) = \frac{\sqrt{\cos^2 \lambda + p^6 \sin^2 \lambda}}{p^2} \quad (2\text{-}4)$$

$$p = \left(\frac{D_i^c}{D_i^a}\right)^{\frac{1}{6}} \quad (2\text{-}5)$$

Schematics of the basal plane diffusion, D_i^a, and c-axis diffusion, D_i^c, for a migrating specie relative to common dislocation lines and surfaces are illustrated in Fig. 2-2 for visual clarity [46]. For the purposes of CD modeling of anisotropic species, it is necessary to modify the reaction-diffusion equations that govern cluster evolution. As a replacement of D_i for isotropic diffusers, it is necessary to instead calculate a mean diffusivity factor [98, 99]:

$$\overline{D}_i = \left(D_i^{a\,2} D_i^c\right)^{\frac{1}{3}} \quad (2\text{-}6)$$

When considering the interaction between any mobile defect with a sink that exhibits a distinct geometry (such as dislocation lines, loops, and surfaces), the rate must be multiplied by the capture efficiency of that sink ($P(\lambda)$, Eq. (2-4)). For example, <a>-type edge dislocations lie parallel to the c-axis ($\lambda = 0°$) while <c>-type dislocations lie perpendicular to the c-axis ($\lambda = 90°$). The sink strength for <a>-type and <c>-type dislocation lines, respectively, can be calculated as such:

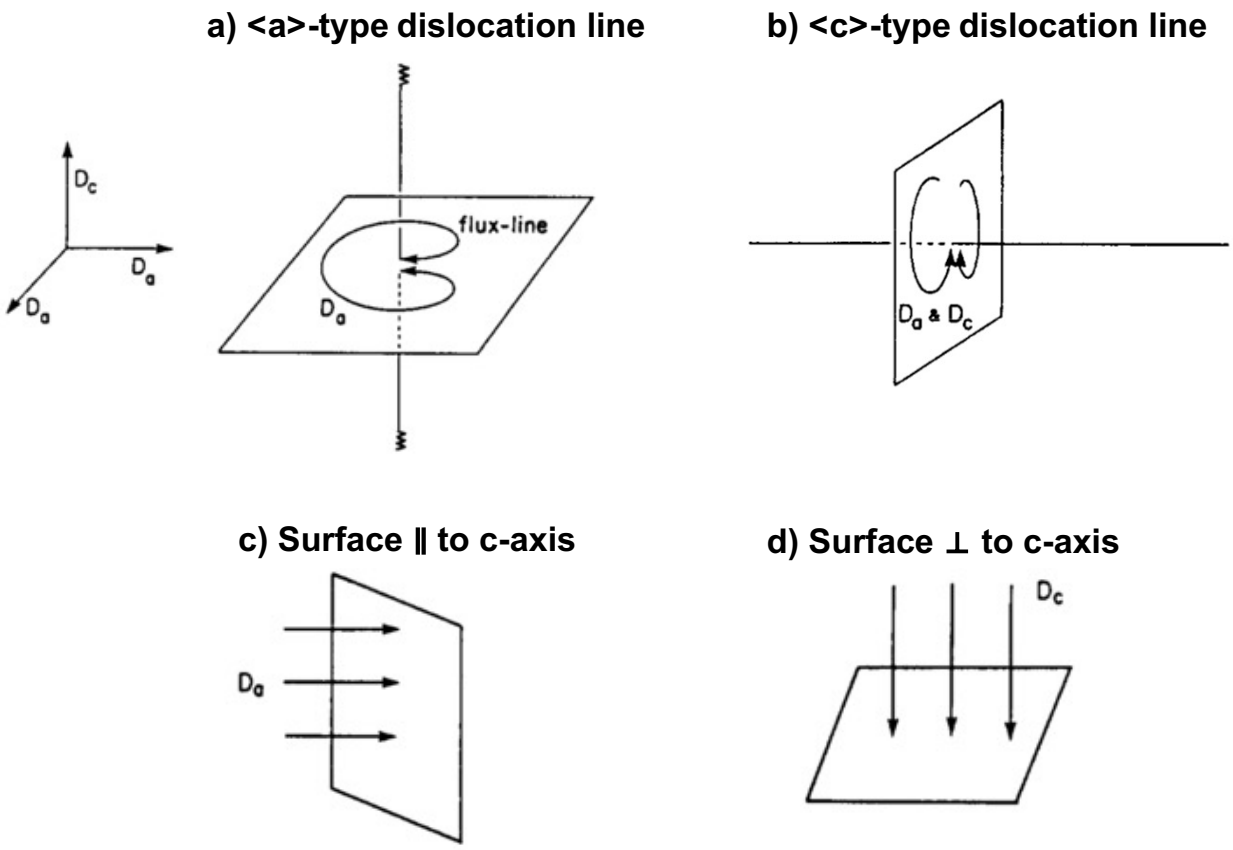

Fig. 2-2. Schematics for the basal plane diffusion (D_a) and c-axis diffusion (D_c) of migrating species relative to a) dislocation lines parallel to the c-axis (<a>-type dislocation lines), b) dislocation lines perpendicular to the c-axis (<c>-type dislocation lines), c) surfaces parallel to the c-axis, and d) surfaces perpendicular to the c-axis, as reproduced from [46].

$$k^{a}{}_{i}^{2} = Z_i \rho_d^a \cdot P(\lambda = 0°) = Z_i \rho_d^a \cdot p^{-2} \quad (2\text{-}7)$$

$$k^{c}{}_{i}^{2} = Z_i \rho_d^c \cdot P(\lambda = 90°) = Z_i \rho_d^c \cdot p \quad (2\text{-}8)$$

where Z_i is the EID bias for mobile defect *i*, ρ_d^a is the dislocation line density of <a>-type edge dislocations, and ρ_d^c is the dislocation line density of <c>-type edge dislocations. The calculation for the capture efficiencies of dislocation loops are more complex than for dislocation lines; the angle between dislocation loop line segments and the c-axis vary along the perimeter of the loop. The CD model of Christien and Barbu approximated dislocation loops as hexagons with an equivalent perimeter [98], but this approach has recently been reformulated for a general case [110]. P. Saidi et al. consider a dislocation loop to consist of dislocation lines on a closed path ζ for which the overall capture efficiency is a summation of the contribution from each length segment:

$$P(\lambda), loops = \frac{\int P(\lambda) d\zeta}{\int d\zeta} = \frac{p^{-2} \int_0^{\pi/2} \left(1 - f(\Theta) + p^6 f(\Theta)\right)^{\frac{1}{2}} (1 - e^2 \sin^2 \Theta)^{\frac{1}{2}} \, d\Theta}{a \int_0^{\frac{\pi}{2}} (1 - e^2 \sin^2 \Theta)^{\frac{1}{2}} \, d\Theta} \quad (2\text{-}9)$$

$$f(\Theta) = \left(\left(\frac{b}{a} \right)^4 \left(\frac{1}{\sin^2 \Theta} - 1 \right) + 1 \right)^{-1} \quad (2\text{-}10)$$

$$\cot \lambda = \left(\frac{b}{a} \right)^2 \cot \Theta \quad (2\text{-}11)$$

where a is the semi-major axis, b is the semi-minor axis, and e is the eccentricity of an elliptical loop, respectively [110]:

$$e = \sqrt{1 - \frac{b^2}{a^2}} \quad (2\text{-}12)$$

The capture efficiency for prismatic a-loops must be determined through numerical integration of Eq. (2-9); for basal c-loops, all dislocation line segments are perpendicular to the c-axis, and $P(\lambda)$ is simply equal to the anisotropy factor, p, as calculated with Eq. (2-4) using $\lambda = 90°$. Interstitial a-loops are known to be less elliptical than vacancy a-loops, with semi-axis ratios of approximately $b/a = 0.95$ and $b/a = 0.80$, respectively [17]. The effect

that this has on capture efficiencies is demonstrated graphically in Fig. 2-3, which compares these efficiencies for interstitial a-loops, vacancy a-loops, c-loops, basal (<c>-type) dislocation lines, and prismatic (<a>-type) dislocation lines as a function of the mobile defect diffusional anisotropy factor, p (Eq. (2-5)). Elliptical loops are more likely to capture basal-plane diffusers than circular loops due to the fact that a greater fraction of the peripheral line segments have small λ angles.

In order to satisfactorily capture this behavior within a CD code, we must know the diffusion prefactors and migration energies for all mobile defects, and these must be separated in terms of basal-plane and c-axis migration. This data is currently only available for point defects [48, 49]. While there has been some work concerning the mobility of SIA clusters, diffusivity data has not been provided [25, 80]. Furthermore, no data exists for the diffusivities of vacancy clusters. Thus, it was necessary to perform MD simulations for long-term trajectories of SIA and vacancy cluster diffusion, and this work is detailed in Chapter Five of this dissertation.

2.1.3 Cluster Reactions (k_{ij}^{+})

Cluster reactions are assumed to be diffusion-limited such that two species *I* and *J* react spontaneously when either one migrates within some defined interaction volume with the other [111]:

$$i + j \xrightarrow{k_{ij}^{+}} ij \qquad (2\text{-}13)$$

The forward reaction constant, k_{ij}^{+}, is dependent upon the rate of transport of the reactants rather than the rate of formation of the product. For clusters or point defects which are expected to have roughly spherical interaction volumes, the clustering rate constant takes a simple form [105]:

$$k_{ij}^{+} = 4\pi r_{ij}\left(\overline{D}_i + \overline{D}_j\right) \qquad (2\text{-}14)$$

where r_{ij} is the interaction distance between clusters *i* and *j*. The quantity r_{ij} depends upon the radii of the reactant clusters in addition to the separation distance at which spontaneous combination occurs, r_{ij}^{0} [105]:

$$r_{ij} = r_i + r_j + r_{ij}^{0} \qquad (2\text{-}15)$$

The calculation of the reactant cluster radii will depend upon their morphology. Small SIA and vacancy clusters can be considered to be spherical in shape; for a cluster with n defects, the radius can be estimated by setting $n\Omega$ equal to the volume of a sphere and solving

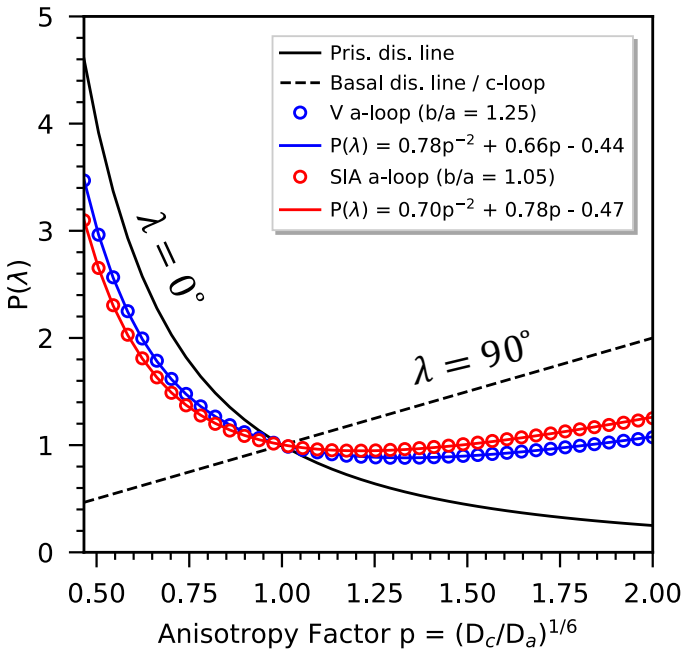

Fig. 2-3. Capture efficiencies for SIA a-loops, vacancy a-loops, vacancy c-loops, prismatic (<a>-type) dislocation lines, and basal (<c>-type) dislocation lines are plotted as a function of the mobile defect anisotropy factor, *p*.

for r_n, where Ω is the atomic volume of the material:

$$r_n = \left(\frac{3n\Omega}{4\pi}\right)^{\frac{1}{3}} \quad (2\text{-}16)$$

$$\Omega = \frac{\sqrt{3}}{4}a^2c \quad (2\text{-}17)$$

where a and c are the hcp lattice parameters. In order to estimate the radii of dislocation loops, n vacancies are assumed to occupy a disk of radius R_n and thickness b_n, the edge component of the loop Burgers vector normal to its habit plane [37]:

$$\pi R_n^2 b_n = n\Omega \quad (2\text{-}18)$$

Considering that $b_n = \sqrt{3}a/2$ for prismatic a-loops and $b_n = c/2$ for basal c-loops, inserting Eq. (2-17) into Eq. (2-18) yields the following expressions for the radii of these dislocation loop types, respectively [37]:

$$R_n^{prism} = \sqrt{\frac{acn}{2\pi}} \quad (2\text{-}19)$$

$$R_n^{basal} = a\left(\frac{\sqrt{3}n}{2\pi}\right)^{\frac{1}{2}} \quad (2\text{-}20)$$

Due to their disk-like nature and capture tendencies, large dislocation loops have toroidal reaction volumes [112]. However, this is only true once the loop radius notably exceeds the interior radius, where the interior radius can be considered equal to the loop radial defect capture distance, r_d. If this condition is not met (i.e. the loop radius and interior radius are comparable in size), the dislocation loop will either have a spherical or mixed reaction volume. A transition parameter, α_{ij}, allows a smooth transition between spherical and toroidal interaction rates [113, 114]. For a mobile defect j interacting with loop i, the isotropic rate expressions are:

$$k_{ij}^{+}, loops = \left(\left(1-\alpha_{ij}\right)z_{ij}^{L} + \alpha_{ij}z_{ij}^{V}\right)\left(\overline{D}_i + \overline{D}_j\right) \quad (2\text{-}21)$$

$$\alpha_{ij} = \left(1 + \left(\frac{r_i}{3\left(r_j + r_d\right)}\right)^2\right)^{-1} \quad (2\text{-}22)$$

$$z_{ij}^{v} = 4\pi(r_i + r_j + r_d) \quad (2\text{-}23)$$

$$z_{ij}^{L} = \frac{4\pi^2 r_i}{\ln(1 + 8r_i/(r_j + r_d))} \quad (2\text{-}24)$$

When considering that the mobile defect *j* will diffuse anisotropically in α-Zr, it is necessary to modify the capture efficiency for dislocation loops, which have distinct geometries. Because the rate constant calculated with Eq. (2-21) contains both spherical and toroidal reaction components, it is not appropriate to modify this constant by an anisotropic capture efficiency; only the toroidal component must be modified, as this pertains to the geometry of the dislocation loop. Thus, for anisotropic systems we can consider a partially modified rate constant expression:

$$k_{ij}^{+}, loops^{*} = \left(\left(1 - \alpha_{ij}\right) z_{ij}^{L} P(\lambda) + \alpha_{ij} z_{ij}^{V}\right)\left(\overline{D}_i + \overline{D}_j\right) \quad (2\text{-}25)$$

where $P(\lambda)$ is the anisotropic capture efficiency. For prismatic a-loops, $P(\lambda)$ is calculated with Eq. (2-9); for basal c-loops, $P(\lambda)$ is simply set equal to *p*, the anisotropy factor of mobile defect *j*. In order to accurately calculate these rate values in a CD model, mobile defect diffusivities and anisotropy must be explicitly known at all temperatures; this will be addressed in Chapter Four. Additionally, the point defect capture radius must be known for each loop type as a function of loops size. As this has not yet been investigated in literature, molecular statics calculations of point defect capture were performed, and the results are outlined in Chapter Five of this document. In Chapter Seven, these rates will be applied for defect cluster interactions in α-Zr, and a list of the possible reactions, along with the equations necessary to calculate the relevant rate constants, will be explicitly tabulated.

2.1.4 Cluster Dissociation (k_{ij}^{-})

In contrast to clustering reactions, dissociation events result in the emission of a defect *i* from cluster *n* to produce a cluster *j* with a size equal to (*n*-*i*):

$$n \xrightarrow{k_{ij}^{-}} i + (n-1) \quad (2\text{-}26)$$

For this dissertation, we assume that only monomers can be emitted from defect clusters. This emission, then, is a thermally activated process for which the thermal concentration of defect *i* at a cluster surface can be written [105]:

$$C_{n,i}^{0} = \frac{1}{\Omega} \exp \frac{-E_{n,i}^{b}}{k_b T} \quad (2\text{-}27)$$

where $E_{n,i}^{b}$ is the binding energy of *i* to *n.* The dissociation rate is determined by setting up an equilibrium expression between the dissociation rate of cluster *n* and the reverse clustering reaction:

$$k_{i,n-i}^{+} C_i^{eq} C_{n-i}^{eq} = k_{n,i}^{-} C_n^{eq} \quad (2\text{-}28)$$

Common expressions for cluster dissociation rates are derived by relating the equilibrium concentrations in Eq. (2-28) to the law of mass action (Eq. (2-29)) and assuming that the free energy change is dominated by the cluster binding energy [105]:

$$\exp \frac{-E_{n,i}^{b}}{k_b T} = \frac{\Omega \mathrm{C}_i^{\mathrm{eq}} \Omega C_{n-i}^{eq}}{\Omega \mathrm{C}_n^{\mathrm{eq}}} \quad (2\text{-}29)$$

$$k_{n,i}^{-} = \frac{k_{i,n-i}^{+}}{\Omega} \exp \frac{-E_{n,i}^{b}}{k_b T} \quad (2\text{-}30)$$

The defining parameter that drives cluster dissociation rates is the cluster binding energy. For tightly bound structures, such as large SIA clusters, one would expect low monomer emissions rates; conversely, small vacancy clusters exhibit characteristically low monovacancy binding energies, and are expected to dissociate more readily. This is particularly true at higher temperatures. *Ab initio* binding energies for small vacancy clusters are available in literature [37], but the binding energies of larger defect clusters have only be determined through molecular statics methods [37, 79-81]. In these cases, the reported binding energies are only as accurate as the semi-empirical potentials that were used. Both the A95 and M07 #2 potentials predict that voids offer the most tightly-bound (lowest formation energy) configuration for vacancy clusters [37, 81] while experiments have shown that this clearly is not the case [13, 45, 115]. In Chapter Five of this dissertation, we compare these predicted binding energy values with those calculated with a modern interatomic potential published in 2020 [78] and comment on the accuracy of these potentials.

2.2 Cluster dynamics code, Xolotl

For this dissertation, microstructure evolution is modeled with Xolotl, a cluster dynamics code that was developed to simulate gas bubble and defect microstructure evolution in plasma facing components and structural materials for fusion applications [116-118]. A system of coupled ordinary differential equations (ODEs) is generated to track the populations of each defect *I,* Eq. (2-1). These ODEs are then solved using the finite difference method and implicit time integration with PETSc [119]. Each defect of interest is assigned to a species sub-type and characteristic parameters such as the defect radius, diffusivity, anisotropy factor of diffusion, binding energy, and generation rate from displacement cascades are explicitly defined within Xolotl. The possible set of reactions between species sub-types are defined, such as clustering, annihilation, and dissociation. For each of the desired reactions, the reaction rate constants are calculated based on the expressions described in Section 2.1. Subsequently, the rates governing all reactions are calculated, and the changes in cluster populations within a user-supplied timestep, dt, can be obtained by

time integration of the set of coupled reaction-diffusion ODEs. In this work, we consider only 0-D calculations, although Xolotl is capable of generating a spatial grid to extend calculations to 1-D, 2-D, and 3-D, which may provide interesting possibilities for future work.

2.3 Necessary parameters for the CD model

Microstructure evolution in α-Zr can be modeled by applying Eq. (2-1) to a large number of interstitial and vacancy clusters and iteratively solving to track their populations over time. The underlying physics behind that evolution is applied through the various cluster characteristics and rate constants derived in Section 2.1. As such, the CD model is only as accurate as the parameters that are used as input, and a considerable amount of data is still lacking in literature. Chapters Three through Six detail various lower-length scale simulations that were performed to fill in the gaps of the existing α-Zr database; in Chapter Seven, the new insight gained from these simulations will be applied to the CD framework defined here. Of most concern are the following fundamental parameters and behavior:

- **Solute and impurity binding energies with c-loops and c-loop precursors:** The binding energies of Fe, Cr, Sn, Nb, Ni, and H to stacking faults and vacancy platelets were calculated using DFT. These can inform nucleation models for c-loops. (Chapter Three)

- **Cluster source term, g_n:** These generation rates must be known for every cluster that is able to be produced from displacement cascades. Production data as a function of PKA energy was calculated, and the impact of electronic stopping quantified, with MD simulations. (Chapter Four)

- **Preferred cluster configurations and binding energies, $E^b_{n,i}$:** Cluster configurations directly impact reaction rates based on the anisotropy capture efficiencies; binding energies define cluster dissociation rates. Preferred geometries and their formation energies were calculated using the modern BMD19 potential with MD simulations. (Chapter Five)

- **Mobile defect diffusivities and anisotropy ($D^a_0, D^c_0, E^a_m, E^c_m, p$):** For anisotropic materials, it is critical to quantify the diffusivity of each mobile defect within the basal plane and along the c-axis. These quantities have been determined through mean-squared-displacement calculations using the modern BMD19 potential with MD simulations. (Chapter Five)

- **Defect capture radii, r_d:** The radial capture distance defines the inner radius for the toroidal reaction rates, and therefore affects both the rate magnitude and the steepness of the transition parameter. These radii were calculated for point defect

capture by common dislocation loops, and correlated to the stress states of these loops with MD simulations. (Chapter Six)

Chapter Three:

Effect of Solute and Impurity Segregation to Stacking Fault and Vacancy Platelet Energetics

The work in this chapter has been previously published in the Journal of Nuclear Materials by myself, Jose March-Rico, as the first author. The article titled, "The effect of local chemical environment on the energetics of stacking faults and vacancy platelets in α-zirconium" was co-authored with Guiyang Huang and Brian D. Wirth [55]. My role as first author included: research conceptualization, methodology development, results validation, formal analysis of the data, visualization, as well as writing the original and revised drafts. Two modifications were made when including the article into this chapter: 1) Figures from Appendix A of the article [55] were integrated into Section 3.1; 2) the implementation of the data obtained from this article into the CD model is described in an addended Section 3.6.

One of the proposed factors for the assisted nucleation of faulted c-loops is the "Suzuki effect", a reduction in stacking fault energy (SFE) by solute and impurity segregation to stacking fault interfaces [59]. This effect has been directly investigated in Cu [120], Ti [121], and Mg [122]. Density functional theory (DFT) calculations of H binding to stacking faults have been reported for the α-Zr system [19], but are lacking for other common alloying elements. The importance of these calculations can be understood by considering the formation of a vacancy dislocation loop with n vacancies and radius R. This energy can be approximated through a line tension model (Eq. (3-1)) containing two terms: 1) the stacking fault contribution, where γ is the SFE for a particular fault type, and 2) the geometric line tension contribution (related to the size of the Burgers vector by the core radius parameter, rc) [37]. Note that f is a shape factor and $\overline{K}$ is an elastic coefficient, and their values can be found in Ref. [37] for the vacancy loops of interest in α-Zr.

$$E_{loop}^{f}(n) = \pi R_1^2 \gamma n + 2\pi f R_1 \overline{K} \sqrt{n} \ln\left(\frac{R_1\sqrt{n}}{r_c}\right) \qquad (3\text{-}1)$$

For reported basal intrinsic (I_1), basal extrinsic (E), and prismatic ($\{10\bar{1}0\}$) SFEs of $\gamma_{I_1} = 147$ mJ/m^2, $\gamma_E = 274$ mJ/m^2, and $\gamma_{10\bar{1}0} = 211$ mJ/m^2 [37], respectively, the formation energies of basal and prismatic vacancy loops are plotted versus the number of vacancies in Fig. 3-1. The stacking fault contribution of vacancy loop energies becomes dominant at large sizes, for which the perfect prismatic *a*-loop is the thermodynamically preferred configuration. This is in agreement with the abundance of perfect *a*-loops and absence of

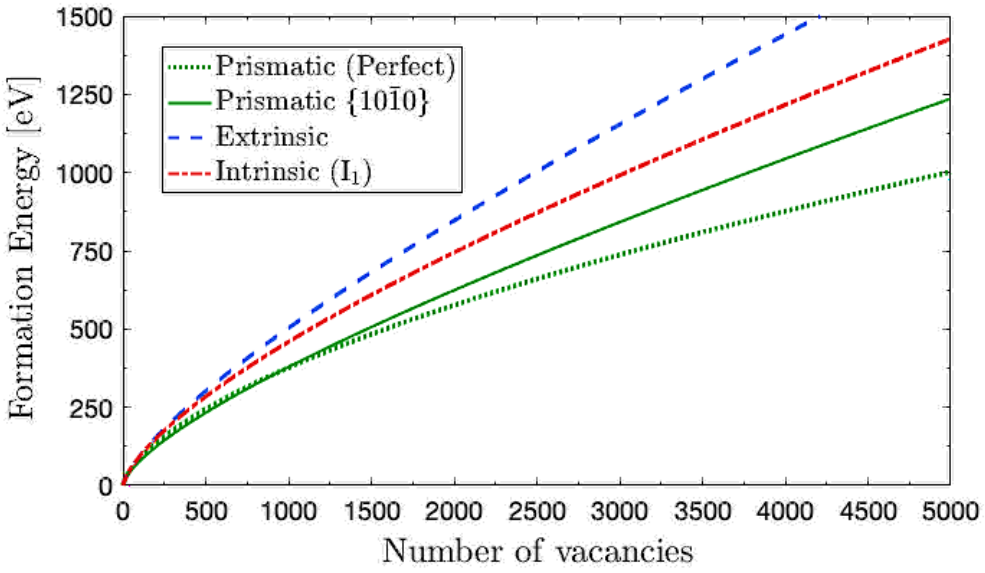

Fig. 3-1. Formation energies for perfect prismatic, prismatic {10$\bar{1}$0} faulted, basal extrinsic-faulted, and basal intrinsic-faulted vacancy loops in α-zirconium as a function of the number of vacancies.

faulted *c*-loops in irradiated α-Zr at low-to-moderate fluences [13, 16]. The work in this Chapter aims to directly investigate the interaction of Fe, Nb, Sn, Cr, and Ni with stacking fault interfaces in Zr through DFT calculations of binding energies. In this way, the impact of these chemical species on *c*-loop stability in the growth regime can be individually assessed. Additionally, their interaction with nucleating *c*-loop structures is investigated to demonstrate their impact in the nucleation regime, and determine any differences in interaction tendencies from the growth regime. The results reported here will support or refute one of the proposed solute-driven stabilization mechanism for *c*-loop formation and, therefore, the onset of breakaway irradiation growth in Zr alloys.

3.1 Modeling method

Ab initio DFT calculations were performed with the Vienna ab initio Simulation Package (VASP) using projector augmented-wave (PAW) pseudopotentials [123-128]. The pseudopotentials treated the following valence electron states: Zr ($4p^6 4d^2 5s^2$), Nb ($4p^6 4d^4 5s^1$), Sn ($5s^2 5p^2$), Fe ($3d^7 4s^1$), Cr ($3d^5 4s^1$), and Ni($3d^8 4s^2$). The generalized gradient approximation (GGA) was employed with the Perdew, Burke, and Ernzerhof (PBE) exchange-correlation functional [129]. The k-meshes for the Brillouin-zone integration were automatically generated using the gamma-centered scheme. Electronic states were occupied with a Methfessel-Paxton smearing width of 0.1 eV. A real-space projection scheme was used for all supercells containing greater than 20 atoms. The wave function optimization procedure was truncated when the energy difference between steps fell below 1E-5 eV and the residual forces for the relaxed atoms fell below 0.01 eV/Å. Spin-polarized calculations are adopted for systems containing Fe; otherwise, non-spin polarized calculations were adopted. The supercell sizes and specific k-mesh dimensions will be described for each of the stacking fault configurations in the following subsections. All binding energies for some element X to a defect structure of interest were calculated by an expression of the form provided in Eq. (3-2), where positive values denote attractive interaction. The calculation of the binding energy for an element X to a stacking fault, γ, is thus:

$$E^b_{X-\gamma} = \left[E_\gamma - E_{Zr}\right] - \left[E_{ZrX+\gamma} - E_{ZrX}\right] \qquad (3\text{-}2)$$

where E_γ is the energy of the structure containing the stacking fault, E_{Zr} is the energy of the perfect Zr lattice, $E_{ZrX+\gamma}$ is the energy of the stacking fault with element X, and E_{ZrX} is the energy of the perfect Zr lattice with element X. The supercell shape and size, k-point mesh, and plane wave energy cutoff were consistent when calculating the four energies involved in each calculation of the binding energy; the supercells used to calculate E_γ and $E_{ZrX+\gamma}$ were the same shape and size, and the supercells used to calculate E_{Zr} and E_{ZrX} were the same shape and size. The plane wave energy cutoff was set to the largest default cutoff energy in the pseudopotential files of the elements involved in each calculation. The default energy cutoffs for Zr, Fe, Sn, Nb, Ni, Cr, and H were 154.6, 267.9, 103.2, 293.2, 269.5, 227.1, and 250.0 eV, respectively. For example, when calculating the binding energy of Fe to any faulted

structure, a plane wave energy cutoff of 267.9 eV was selected when calculating E_γ, $E_{ZrFe+\gamma}$, E_{Zr}, and E_{ZrFe}.

The hcp crystal structure of α-Zr was considered with lattice constants of a = 3.236 Å and c = 5.173 Å calculated at 0 K, in good agreement with reported values of a = 3.234 Å and c = 5.169 Å calculated with DFT at 0 K [78]. For each supercell containing a stacking fault, the length perpendicular to the fault plane was manually relaxed to accommodate the excess volume introduced by the fault. The length is changed until an energy minimum is found, and this corresponding equilibrium length is used when constructing the faulted supercells. This process is shown graphically in Fig. 3-2(a,b,c) for basal intrinsic, basal extrinsic, and prismatic stacking faults (which will be further explained in the following sections). After applying the optimized relaxation coefficient to the supercell length perpendicular to the fault, all calculations were performed at fixed volume. The lattice constant parallel to the stacking fault is fixed to the calculated equilibrium value of hcp α-Zr. When solute atoms are added to the faulted supercells, the shape and volume are fixed to those of the supercell without the solute atom. Convergence of accurate binding energies is only possible with an adequately large supercell, as is demonstrated in Fig. 3-3.

3.1.1 Basal stacking faults

The collapse of a vacancy platelet onto a single basal plane within the perfect ABABAB hcp stacking sequence introduces a high-energy contact of two similar atomic layers as demonstrated in Eq. (3-3) [86]. In Zr, this metastable configuration is relieved by the formation of one of two basal stacking faults: the extrinsic (E) or intrinsic (I_1) faults. The extrinsic fault results from the shear of one layer adjacent to the fault plane (Eq. (3-4)) while the intrinsic fault is produced by the shear of multiple layers above the fault plane (Eq. (3-5)).

$$\ldots ABAB\boldsymbol{A}BAB \ldots \longrightarrow \ldots ABAB|BAB \ldots \quad (3\text{-}3)$$

$$\ldots ABAB|BAB \ldots \longrightarrow \ldots ABA\boldsymbol{BCA}BAB \ldots \quad (3\text{-}4)$$

$$\ldots ABAB|BAB \ldots \longrightarrow \ldots ABAB\boldsymbol{CBCB} \ldots \quad (3\text{-}5)$$

To construct the bulk reference supercell for the basal intrinsic and basal extrinsic stacking faults, the primitive cell was replicated 8 times in the [0001] direction (16 atomic layers, 41.4 Å), 5 times in the $[10\bar{1}0]$ direction (10 atomic layers, 16.2 Å), and 5 times in the $[1\bar{2}10]$ direction (10 atomic layers, 14.0 Å). This corresponds to a supercell containing 400 atoms. The basal intrinsic I_1 fault was constructed by shearing the atoms above the fault plane (half of the atoms in the supercell) by the displacement $1/3\,[\bar{1}100]$. This structure contains two stacking faults in one slab supercell with interfaces separating the ABABAB and

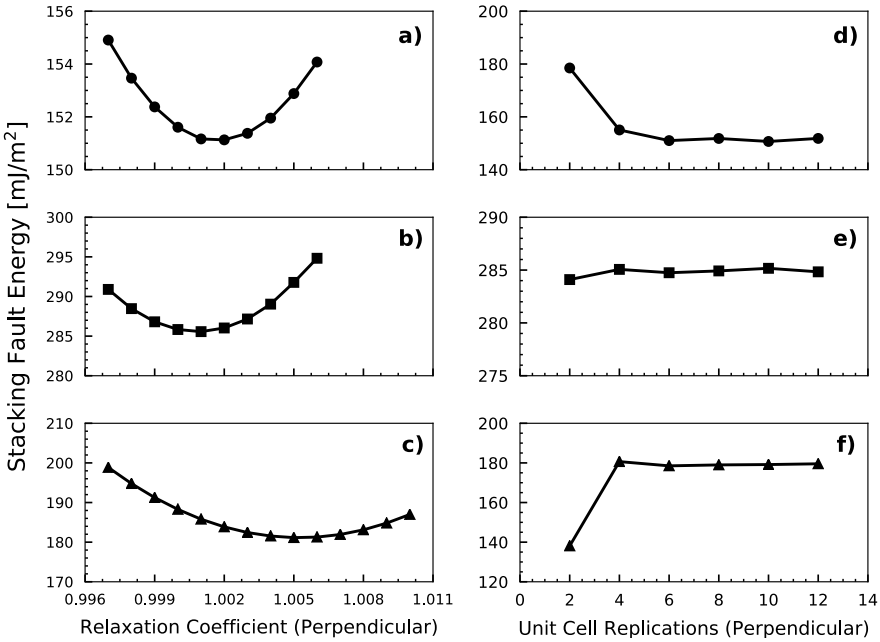

Fig. 3-2. Stacking fault energies as a function of the relaxation coefficient applied to the length perpendicular to the fault plane for the basal intrinsic I1 (a), basal extrinsic (b), and prismatic $\{10\bar{1}0\}$ (c) faults. Additionally, stacking fault energies are shown as a function of the number of unit cell replications perpendicular to the fault plane for the basal intrinsic I1 (d), basal extrinsic (e), and prismatic $\{10\bar{1}0\}$ (f) faults [55].

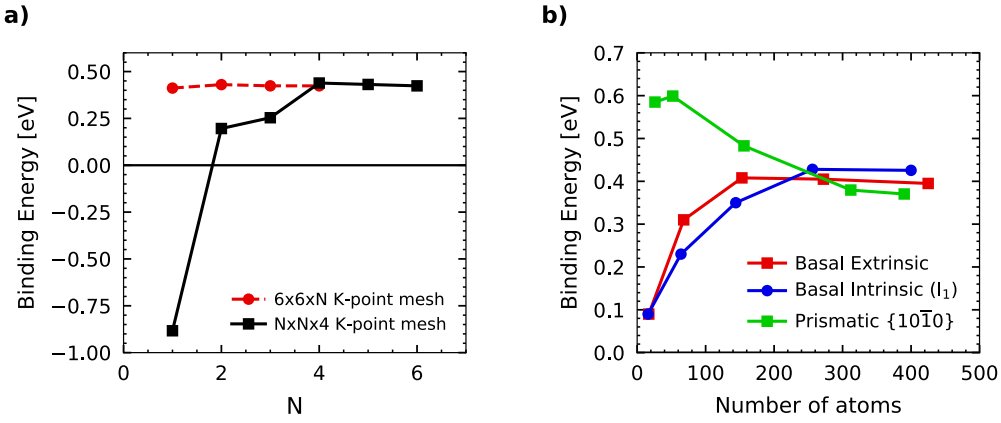

Fig. 3-3. a) Convergence of Fe(i) binding energies to the first insertion site in the basal intrinsic I1 fault are shown as a function of the K-point mesh; meshes were constructed with variable dimensions along the z-direction (dotted line) and along the x- and y- directions (solid line). b) Convergence of Fe(i) binding energies are shown as a function of supercell size for the basal intrinsic, basal extrinsic, and prismatic faults [55].

CBCBCB stacking regions. The basal extrinsic fault was constructed by placing an additional atomic layer in the [0001] direction due to the nature of the single-layer fault. This corresponds to a supercell with 425 atoms and an unrelaxed length of 43.95 Å. The relaxed SFE for the basal intrinsic structure is 151.1 mJ/m^2, in good agreement with calculated values of 147 mJ/m^2 [37] and 124 mJ/m^2 [130]. Similarly, the relaxed basal extrinsic SFE of 285.6 mJ/m^2 is in good agreement with literature values of 274 mJ/m^2 [37] and 249 mJ/m^2 [130]. Binding energies to these structures were calculated with a 6x6x4 k-point mesh, allowing a sufficient k-point density for converged energies (Fig. 3-3).

3.1.2 The $\{10\bar{1}0\}$ *prismatic stacking fault*

A stacking fault along the $\{10\bar{1}0\}$ prism planes nucleates through the collapse of vacancy platelets along one or two layers of the hcp prismatic stacking sequence (ABCDABCD) [82]. The removal of a single layer (Eq. (3-6)) results in a much greater energy fault than the removal of a corrugated A-B or C-D pair of layers (Eq. (3-7)) [82]; therefore, the fault formed by the collapse of vacancy platelets onto two atomic layers was the only prismatic fault considered in this investigation. Once faulted a-loops reach large sizes, these defects unfault by a $1/6\langle 1\bar{2}10\rangle$ shear of the fault plane to produce the perfect loops observed in irradiated microstructure, as predicted by their favorable formation energies (Fig. 3-1) [37].

$$\ldots ABC\boldsymbol{D}ABCD \ldots \longrightarrow \ldots ABCDAB\boldsymbol{C}|\boldsymbol{A}BCD \ldots \quad (3\text{-}6)$$

$$\ldots AB\boldsymbol{CD}ABCD \ldots \longrightarrow \ldots ABCDA\boldsymbol{B}|\boldsymbol{A}BCD \ldots \quad (3\text{-}7)$$

To construct the bulk reference supercell for the $\{10\bar{1}0\}$ prismatic fault, the primitive cell was replicated 7 times in the $[10\bar{1}0]$ direction (28 atomic layers, 39.2 Å). For the $[1\bar{2}10]$ and [0001] directions, the supercell was replicated 5 times (10 atomic layers, 16.1 Å) and 3 times (9 atomic layers, 15.5 Å), respectively. This corresponds to a supercell containing 420 atoms. The prismatic faulted supercell was constructed with the same unit cell replications, but consisted of 26 atomic layers in the $[10\bar{1}0]$ direction (36.4 Å) due to the removal of one corrugated pair of prismatic planes. This supercell contained 390 atoms. The relaxed SFE for this structure was calculated to be 181.1 mJ/m^2, in close agreement with literature values of 211 mJ/m^2 [37] and 197 mJ/m^2 [130]. A k-point mesh of 4x6x6 was utilized for the calculation of binding energies.

3.1.3 The high-energy B-B layer structure (vacancy platelet)

In addition to modeling stacking faults in Zr to indirectly relate *ab initio* binding energies to vacancy loop formation energies, solute interaction with a nucleating *c*-loop defect was directly investigated. The high-energy B-B layer structure is formed when a

vacancy platelet condenses onto a single basal plane (Eq. (3-3)). Although pyramidal structures may offer lower energy states for small basal clusters [21, 84, 85], computational limits on supercell size do not allow the direct simulation of these occurrences with DFT. Therefore, the analysis focuses on interactions between solute and impurities with nucleating basal platelets that may transform to the pyramidal structure through vacancy capture if stabilized in the matrix. This structure was formed by introducing a hexagonal vacancy platelet containing 19 vacancies into a perfect Zr supercell (22.4 Å x 22.6 Å x 20.7 Å) containing 448 atoms. The supercell was then relaxed to allow the similar atomic rows to come into contact with one another, forming the B-B layer structure. This process is demonstrated in Fig. 3-4. The binding energies for Fe, Sn, Nb, Cr, Ni, and H were then calculated to this relaxed structure through an expression of the form given by Eq. (3-2).

3.2 Solute interaction with prismatic and basal stacking faults

3.2.1 Preferred sites of Fe, Nb, Sn, Cr, and Ni in the hcp α-Zr matrix

Due to the similarity of the atomic numbers and size for Zr and Nb, Nb will unquestionably occupy substitutional positions. A preference for the substitutional position has also been indicated for Sn and Ni by DFT calculations [30]. Conversely, reports for the site preference of Fe and Cr are contradictory in the literature. Burr et al. report that Fe is expected to occupy the octahedral interstitial position while Cr exhibits a dual occupancy of the octahedral interstitial and substitutional positions [62]. The reported octahedral interstitial occupancy of Fe is in agreement with the results of Pasianot and Pérez et al. [57, 58], while the dual occupancy of interstitial and substitutional sites was indicated by Christensen et al. [30]. The high-symmetry substitutional position of Fe is stated to be stabilized by a large magnetic moment, but the octahedral interstitial position is favored if the magnetic moment does not persist at higher temperatures.

Due to the disagreement in past studies, the site preference of Fe and Cr were investigated with a 288-atom supercell (22.4 Å x 19.4 Å x 15.5 Å) and a dense k-point mesh of 5x5x5. The magnetic moment of Cr was found to diminish for minor perturbations in its high-symmetry position, and is not expected to persist to high temperatures; therefore, all calculations involving Cr were non-spin polarized. Conversely, the calculations involving Fe were spin-polarized due to the persistence of a magnetic moment when placed in off-symmetry substitutional positions. Both Fe and Cr were found to be unstable in the tetrahedral interstitial position (resulting in migration to the nearest octahedral site). A strong magnetic moment is noted for Fe in the high-symmetry substitutional position (3.74 μ_B), but diminishes to zero for the octahedral interstitial position; the difference in formation energies is 0.04 eV, with a slight preference for the octahedral position. A Cr atom placed in a high-symmetry substitutional position migrates to an off-site substitutional position,

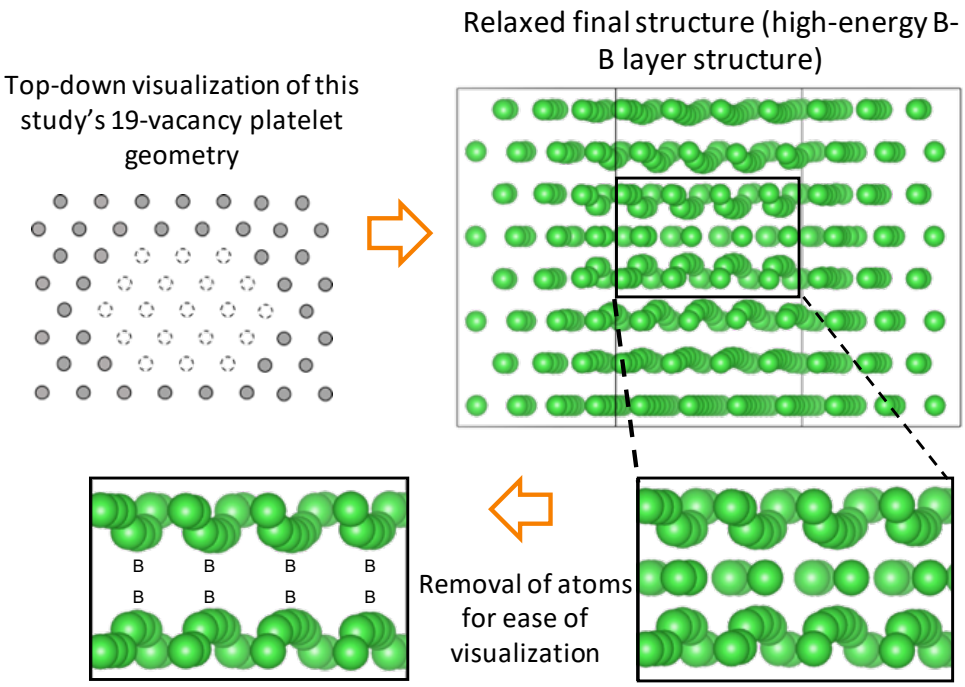

Fig. 3-4. Visualization of the high-energy B-B layer structure of a 19-vacancy hexagonal platelet. The grey and green spheres represent zirconium atoms, while the dashed open circles represent the individual vacancies [55].

although the octahedral interstitial site is preferred by 0.02 eV. Due to the similarities in formation energies for substitutional and interstitial sites for Fe and Cr, both sites were considered for these elements.

3.2.2 Binding energies of Fe, Nb, Sn, Cr, and Ni to stacking faults in α-Zr

The basal extrinsic, basal intrinsic, and prismatic stacking faults (as described in *Sections 3.1.1 and 3.1.2*) are illustrated in Fig. 3-5. Substitutional and octahedral interstitial insertion sites are marked with closed and open red circles, respectively. Binding energies were calculated as a function of separation distance from the fault plane to investigate both the magnitude of solute binding and its range of interaction. The binding energies of each of the chemical species to the three stacking faults are shown individually for each element in Fig. 3-6(a)-(g); note that (s) indicates a substitutional insertion while (i) indicates an octahedral interstitial insertion.

Fe and Sn show the strongest positive binding to basal stacking faults. In particular, Fe in its interstitial form shows considerable attractive interaction with basal stacking faults (~0.35-0.4 eV binding) while Fe in its substitutional form exhibits much weaker interactions. Due to the similar magnitudes of their formation energies and the large binding of the Fe interstitial, Fe would be expected to occupy octahedral interstitial sites near basal stacking fault interfaces. The formation of a double-layer $\{10\bar{1}0\}$ prismatic stacking fault introduces a unique octahedral interstitial position at the fault interface to which the Fe interstitial is tightly bound [131], but this attractive binding rapidly decays when inserting Fe at further distances from the interface. Sn shows repulsive interaction near the prismatic fault interface with negligible interaction at greater separation distances. Therefore, Fe and Sn are expected to preferentially segregate to basal stacking faults rather than prismatic faults. Cr in its interstitial position shows binding interactions with similar values as substitutional Sn; conversely, Cr in the off-site substitutional position (as well as Nb and Ni), exhibits only weak interaction with all stacking faults. Similar to Fe, Cr is expected to occupy interstitial positions near the basal fault interfaces due to its large attractive binding with respect to that of substitutional Cr.

3.2.3 Solute segregation profiles

The segregation behavior of a particular solute, S, lying on a plane p at some distance d_p from a stacking fault interface (γ) can be related to its binding energy ($E^b_{S-\gamma}(d_p)$). An approach for modeling the segregation behavior of interstitial H has been detailed by Varvenne et al. with reference to the tetrahedral interstitial site [19]. The model considered a bicrystal of two semi-infinite bulk regions separated by a stacking fault plane. Each side

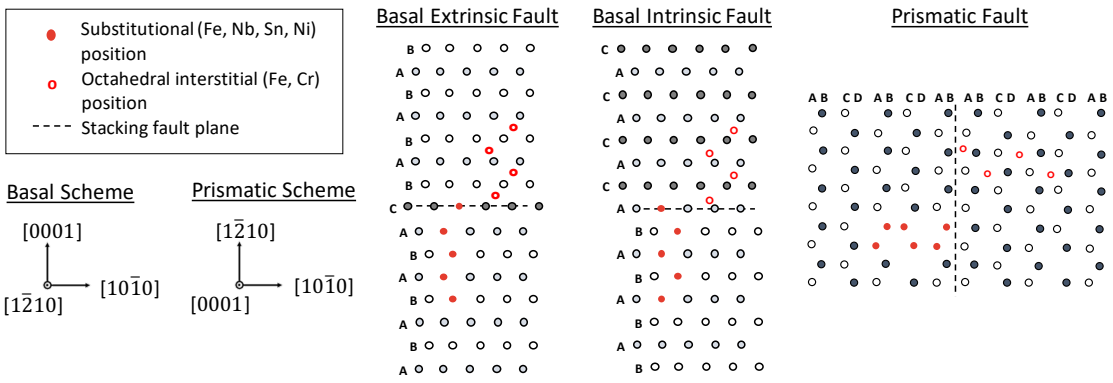

Fig. 3-5. Substitutional (closed red circle) and octahedral interstitial (open red circle) insertion sites within the basal extrinsic, basal intrinsic, and prismatic stacking faults [55].

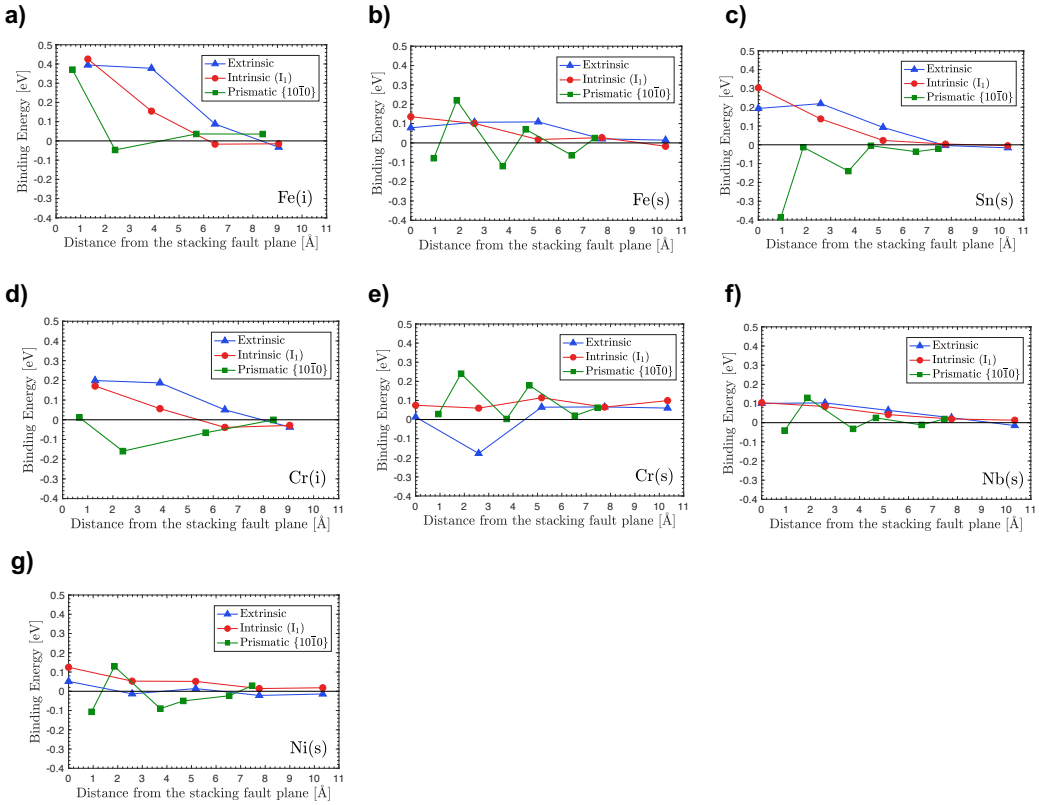

Fig. 3-6. Binding energies to basal extrinsic, basal intrinsic, and prismatic stacking faults as a function of separation distance from the stacking fault plane for the following chemical species: (a) octahedral interstitial Fe, (b) on-site substitutional Fe, (c) on-site substitutional Sn, (d) octahedral interstitial Cr, (e) off-site substitutional Cr, (f) on-site substitutional Nb, and (g) on-site substitutional Ni [55].

acts as a reservoir for H such that the chemical potential, μ_H, is fixed at equilibrium:

$$E_H^{sol} - E_{H-\gamma}^b + kT\ln\left(\frac{c_p}{1-c_p}\right) = \mu_H \qquad (3\text{-}8)$$

where E_H^{sol} is the hydrogen solution energy in bulk zirconium, $E_{H-\gamma}^b$ is the binding energy of H to the stacking fault interface, and c_p is the site occupation fraction of H on plane p. The model assumes that the interaction between H atoms is negligible. By considering a point far enough from the fault interface such that the H concentration approaches that of bulk Zr and the binding energy approaches 0, μ_H can be eliminated in Eq. (3-8) using the assumption of an equilibrium partitioning of H atoms between the matrix (reservoir) and the stacking fault, and the segregation profile, c_p, can be solved for as a function of H binding energy. That approach detailed by Varvenne et al. [19] has been expanded here to include expressions with reference to the octahedral interstitial site (Eq. (3-9)) and the substitutional site (Eq. (3-10)), where the concentration profile on a plane p is related to the nominal solute concentration in the alloy, x. The parameter $\Delta E^{T/O}$ is the energy difference between the tetrahedral and octahedral positions; for interstitial elements such as Fe and Cr that exhibit instability in the tetrahedral position, this parameter can be considered infinitely large such that these solute segregate only on planes containing octahedral sites. For every substitutional site in hcp α-Zr there exists one octahedral interstitial site; therefore Eq. (3-9) reduces to the form of Eq. (3-10) within this analysis.

$$c_p^O = \frac{x \cdot \exp\left(\frac{E_{S-\gamma}^b(d_p)}{kT}\right)}{1 + 2\cdot\exp\left(\frac{-\Delta E^{T/O}}{kT}\right) + x\cdot\exp\left(\frac{E_{S-\gamma}^b(d_p)}{kT}\right)} \qquad (3\text{-}9)$$

$$c_p = \frac{x \cdot \exp\left(\frac{E_{S-\gamma}^b(d_p)}{kT}\right)}{1 + x\cdot\exp\left(\frac{E_{S-\gamma}^b(d_p)}{kT}\right)} \qquad (3\text{-}10)$$

The extent of segregation is highly sensitive to the selected temperature due to the fact that solute binding effectively lowers the species formation energy in the vicinity of the stacking fault interface. The magnitude of segregation for a given binding energy will be greater at lower temperatures. For this analysis, a temperature of 600 K was selected to represent the service temperature of pressurized water reactors. The extent of segregation will also depend on both the binding energy (Fig. 3-6) and the matrix solute concentration during irradiation, which may exceed the nominal solubility due to ballistic dissolution effects.

The elements Fe, Cr, and Ni have negligible solubilities within the hcp α-Zr matrix and are initially contained within secondary phase precipitates (SPPs) such as $Zr(Fe,Cr)_2$ and $Zr_2(Fe,Ni)$ [60]. These SPPs ballistically dissolve under irradiation, releasing the constituent elements to supersaturate the matrix. For instance, atom probe tomography (APT) has demonstrated that the matrix Fe concentration increases from ~0.01 at% to ~0.10 at% in

Zircaloy-2 following neutron irradiation to $2x10^{25}$ n/m^2 (E > 1.0 MeV), and remains at this concentration of ~0.10 at% up to the highest reported fluence of $6x10^{25}$ n/m^2 (E > 1.0 MeV), for an ingot containing a nominal concentration of 0.18 at% Fe [60]. Thus, Fe reaches a super-saturated dynamic steady-state matrix concentration considerably greater than the solubility limit in α-Zr. Fig. 3-7(a) demonstrates the segregation potential of Fe prior to significant irradiation, invoking Eq. (3-10) for a bulk Fe concentration of $x_{Fe} = 0.0001$ (0.01 at% solubility) at T = 600 K. For this concentration of Fe, the rigorous thermodynamic equilibrium assumed by Eq. (3-8) is valid. Despite the large binding energies of the Fe interstitial, the negligible solubility of iron in the Zr matrix at low fluence does not lead to significant segregation.

When instead considering the supersaturated matrix concentration of 0.10 at% Fe, it can be assumed that a dynamic equilibrium has been reached between the matrix and the stacking fault in question (such that the chemical potential of Fe in the matrix is equal to the chemical potential near the stacking fault). When considering this supersaturated Fe matrix concentration (0.10 at%) as the value for the reservoir in the model, the segregation potential of Fe containing bulk concentrations of $x_{Fe} = 0.0010$ (high-fluence case of 0.10 at% supersaturation as observed in Ref. [60]), and $x_{Fe} = 0.003$ (upper-bound case for the maximum Zircaloy-2 nominal Fe concentration of 0.30 at%) can be roughly estimated using Eq. (3-10), and are plotted in Fig. 3-7(b) and Fig. 3-7(c), respectively. In contrast to the behavior shown for Fe near the solubility limit, the segregation potential of Fe is greatly enhanced at higher fluence upon the dynamic super-saturation of the solute in the matrix. The concentration-dependent segregation of interstitial Fe to stacking faults is qualitatively consistent with the high-fluence nucleation of *c*-loops, which may be linked to the ballistic dissolution of elements such as Fe into the matrix. However, because the Varvenne model is based on a rigorous thermodynamic equilibrium, as opposed to the dynamic steady-state behavior assumed here, the results shown in Fig. 3-7(b) and Fig. 3-7(c) likely represent an upper bound for the estimation of segregation behavior. Regardless, consideration of the calculated binding energies and the experimentally observed super-saturated matrix concentrations support the conclusion of a significant potential for Fe segregation to stacking faults once Fe has ballistically dissolved from SPPs into a highly super-saturated concentration. Future analyses should further investigate the dynamic, thermodynamic, and kinetic phenomena as well as the various sources and sinks of Fe in the Zr matrix that may impact the segregation potential of Fe.

A similar analysis of segregation behavior for other solute requires reasonable estimates of their nominal matrix concentration under irradiation. Binary equilibrium phase diagrams show ~0 at% solubility at T = 600 K for Cr [132], and Ni [133]. As discussed previously for the case of Fe, APT analyses indicate that matrix concentrations of Cr and Ni are expected to increase as the SPPs ballistically dissolve under irradiation [60]. Nb is expected to have a higher inherent solubility of ~0.30 at% [134]. On the other hand, Sn is predicted to have a solubility of ~4 at% at T = 600 K. Considering traditional alloying concentrations, the Zircaloy family of alloys typically contains ~0.9 – 1.3 at% Sn, ~0.1 – 0.3 at% Fe and Cr, and ~0.05 – 0.1 at% Ni; Nb is commonly included in amounts of ~1 at% in

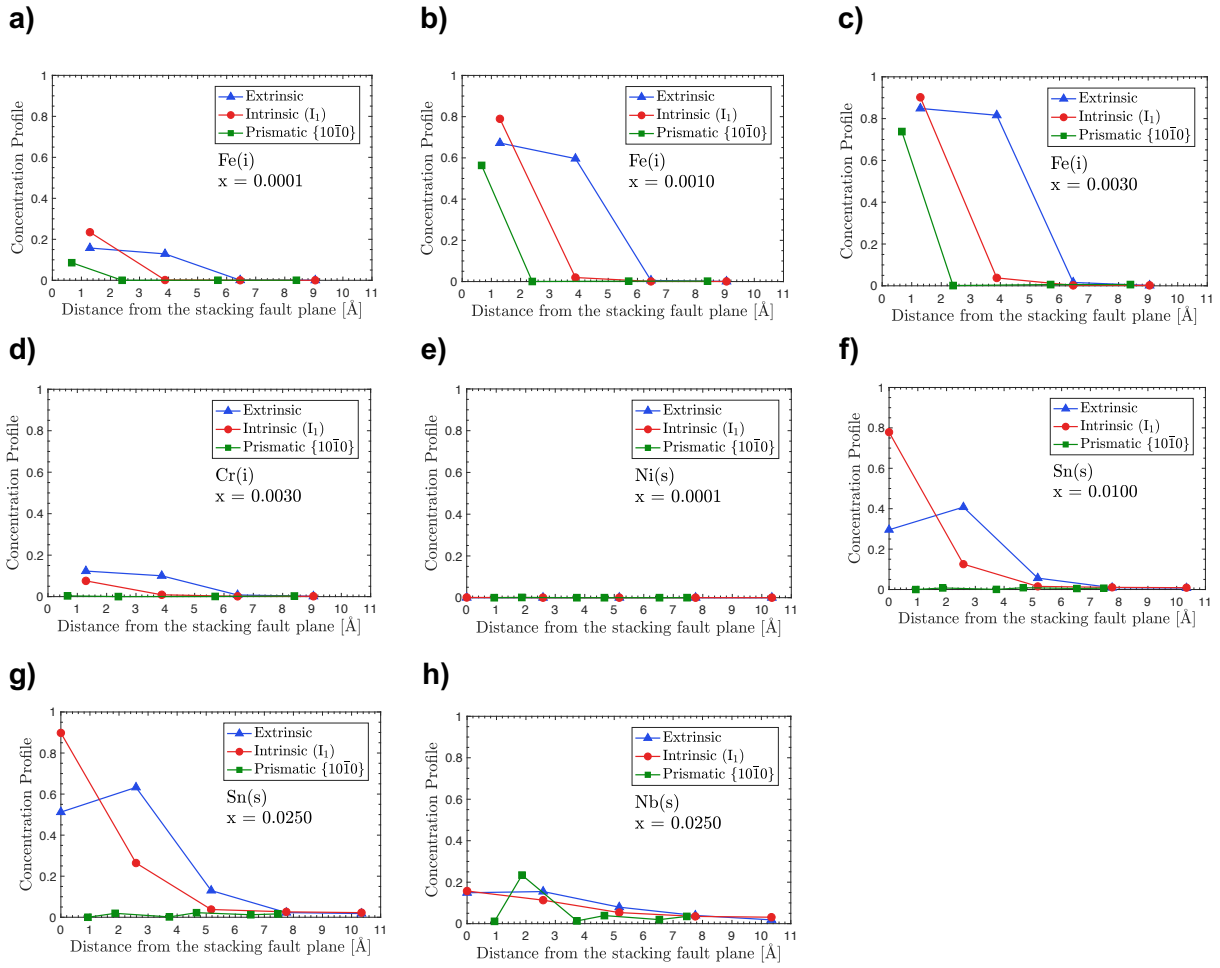

Fig. 3-7. Segregation profiles at T = 600 K for (a) 0.01 at% interstitial Fe, (b) 0.10 at% interstitial Fe, (c) 0.30 at% interstitial Fe, (d) 0.30 at% interstitial Cr, (e) 0.01 at% Ni, (f) 1.0 at% Sn, (g) 2.5 at% Sn, and (h) 2.5 at% Nb [55].

ZIRLO and M5 alloys [135]. Excel and Zr-2.5Nb alloys contain ~2.5 at% of Sn or Nb, respectively. A comparison of Fe and Cr segregation at comparable nominal matrix concentrations (x = 0.30 at%) in Fig. 3-7(c) and Fig. 3-7(d) illustrates the dependence of the segregation profile on the magnitude of solute binding, in which Fe exhibits a much broader segregation profile. The maximum binding energy of ~0.40 eV calculated for interstitial Fe is nearly twice as large as that for interstitial Cr. The consequence is reduced segregation of Cr to all stacking faults in α-Zr (relative to Fe); we therefore conclude that a large binding energy is required in order for solute segregation to be observed for elements with limited matrix solubility. Therefore, it is not surprising to find that Ni (with low binding energies and limited solubility) exhibits negligible segregation tendencies in Fig. 3-7(e).

The segregation profiles for Sn are plotted in Fig. 3-7(f) and Fig. 3-7(g) for nominal concentrations of 1 at% (an approximate Zircaloy alloying content) and 2.5 at% (an upper bound condition for Sn alloying content in Excel alloys). Despite the lower binding energy of Sn compared to interstitial Fe, its segregation is comparable due to much larger matrix concentrations in Zr alloys. While Nb is often alloyed with similarly large concentrations, the weak binding of Nb to these stacking faults leads to minimal segregation. Therefore, this analysis indicates that only interstitial Fe and substitutional Sn should segregate in sufficient quantities to produce notable reductions in faulted *c*-loop formation energies.

It should be stated that the predicted segregation of Fe and Sn is quite large and can no longer be considered "dilute". Solute segregation is driven by a local reduction in the formation energy in the vicinity of the stacking fault interface. Solute-solute interactions between Fe-Fe and Sn-Sn will affect the extent of segregation depending on the repulsive or attractive nature of the interaction, as well as the presence of other defects to which these solutes will bind or precipitation sites (especially for Fe). Although a detailed quantitative analysis on solute-solute interactions and a quantitative prediction of segregation profiles is outside the scope of this work, preliminary DFT results have been reported by Burr et al. for Fe-Fe, Cr-Cr, and Fe-Cr interactions between pairs of the respective solute atoms in α-Zr [62]. Dumbbell configuration pairs of Fe-Fe, Cr-Cr, and Fe-Cr were strongly attractive, and the positive binding energy for atom pairs persisted up to the largest investigated separation distance of 7 Å. This result of attractive binding is unsurprising considering the extent of clustering of Fe and Cr prior to c-loop formation [20, 63]. While a similar analysis has not been performed for Sn, Nb, or Ni, the banding and clustering of Sn observed in irradiated Zr [20] indicates a positive, rather than repulsive, interaction of Sn while strong segregation of Fe and Ni to dislocation loops has been shown through molecular dynamics simulations [31, 61]. Therefore, the segregation tendencies demonstrated in Fig. 3-7 are in agreement with general solute behavior reported in literature, although an extensive quantification of solute-solute interactions in future work would provide useful input to modify the planar segregation predicted by Eq. (3-9) and Eq. (3-10), in addition to a more detailed calculation of solute partitioning amongst a variety of radiation-induced defects.

3.2.4 *Modified stacking fault energies*

The reduction in SFE by solute segregation can be considered through the difference in the grand potentials of the system for the faulted (Ω_f) and perfect (Ω_i) crystal (Eq. (3-11)), where S_0 is the area of the dividing interface for one insertion site per plane [19]. The area of this interface is given by $S_0 = a^2\sqrt{3}/2$ for basal faults and $S_0 = ac/2$ for the prismatic fault. Considering the thermodynamic model proposed by Varvenne et al., the modified SFE for solute segregation on planes p can be calculated via Eq. (3-12) for substitutional and octahedral interstitial solute [19].

$$\gamma(\{c_p\}) = \frac{\Omega_f(\{c_p\}) - \Omega_i(x)}{S_0} \quad (3\text{-}11)$$

$$\gamma(\{c_p\}) = \gamma_0 + \frac{kT}{S_0}\sum_p \ln\left(\frac{1-c_p}{1-x}\right) \quad (3\text{-}12)$$

The modified SFEs as a function of the nominal concentration, x, are plotted in Fig. 3-8 for Fe, Cr, Ni, Sn and Nb. The tight, preferential binding of Fe to basal stacking faults is responsible for its strong segregation to these interfaces, and the consequence is a greater reduction in basal SFEs with respect to the prismatic SFE as the nominal concentration is increased (Fig. 3-8(a)). At high fluence, for which the Fe concentration in the matrix has been shown to approach 0.10 at% (x = 0.0010) [60], the basal extrinsic and basal intrinsic SFEs are seen to approach zero and, eventually, negative values. Thus, significant Fe segregation locally establishes a thermodynamic preference for the faulted stacking configurations present in the vicinity of basal *c*-loops. A similar effect is noted as a result of Sn segregation (Fig. 3-8(b)), as would be expected due to the comparable segregation tendencies predicted in Fig. 3-7(f). The low binding energies or nominal concentrations of Cr, Ni, and Nb prevent these elements from having a noteworthy effect on the reduction of SFEs in α-Zr.

3.2.5 *Effect of solute segregation on vacancy loop formation energies*

The formation energies of faulted *c*-loops cannot be directly investigated by *ab initio* methods due to the current limitations in supercell size for modern DFT methods (a task that would require millions of atoms). Rather, the formation energies (expressed through Eq. (3-1)) can be related to *ab initio* binding energies through the modification of γ, the SFE. The vacancy loop formation energies for faulted *c*-loops (basal extrinsic and intrinsic), faulted *a*-loops (prismatic $\{10\bar{1}0\}$ faulted), and perfect *a*-loops (prismatic perfect) are compared in the absence of impurity segregation in Fig. 3-9(a). Due to the lack of a SFE contribution, the perfect a-loop is thermodynamically favored and this observation explains their high number-density in irradiated α-Zr [13, 16]. Fe segregation has little impact on this behavior at low fluence (x = 0.01 at%, Fig. 3-9(b)) but is incredibly influential at high fluence with an

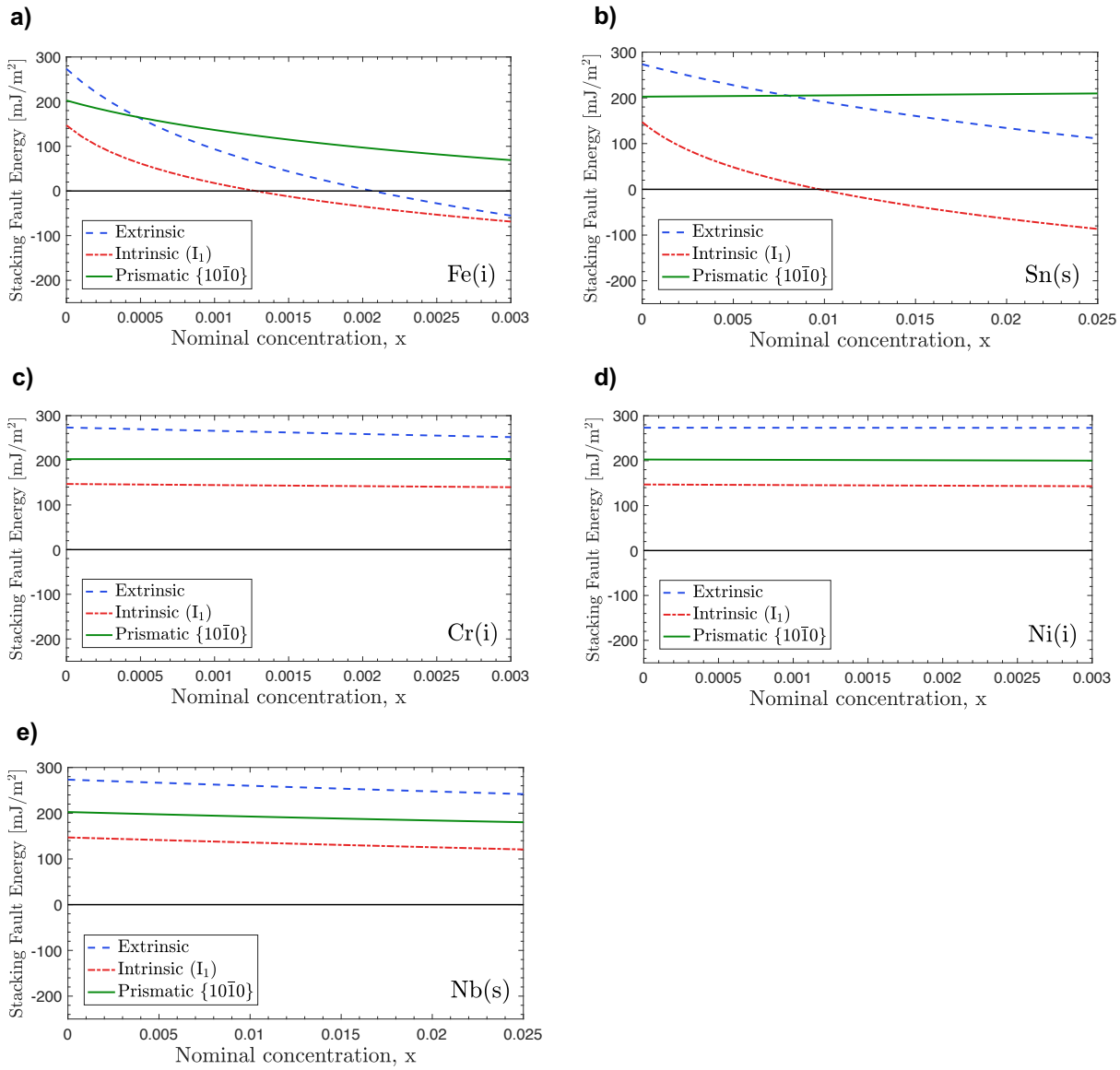

Fig. 3-8. Modified stacking fault energies at T = 600 K as a function of nominal concentration for (a) interstitial Fe, (b) substitutional Sn, (c) interstitial Cr, (d) substitutional Ni, and (e) substitutional Nb [55].

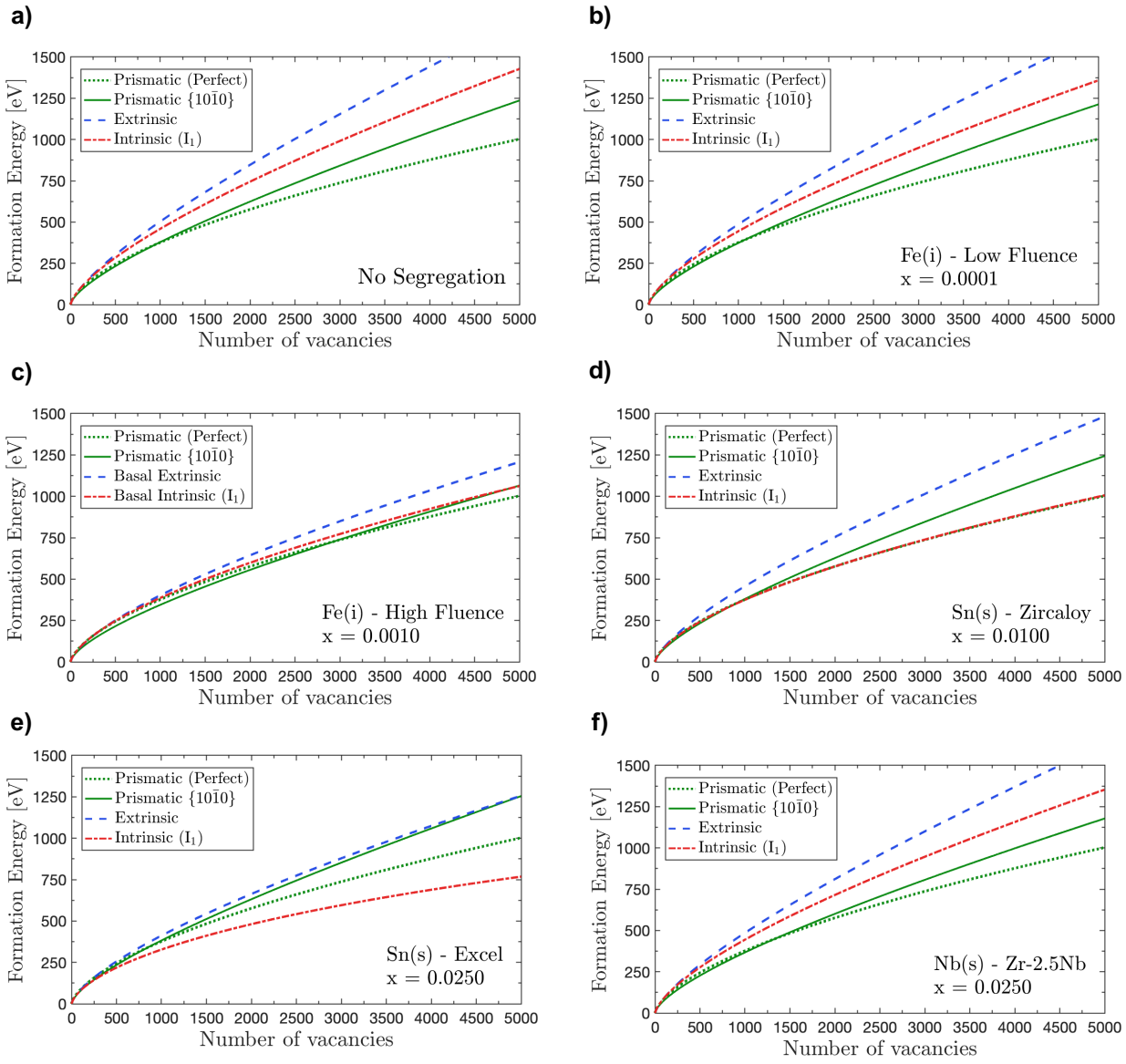

Fig. 3-9. Modified formation energies of basal extrinsic, basal intrinsic, faulted prismatic, and perfect prismatic vacancy loops at T = 600 K for (a) no impurity segregation, (b) interstitial Fe at a x = 0.01 at%, (c) interstitial Fe at x = 0.10 at%, (d) Sn at x = 1.0 at%, (e) Sn at x = 2.5 at%, and (f) Nb at x= 2.5 at%. Note that the Nb behavior is representative of interstitial Cr and Ni due to similar SFE modifications [55].

assumed increase in matrix Fe concentration, as shown in Fig. 3-9(c). The reduction in basal, and to a lesser effect prismatic, SFEs severely diminishes the gap between formation energies.

Consistent with the results presented in Fig. 3-8, Sn has a similar effect on reducing the formation energy gap for faulted basal loops and, for very large nominal concentrations, even establishing a thermodynamic preference for the basal intrinsic *c*-loop configuration. This data is in agreement with experimental data indicating that breakaway irradiation growth occurs at uncharacteristically low fluence in the Excel alloy, which contains approximately 3.5 at% Sn, as compared to high purity α-Zr, or commercial Zircaloy-2 or Zircaloy-4, which contain approximately 1 at% Sn [136]. While these experimental reports are consistent with the analysis performed here, it must be questioned why a threshold, or incubation, fluence exists for *c*-loop nucleation in these alloys, in which Sn is evenly dispersed in the matrix at low fluence (unlike Fe) [60]. One possibility is that Sn is not strongly attracted to the high-energy B-B layer structure that acts as a nucleation barrier for faulted *c*-loop formation, and only segregates to growing, rather than nucleating, *c*-loops. This possibility is further discussed in the following section. In contrast to the effects of Fe and Sn, the elements Cr, Ni, and Nb (all sharing a similar behavior to that demonstrated in Fig. 3-8(f)) are not expected to play a large role in the reduction of SFEs for large *c*-loops.

It must be stressed that the current approach does not consider the reduction in formation energy due to solute segregation to the core of the prismatic dislocation loops, as noted for Fe, Cr, and Ni segregation to the periphery of non-faulted loops [20, 31, 61] or Fe and Sn segregation to the periphery of faulted c-loops [63]. Notably, the formation energies in Fig. 3-8 are not expected to represent the true energetic state of dislocation loops in irradiated α-Zr, which must include the effects of several other factors such as stress or solute segregation to dislocation cores. The intent of this study is to show the significant impact that solute segregation has on reducing the SFE and lowering formation energy difference between perfect a-loops and faulted c-loops. The number of possible segregation sites for solute to the periphery of a dislocation loop or the faulted loop interface will be related to its circumference ($2\pi R$ for a circular loop) and its surface area (πR^2 for a circular loop), respectively. While solute segregation to dislocation cores would be present for both vacancy a-loops and c-loops, the faulted c-loop offers a greater number of segregation sites to its faulted interface with increasing size. Considering that c-loops often reach sizes greater than 100 nm, the stacking fault energy contribution will dominate and the solute segregation mechanism proposed here may explain the observed c-loop growth and formation with respect to the originally thermodynamically-favored perfect a-loop.

3.3 Solute interaction with prismatic and basal stacking faults

Unlike large faulted *c*-loops, it is possible to directly simulate the high-energy B-B layer configuration by *ab initio* methods as shown in Fig. 3-4. This defect structure may act as a nucleation barrier for *c*-loop formation as vacancies condense into a platelet on a single

basal plane. The high-energy B-B layer contact is eventually resolved by the formation of a basal extrinsic stacking fault once a sufficient number of vacancies have been captured, although recent work shows that the platelet may instead transform into a lower-energy pyramidal configuration [84, 85]. While the platelet structure is not representative of large, faulted *c*-loops, a demonstration of strong binding of Fe, Sn, Nb, Cr, Ni, or H to this nucleating vacancy loop structure could support an impurity-assisted mechanism for the reduction of the nucleation barrier. This would stabilize the platelet structure long enough to capture vacancies and possibly transform to a lower-energy configuration.

Two insertion locations within the B-B structure were considered: the center of the vacancy platelet (within the B-B layer contact) versus the periphery of the platelet. For the "center" location, one element is either substituted for a Zr atom in the B-B layer contact, or an element is placed interstitially; for the "periphery" location, one element is substituted for a Zr atom adjacent to the vacancy platelet, or an element is placed interstitially within the available free space. Fig. 3-10 displays the binding energies and final relaxed positions for chemical species inserted in the center of the platelet. The only element to exhibit strong binding to this substitutional accommodation is Cr; however, Cr and Fe atoms are both more tightly bound to the free (interstitial) space between the B-B layer contact and would be expected to migrate towards those sites instead. The greater amount of free space available in the B-B contact layer compared to that of the traditional hcp octahedral interstitial positions could provide an explanation for the tight binding. Despite this greater free space, however, the H interstitial is shown to have particularly weak binding to this location of the nucleating platelet defect. The insertion of substitutional Fe and Ni resulted in distortion of the metastable structure, and their binding energies could not be adequately calculated.

The binding energies and final relaxed positions of the chemical species to the periphery insertion site are shown in Fig. 3-11. Sn has been investigated in both substitutional and interstitial positions, but strong binding is only observed for interstitial insertion. It must be noted, however, that Sn is partially substituting for a vacancy, skewing the binding energy calculation to higher values (due to the reduction of the number of vacancies in the system). When a vacancy is placed adjacent to Sn (as if substitutional Sn is exchanging with a vacancy from the platelet), the Sn atom migrates to fill the vacancy adjacent to the platelet, rather than remaining in the free space of the platelet periphery. This indicates that the 0.75 eV reported binding energy is primarily due to the partial removal of vacant space from the system; thus, Sn is expected to only exhibit weak binding on the order of 0.07 eV to this nucleating defect. A similar skew effect of the binding energies for interstitial Fe and Cr would also be expected, but their significant binding energies of 1.90 and 2.12 eV indicate unambiguously that these elements are tightly bound to this periphery position. When compared to their binding energies at the center of the platelet, both Nb(s) and H(i) show tighter binding at the periphery, but neither element demonstrates strong interactions. Substitutional Ni exhibits a greater binding energy than Nb(s) and H(i), but much lower binding interaction than Fe(i) and Cr(i).

The large binding of Fe and Cr to these nucleating structures supports the experimental observation of c-loop bundles near amorphizing precipitates under neutron

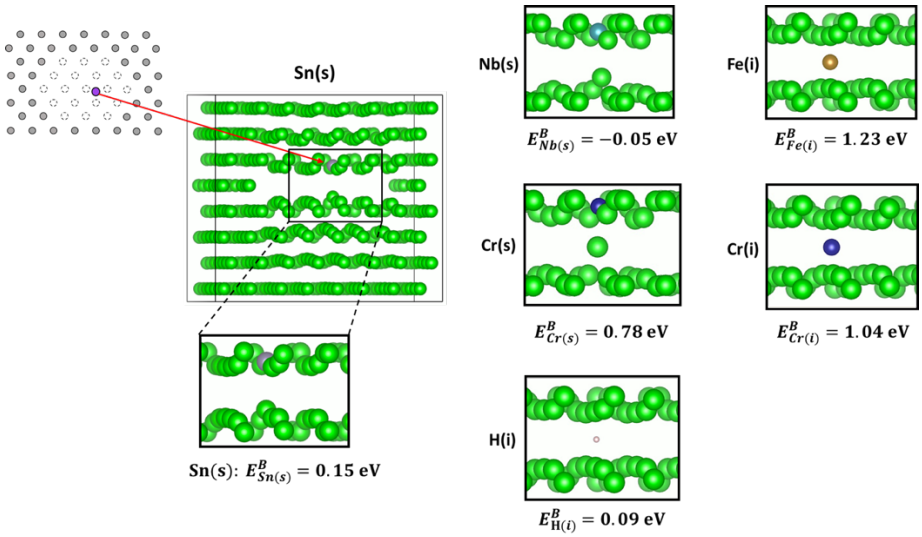

Fig. 3-10. Binding energies and final relaxed positions of Sn(s), Nb(s), Cr(s), H(i), Fe(i), and Cr(i) when placed in the center of the high-energy B-B contact within the 19-vacancy platelet [55].

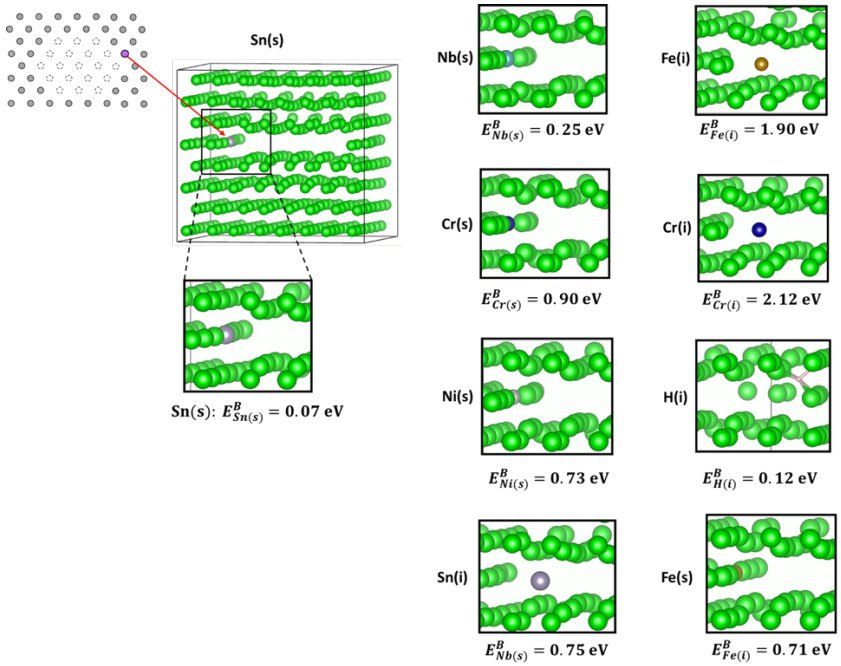

Fig. 3-11. Binding energies and final relaxed positions of Sn(s), Nb(s), Cr(s), Ni(s), Fe(s), H(i), Fe(i), and Cr(i) when placed at the periphery of the 19-vacancy platelet [55].

irradiation (consider Fig. 6 in Ref. [33]). Harte et al. propose that reports of c-loops nucleating near amorphizing precipitates may, instead, be mistakenly referencing discontinuous irradiation-induced clusters of Fe and Cr along the basal plane [20, 137]. Considering the extent of binding and segregation behavior of solutes described in this work, it is possible that these discontinuous clusters are initially due to Fe and Cr segregation to nucleating c-loops in the basal plane. Continued absorption of vacancies could then eventually lead to full c-loop formation as seen in Refs. [33] and [32]. A similar nucleation mechanism was originally proposed by de Carlan et al. for c-loop formation in Zircaloy-4 [35]. Sn, on the other hand, does not show strong binding to nucleating c-loop precursors and may only play a role in the stabilization and growth of fully-formed faulted c-loops. This is consistent with the fact that breakaway growth is not immediate in alloys with high Sn content despite the fact that Sn is dissolved in solid solution at all fluences in Zr alloys [60]. The binding of H is similarly weak. However, it must be considered that our calculations have involved the addition of single atomic species to the fault or vacancy platelet, and the segregation of multiple H atoms may induce a greater stability for basal defects. However, due to its weak binding, H would be expected to interact with other potential capture sites rather than nucleating basal platelets. These observations therefore indicate that Fe is likely the most significant contributor to *c*-loop stabilization in the nucleation regime. However, confirmation of this assessment will require further computational modeling of the dynamic Fe concentration under irradiation that accounts for all possible fates of the supersaturated matrix Fe, including precipitation and radiation induced segregation to all of the possible extended defect structures.

3.4 Differential electron density analysis

It remains unclear whether the calculated binding energies are predominantly a result of elastic effects (relating to the size of the investigated solute) or electronic interactions. Each of the investigated solutes are undersized when compared to the metallic radius of approximately 1.6 Å for hcp α-Zr [138]. Fe, Cr, and Ni are the smallest solute (with metallic radii of 1.26, 1.28, and 1.24 Å, respectively) while Nb and Sn have metallic radii of 1.46 and 1.53 Å, respectively. The binding energies (Fig. 3-6) do not monotonically vary with size (for example, the binding energy of Fe to the basal intrinsic stacking fault is larger than both Cr and Ni despite similar metallic radii). Thus, we have evaluated the electronic interactions, using differential electron density plots to graphically represent the difference in electron densities between interacting and non-interacting calculations, to identify the extent to which these interactions contribute to the binding energy trends. The differential electron densities were calculated by the lev00 software [139] using the total charge densities of the solute in the state of interest (the stacking fault interface or vacancy platelet) and its reference bulk state in Zr.

Fig. 3-12 plots differential electron densities in bulk Zr, basal intrinsic faulted Zr, and the vacancy platelet for the substitutional elements of Sn, Nb, and Ni, while Fig. 3-13

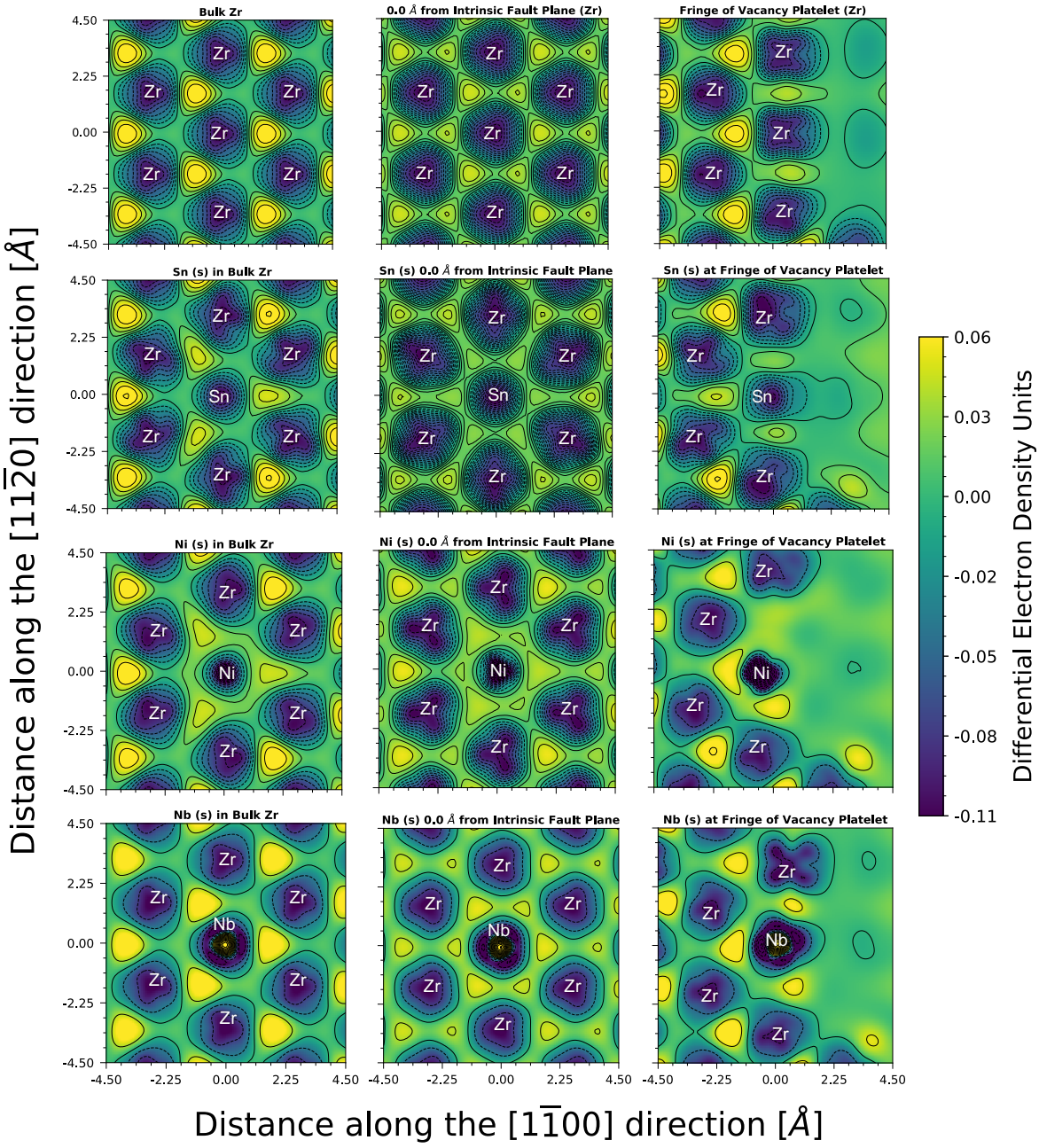

Fig. 3-12. Differential electron density plots for substitutional Sn (row 2), Ni (row 3), and Nb (row 4) solute in bulk Zr (column 1), the basal intrinsic fault plane (column 2), and the vacancy platelet fringe (column 3) with pure Zr as a reference (row 1) [55].

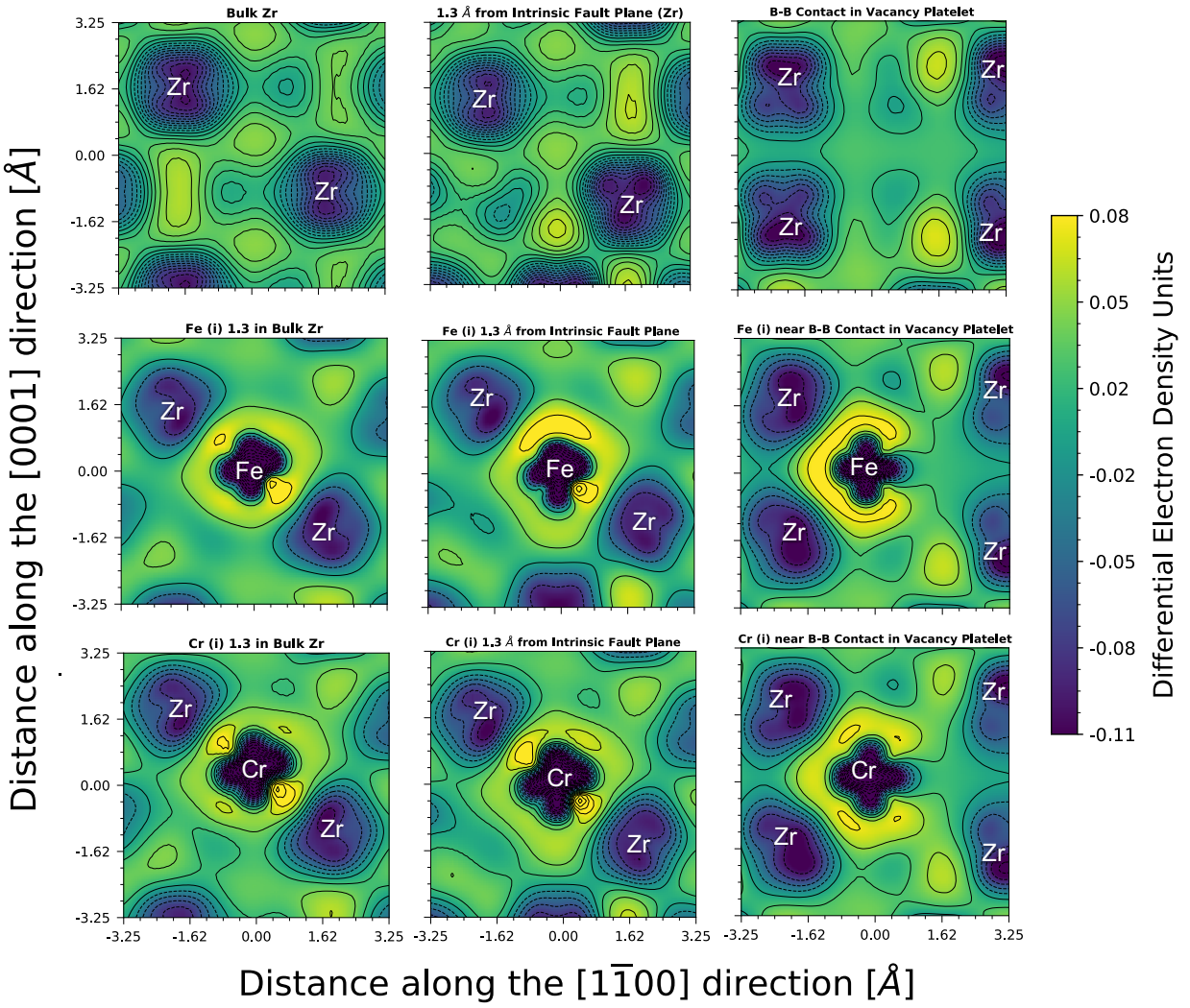

Fig. 3-13. Differential electron density plots for interstitial Fe (row 2) and Cr (row 3) solute in bulk Zr (column 1), near the basal intrinsic fault plane (column 2), and near the vacancy platelet B-B contact (column 3) with pure Zr as a reference (row 1) [55].

provides these plots for the interstitial elements of Fe and Cr, with pure Zr used as a reference. Amongst the substitutional solutes, it can be seen that Sn and Ni locally alter the electron density characteristics in bulk Zr while Nb has little impact. The interaction between Sn and nearby Zr atoms is fully diminished for Sn in the basal intrinsic fault but only partially diminished in the vacancy platelet fringe configuration, which could account for the large binding energy of Sn to stacking faults but significantly reduced Sn binding energy to vacancy platelets. Conversely, the interaction between Ni and Zr is only partially diminished in the stacking fault configuration but fully diminished near the vacancy platelet, which is consistent with the opposite binding behavior for Ni (compared to Sn). As expected by the low Nb binding energy, there is little indication of any electron interaction differences for Nb relative to those normally experienced in bulk Zr. For both interstitial Fe and Cr (Fig. 3-13), there is local partitioning of the surrounding electron densities in the stacking fault and vacancy platelet configurations when compared to the more symmetric distributions in bulk Zr. This local partitioning is strong for Fe but weak for Cr near the intrinsic fault plane, consistent with the larger and weaker calculated binding of these elements, respectively, to these basal faults. Both elements show similar strong electron density partitioning in the vacancy platelet, which indicates that the larger binding of Cr could result from elastic interactions.

3.5 Summary and Conclusions

Irradiation growth in α-Zr results from the volume-conservative expansion of its unit cells in the a-axis with a corresponding contraction in the c-axis. These growth strains are known to become greatly accelerated at high neutron irradiation fluence that correspond with the observed nucleation and growth of faulted vacancy loops on basal planes, termed c-loops. One hypothesis for the stabilization of c-loops is the reduction in stacking fault energy by solute segregation via the "Suzuki effect." The binding energy interaction of Fe, Sn, Nb, Cr, and Ni with basal extrinsic, basal intrinsic, and prismatic stacking faults in Zr has been investigated by DFT calculations and these results are then correlated to segregation profiles. Through a thermodynamic model, the segregation of these elements has been related to the reduction of SFEs and, indirectly, to the formation energies of faulted vacancy loops in Zr. For the case of the experimentally observed super-saturation of Fe, we assume that a dynamical equilibrium distribution is achieved between the solute in the matrix and near the stacking fault, which leads to a prediction of strong segregation of Fe to basal stacking faults. It is important to note that the assumed dynamic steady-state Fe super-saturation assumed here is not fully consistent with a rigorous thermodynamic equilibrium, and thus should be considered as an upper bound estimation of the segregation potential. However, the prediction of Fe segregation to stacking faults in irradiated Zr alloys should be robust. Future analysis should investigate the dynamic, thermodynamic, and kinetic phenomena as well as the various sources and sinks of Fe in the Zr matrix that may impact the segregation potential of Fe. The impact of all the investigated chemical species is summarized as follows:

- **Fe (interstitial):** Large, long-range binding to basal faults with limited matrix solubility at low fluence. Significant effect at reducing *c*-loop formation energies at high fluence once matrix concentrations are observed to increase.
- **Sn (substitutional):** Moderate binding energies to basal faults with high matrix concentrations. Significant effect on reducing *c*-loop formation energies.
- **Nb (substitutional):** Low binding energies to all stacking faults. Negligible impact.
- **Cr (interstitial):** Low-to-moderate binding energies to basal faults with low matrix solubility. Negligible impact on faulted c-loop formation energies.
- **Ni (substitutional)**: Low binding energies and matrix solubility. Negligible impact.

The condensation of vacancies onto a single basal plane results in the close contact of two B layers. This structure is a high-energy precursor to larger faulted c-loops or intermediate pyramidal vacancy configurations [84, 85]. The binding energies of Sn, Nb, Fe, Cr, Ni, and H were calculated to a 19-vacancy platelet to simulate their interaction with this nucleating defect. Fe and Cr were shown to have the strongest binding interactions and may have a substantial effect in stabilizing these defects at high fluence, when these solute species become available within the matrix as a result of intermetallic precipitate dissolution. Ni demonstrated moderate binding energies but is not expect to have as significant of an effect on *c*-loop nucleation due to its lower alloying content and limited solubility in the α-Zr matrix. Segregation of multiple H atoms could enhance the weak per-atom effect reported here, but H may be preferentially attracted to alternate, more tightly-binding trapping sites. Sn, Nb, and H all exhibited low binding energies to the vacancy platelet structure; thus, Sn is most likely a larger contributor in the growth regime of *c*-loops once the dislocation loops have fully developed their faulted nature. Considering that c-loops often reach sizes greater than 100 nm, the stacking fault energy contribution will dominate and the solute segregation mechanism proposed here may explain the observed c-loop growth and formation with respect to the originally thermodynamically-favored perfect a-loop.

3.6 Implementation of results in the CD model

The results and mechanisms discussed in this Chapter can be divided into two categories: c-loop growth or c-loop nucleation. For c-loop growth, the predominant impact of solute is a reduction in SFE. In terms of the CD model, this impact is best implemented via a modification of the binding energies of c-loop defect clusters. Considering Eq. (3-1) and parameters based on *ab initio* simulations [37], it is possible to estimate faulted basal extrinsic and basal intrinsic c-loop formation energies, respectively:

$$E^{f}_{E,c-loop}(n) = 9.08\gamma_E n + 2.87\sqrt{n}\,ln\left(1.50\sqrt{n}\right) \qquad (3\text{-}13)$$

$$E^{f}_{I_1,c-loop}(n) = 9.08\gamma_{I_1} n + 3.02\sqrt{n}\, ln\left(1.64\sqrt{n}\right) \quad (3\text{-}14)$$

The binding energy is related to the change in energy that results from the emission of a monovacancy from these c-loops:

$$E^{b}_{n,1v} = E^{f}_{1v} + E^{f}_{n-1} - E^{f}_{n} \quad (3\text{-}15)$$

Therefore, expressions for basal extrinsic and basal intrinsic c-loop monovacancy binding energies can be determined as a function of the SFE by plugging in Eq. (3-13) and Eq. (3-14) into Eq. (3-15), respectively:

$$E^{b}_{n,1v,E} = 2.03 + 2.87\left[\sqrt{n-1}\, ln\left(1.50\sqrt{n-1}\right) - \sqrt{n}\, ln\left(1.50\sqrt{n}\right)\right] - 9.08\gamma_{E} \quad (3\text{-}16)$$

$$E^{b}_{n,1v,I_1} = 2.03 + 3.02\left[\sqrt{n-1}\, ln\left(1.64\sqrt{n-1}\right) - \sqrt{n}\, ln\left(1.64\sqrt{n}\right)\right] - 9.08\gamma_{I_1} \quad (3\text{-}17)$$

A reduction in the c-loop SFE will increase c-loop binding energies and, therefore, enhance their growth within the CD model. For a given matrix concentration of some solute, its segregation profile can be calculated through Eq. (3-10) with the binding energies reported here in Fig. 3-6. Finally, the calculations can be propagated to calculate modified SFEs with Eq. (3-12) and inform the monovacancy binding energies through Eq. (3-16) and Eq. (3-17). The only model input in this approach is the matrix concentration of solute which can be estimated based on alloy content and APT data, such as in [60]. A delay in the release of key solute such as Fe and Cr from precipitates may play a role in the delayed onset of c-loop growth. Another contributor to this phenomenon could be related to solute interaction with c-loop precursors, as was discussed in Sections 3.3 and 3.4 of this Chapter. Describing the impact that this might have in the CD model requires information from future Chapters, and as such, it will be further described in Chapter Eight.

Chapter Four:

Defect Production from Displacement Cascades: Quantifying the Effect of Electronic Stopping

The work in this chapter has been previously published in the Journal of Nuclear Materials by myself, Jose March-Rico, as the first author. The article titled, "Quantifying the impact of an electronic drag force on defect production from high-energy displacement cascades in α-zirconium" was co-authored with C. Miller McSwain and Brian D. Wirth [9]. My role as first author included: research conceptualization, methodology development, results validation, formal analysis of the data, visualization, as well as writing the original and revised drafts. The only modification to this article is the addendum of Section 4.4, which describes the implementation of the results described in this chapter into the CD model

Displacement cascades are the primary unit of irradiation damage which occurs on the picosecond and nanometer scale: a displacement cascade of atomic collisions between lattice atoms, initiating with the production of an energetic primary knock-on atom (PKA) from the elastic collision with a high-energy neutron. As discussed in Chapter Two, the defect source term is a critical parameter in the CD model and can only be calculated from MD simulations of displacement cascades; the accuracy of these simulations will directly affect the predictions of the CD model. One possibility to increase the accuracy of these simulations is to incorporate electronic stopping effects which reduce the total energy available for the displacement of target atoms, E_{dam}. This damage energy is determined by subtracting the total inelastic energy losses to target electrons from the energy of the incident PKA. One of the earliest theories to quantify electronic stopping effects in monoatomic targets was developed by Lindhard, Scharff, and Schiott (LSS) in 1963 [140]. This approach enables the calculation of E_{dam} using a numerical approximation to the universal function $g(\epsilon)$ [67]:

$$E_{dam} = \frac{E_{PKA}}{1 + kg(\epsilon)} \quad (4\text{-}1)$$

$$g(\epsilon) = 3.4008\,\epsilon^{1/6} + 0.40244\,\epsilon^{3/4} + \epsilon \quad (4\text{-}2)$$

$$k = 0.1337\,Z_1^{1/6}(Z_1/A_1)^{1/2} \quad (4\text{-}3)$$

where Z_1 and A_1 are the atomic number and mass number, respectively, of the projectile; a full description of ϵ is provided in Ref. [67].

One of the most common tools for the estimation of ion-induced damage profiles and nuclear damage energies is the Stopping and Range of Ions in Matter (SRIM) code [141]. SRIM predicts electronic stopping powers based on fits to experimental data, and describes nuclear scattering with the universal ZBL scattering potential developed by Ziegler, Biersack, and Littmark [142]. For a user-specified combination of incident ion and target atoms, the SRIM calculation can be run with either the quick TRIM (modified Kinchin-Pease) option, or the full-cascade TRIM option. Both options treat the energy loss of the incident ion with a stochastic Monte Carlo approach based on a binary collision approximation [141, 143, 144]. The discrepancy between the two approaches is found in the treatment of the energy loss by the secondary recoil atoms [145]. In the quick TRIM option, the energy loss of secondary recoils to electrons and target atom interactions is determined by the energy partition model of Lindhard et al. [146] which implements electronic stopping based on LSS theory and atomic scattering based on the Thomas-Fermi potential. Alternatively, the full-cascade TRIM option extends the Monte Carlo approach to follow each individual target recoil and determine energy losses based on the SRIM-predicted electronic stopping powers and atomic scattering governed by the ZBL universal potential. Stoller et al. recommend the use of the quick TRIM (modified Kinchin-Pease) option to maintain consistency with the international standard [107, 147] while Weber and Yhang argue that the full-cascade option provides a more accurate determination of the damage energy, number of displacements, and damage depth profiles [145].

Cascade studies in α-zirconium have traditionally omitted simultaneous electronic energy losses [10, 11, 68], with the exception of very recent work [12]. This therefore implies the omission of two mechanisms during displacement cascades: 1) the additional slowing down of energetic atoms from electronic ionization and excitation losses and 2) the cooling of cascade temperatures through energy transfer between the atomic and electronic sub-systems (electron-phonon coupling) [148]. The first of these mechanisms has been addressed through the application of a drag force on energetic atoms with a strength proportional to the energy-dependent electronic stopping power [12, 149, 150]. Electronic drag force implementation in MD simulations has been shown to have a sizeable effect on the number of defects produced by metal sputtering, resulting in better agreement with experimental data [151, 152], although care must be taken in selecting a cut-off energy for the inclusion of electronic stopping effects [153]. This method represents a simplistic approach to remove kinetic energy from energetic atoms, but does not transfer energy into the electronic subsystem. Simulating an exchange of energy between the atomic and electronic sub-systems would require the implementation of a two-temperature model [150, 154-156]. A model of this nature would allow energy transport away from the cascade, dependent upon the electronic thermal conductivity and electron-ion coupling factor, and may provide an important pathway for cascade cooling. However, the impact of the two-temperature model on cascade cooling and defect production is very sensitive to the selected electron-ion coupling factor as well as the density of the numerical grid used to solve the electronic heat-diffusion equation. Due to this strong dependence on selected model parameters, it is currently difficult to definitively assess the impact of the two-temperature model.

In this chapter, we specifically isolate the effect of an electronic drag force on defect production within displacement cascades in α-Zr. While this approach does not consider a two-temperature interaction between sub-systems, cascade cooling is facilitated through a heat-dissipating barrier to simulate heat loss to the surrounding bulk. A similar method has been recently implemented in α-zirconium [12], but a comparison to equivalent data collected without the electronic drag force was not provided. Here, we directly compare defect production considering: 1) nuclear stopping only and 2) simultaneous nuclear and electronic stopping to assess the impact of an electronic drag force in the Large-Scale Atomic/Molecular Massively Parallel Simulator (LAMMPS) code [157]. The equivalent nuclear damage energy is then compared to the theoretical values predicted by the LSS model (Eq. (4-1) through Eq. (4-3)) and the SRIM code.

4.1 Modeling Method

Displacement cascades were simulated with MD using the Large-Scale Atomic/Molecular Massively Parallel Simulator (LAMMPS) code [157]. An embedded-atom method (EAM) interatomic interaction between Zr atoms was described by the #3 potential developed by Mendelev and Ackland in 2007 (termed the M07 potential) [70], with the Ziegler-Biersack-Littmark (ZBL) universal repulsive potential [142] fit at distances less than 1 Å for short-distance interactions. The M07 potential is superior to an earlier EAM Zr interatomic potential developed in 1995 by Ackland et al. [69] for the re-production of *ab initio* properties and defect configurations [70, 80]. All simulation cells were thermally equilibrated for 100 ps at 600 K in an NPT (constant atoms, pressure, and temperature) ensemble to ensure that the cascades were simulated under zero-strain conditions, and that lattice thermal vibrations (phonon waves) were established for the selected temperature as recommended in Ref. [148]. During the simulations, an NVT (constant atoms, volume, and temperature) ensemble was applied to a 10 Å-thick layer at the boundary of the simulation box to simulate heat-dissipation into the surrounding bulk while an NVE (constant atoms, volume, and energy) ensemble was applied to the interior of the box. Periodic boundary conditions were applied in all three directions. The simulation box sizes were selected such that, on average, a distance of at least one cascade width was maintained between the cascade periphery and the heat-dissipating boundary. These supercell sizes, as well as the selected primary knock-on atom (PKA) energies, are summarized in Table 4-1. A variable timestep was implemented to ensure that no atom moves more than 0.5% of a lattice parameter (0.016 Å) in a given timestep. Any simulations for which a channeling PKA passed through the periodic boundary were discarded from analysis.

PKAs were randomly selected from a 2 Å-thick spherical shell with a radius equivalent to one-third the simulation cell diameter, and given a velocity vector towards the center of the supercell. The number of defects were monitored throughout the duration of the cascade using Wigner-Seitz analysis as implemented in the "compute voronoi/atom" command with the occupation keyword in LAMMPS. This analysis identifies defects through

Table 4-1. PKA energies and simulation box characteristics for displacement cascades in α-Zr. [9]

PKA Energy (keV)	Simulation Box Size (Å x Å x Å)	Number of Atoms
1	233 x 235 x 238	556,416
2.5	310 x 314 x 320	1,333,248
5	342 x 346 x 350	1,787,584
7.5	368 x 370 x 372	2,166,912
10	420 x 426 x 429	3,240,640
15	484 x 492 x 496	5,068,800
20	530 x 538 x 538	6,549,504
30	582 x 582 x 588	8,536,320
40	634 x 639 x 641	11,082,624

the comparison of tessellation volume occupancies in the displaced atomic configuration to those in a reference atomic configuration state. Once the number of defects remained constant for a period of 3 ps, the cascade was considered quenched, and atomic positions were analyzed in the OVITO software [158]. Interstitial and vacancy cluster size identification was initially performed with a second-nearest-neighbor cutoff distance of 3.232 Å as recommended in Ref. [148], but a cutoff of 3.6 Å was found to more appropriately capture the defect cluster states. In particular, di-interstitials were often mis-interpreted as two single interstitials when analyzed with the 3.232 Å second-nearest-neighbor cutoff distance at 600 K.

Electronic energy losses were incorporated through a friction force applied to all atoms with an energy above a defined cutoff, E_c. An energy cutoff of 10 eV is recommended by Sand and Nordlund [153]. LAMMPS adjusts the strength of this friction force based on the velocity of each atom and its energy-dependent stopping power:

$$\overrightarrow{F_i} = \overrightarrow{F_i}^0 - \frac{\overrightarrow{v_i}}{||v_i||} \cdot S_e \qquad (4\text{-}4)$$

where $\overrightarrow{F_i}^0$ is the un-modified force calculated for each atom, $\overrightarrow{v_i}$ is the atom velocity, and S_e is the energy-dependent electronic stopping power. The electronic stopping powers for Zr were tabulated using the SRIM-predicted values based on the fitting and extrapolation of experimental data [141]. Two MD data sets with 50 simulations per PKA energy were collected for comparison: 1) cascades performed with nuclear stopping only (S_n) and 2) cascades performed with simultaneous nuclear and electronic stopping ($S_n + S_e$). SRIM calculations were performed to estimate the expected nuclear damage energy of the Zr PKAs and to calculate the NRT-predicted number of defects using Eq. (1-2). The full-cascade TRIM calculation option was selected as recently recommended by Weber et al. [145]. This provides a closer representation of the energy loss conditions in the LAMMPS simulations (which utilizes the SRIM-predicted electronic stopping powers for electronic losses of each atom and the ZBL scattering potential at close distances for atomic scattering) than the quick TRIM option (which simply calculates the energy partitioning of secondary recoils based on the model by Lindhard et al. [146]). The target density was set to 6.49 g/cm^3. The lattice binding energy was set to 0 eV as recommended by Stoller et al. [147], and the threshold displacement energy was set to 40 eV for α-Zr as specified by the NRT standard [107].

4.2 Results and Discussion

4.2.1 Predicting electronic losses and estimated nuclear damage energies

Due to the relatively low energies of Zr PKAs in comparison to their rest mass, energy-loss interactions are expected to be predominantly nuclear. This is demonstrated in Fig. 4-1

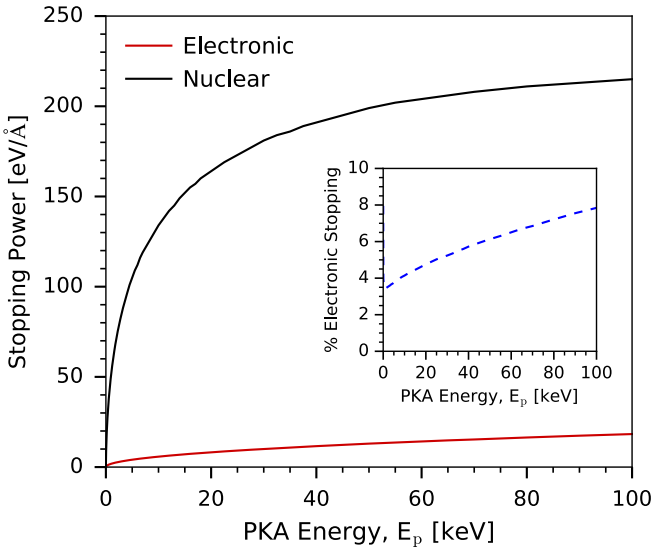

Fig. 4-1. Electronic and nuclear stopping powers for Zr PKAs in an α-Zr target lattice as calculated by the SRIM code [141]. The insert demonstrates the percentage of electronic stopping relative to total stopping. [9]

with a comparison between the nuclear and electronic stopping powers of Zr PKAs up to 100 keV in energy, as predicted by the SRIM code [147]. The nuclear damage energies of the Zr PKAs is calculated by subtracting the total electronic energy losses of both the PKA and the target recoils in SRIM. The integrated electronic energy losses and nuclear damage energies predicted by SRIM with the full-cascade option are provided in Table 2 and compared to the nuclear damage energies predicted by the LSS model (Eq. (4-1) through (4-3)). The losses are moderate at low PKA energies (a 0.13 keV loss for a 1 keV PKA) but are greater at high PKA energies (a 7.5 keV loss for a 40 keV PKA). For all PKA energies, SRIM (full-cascade) predicts greater nuclear damage energies than the LSS model. The quick TRIM option in SRIM has been stated to overestimate the amount of energy lost by target recoil atoms to ionization [145]. For the case of a 40 keV Zr PKA, the quick TRIM option predicts a ~19.6 % loss of the initial energy by target recoils to ionization (E_{dam} = 30.1 keV) while the full-cascade option predicts only 13.8 % losses to these interactions (E_{dam} = 32.5 keV). In contrast, both options predict approximately 5 % energy loss (~2 keV) by the incident ion to electronic interactions.

These nuclear damage energies can be used as input to the NRT equation (Eq. (1-2)) to assess the theoretical production of Frenkel pairs for each PKA energy with an average displacement threshold energy of 40 eV as specified by the NRT standard for α-Zr [107]. It is well documented, however, that the NRT prediction is several times greater than the surviving number of defects largely due to significant athermal recombination of in-cascade defects [10, 11]. Regardless, the general expected trend for increasing PKA energy is a greater number of produced defects despite greater electronic energy losses in this energy regime.

4.2.2 Defect production

Fig. 4-2 plots the time evolution of the number of Frenkel pair defects as a function of PKA energy, and shows the expected rapid formation of Frenkel pairs as the Zr PKA initially deposits its energy through high-energy, elastic collision with lattice atoms. The curves displayed in the figure represent the average number of defects over all 50 simulations per PKA energy, where averages are plotted in 0.5 ps bins. The peak damage state is observed within the first 3-4 ps, and then defects rapidly begin to athermally recombine during the heat-spike phase of the displacement cascade before reaching an effectively constant number of surviving defects. A greater number of maximum and surviving defects are formed as the PKA energy increases from 1 keV to 40 keV. The effect of simultaneous electronic energy loss is clear: a reduction in both the maximum and surviving number of defects as the PKA energy increases. This electronic stopping effect is more significant with increasing PKA energy. This is due to the decreased energy available for elastic collisions, and earlier stopping of energetic atoms when compared to the condition of nuclear stopping power only.

The impact of electronic stopping on final defect production is demonstrated by comparing the surviving number of Frenkel pair defects versus the PKA energy in Fig. 4-3.

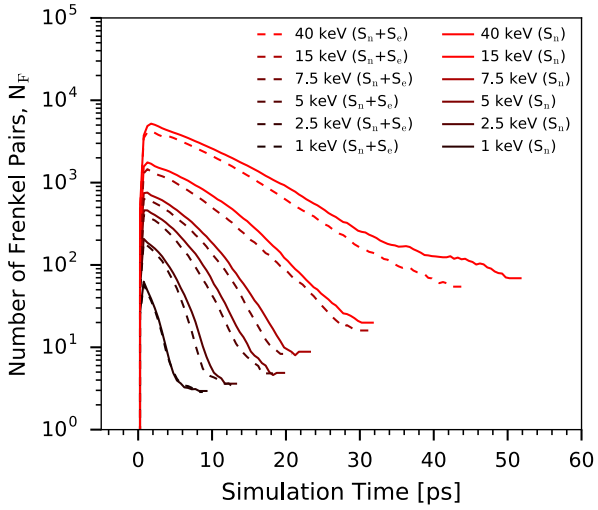

Fig. 4-2. The number of Frenkel pairs versus simulation time are plotted for 1) nuclear stopping only ($\mathbf{S_n}$, solid lines) and 2) simultaneous nuclear and electronic stopping ($\mathbf{S_n + S_e}$, dashed lines) for PKAs with energies of 1, 2.5, 5, 7.5, 15, and 40 keV. The curves represent the average values from 50 simulations per PKA energy [9].

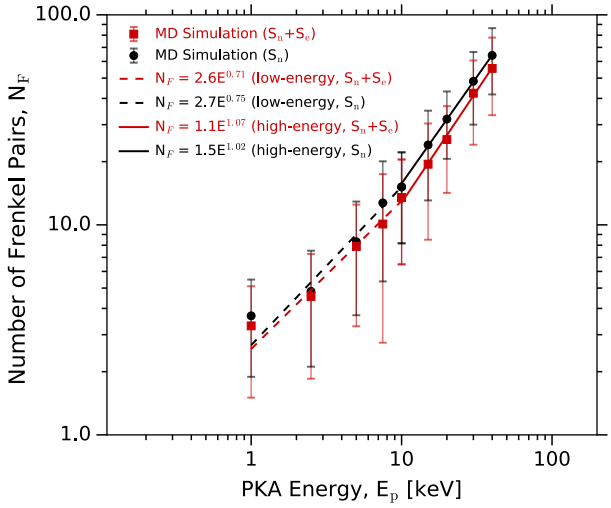

Fig. 4-3. The number of surviving Frenkel pairs versus PKA energy are plotted for 1) nuclear stopping only ($\mathbf{S_n}$, black closed circles) and 2) simultaneous nuclear and electronic stopping ($\mathbf{S_n + S_e}$, red closed squares) for PKAs energies up to 40 keV. Error bars represent the standard deviation of the average values for 50 simulations per PKA energy. [9]

Power-law curves of the form $N_F = A(E_p)^m$ have been fit to both data sets to describe the energy dependence of defect production. There are a number of trends that define the characteristics of defect production via displacement cascades. First, as expected, the number of surviving defects is only a small fraction of the NRT-predicted values (Table 4-2, Fig. 4-4) and this fraction saturates at high PKA energies. Second, there is a distinction between the low-energy and high-energy regimes for the power-law dependence of defect production. These regimes are correlated to the onset of sub-cascade formation at approximately 10 keV PKA energy [11], which accounts for the plateau of the NRT survival fraction at high PKA energies in Fig. 4-4. Electronic energy losses do not affect the general behavior of defect production. Rather, an electronic drag force acts to reduce the magnitude of the surviving defect number while following the same behavior as the nuclear stopping simulations. It is worth noting that the predicted high-energy power-law fit for the electronic stopping data will not extend to very high PKA energies for which the electronic stopping becomes dominant. However, a significant deviation is not expected up to a PKA energy of 100 keV as predicted by the stopping power analysis in Fig. 4-1, and PKAs above this energy are unlikely to be produced with the anticipated energy dependence of fission neutrons in pressurized water reactors (Fig. 2-1).

It is curious to consider how the defect production from the simultaneous electronic drag force approach compares to simply subtracting the total expected electronic energy losses from the incident PKA (i.e. considering the nuclear damage energy in lieu of the total PKA energy). The predicted number of Frenkel pairs for this scenario can be determined by inputting the SRIM-predicted nuclear damage energies calculated in Table 4-2 into the power-law expressions of Frenkel pair production for the case of nuclear stopping only (S_n). From Fig. 4-3, the expressions for low-energy and high-energy Frenkel pair production as a function of PKA energy, respectively, are:

$$N_F = \begin{cases} 2.7E^{0.75}, (\mathrm{E} < 10\ \mathrm{keV}) \\ \\ 1.5E^{1.02}, (\mathrm{E} \geq 10\ \mathrm{keV}) \end{cases} \qquad (4\text{-}5)$$

The Frenkel pair production as calculated with LAMMPS is compared for the (S_n) and ($S_n + S_e$) conditions in Table 4-3. The effect of simultaneous electronic losses is notable—a 10 to 20 % reduction in the surviving number of Frenkel pairs. The equivalent nuclear damage energy of the incident PKA simulated with the ($S_n + S_e$) condition can be determined by solving for E in Eq. (4-5) using the calculated number of Frenkel pairs in Table 4-3. For example, a 40 keV PKA is shown to have a 35.7 keV nuclear damage energy when implementing the electronic drag force in LAMMPS. This is in contrast to the values of 32.5 keV and 28.7 keV predicted by SRIM (full-cascade) and the LSS model, respectively (Table 4-2). As expected, there is a closer agreement between LAMMPS and the SRIM calculations with the full-cascade option than there is with the LSS model. This is due to the fact that the LSS theory (and, therefore, the quick TRIM calculation option in SRIM) may overestimate the amount of energy lost to ionization by target recoils [145].

Table 4-2. SRIM-determined electronic energy losses (full-cascade), the nuclear damage energies predicted by SRIM (full-cascade) and the LSS model (Eq. (4-1) through Eq. (4-3)), and the NRT-calculated number of Frenkel pairs (Eq. (1-2)) for PKA energies between 1 and 40 keV. [9]

PKA Energy (keV)	1	2.5	5	7.5	10	15	20	30	40
Electronic Energy Losses (SRIM) (keV)	0.13	0.41	0.81	1.23	1.66	2.55	3.48	5.45	7.49
E_{dam} (SRIM) (keV)	0.87	2.09	4.19	6.27	8.34	12.4	16.5	24.5	32.5
E_{dam} (LSS) (keV)	0.83	2.03	3.95	5.83	7.69	11.3	14.9	21.9	28.7
$N_{F,NRT}$ (E_{dam} SRIM)	8.77	20.9	41.9	62.7	83.4	124.4	165.1	245.5	325.1

Table 4-3. The calculated number of Frenkel pairs produced in MD simulations using nuclear stopping only (S_n) versus that of simultaneous nuclear and electronic stopping ($S_n + S_e$) conditions (averaged over 50 simulations). The calculated nuclear damage energy for the ($S_n + S_e$) condition is solved from Eq. (4-5). The predicted number of Frenkel pairs is determined by inputting the SRIM-determined nuclear damage energies (E_{dam}, Table 4-2) into the power-law expressions of Frenkel pair production for the (S_n) condition, given by Eq. (4-5). [9]

PKA Energy (keV)	1	2.5	5	7.5	10	15	20	30	40
Electronic Energy Losses (SRIM) (keV)	0.13	0.41	0.81	1.23	1.66	2.55	3.48	5.45	7.49
E_{dam} (SRIM) (keV)	0.87	2.09	4.19	6.27	8.34	12.4	16.5	24.5	32.5
E_{dam} (LSS) (keV)	0.83	2.03	3.95	5.83	7.69	11.3	14.9	21.9	28.7
$N_{F,NRT}$ (E_{dam} SRIM)	8.77	20.9	41.9	62.7	83.4	124.4	165.1	245.5	325.1

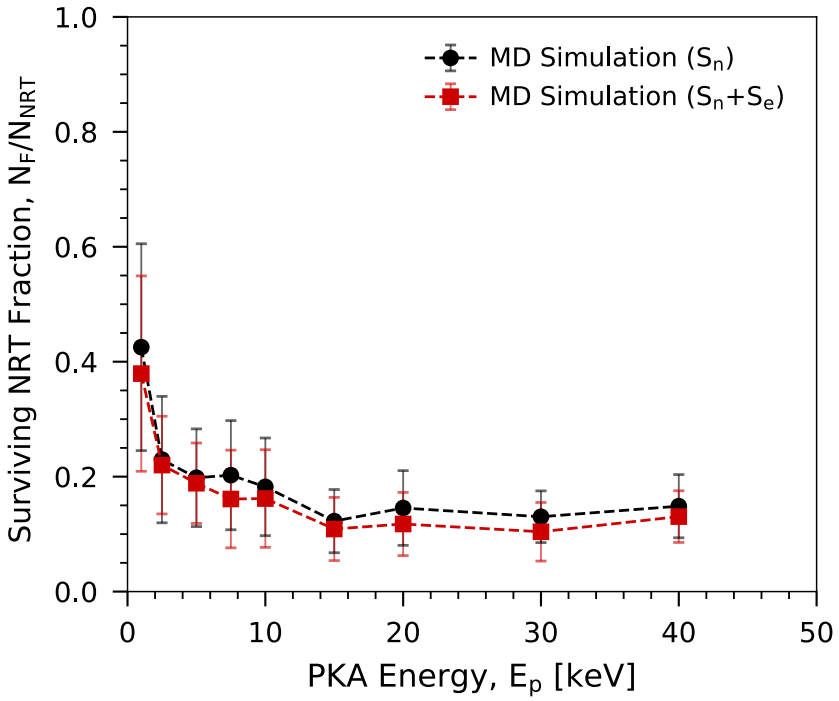

Fig. 4-4. The fraction of surviving defects compared to the NRT-predicted value (Table 4-2) for 1) nuclear stopping only (S_n, black closed circles) and 2) simultaneous nuclear and electronic stopping ($S_n + S_e$, red closed squares) for PKAs with energies up to 40 keV. The curves represent the average values from 50 simulations per PKA energy. [9]

It would appear that LAMMPS has a tendency to slightly underestimate the impact of electronic stopping for the 30 and 40 keV PKAs when compared to the SRIM full-cascade calculations. It is possible that this is due to the difference in the cascade shape when simulating cascades with simultaneous nuclear and electronic losses rather than simply using the nuclear damage energy and neglecting ionization losses. Because electronic energy losses occur over the duration of the cascade, the initial energetic PKA and its secondary recoils may create a more disperse cascade shape than if the cascades were run using the nuclear damage energy for the initial PKA without simultaneous ionization losses. However, the nuclear damage energies are within statistical error and any discrepancies between LAMMPS and SRIM-predicted values are most likely insignificant to overall defect production in α-Zr.

4.2.3 Defect cluster size distributions

For modeling methods that aim to simulate the migration, recombination, and clustering of irradiation defects, it is imperative to assess the defect cluster distribution for the incorporation of a defect generation term [105]. The clustering tendencies of interstitials and vacancies are presented in Fig. 4-5. Two trends in the defect clustering are clear: 1) vacancies cluster more readily than interstitials and 2) defect clustering fractions increase with increasing PKA energy. These trends are consistent with displacement cascade structures, which are comprised of vacancy-rich cores and sparser, ejected interstitials at the defect periphery, with greater defect densities at higher PKA energies. The effect of simultaneous energy losses on the clustering behavior is a slight reduction in the magnitude of clustering while maintaining the same trend of increasing clustering fraction with increasing PKA energy.

The full cluster size distributions for interstitials and vacancies are visually represented in Fig. 4-6(a) and Fig. 4-6(b), respectively, for low-energy 5 keV and high-energy 40 keV displacement cascades. Tabulated values are provided in Table 4-4 and Table 4-5 for interstitials and vacancies, respectively. Plotted in this way, it is not only clear that vacancies cluster more readily than interstitials, but that vacancies exhibit a greater tendency to form larger clusters than interstitials. In particular, vacancy clusters containing 85 and 99 vacancies were observed to form directly in cascades induced by 40 keV PKAs under the nuclear stopping only condition. This tendency to form large clusters is again likely attributable to the vacancy-rich core structure of displacement cascades. In contrast, interstitial clusters rarely exceed the size of n = 26 interstitials and produce a greater number of single, di-, and tri- defect clusters than vacancies. The greater mobility of these smaller defects could lead to rapid clustering post-cascade, but defect evolution over longer time scales should be captured by pertinent mesoscale codes. The effect of incorporating an electronic drag force on the cluster size distribution is, in general, only a slight reduction in the average number of large defect clusters.

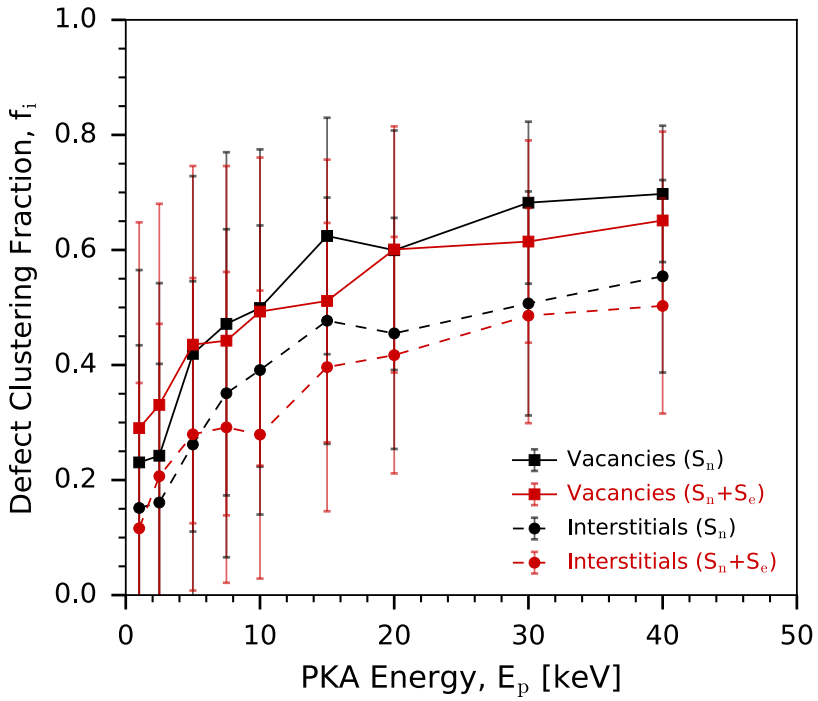

Fig. 4-5. The fraction of vacancies (solid lines) and interstitials (dashed lines) that reside in clusters of size n = 2 or greater as a function of incident PKA energy for the nuclear stopping only (S_n, black data points) and the simultaneous nuclear and electronic stopping conditions ($S_n + S_e$, red data points). Error bars represent the standard deviation of the average values for 50 simulations per PKA energy. [9]

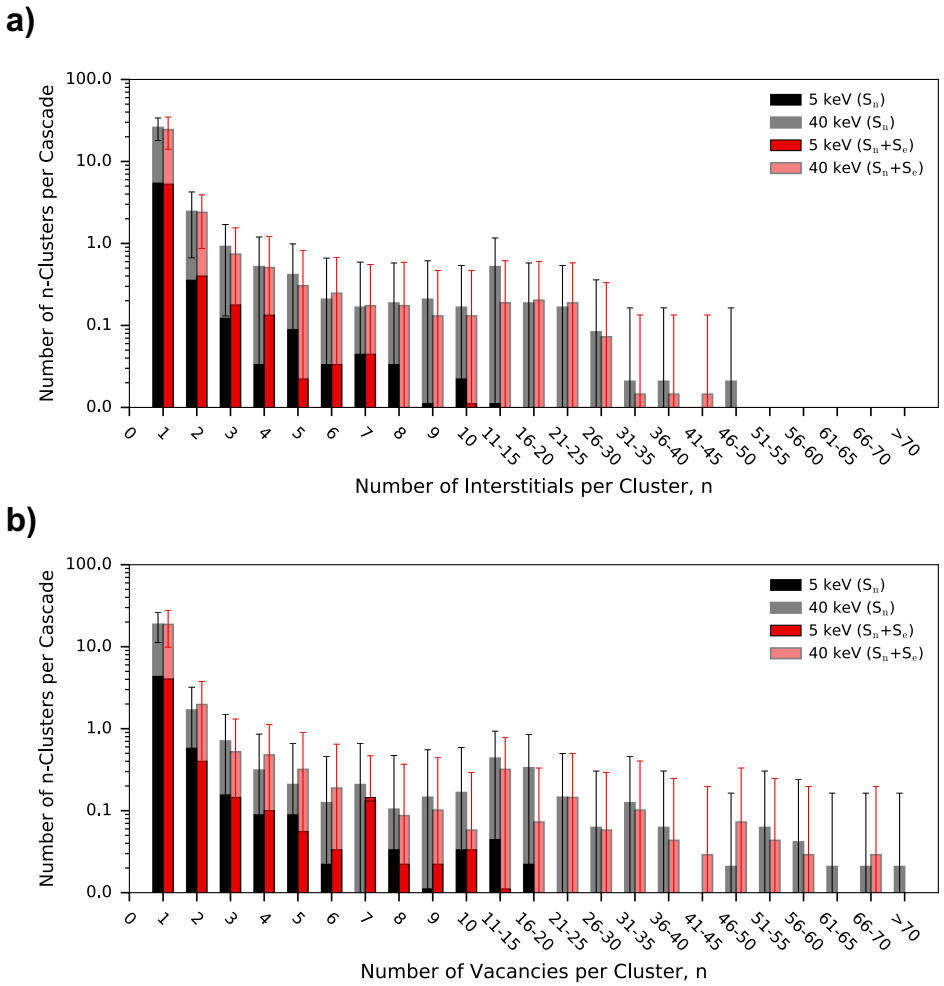

Fig. 4-6. The cluster size distribution for a) interstitials and b) vacancies produced by 5 keV and 40 keV PKAs with nuclear stopping only (S_n, gray/black bars) and simultaneous nuclear and electronic energy losses ($S_n + S_e$, red/pink bars). Error bars are only provided for the 40 keV PKA data set and represent the standard deviation for 50 simulations. [9]

Table 4-4. The cluster size distribution for interstitial defects produced with nuclear stopping only (S_n) and simultaneous nuclear and electronic energy losses ($S_n + S_e$). The values represent averages over 50 simulations per PKA energy with the standard deviation ranges provided. [9]

E_p (keV)	Size of interstitial clusters, n (S_n)									
	1	2	3	4	5	6 – 10	11 – 20	21 – 40	40 – 70	> 70
1	3.02±1.70	0.22±0.44	0.04±0.25	0.02±0.15	0	0	0	0	0	0
2.5	3.78±2.10	0.24±0.48	0.09±0.28	0.04±0.21	0.02±0.15	0	0	0	0	0
5	5.43±2.84	0.36±0.67	0.12±0.36	0.03±0.18	0.09±0.28	0.14±0.35	0.01±0.10	0	0	0
7.5	7.10±3.75	0.59±0.78	0.26±0.51	0.09±0.29	0.08±0.27	0.24±0.43	0.05±0.21	0.01±0.11	0	0
10	8.00±3.11	0.56±0.83	0.36±0.52	0.12±0.32	0.02±0.14	0.26±0.44	0.16±0.37	0.02±0.14	0	0
15	11.27±4.65	0.89±0.82	0.42±0.61	0.22±0.42	0.16±0.36	0.38±0.53	0.31±0.46	0.02±0.15	0	0
20	15.96±5.61	1.65±1.59	0.58±0.81	0.31±0.55	0.23±0.51	0.33±0.51	0.19±0.44	0.12±0.33	0	0
30	21.00±5.89	1.84±1.39	1.00±1.27	0.42±0.66	0.26±0.44	0.65±0.48	0.65±0.48	0.16±0.37	0	0
40	26.00±7.91	2.46±1.79	0.92±0.79	0.52±0.68	0.42±0.57	0.94±0.38	0.71±0.61	0.29±0.45	0.02±0.14	0
E_p (keV)	Size of interstitial clusters, n ($S_n + S_e$)									
	1	2	3	4	5	6 – 10	11 – 20	21 – 40	40 – 70	> 70
1	2.80±1.42	0.18±0.46	0.03±0.18	0.01±0.11	0	0	0	0	0	0
2.5	3.39±1.56	0.27±0.47	0.10±0.30	0.03±0.18	0.01±0.11	0.02±0.15	0	0	0	0
5	5.29±2.76	0.40±0.63	0.18±0.44	0.13±0.34	0.02±0.15	0.09±0.28	0	0	0	0
7.5	6.28±3.21	0.57±0.72	0.13±0.33	0.03±0.18	0.10±0.30	0.11±0.32	0.07±0.25	0	0	0
10	8.74±4.31	0.75±0.89	0.23±0.51	0.19±0.43	0.04±0.20	0.07±0.26	0.06±0.23	0.01±0.12	0	0
15	10.70±4.76	1.04±1.07	0.48±0.73	0.23±0.49	0.07±0.26	0.38±0.48	0.07±0.26	0	0	0
20	12.50±4.80	1.31±1.14	0.32±0.70	0.25±0.47	0.21±0.44	0.43±0.52	0.24±0.42	0.03±0.17	0	0
30	18.97±7.10	2.36±1.73	0.52±0.70	0.37±0.57	0.31±0.55	0.64±0.59	0.27±0.44	0.16±0.37	0.01±0.12	0
40	24.45±10.34	2.39±1.52	0.74±0.81	0.51±0.71	0.30±0.52	0.86±0.39	0.39±0.52	0.29±0.45	0.01±0.12	0

Table 4-5. The cluster size distribution for vacancy defects produced with nuclear stopping only (S_n) and simultaneous nuclear and electronic energy losses ($S_n + S_e$). The values represent averages over 50 simulations per PKA energy with the standard deviation ranges provided. [9]

E_p (keV)	Size of vacancy clusters, n (S_n)									
	1	2	3	4	5	6 – 10	11 – 20	21 – 40	40 – 70	> 70
1	2.62±1.54	0.22±0.42	0.12±0.33	0.02±0.15	0.01±0.10	0.02±0.15	0	0	0	0
2.5	3.33±1.89	0.29±0.54	0.11±0.31	0.04±0.21	0.04±0.21	0.03±0.18	0	0	0	0
5	4.34±2.74	0.58±0.79	0.16±0.36	0.09±0.28	0.09±0.28	0.10±0.30	0.07±0.25	0	0	0
7.5	5.69±3.26	0.52±0.62	0.25±0.46	0.09±0.29	0.09±0.29	0.18±0.39	0.17±0.38	0.03±0.18	0	0
10	6.40±2.80	0.40±0.63	0.26±0.59	0.18±0.38	0.16±0.50	0.34±0.51	0.10±0.30	0.10±0.30	0	0
15	8.18±4.28	0.78±0.99	0.20±0.40	0.09±0.28	0.20±0.45	0.31±0.46	0.29±0.45	0.22±0.42	0.02±0.15	0
20	11.71±5.26	1.17±1.14	0.38±0.48	0.23±0.47	0.08±0.28	0.38±0.48	0.44±0.50	0.17±0.37	0.06±0.24	0
30	15.06±5.58	1.52±1.13	0.39±0.61	0.35±0.54	0.19±0.47	0.52±0.56	0.71±0.45	0.35±0.48	0.06±0.25	0
40	18.79±7.50	1.69±1.52	0.71±0.79	0.31±0.55	0.21±0.45	0.75±0.60	0.77±0.47	0.40±0.49	0.17±0.37	0.02±0.14
E_p (keV)	Size of vacancy clusters, n ($S_n + S_e$)									
	1	2	3	4	5	6 – 10	11 – 20	21 – 40	40 – 70	> 70
1	2.04±1.14	0.26±0.49	0.15±0.35	0.02±0.15	0.01±0.11	0.02±0.15	0	0	0	0
2.5	2.83±1.78	0.40±0.59	0.13±0.34	0.03±0.18	0.02±0.15	0.04±0.21	0	0	0	0
5	4.04±2.38	0.40±0.61	0.14±0.35	0.10±0.30	0.06±0.23	0.26±0.44	0.01±0.10	0	0	0
7.5	4.90±3.12	0.62±0.73	0.24±0.45	0.10±0.30	0.06±0.28	0.18±0.42	0.07±0.25	0.01±0.11	0	0
10	5.94±3.25	0.74±0.91	0.19±0.43	0.16±0.37	0.10±0.30	0.22±0.45	0.16±0.37	0.03±0.17	0	0
15	7.94±4.37	0.62±0.78	0.26±0.53	0.13±0.41	0.09±0.28	0.35±0.51	0.28±0.45	0.10±0.30	0	0
20	9.06±5.10	0.93±0.99	0.37±0.62	0.26±0.58	0.12±0.36	0.31±0.46	0.34±0.47	0.15±0.35	0.03±0.17	0
30	15.01±6.03	1.61±1.29	0.46±0.76	0.25±0.56	0.13±0.38	0.49±0.56	0.52±0.53	0.22±0.42	0.10±0.31	0
40	18.70±8.83	1.97±1.79	0.52±0.79	0.48±0.65	0.32±0.58	0.57±0.58	0.39±0.49	0.35±0.48	0.20±0.40	0

4.2.4 Defect cluster morphologies

Representative interstitial and vacancy clusters observed to form in-cascade were annealed at 600 K for 50 ps to investigate whether they would form more stable cluster morphologies. Interestingly, this annealing cycle was sufficient to directly collapse an 85-vacancy cluster into a dislocation loop geometry on a corrugated type-1 $(1\bar{1}00)$ prism plane (Fig. 4-7). Basal plane projections demonstrate this structure at the bottom of the loop (Fig. 4-7(b)) and on adjacent basal planes near the center of the loop Fig. 4-7(c,d). The condensation of vacancies onto a corrugated prism plane causes the surrounding atomic planes to collapse and produce a prismatic stacking fault [82]. At larger sizes and longer time scales, it is expected that this structure will un-fault to form the perfect prismatic a-loop that is prevalent in irradiated α-Zr [13, 16]. Basal-plane vacancy structures were not observed to form in-cascade in this study. The large vacancy clusters produced in-cascade are all prismatic in nature, although annealing at temperature is necessary for the clusters to condense into planar geometries. All vacancy clusters and monovacancies are immobile at 600 K.

Single interstitials occupied octahedral sites, as predicted by the M07 potential [70], while small clusters tended to consist of parallel basal crowdions. These single interstitials and small basal crowdion clusters were highly mobile at 600 K, which is unsurprising considering the low in-plane migration energy of 0.06 eV reported for SIA diffusion [48]. However, larger clusters formed in metastable configurations consisted of a mix of crowdions and split interstitials. Annealing for 50 ps at 600 K was not sufficient for these clusters to re-orient into stable cluster configurations; larger clusters were entirely immobile throughout the 50 ps duration. Fig. 4-8(b) and Fig. 4-8(c) highlight interstitial positions in green for a 48-interstitial and a 15-interstitial cluster, respectively. The M07 potential predicts that these larger clusters form in columnar configurations rather than dislocation loop geometries. It is unclear whether or not the stability of this metastable interstitial cluster is a peculiarity of the M07 potential, which predicts the octahedral configuration rather than the expected basal octahedral configuration for single SIAs [70, 75]. Much longer annealing times or growth by interstitial capture may be necessary for these large clusters to adopt stable, mobile cluster configurations.

4.3 Conclusions

Defect production characteristics are analyzed for displacement cascades with PKA energies up to 40 keV in α-Zr under two conditions in the LAMMPS molecular dynamics code: 1) nuclear stopping only (S_n) and 2) simultaneous nuclear and electronic stopping ($S_n + S_e$). Electronic stopping is incorporated as a drag force that acts against energetic atoms with a strength proportional to the energy-dependent electronic stopping power in α-Zr. This drag

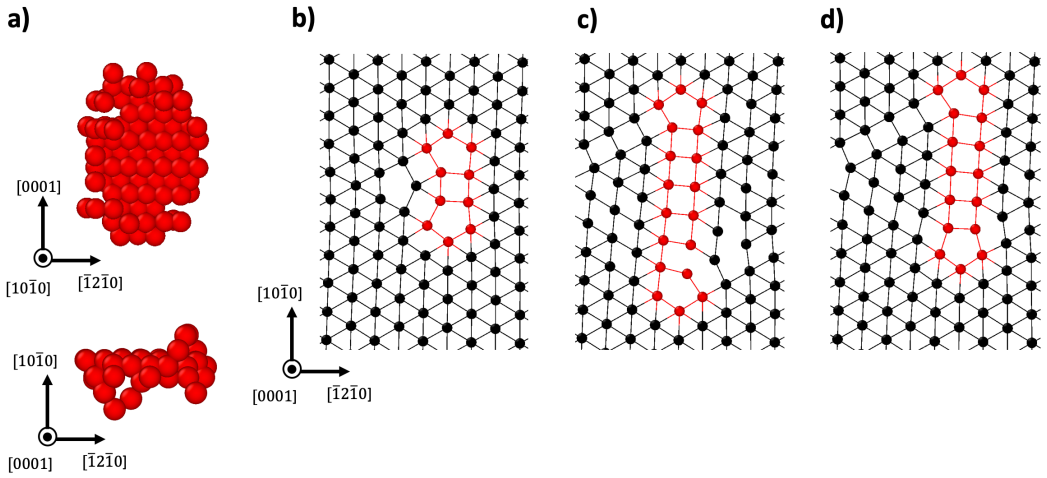

Fig. 4-7. Visualization of an 85-vacancy cluster that collapsed into a dislocation loop geometry on a corrugated type I prismatic plane {1$\bar{1}$00} following a 50 ps anneal at 600K. The full loop is shown in the OVITO software in a); basal plane projections are shown in b), c), and d). [9]

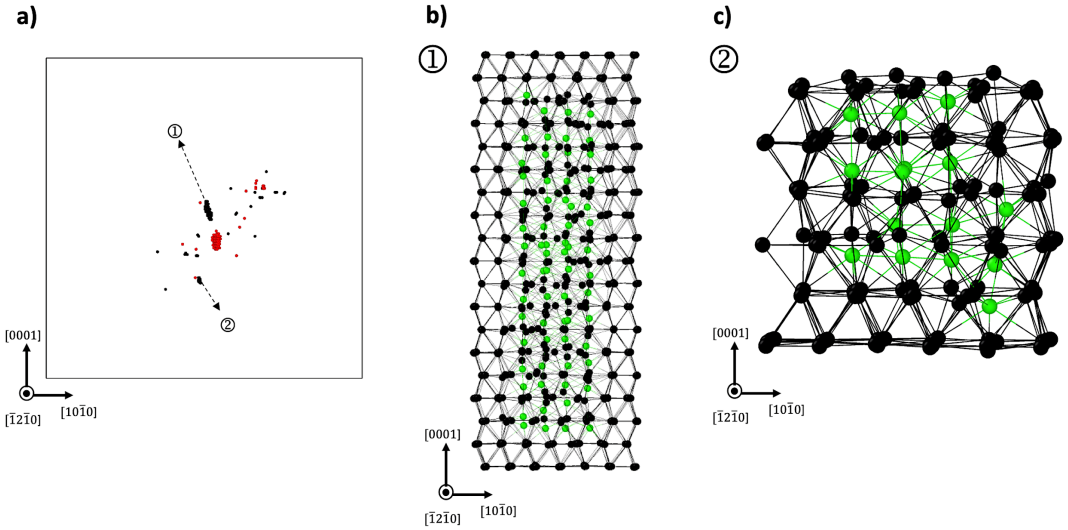

Fig. 4-8. (a) OVITO visualization of the defects produced by a 40 keV PKA (where interstitials and vacancies are represented as black and red spheres, respectively). A particular emphasis is placed on the morphology of a large 48-interstitial cluster (b) and a smaller 15-interstitial cluster (c) where interstitial positions are highlighted in green. These large interstitial clusters consist of parallel crowdion or split interstitials with prismatic character. [9]

force is implemented with the intrinsic "fix electron/stopping" command in LAMMPS and represents an alternative to the traditional method of subtracting the expected total electronic losses from the original PKA energy (i.e. using the nuclear damage energy).

The general trends of defect production as a function of PKA energy are consistent with typical cascade characteristics: the surviving number of Frenkel pairs obeys a power-law dependence of the form $N_F = A \cdot E^m$ (with unique variables m and A in the low-energy and high-energy regimes, distinguished by the onset of subcascade formation), NRT survival fractions approach a value of $\sim$20% for high PKA energies, and defect clustering increases with PKA energy. All large interstitial and vacancy clusters were prismatic in nature (no basal clusters were observed). An 85-vacancy cluster directly collapsed onto a corrugated type-I $(1\bar{1}00)$ prism plane to directly form a prismatic-faulted dislocation loop after annealing for 50 ps at 600 K. Large interstitial clusters did not form stable configurations for the same annealing cycle; immobile, columnar configuration of parallel crowdions and split interstitials persisted throughout the annealing cycle.

An electronic drag force was found to reduce the maximum number of defects produced during the displacement cascade heat spike phase and resulted in an approximate 10 to 20 % reduction in surviving Frenkel pairs. Defect clustering is slightly reduced with electronic stopping. The equivalent nuclear damage energies that were calculated based on the defect production observed through LAMMPS simulations were comparable to the SRIM-predicted energies when using the full-cascade option. In contrast, the LSS theory (and, therefore, the quick TRIM calculation option in SRIM) predicts more substantial energy losses to ionization. Overall, the intrinsic "fix electron/stopping" command in LAMMPS offers a user-friendly and effective means to incorporate simultaneous electronic stopping effects in MD displacement cascade simulations.

4.4 Implementation of results in the CD model

With the data collected in this chapter, we can explicitly quantify the total number of point defects and defect clusters produced by PKAs with energies between 1 and 40 keV while taking into account electronic stopping impacts. PKAs with energies greater than 40 keV are a relatively rare occurrence, but the defect production from these events can be estimated based on lower PKA energy data. Cascades produced by PKAs with greater than $\sim$10-20 keV are characterized by subcascade formation [12] and the defect production from these events is equivalent to the production from several lower-energy cascades. The method to calculate volumetric defect generation rates for implementation into our CD model was outlined in detail in Section 2.1.1. In summary, the number of displacement cascades per unit time per unit volume, $\phi(E)$, is known for each possible PKA energy based on a typical neutron flux in a PWR (Fig. 2-1). In this chapter, MD simulations have provided a tabulated database for the number of defects produced per displacement cascade of a given PKA energy, $N_i(E)$, (Table 4-4 and Table 4-5). Using Eq. (2-2) to sum up the contributions from all PKA energies along the possible energy spectrum, the calculated volumetric defect

source terms are plotted in Fig. 4-9. For these calculations, we considered the tabulated data that included electronic stopping effects, which tend to account for a 10-20 % reduction in the total produced defects, as previously shown in Fig. 4-3.

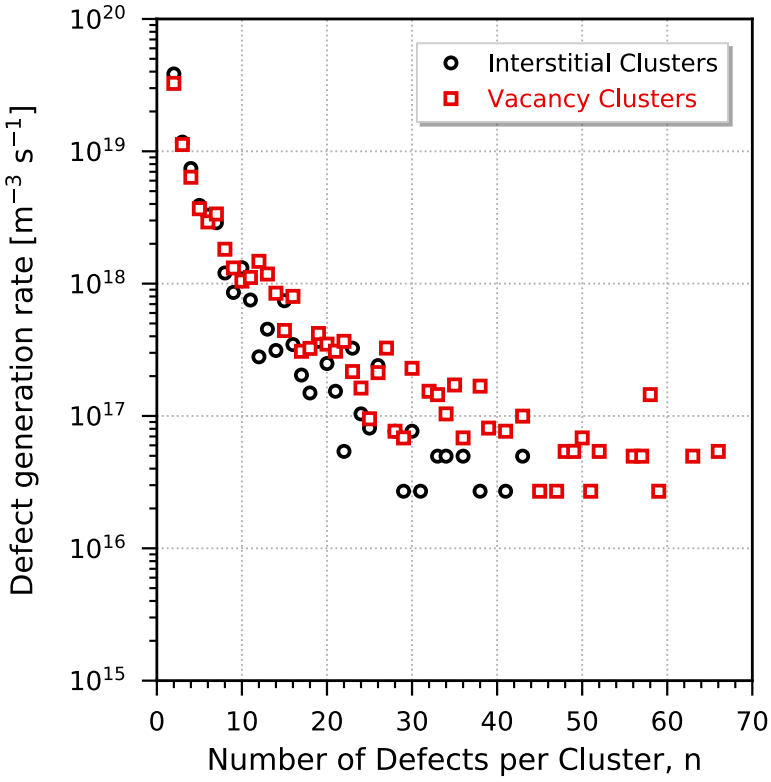

Fig. 4-9. Volumetric defect generation rates, $\dot{g}_i$, calculated with Eq. (2-2)based on a typical PWR PKA energy spectrum (Fig. 2-1) and tabulated data for defect production from displacement cascades (Table 4-4 and Table 4-5).

Chapter Five:

Defect Cluster Configurations and Mobilities

The work in this chapter has been previously published in the Journal of Nuclear Materials by myself, Jose March-Rico, as the first author. The article titled, "Defect cluster configurations and mobilities in α-Zr: A comparison of the BMD19 and M07 interatomic potentials" was co-authored with Brian D. Wirth [159]. My role as first author included: research conceptualization, methodology development, results validation, formal analysis of the data, visualization, as well as writing the original and revised drafts. The article has been modified to include the addendum of Section 5.6, which describes the implementation of the results described in this chapter into the CD model.

Within each displacement cascade event, many of the newly-generated defects will cluster or recombine, and the resultant damage state is a wide distribution of varying defect sizes, as seen in Chapter Four of this dissertation. The subsequent diffusional transport of defects within the lattice promotes interactions with existing microstructure that lead to defect accumulation or elimination. Over time this can cause a range of consequences such as low temperature hardening [160], high-temperature irradiation creep [161], and breakaway irradiation growth [4]. It is imperative, then, to develop a mechanistic understanding of mobile defect configurations and their transport within the anisotropic α-Zr lattice.

Molecular statics calculations are one of the only tools capable of assessing preferred configurations of large defect clusters such as dislocation loops or voids. One of the main drawbacks of these calculations, however, is the accuracy of the selected interatomic potentials. For example, the A95 and M07 Zr-Zr potentials both predict that voids offer the lowest energy configuration for extended vacancy defects [81] despite the fact that voids are rarely observed in irradiated Zr [13, 32]. It is expected that more modern potentials, such as the recently published BMD19 potential [78], may offer significant improvements to modeling accuracy, although no data yet exists to confirm this fact. Considering defect mobility in α-Zr, reports in literature are broadly available for point defect migration and their anisotropy [47-49], but data is lacking for defect cluster diffusion beyond a few small SIA clusters [48, 80].

The goal of this work is to compare the preferred defect configurations and their mobilities as predicted by the M07 #3 potential with the recently-published BMD19 potential. An extensive database of migration energies and diffusivities is lacking for the M07 potential and this topic has not yet been investigated with the BMD19 potential. In order to adequately implement defect mobility into a CD model, the diffusivities within the basal

plane and along the c-axis must be able to be calculated for any temperature for all mobile defects. This diffusivity data will be tabulated and the impact of defect anisotropy will be discussed in the framework of the breakaway irradiation growth phenomenon.

5.1 Modeling Method

MD simulations were performed as implemented in the Large-Scale Atomic/Molecular Massively Parallel Simulator (LAMMPS) [157]. A comparison is drawn between potentials published in 2007 by Mendelev and Ackland (referred to as M07 #2 and M07 #3) [70] and a potential published in 2020 by Wimmer et al. (BMD19.1, referred to simply as "BMD19") [78]. The M07 #3 potential predicts stacking fault energies and point defect properties with greater accuracy than the potential previously published by Ackland et al. in 1995 [69]. The M07 #3 is recommended over the M07 #2 potential for the study of pure hcp zirconium while the latter better describes the hcp to bcc phase-transition and liquid-structure data [70]. As such, the M07 #3 potential has been the preferred choice for a multitude of computational studies concerning radiation effects in α-zirconium [9, 12, 21, 31, 61, 73, 74, 84, 162]. However, it must be noted that the M07 #3 potential is inadequate for the simulation of small vacancy cluster binding energies, while the #2 potential provides greater agreement with *ab initio* calculations [37]. There are fewer differences between the BMD19.1 and BMD19.2 potentials [78]; the BMD19.1 potential is based entirely on a DFT training set using the PBE exchange-correlation function while the BMD19.2 potential is slightly modified to match experimental values of α-zirconium density at room temperature (a difference of $\sim$1.4%). As such, only the BMD19.1 potential, simply referred to as "BMD19", is considered here. The BMD19 potential offers a superior representation of point defect properties (such as predicting a stable BO SIA configuration in agreement with modern *ab initio* calculations [75]) at the cost of a considerable underestimation of basal SFEs. When considering vacancy cluster configurations, we compare results between the M07 #2, M07 #3, and BMD19 potentials; for SIA cluster simulations, we only consider the M07 #3 and BMD19 potentials.

All energy minimizations were performed with the Polak-Ribiere version of the conjugate gradient algorithm with a relative energy tolerance of 10^{-12} and a force tolerance of 10^{-12} (eV/ Å). An energy-minimization was performed before and after defects are inserted into the simulation box. Due to the significant strain field imposed by SIA defects, these clusters did not require annealing to reach their equilibrium configurations. Periodic boundary conditions were implemented for all simulations. The USER-OMP and USER-INTEL acceleration packages were integrated into LAMMPS to minimize computational time. All atomic positions were observed in the OVITO software [158]. Defect structures were analyzed with the common neighbor analysis (CNA) [163] and dislocation extraction analysis (DXA) [164] methods.

5.1.1 Calculating preferred configurations for SIA and vacancy clusters

The M07 #3 and BMD19 potentials predict that the O and BO configurations, respectively, are the most stable for single SIAs [70, 78]. Despite this, the M07 #3 predicts that SIA clusters with $n \geq 2$ had the largest binding energies when instead formed from planar arrangements of BC, rather than O, interstitials [80]. A similar preference for larger SIA clusters to form planar configurations of parallel BC SIAs on prism planes has been noted with the A95 potential [25, 79]. Thus, only planar configurations are considered for SIA clusters, and we consider BC interstitials in addition to O and BO interstitials.

Fig. 5-1 illustrates potential insertion sites for parallel BC, BO, and O SIAs. Considering the ABABAB stacking sequence of the hcp structure, both BO and O SIAs occupy similar "C" layer sites; the BO configuration lies within the basal plane (z = 0) while the O configuration lies between two atomic layers (z = 0.25). SIA clusters consisting of parallel BC interstitials are formed on first-order prism planes (denoted as "BC-PPI"). For example, a 7-SIA BC-PPI structure would consist of BC interstitials on sites 1, 2, and 3 in the A layer (z = 0), with two additional BC interstitials on equivalent 1' and 2' sites on the two adjacent B-layer basal planes (z = 0.5 and z = -0.5). This algorithm is expanded for clusters with $n \geq 19$ defects by placing BC interstitials in a cylindrical region of radius R to approximate dislocation loop geometries on PPI $\{1\bar{1}00\}$ habit planes. Clusters of BO and O SIAs are formed by the same method except using the BO and O sites as references; these clusters are denoted "BO-PPI" and "O-PPI". The final SIA cluster configuration consists of interstitials contained entirely within a single basal plane, denoted as the "BP configuration". For example, a 3-BP configuration would consist of BO interstitials initially placed on sites 1, 2, and 4 in Fig. 5-1(b) and then energy minimized to adopt an equilibrium configuration. The final structure is relatively insensitive to the initial placement and configuration of SIAs (i.e. BC vs BO). Due to the significant strain field imposed by SIA defects, these clusters did not require annealing to reach their equilibrium configurations.

Both the A95 and M07 potentials predict that spherical cavities are the lowest energy configuration for extended vacancy clusters, rather than the dislocation loop geometries that vacancies are known to adopt in irradiated α-zirconium [13, 34, 37, 81, 165]. In order to compare this behavior with the BMD19 potential, three configurations of vacancy clusters are considered: planar clusters with PPI habit planes (*a*-loops), planar clusters with basal habit planes (*c*-loops), and spherical voids. These are denoted as "PPI", "Basal", and "Volume" respectively. PPI clusters are formed by removing a corrugated double-layer of PPI planes from a cylindrical region of radius R while basal clusters are formed by removing a single basal plane from a cylindrical region of radius R, and thus corresponds to a faulted Burgers vector. At small sizes, the "Volume" clusters form 3-dimensional vacancy shapes (as described by N de Diego et al. in Fig. 8 of Ref. [80]). Larger "Volume" clusters with $n \geq 19$ are formed by removing material within a sphere of radius R to form a faceted spherical cavity. Small vacancy clusters ($n < 19$) were investigated through molecular statics calculations at 0 K only, while larger clusters were annealed at 600 K for 500 ps utilizing a constant atom, pressure, and temperature (NPT) ensemble to achieve equilibrium configurations. Following

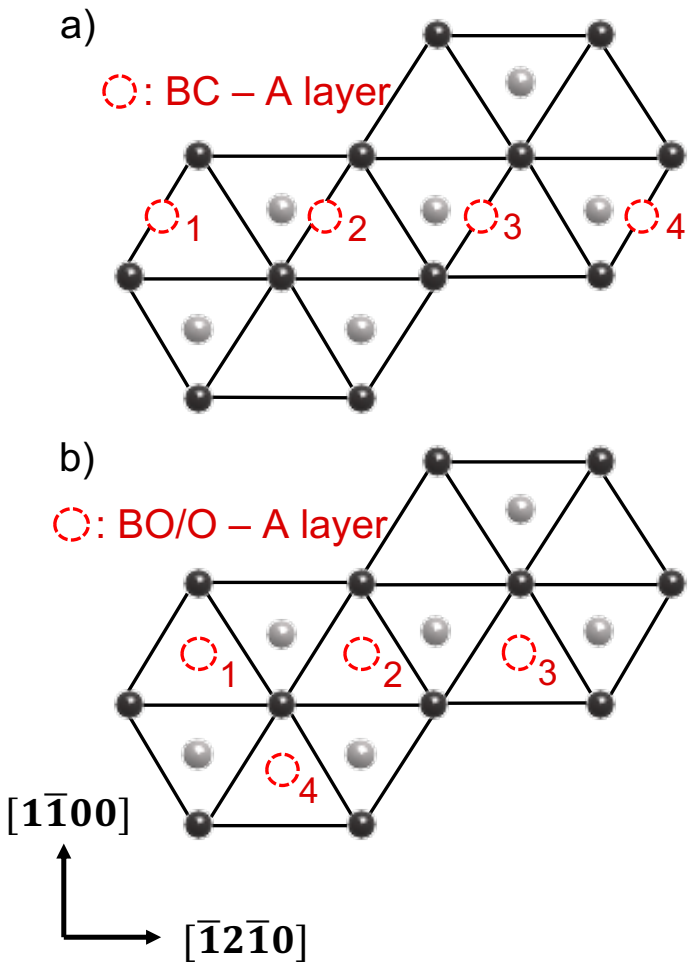

Fig. 5-1. Schematic of (0001) basal plane projections in hcp α-zirconium; dark spheres indicate zirconium atoms in an A-layer while light spheres indicate atom positions on an adjacent B-layer. Potential insertion sites are illustrated with dashed red circles for a) basal crowdion (BC) SIAs within the A-layer and b) basal octahedral (BO) within the A-layer or octahedral (O) SIAs between the A and B layers. [159]

the anneal, the box was again energy-minimized to determine the energetics of the system. It is worth noting that these 0K minimizations do not include temperature-dependent vibrational effects which may otherwise alter the entropy and enthalpy of formation at elevated temperatures. For example, incorporating vibrational effects in *ab initio* calculations has demonstrated a linear temperature dependence of the formation entropy of vacancy defects in aluminum and copper [166] and may affect the relative stability of interstitial insertion sites for impurities such as hydrogen in zirconium [19].

The formation energies of SIA clusters of size n are calculated with Eq. (5-1), where $E(N+n)$ is the total energy of the simulation box containing N zirconium atoms and the n-sized cluster, $E(N)$ is the total energy of the box containing N zirconium atoms, and E_{Zr}^{coh} is the cohesive energy of a single zirconium atom (-6.432, -6.469, and -6.635 eV/atom for the BMD19, M07 #2, and M07 #3 potentials, respectively). The formation energies of vacancy clusters are determined by a similar expression (Eq. (5-2)).

$$E_I^f(n) = E(N+n) - (E(N) + n * E_{Zr}^{coh}) \quad (5\text{-}1)$$

$$E_V^f(n) = (E(N-n) + n * E_{Zr}^{coh}) - E(N) \quad (5\text{-}2)$$

The total binding energy per defect in a cluster may then be calculated by Eq. (5-3), where α = I or V for interstitial or vacancy clusters and $E_\alpha^f(1)$ is the formation energy of a single point defect. For single vacancies, this value is 2.03, 2.31, and 1.76 eV for the BMD19, M07 #2, and M07 #3, respectively. For single interstitials, this value is 2.94 and 2.88 eV for the BO and O interstitials as reference states for the BMD19 and M07 #3 potentials.

$$E_\alpha^b(n)/_n = E_\alpha^f(1) - E_\alpha^f(n)/_n \quad (5\text{-}3)$$

All simulations regarding preferred defect configurations utilized orthogonal simulation boxes. For defects containing $1 \leq n \leq 13$ SIAs or vacancies, the box size was 77.6 Å x 78.4 Å x 41.3 Å (10,752 atoms). Defects with $n \geq 19$ are generated within a cylindrical region of radius R for prismatic or basal loops, while spherical voids are created within a sphere of radius R. In this case, the simulation box size is approximately 12R x 12R x 12R. Thus, defect clusters ranging from sizes of n = 19 (R = 6.5 Å) to n = ~950 (R = 50 Å) are also considered in this investigation with box sizes ranging from approximately 78 Å x 78 Å x 78 Å (274,176 atoms) to 600 Å x 600 Å x 600 Å (15,162,336 atoms).

5.1.2 Calculating defect cluster mobilities

The mobilities of SIA and vacancy clusters containing between n = 1 and n = ~333 defects were investigated with the initial configurations listed in Table 5-1. All clusters are simulated with both the BMD19 and M07 #3 potentials; additionally, small vacancy clusters

Table 5-1. Simulation parameters for the calculation of SIA and vacancy cluster mobilities. The box dimensions and the defect size along the a-axis, d^a, and along the c-axis, d^c, are given in terms of the lattice parameter a = 3.232 Å. [159]

Cluster Size (n)	SIA Cluster Parameters					
	Structure	d^a_{SIA}	d^c_{SIA}	Simulation Box Dimensions	Number of Atoms	Simulation Time (ns)
1	-	3a	2a	16a x 17a x 13a	5,120	50
2	BP Configuration	4a	2a	16a x 17a x 13a	5,120	50
3	BP Configuration	5a	3a	16a x 17a x 13a	5,120	50
4	BP Configuration	5a	3a	16a x 17a x 13a	5,120	50
5	BP Configuration	5a	3a	16a x 17a x 13a	5,120	50
9	BC-PPI	6a	5a	22a x 24a x 13a	9,856	50
19	BC-PPI	12a	9a	28a x 31a x 19a	24,192	25
55	BC-PPI	15a	12a	38a x 38a x 22a	46,816	25
91	BC-PPI	19a	14a	48a x 48a x 26a	86,016	25
151	BC-PPI	22a	16a	56a x 56a x 32a	152,320	25
333	BC-PPI	35a	23a	76a x 76a x 48a	401,280	15

Cluster Size (n)	Vacancy Cluster Parameters					
	Structure	d^a_{VAC}	d^c_{VAC}	Simulation Box Dimensions	Number of Atoms	Simulation Time (ns)
1	-	2a	2a	16a x 17a x 13a	5,120	50
2	Basal	2a	2a	16a x 17a x 13a	5,120	50
3	Volume	2a	2a	16a x 17a x 13a	5,120	50
4	Volume	4a	4a	16a x 17a x 13a	5,120	50
5	Volume	4a	4a	16a x 17a x 13a	5,120	50
9	PPI	5a	5a	16a x 17a x 13a	5,120	50
19	PPI	5a	5a	16a x 17a x 13a	5,120	50
55	PPI	6a	6a	24a x 24a x 16a	13,440	50
85	PPI	9a	9a	26a x 26a x 22a	23,296	50
121	PPI	13a	13a	32a x 32a x 26a	40,960	50
337	PPI	19a	19a	48a x 48a x 38a	129,024	25

(n < 19) are simulated with the M07 #2 potential, which provides a better description of vacancy cluster binding energies [37]. The calculation of defect cluster mobilities requires considerable simulation times and, therefore, smaller simulation box sizes are necessary to minimize the computational load. Osetsky *et al.* quantified the effect of the simulated crystallite size on the jump frequency of a 19-SIA cluster in Fe in Ref. [93] and recommended that the crystallite size should be at least twice the size of the cluster along its Burgers vector direction. The cluster size, d_{SIA}, is defined as the length at which the change in the interatomic spacing approaches half of the maximum value [93]. Using this criteria, the size of each defect cluster along the a-axis and c-axis has been provided in Table 5-1 along with the simulation box dimensions given in terms of the lattice parameter, a (~3.23 Å).

The LAMMPS compute style, "voronoi/atom", was implemented with the "occupation" keyword to track individual SIAs and vacancies during the MD simulations. When first evoked, "compute voronoi/atom occupation" calculates the Voronoi tessellation of all atoms in the simulation box. By comparing the number of atoms in each Voronoi volume throughout the simulation, point defects can be identified and their positions monitored as a function of simulation time. Following the method first described by Guinan *et al.*, the diffusion coefficient, *D*, of a defect cluster at a given temperature can be related to the mean-squared displacement (MSD) of its center-of-mass [167]:

$$\lim_{t\to\infty} \frac{\overline{[R(t)-R(0)]^2}}{2n_d t} = \frac{k_b T}{\gamma} = D \qquad (5\text{-}4)$$

where *R(t)* is the displacement of the defect cluster center-of-mass at time t, n_d is the dimensionality of diffusion, k_b is the Boltzmann constant, T is the simulation temperature, and γ is a friction coefficient. The accuracy of the expression given in Eq. (5-4) relies on a few key assumptions. The diffusing species in question is assumed to migrate in a Brownian nature with random jumps from one equilibrium position to another. This approach has been successfully applied to the diffusion of point defects in α-zirconium [48], although errors may be present in the quantification of diffusion coefficients for larger defect clusters that exhibit correlated 1-D motion [25]. Furthermore, Eq. (5-4) is only relevant at long time scales for which the MSD grows linearly, rather than quadratically, with time:

$$t \gg \tau_{min} = \frac{m}{\gamma} = \frac{mD}{k_b T} \qquad (5\text{-}5)$$

If these assumptions are met, the diffusion coefficient is expected to follow an Arrhenius behavior with temperature (Eq. (5-6)), although the literature contains discussion pertaining to a non-Arrhenius behavior of interstitial clusters in bcc metals [168].

$$D(T) = D_0 e^{-\frac{E_m}{k_b T}} \qquad (5\text{-}6)$$

Defect migration was monitored for times ranging between 15 and 50 ns depending on the cluster size (Table 5-1). Each simulation was then decomposed into N equal-length sub-trajectories with time lengths, $t_{trajectory}$ = 0.5, 1, 2, 3, 4, and 5 ns; the squared-displacement is then time-averaged over all time intervals $[t_1, t_2]$ such that $t_2 - t_1 = t$. A diffusion coefficient is calculated with each averaged MSD($t_{trajectory}$), and then the total ensemble average diffusion coefficient is calculated at each temperature. The maximum allowable simulation temperature is dictated by the melting temperature of the M07 #3 potential (1363 K) and the hcp-to-bcc transition temperature of the M07 #2 potential (1233 K). Therefore, the considered temperature range for SIA and vacancy clusters are 300 K $\leq$ T $\leq$ 1100 K and 600 K $\leq$ T $\leq$ 1100 K, respectively. For each simulation, the box containing the defect cluster was first thermally equilibrated for 1 ns using an NPT ensemble, and then migration data is collected over the total simulation time using an NVT ensemble (constant atom, volume, and temperature). The equations of motion were integrated with the velocity-Verlet algorithm and a fine timestep of 1 fs. Defect positions were output every 500 timesteps (0.5 ps) for analysis.

5.2 Results: Preferred Defect Cluster Configurations

5.2.1 Self-interstitial cluster configurations

The binding energy per defect as calculated by molecular statics simulations at 0 K are presented for the BMD19 and M07 #3 potentials in Fig. 5-2(a) and Fig. 5-2(b), respectively. In agreement with N de Diego *et al.* [80], the M07 #3 potential predicts similar energies for various SIA cluster configurations at small sizes, with the highest binding energies exhibited by interstitials in the basal-plane (BP) configuration. Interestingly, the BMD19 potential also predicts that SIAs clusters with n < 13 will preferentially reside within a single basal plane. In contrast to the behavior of the M07 #3 potential, however, the BP configuration is clearly preferred to other configurations of SIAs for sizes n < 13. The BP configuration is described by N de Diego *et al.* as a "form of small platelets within a basal plane, inside which the ..ABABABAB.. basal stacking sequence is changed to ..ABABCBAB…" [80]. In order to better visualize this concept, the structures of 3-BP and 5-BP configurations are plotted in Fig. 5-3(b) and Fig. 5-3(c) to compare with the perfect hcp α-zirconium structure in Fig. 5-3(a). Compressive and tensile atomic stresses are indicated via a heatmap contour. The 3-BP configuration consists of 6 atoms sharing 3 lattice sites while the 5-BP configuration consists of 15 atoms sharing 10 lattice sites. The compressive stress field surrounding these triangular defects is symmetric within the basal plane containing the cluster and does not extend along the c-axis.

Both potentials predict that larger SIA clusters (n > ~13) approach perfect loop geometries consisting of parallel BC interstitials with a $\{10\bar{1}0\}$ PPI habit plane and a Burgers

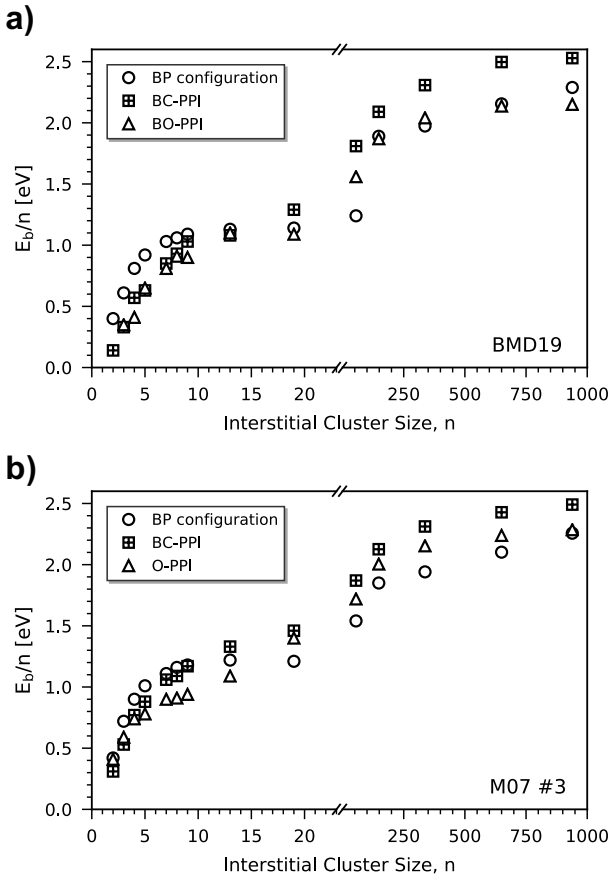

Fig. 5-2. The binding energy per defect as calculated with molecular statics at 0 K for interstitial clusters simulated with the a) BMD19 and b) M07 #3 potentials. [159]

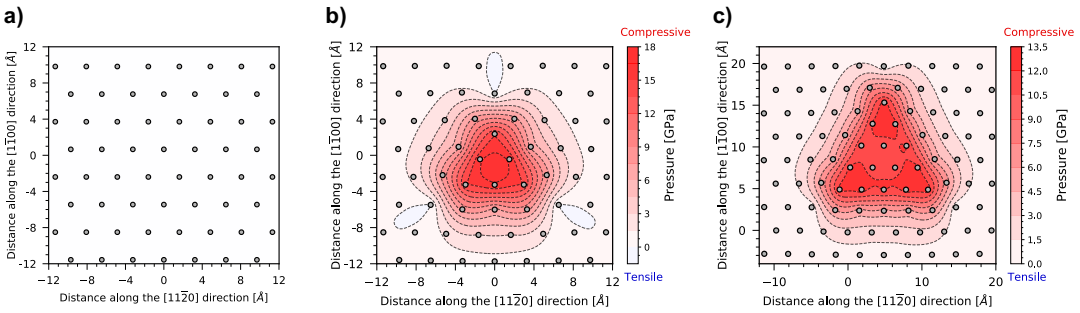

Fig. 5-3. Atomic structures are plotted for a) the perfect hcp α-zirconium lattice, b) the BP configuration with n = 3 defects, and c) the BP configuration with n = 5 defects. Hydrostatic atomic pressure is indicated via a heatmap for which red corresponds to compressive stress and blue corresponds to tensile stress. [159]

vector of $\vec{\boldsymbol{b}} = \frac{1}{3}\langle 11\bar{2}0\rangle$. These structures are identical to those described for interstitial a-loops in neutron-irradiated zirconium [13, 32]. We have used three separate techniques to analyze the structure of a 55-interstitial loop in Fig. 5-4: CNA to determine the local atomic structure (where grey and green atoms indicate unknown and FCC stacking, respectively), DXA to determine the character of the dislocation segments, and by directly plotting a (0001) basal plane projection to indicate the Burgers vector direction and glide cylinder near the center of the loop. It is clear that interstitial a-loops consist of disordered atomic structure at the loop periphery with a restored hcp crystallite at the center of the loop face. Although not plotted here, the interatomic spacing is compressed at the center of the loop face and gradually restores to that of bulk zirconium with increased normal distance from the loop, in agreement with the reported behavior in hcp α-zirconium [79] and bcc-iron [91]. DXA reveals two dislocation segment types: perfect segments and dislocation partials characterized by $\vec{\boldsymbol{b}} = \frac{1}{3}\langle 11\bar{2}0\rangle$ and $\vec{\boldsymbol{b}} = \frac{1}{3}\langle 1\bar{1}00\rangle$, respectively. The latter are formed through the dissociation of the perfect dislocation into two Shockley partials bounding ribbons of basal intrinsic I_2 stacking faults at the top and bottom of the loop [86]:

$$\frac{1}{3}[11\bar{2}0] \rightarrow \frac{1}{3}[10\bar{1}0] + \frac{1}{3}[01\bar{1}0] \qquad (5\text{-}7)$$

This analysis indicates two important characteristics of SIA configurations in α-zirconium: 1) larger SIA clusters do not form as parallel arrangements of the most stable single SIA configuration and 2) small SIA clusters do not share the same configurations as large SIA clusters. These phenomena predicted by both the BMD19 and M07 #3 potentials are in contrast to the older A95 potential, for which single interstitials, small SIA clusters, and large SIA clusters all form based on the <$11\bar{2}0$> crowdion configuration [25, 79]. This behavior is also in contrast to the configurations of SIA clusters in bcc-iron, which are all based on crowdion configurations [92, 93]. The implications of these unique basal-plane defect structures on the transport behavior of SIA defects in hcp α-zirconium will be discussed and contrasted to those of isotropic materials in Section 5.3.1.

5.2.2 Vacancy cluster configurations

The stability of extended vacancy defects is of great interest to understanding the breakaway irradiation growth phenomenon, with particular interest being placed on the stability of faulted vacancy c-loops on basal planes and the existence of potential pre-cursor structures [21, 34, 38, 74, 84]. We first assessed the stability of single-layered versus double-layered vacancy clusters on basal, PPI, and PPII habit planes, as shown in Fig. 5-5. Considering basal clusters, the single-layered configuration results in the high-energy close contact of two adjacent "B" atomic layers in the …ABABAB… hcp stacking. Nevertheless, it is quite clear that vacancies preferentially condense onto a single basal plane rather than form perfect c-loops through the removal of two atomic layers. Considering PPI and PPII clusters,

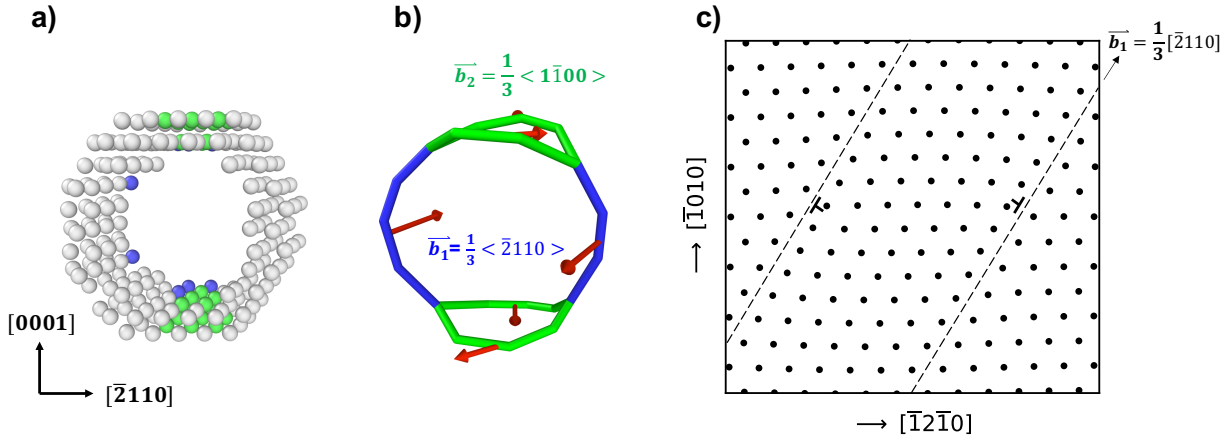

Fig. 5-4. The structure of a perfect loop consisting of 55 parallel BC interstitials with a $\{10\bar{1}0\}$ PPI habit plane and a Burgers vector of $\vec{b} = \frac{1}{3}\langle 11\bar{2}0\rangle$ is visualized using: a) common-neighbor analysis, b) dislocation extraction analysis, and c) directly plotting the atomic structure in a (0001) basal plane projection through the center of the loop. [159]

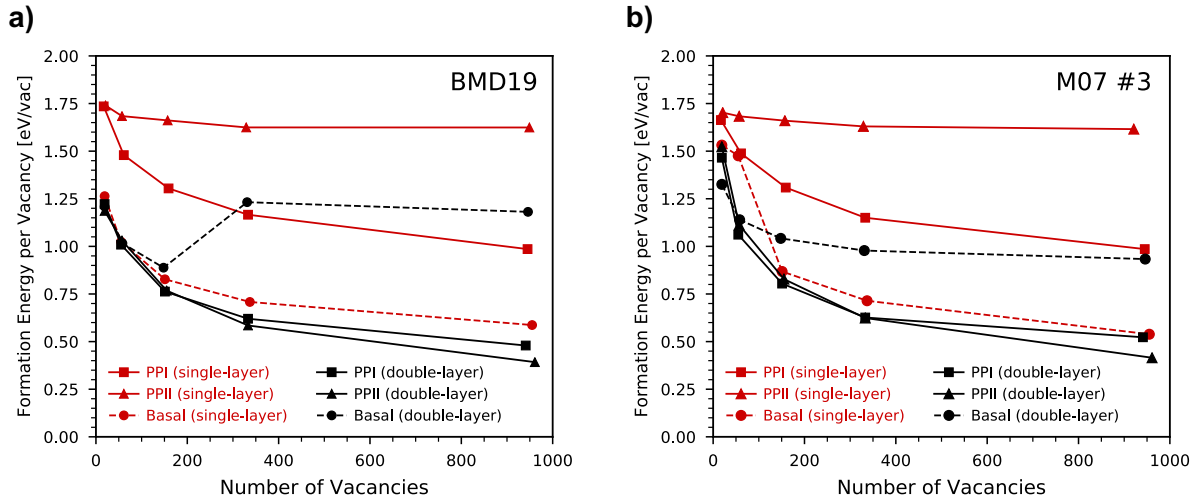

Fig. 5-5. Molecular statics calculations of the formation energies per defects for single-layer (red curves) and double-layer (black curves) vacancy dislocation loops on basal, PPI, and PPII habit planes. Results are compared between a) the BMD19 potential and b) the M07 #3 potential. [159]

both interatomic potentials predict that corrugated double-layered structures are significantly lower in energy compared to single-layered configurations, as expected, due to the higher energy of the single-layer prismatic stacking fault [82]. Interestingly, Fig. 5-5 indicates that prismatic vacancy loops are similar in energy regardless of whether or not they initially form on PPI or PPII planes (consistent with the fact that vacancy a-loops are known to have habit planes ranging from PPI to PPII [17]). Based on this analysis, the only dislocation loop geometries that we consider for the remainder of this investigation are single-layered basal-plane loops and corrugated double-layered PPI loops.

Varvenne and co-workers have demonstrated that the M07 #3 potential does not accurately capture the binding energy of di-vacancies [37]. Therefore, in addition to calculations with the BMD19 and M07 #3 potential, we have also calculated vacancy cluster binding energies with the M07 #2 potential. The results of these calculations are given as the total binding energy per defect for basal, PPI, and volume vacancy configurations in Fig. 5-6. It is clear that the M07 #3 potential underestimates vacancy cluster binding energies for clusters with $n \leq 13$, regardless of their configuration, when compared to the BMD19 and M07 #2 potentials. The binding energy per defect increases sharply for clusters with $n \geq 19$, although the magnitude of binding predicted by the M07 #3 potential remains the lowest of the three potentials. This is most likely attributable to the low single vacancy formation energy (1.76 eV) when compared to those of the BMD19 (2.03 eV) and M07 #2 (2.31 eV) potentials, which shifts the magnitude of the total binding energy (Eq. (5-3)).

Fig. 5-6(b) demonstrates that vacancy clusters in 3-dimensional volumes are clearly predicted as the preferred configuration for every cluster size by the M07 #2 and #3 potentials. On the other hand, the BMD19 potential predicts that basal and PPI configurations are preferable to the formation of spherical cavities (Fig. 5-6(b)), consistent with experimental observations of vacancy type loops in irradiated α-zirconium. In particular, the M07 potentials predict that all small clusters will form 3-dimensional shapes while the BMD19 potential predicts favorable PPI cluster formation for clusters with $6 < n < 19$ vacancies. This is a substantial difference from the M07 potentials, and is especially important considering that displacement cascades generate damage primarily in the form of monovacancies and clusters containing $n \leq 20$ vacancies [9-12]. While cascade data for the BMD19 potential is currently lacking, it is likely from the results of Fig. 5-6(a) that the small clusters produced via cascades would either directly form PPI configurations, or eventually cluster to form these configurations through the absorption of additional vacancies. This would be qualitatively consistent with the prevalence of prismatic vacancy a-loops (rather than basal c-loops) in irradiated zirconium at low-to-moderate fluences. Although, it should be noted that the localized "temperature" within the collision cascade core is expected to be significantly higher than the equilibrium temperature of the system, and this may affect the relative stability of the defects that form. There are two oddities predicted by the BMD19 potential for vacancy clusters with $n \geq 55$: 1) the basal configuration is energetically preferred for an $n = 55$ vacancy cluster and 2) PPI and basal configurations exhibit similar formation energies in the range of $151 < n < 939$ vacancies. These oddities can be rationalized through a description of the vacancy cluster structures and the stacking fault energies predicted by the BMD19 potential.

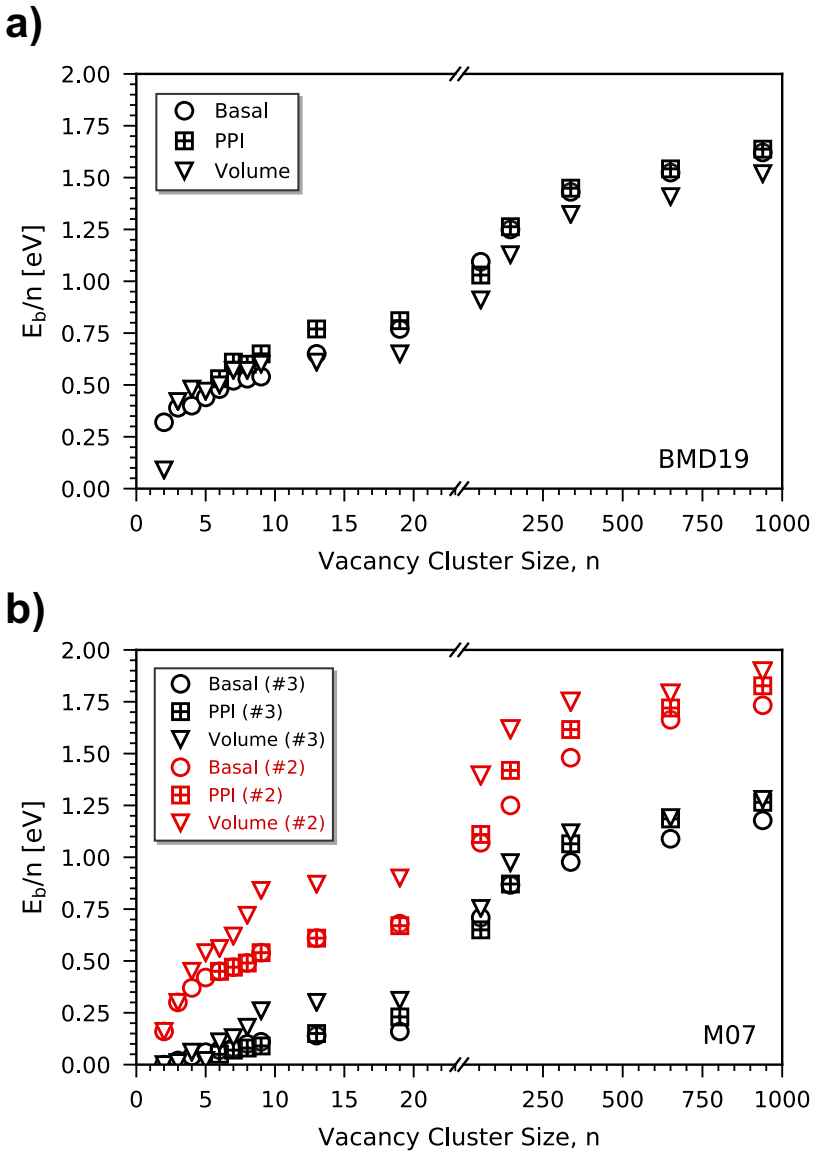

Fig. 5-6. The binding energy per defect for vacancy clusters oriented on PPI and basal planes, as well as in 3-dimensional volumes. Results are compared between a) the BMD19 potential and b) the M07 #2 (red markers) and M07 #3 (black markers). [159]

In order to create a PPI vacancy a-loop, atoms are removed from a corrugated layer of PPI planes such that the …ABCDABCD… stacking along any <$10\bar{1}0$> direction becomes …ABCDCD… (a prismatic $\{10\bar{1}0\}$ fault). These faulted loops initially contain a Burgers vector of $\vec{b} = \frac{1}{2}\langle 1\bar{1}00\rangle$ but unfault at larger sizes by a $\frac{1}{6}\langle 1\bar{2}10\rangle$ shear of the fault plane to produce a perfect vacancy a-loop with Burgers vector $\vec{b} = \frac{1}{2}\langle 2\bar{1}\bar{1}0\rangle$ [37]. Formation energy expressions parameterized on *ab initio* calculations predict that the shearing of faulted to perfect vacancy a-loops should occur at a size of ~1,000 vacancies (R = 5.2 nm). In MD simulations with an annealing cycle of 500 ps at 600 K, faulted vacancy a-loops shear to perfect loops at a critical size between $151 < n < 333$ vacancies when using the M07 #2 potential; conversely, a-loops remain faulted up to a size of 939 vacancies (R = 5 nm) when annealing with the M07 #3 potential. This is qualitatively consistent with the fact that the M07 #2 and #3 potentials overestimate and underestimate the prismatic $\{10\bar{1}0\}$ fault energy, respectively [37]. When annealing with the BDM19 potential, vacancy a-loops unfault at a critical size between $55 < n < 151$ vacancies. While the prismatic stacking fault energy has not yet been calculated with this potential, this observation indicates that the BMD19 potential overestimates the prismatic stacking fault energy. The preferential formation of a 55-vacancy basal configuration, rather than a prismatic a-loop, indicated in Fig. 5-6(a) may be a consequence of the overestimated prismatic stacking fault energy. The structure of a perfect vacancy a-loop with n = 151 vacancies has been analyzed with CNA, DXA, and by directly plotting the atomic positions in Fig. 5-7. For the most part, this structure is qualitatively identical to that of the 55-interstitial loop analyzed in Fig. 5-4 (refer to Section 5.2.1) with one exception: the vacancy loop does not have a pure edge orientation on a single $\{10\bar{1}0\}$ habit plane (Fig. 5-7(c)). Rather, there is some angle of mismatch (tilt of the loop) from this pure-edge orientation; the magnitude of this angle is found to increase with loop size. This is consistent with the observation that vacancy a-loops have been characterized with habit planes ranging between PPI to PPII planes [17].

Of greater interest to the breakaway growth phenomenon, however, is the structure and stability of basal-plane vacancy defects. There has been recent discussion in the literature about the possibility that pyramidal structures consisting of faulted bases on (0001) planes and six side facets close to $\{10\bar{1}1\}$ pyramidal planes may act as pre-cursors to faulted c-loop formation [84]; in fact, these structures have been observed to form during displacement cascades with the A95 potential [85]. We have investigated the formation of basal plane structures by removing a single-layer platelet within a basal plane and subsequently annealing at 600 K for 500 ps; the resultant structures as predicted by the BMD19 potential for 55-V, 151-V, and 333-V clusters are visually illustrated in Fig. 5-8 using CNA. For a 55-V cluster, a faulted pyramidal structure is directly formed during the annealing cycle. A similar structure is predicted by the M07 #3 potential, although the object retains the BB atomic stacking structure in the basal plane rather than a basal extrinsic fault (due to the fact that the M07 #3 potential inaccurately predicts that BB stacking is a local energy minimum rather than a maximum [37]). The BMD19 potential predicts that the 151-V and 333-V structures form a basal-extrinsic (E) faulted loop ($\overrightarrow{\boldsymbol{b_E}} = \frac{1}{2}[0001]$) and a basal-

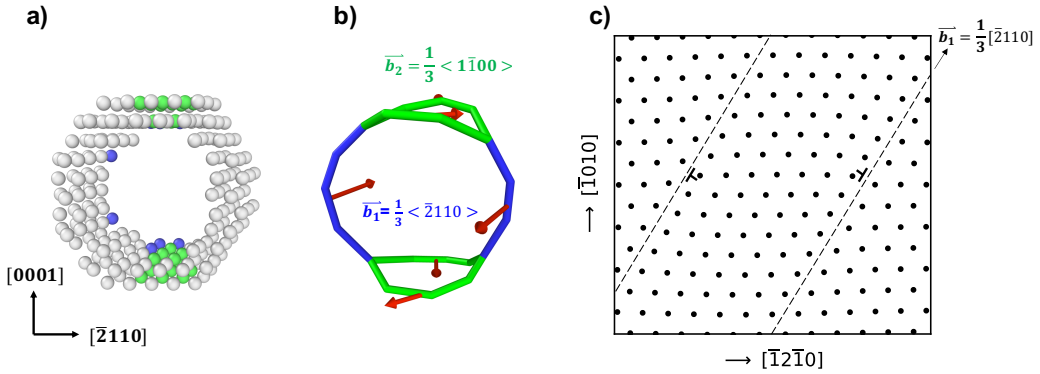

Fig. 5-7. The structure of a perfect loop consisting of 151 vacancies with a $\{10\bar{1}0\}$ PPI habit plane and a Burgers vector of $\vec{b} = \frac{1}{3}\langle 11\bar{2}0\rangle$ is visualized using: a) common-neighbor analysis, b) dislocation extraction analysis, and c) directly plotting the atomic structure in a (0001) basal plane projection through the center of the loop. [159]

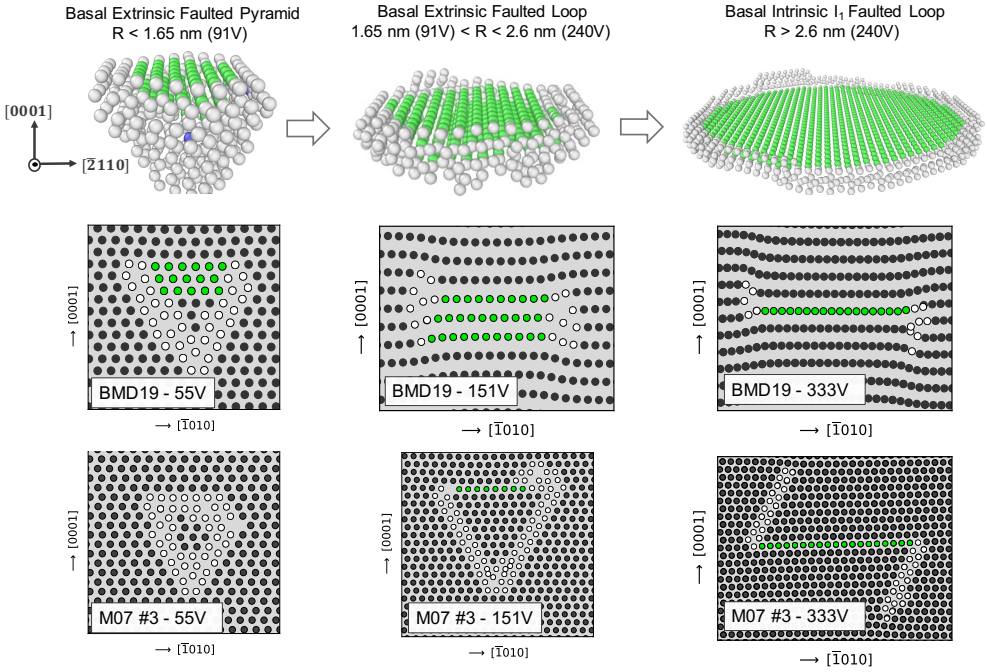

Fig. 5-8. Common neighbor analysis (grey atoms are "unknown structure" and green atoms are FCC structure) was used to visualize basal-plane defects generated with the BMD19 potential. The equivalent atomic positions are plotted as a $\{1\bar{2}10\}$ projection using the BMD19 and M07 potentials. [159]

intrinsic (I_1) faulted loop ($\overrightarrow{\boldsymbol{b}_{\boldsymbol{I_1}}} = 1/6\langle 20\bar{2}3\rangle$), respectively. These two loop structures are surrounded by Frank partials with $b_E^2 \cong \frac{2a^2}{3}$ and $b_{I_1}^2 \cong a^2$ [86]. The basal E and I_1 faults change the second-neighbor stacking sequences of three planes and one plane, respectively; thus, a rough approximation follows that $\gamma_E \approx 3\gamma_{I1}$. Because $b_E^2 < b_{I_1}^2$ and $\gamma_E > \gamma_{I_1}$, the BDM19 predicts the expected behavior: basal E-faulted loops should form at small sizes for which the line energy dominates while basal I_1-faulted loops should form at large sizes for which the stacking fault energy dominates. This suggests that the nucleation and growth of faulted basal c-loops may take the following sequence:

1) Basal-E faulted pyramids may form directly from displacement cascades (see Ref. [85]), or from the growth of small basal platelets that initially contain BB stacking sequences.
2) Basal-E faulted pyramids grow by vacancy capture until they eventually collapse into a basal-E faulted loop.
3) Basal-E faulted loops grow by vacancy capture until they eventually transform into basal-I_1 faulted loops.

Specifically, the BMD19 potential indicates that basal-E faulted loops should become stable at a cluster size of 91-V (R ~ 1.65 nm) and that basal-I_1 faulted loops should become stable at a cluster size of 240-V (R ~ 2.6 nm). Naturally, the magnitude of these critical transformation radii should be considered cautiously due to the considerable underestimation of basal stacking fault energies by the BMD19 potential (2.1 meV/Å^2 for the basal I_2-type fault compared to 13.8 meV/Å^2 as computed with DFT) [78]. Qualitatively, this suggested growth pattern for *c*-loops is quite plausible. It should be noted that recent modeling efforts have predicted that a stability crossover between the faulted pyramidal structure and faulted c-loops would occur at a size of approximately 325 vacancies [84], however the authors considered only the energetics of a basal-I_1 loop in this comparison. MD simulations with the BMD19 potential suggest that the crossover in stability would likely occur at a smaller size through the transformation into a basal-E faulted loop instead.

The formation energies for vacancy a-loops, vacancy c-loops, spherical cavities, and interstitial a-loops are compared in Fig. 5-9 and fit to power-law expressions of the form given in Eq. (5-8). One obvious issue with the BMD19 potential is highlighted in Fig. 5-9(a): faulted vacancy *c*-loops are considered the lowest energy configuration for extended vacancy defects, a consequence of the underestimation of basal stacking fault energies [78]. On the other hand, the M07 #3 potential predicts that spherical cavities offer the lowest energy (Fig. 5-9(b)). Neither of these potentials accurately predict the expected thermodynamic preference for perfect prismatic a-loops [19]. While the BMD19 potential does offer several advantages over the M07 #3 potential for the simulation of irradiation defects, caution must be taken when considering the quantitative magnitude of basal c-loop formation energies.

$$E_f(n) = AN^m \qquad (5\text{-}8)$$

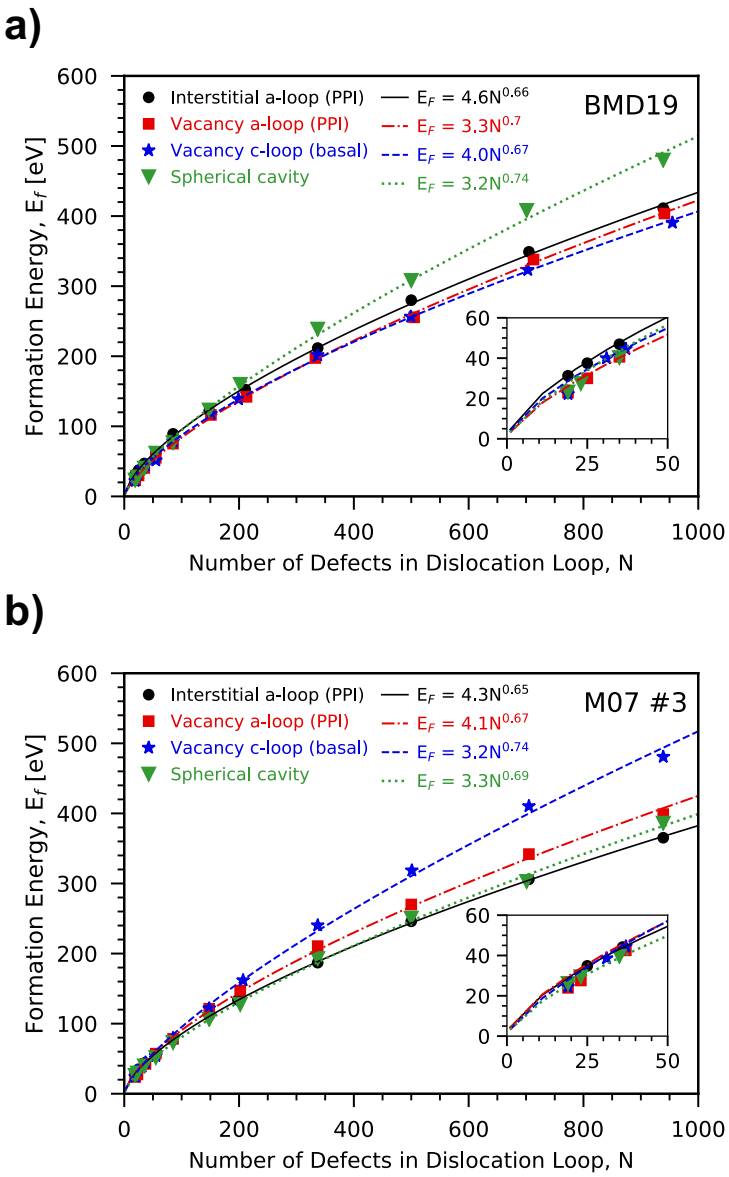

Fig. 5-9. The formation energies for interstitial a-loops, vacancy a-loops, vacancy c-loops, and spherical cavities are compared as predicted by a) the BMD19 potential and b) the M07 #3 potential. Power-law fits are provided for the formation energies as a function of the number of defects. [159]

5.3 Results: Point defect and defect cluster mobilities

5.3.1 Point defect mobility

The mobility characteristics and, particularly, the anisotropy of the diffusion of point defects was a critical component for the early modeling of irradiation growth strains in zirconium [40, 98, 99]. We first consider the anisotropy of diffusion of single SIAs in Fig. 5-10, which contrasts the diffusivities of single SIAs within the basal plane and perpendicular to the basal plane as predicted by the M07 #3 and BMD19 potentials. The effective migration energies for basal-plane and c-axis migration of the O interstitial simulated with the M07 #3 potential are similar (0.061 and 0.067 eV, respectively), although c-axis diffusion is lower in magnitude at all temperatures. When considering the BO interstitial simulated with the BMD19 potential, c-axis diffusion is characterized by a much larger migration energy than basal-plane diffusion (0.298 eV and 0.171 eV, respectively). Both the BO and the O interstitials migrate almost exclusively by indirect interstitial mechanisms. That is to say, these interstitials do not simply jump from one lower energy site to an adjacent low energy site. Rather, they migrate via the correlated motion of a neighboring lattice atom. For example, in-plane migration of a BO interstitial occurs via the concurrent migration of a neighboring lattice atom to an adjacent BO interstitial site at the same time that the original BO interstitial migrates to the now-vacant lattice site. This effectively results in the migration of the BO interstitial from one "C" site to another (basal-plane migration). For the case of the O interstitial, which initially resides between two atomic layers, similar correlated migration occurs with a lattice atom on one of the neighboring atomic planes. The lattice atom is effectively ejected to an adjacent O interstitial site while the original O interstitial replaces the lattice atom.

When considering monovacancy diffusion, both interatomic potentials are in close agreement with the expected migration behavior (Fig. 5-11). Vacancy diffusion is characterized by migration energies that are higher perpendicular to the basal plane than within the basal plane, indicating that migration should be anisotropic. In order to better conceptualize the degree of anisotropy, the ratio of diffusional anisotropies (AR) can be calculated as a function of the diffusion pre-factors, D_0, and migration energies, E^m, for basal-plane and c-axis diffusion. Taking the ratio of the temperature-dependent diffusivity expressions (Eq. (5-6)) results in the following estimate for the anisotropy ratio as a function of temperature:

$$AR = \frac{D_{basal}(T)}{D_c(T)} = \frac{D_0^{basal}}{D_0^c} * e^{\frac{-(E^m_{basal}-E^m_c)}{k_b T}} \qquad (5\text{-}9)$$

The anisotropy ratios calculated for both monovacancies and single SIAs are plotted in Fig. 5-12 for comparison; additionally, the ratios of the individual diffusivities from Fig. 5-10 and Fig. 5-11 are provided as data point markers. The diffusional anisotropy of the O

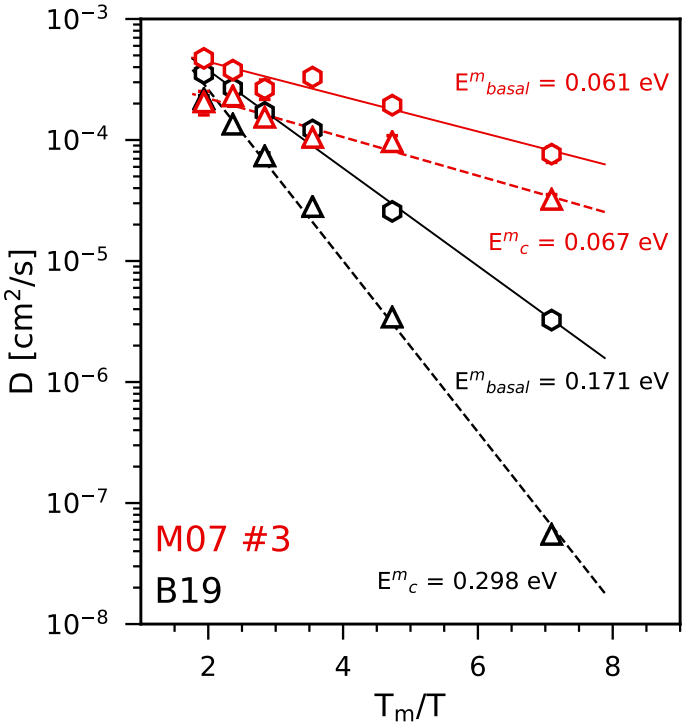

Fig. 5-10. The diffusivities of single SIAs are provided as a function of Tm/T as predicted by the M07 #3 (red curves) and BMD19 (black curves) interatomic potentials. The migration energies for diffusion within the basal plane and perpendicular to the basal plane are provided adjacent to the respective curves. [159]

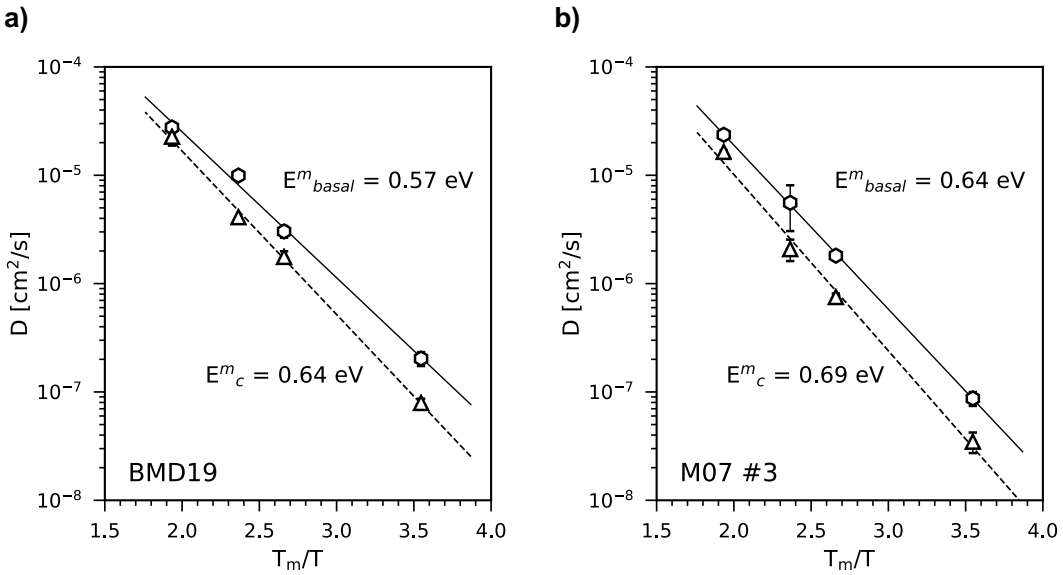

Fig. 5-11. The diffusivities of single vacancies are provided as a function of Tm/T as predicted by a) the BMD19 and b) the M07 #3 interatomic potentials. [159]

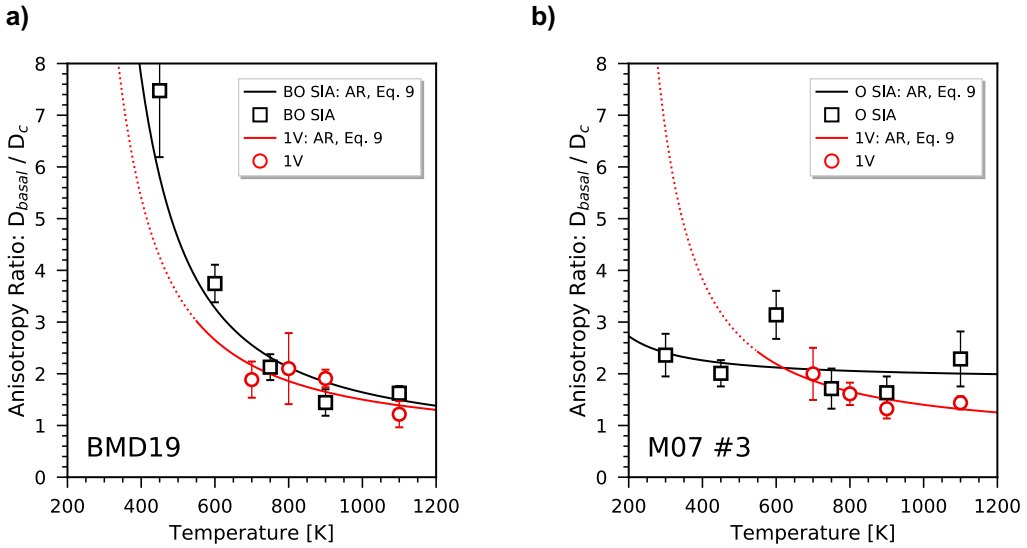

Fig. 5-12. The anisotropy ratio of point defect diffusivities within the basal plane to the diffusivities perpendicular to the basal plane are provided as a function of temperature for the a) BMD19 and b) M07 #3 interatomic potentials. The markers are calculated by directly dividing the averaged diffusivities from the MD simulations. [159]

interstitial (M07 #3 potential, Fig. 5-12(b)) is relatively temperature-independent and generally lower than the vacancy diffusional anisotropy for temperatures less than 900 K. However, single SIAs are expected to occupy BO sites rather than O sites [75]. For the case of BO SIA diffusion with the BMD19 potential (Fig. 5-12(a)), single SIAs and monovacancies exhibit comparable anisotropy ratios at all temperatures. Migration is clearly preferred within the basal plane for both point defects. This is qualitatively different than the concept of a "diffusional anisotropy difference" between point defects that was originally postulated by C. H. Woo [40, 41, 46]. The behavior reported here also contradicts recent joint DFT and Monte Carlo simulations which indicated that vacancies migrate with a higher anisotropy ratio than the BO interstitial [49]. This discrepancy is likely related to the authors' assumption that the BO interstitial migrates traditionally between low-energy interstitial sites. Conversely, our MD simulations indicate that BO SIA migration occurs through correlated movements between the BO interstitial and a neighboring lattice atom; this undoubtedly encourages basal-plane jumps preferentially to out-of-plane jumps.

5.3.2 Self-interstitial cluster mobility

Considering the fact that such a large fraction of generated damage is immediately clustered in displacement cascades, understanding the migration characteristics of these clusters is paramount to effectively modeling defect transport and cluster evolution. As discussed in Section 5.2.1, small SIA clusters are lowest in energy when they adopt configurations that lie entirely within a single basal plane (the BP configuration). We consider first the total diffusivities of these small SIA defects with $n \leq 5$ defects in Fig. 5-13(a) and Fig. 5-13(b) for the BMD19 and M07 #3 potentials, respectively. The diffusivity pre-factors and migration energies were calculated with Eq. (5-6) and are summarized in Table 5-2 for all defect cluster sizes. Three values for D^0 and E_m are given for each cluster: the "total" value (calculated using the dimensionality n_d listed in Table 5-2 for each cluster size), the "basal" value corresponding to migration parallel to the basal plane (n = 2), and the "c" value corresponding to migration along the c-axis (n = 1).

Fig. 5-13(a) shows a very clear trend for small SIA cluster mobility as predicted by the BMD19 potential: as the cluster size increases, their mobilities decrease significantly and are characterized by increasingly larger migration energies. This behavior is in stark contrast with the migration behavior predicted by the older A95 zirconium potential for which migration energies were found to be roughly constant with cluster size [25]. While the A95 potential predicted that all SIA clusters consist of parallel BC interstitials, the BMD19 potential predicts that small SIA clusters will assume increasingly larger basal-plane configurations (Fig. 5-3). The ability of these clusters to perform coordinated jumps diminishes with size such that a 5-interstitial cluster was found to be entirely immobile even at a temperature of 600 K. Clusters with n > 2 were largely incapable of performing out-of-plane jumps at lower temperatures. The effect that this has on the anisotropy ratio of

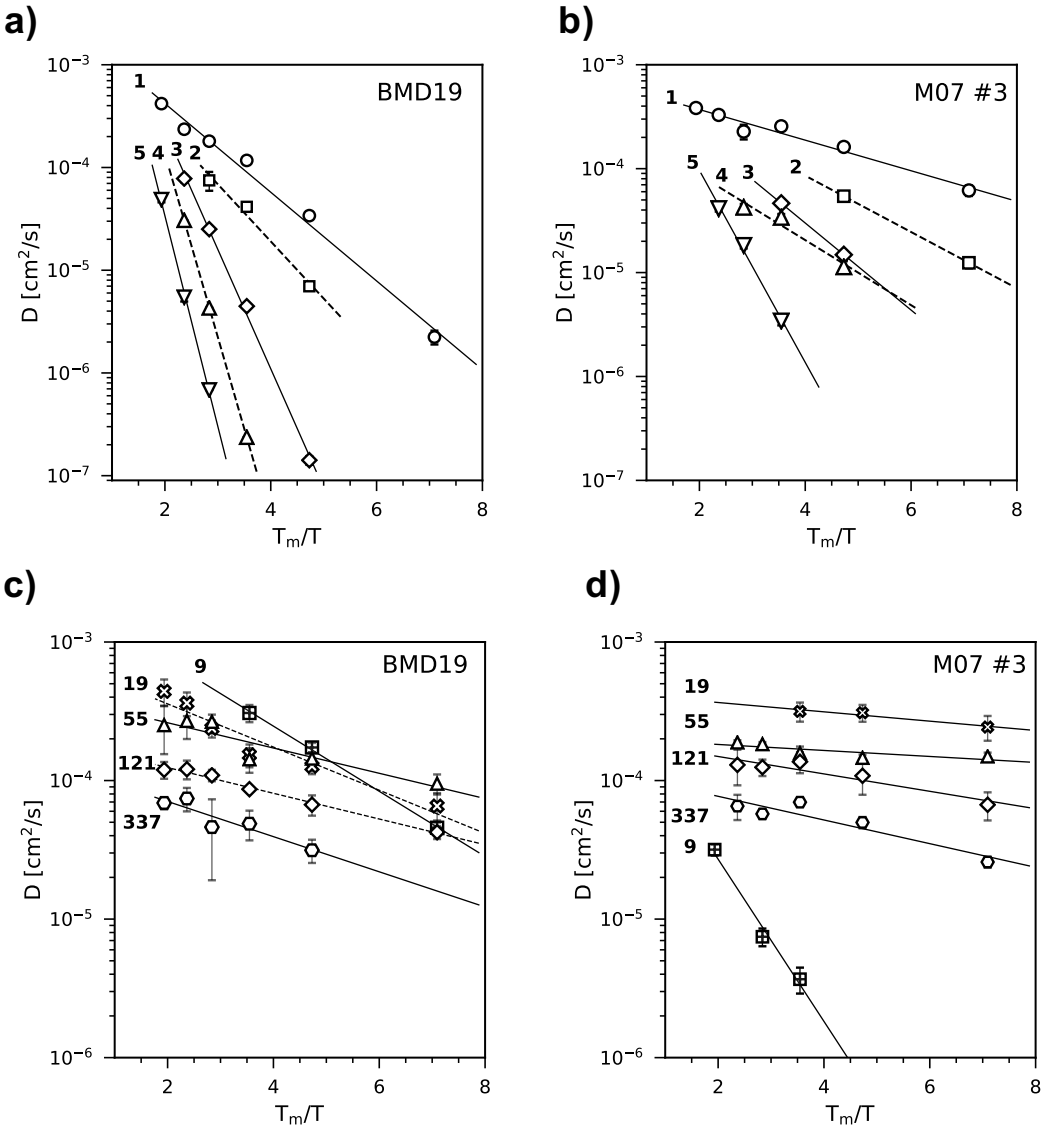

Fig. 5-13. Defect cluster diffusivities are considered as a function of T_m/T for small SIA defects ($1 \leq n \leq 5$) using a) the BMD19 and b) the M07 #3 potentials and large SIA defects ($n \geq 9$) are considered using the c) BMD19 and d) M07 #3 potentials. [159]

Table 5-2. Diffusivity pre-factors and migration energies are given to characterize total diffusion (using n = n_d), basal diffusion (n = 2), and diffusion along the c-axis (n = 1) for SIA clusters of various sizes. [159]

Cluster Size (n_I)	n_d	BMD19 Potential (SIA clusters)					
		D_0 (cm^2 s^{-1})			E_m (eV)		
		D_0^{total}	D_0^{basal}	D_0^c	E_m^{total}	E_m^{basal}	E_m^c
1	3	2.8×10^{-3}	2.4×10^{-3}	6.8×10^{-3}	0.19	0.17	0.30
2	3	2.4×10^{-3}	3.2×10^{-3}	0.026	0.24	0.23	0.54
3	3	0.034	0.049	0.68	0.49	0.49	0.93
4	2 (basal)	0.51	0.51	–	0.75	0.75	–
5	2 (basal)	0.43	0.43	–	0.87	0.87	–
9	1 (a)	2.2×10^{-3}	–	–	0.10	–	–
19	1 (a)	7.3×10^{-4}	–	–	0.066	–	–
55	1 (a)	3.9×10^{-4}	–	–	0.039	–	–
85	1 (a)	2.3×10^{-4}	–	–	0.034	–	–
121	1 (a)	1.9×10^{-4}	–	–	0.039	–	–
337	1 (a)	1.3×10^{-4}	–	–	0.053	–	–

Cluster Size (n_I)	n_d	M07 #3 Potential (SIA clusters)					
		D_0 (cm^2 s^{-1})			E_m (eV)		
		D_0^{total}	D_0^{basal}	D_0^c	E_m^{total}	E_m^{basal}	E_m^c
1	3	7.3×10^{-4}	8.6×10^{-4}	4.6×10^{-4}	0.062	0.061	0.067
2	3	1.0×10^{-3}	1.7×10^{-3}	2.1×10^{-4}	0.11	0.13	0.076
3	3	1.4×10^{-3}	1.8×10^{-3}	8.1×10^{-4}	0.18	0.18	0.16
4	3	3.7×10^{-4}	3.1×10^{-4}	9.8×10^{-3}	0.13	0.11	0.37
5	3	6.7×10^{-3}	7.1×10^{-3}	8.6×10^{-3}	0.39	0.38	0.46
9	3	3.9×10^{-4}	3.5×10^{-4}	1.8×10^{-3}	0.25	0.23	0.40
19	1 (a)	4.3×10^{-4}	–	–	0.018	–	–
55	1 (a)	2.1×10^{-4}	–	–	0.012	–	–
85	1 (a)	3.2×10^{-4}	–	–	0.026	–	–
121	1 (a)	1.9×10^{-4}	–	–	0.027	–	–
337	1 (a)	1.1×10^{-4}	–	–	0.036	–	–

diffusion is evident in Fig. 5-14(a). While a single BO interstitial was found to be almost equivalently anisotropic to a single vacancy, it is evident that SIA clusters are considerably more anisotropic and exhibit predominantly 2-D transport parallel to the basal plane.

Generally, the M07 #3 potential predicts that SIA clusters are more mobile and less anisotropic than predicted by the BMD19 potential (Fig. 5-13(b) and Fig. 5-14(b)). In fact, di-interstitials and tri-interstitials were found to be biased towards diffusion along the c-axis at low temperatures. This can be attributed to the greater stability of metastable configurations with the M07 #3 potential, as was indicated by the similar binding energies of various interstitial configurations presented in Fig. 5-2. SIA clusters consistently transform between the stable BP configuration and temporary metastable configurations, which results in migration patterns that vary between 2-D and 3-D motion. With increasing cluster size, the frequency of transformation to metastable configurations decreases, and the mobility of n = 4 and n = 5 clusters is therefore lowered with a corresponding affinity for basal-plane anisotropic migration. On the other hand, the BMD19 potential predicts enhanced stability of the BP configuration, and the diffusion of SIA clusters is therefore more sluggish and significantly anisotropic.

Larger SIA clusters prefer to form perfect dislocation loop geometries consisting of parallel BC interstitials. The migration characteristics shown in Fig. 5-13(c) and Fig. 5-13(d) are consistent between the two potentials: migration energies are roughly constant with increasing cluster size while the magnitude of the diffusivity (quantified by the diffusivity pre-factor) decreases with increasing size. The clusters migrate rapidly in 1-D along the direction of their Burgers vector, $\vec{b} = 1/3\,\langle 11\bar{2}0\rangle$; rotations of cluster orientations to equivalent directions were not observed to occur in the MD simulations at any temperature. This migration behavior is comparable to what was predicted by the previous A95 potential [25], in addition to potentials used to study cubic metals such as Fe and Cu [91-93, 108, 169, 170]. It should be noted that because all possible directions of 1-D glide are contained within the basal plane, the total mass transport of these clusters will be 2-dimensional.

Efforts to describe the 1-D motion of large SIA clusters and develop phenomenological expressions for the diffusivity pre-factors and migration energies have varied in the literature. Some approaches, such as those by N. de Diego *et al.* [25] and Osetsky *et al.* [91-93], describe the motion of SIA clusters as essentially independent jumps of individual crowdions. This is an attractive framework for materials such as bcc iron that allows a direct correlation between the movement of SIA clusters with the migration characteristics of the single crowdion interstitial. On the other hand, approaches by Soneda and Diaz de la Rubia [171] and Marian *et al.* [169, 170] describe the motion of large clusters through a kink-pair nucleation and propagation model. Under this approach, the migration energy as a function of cluster size approaches an asymptotic value corresponding to the kink-pair nucleation energy (which is roughly constant for large dislocation loops) while the exponential pre-factor decreases monotonically with size as a consequence of the increasing cluster perimeter length, L [169]. For the case of anisotropic hcp zirconium, it is clear that neither of these traditional approaches will perfectly describe SIA cluster mobility as a continuous function of increasing size. Because small clusters prefer the BP configuration,

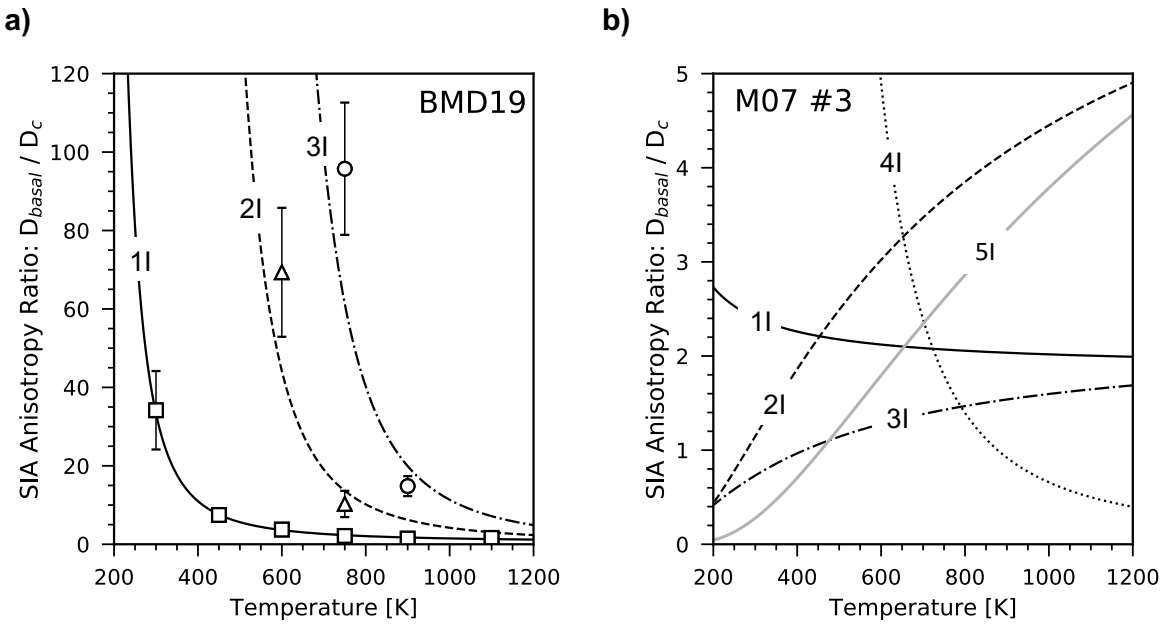

Fig. 5-14. Anisotropy ratios as calculated with Eq. (5-9) are plotted versus temperature for small SIA defects (n < 6) using the a) BMD19 and b) M07 #3 potentials. [159]

the migration energy and pre-factor values increase rapidly with cluster size. For example, an n = 5 SIA cluster is characterized by E_m = 0.87 eV and D_0 = 0.43 cm^2 s^{-1} compared to the values of E_m = 0.19 eV and D_0 = 2.8x10^{-3} cm^2 s^{-1} for the single BO interstitial (Table 5-2). Larger clusters, on the other hand, follow the traditional behavior with roughly constant values of E_m = ~0.05 eV and with diffusivities pre-factors that decrease monotonically with size.

As will be described in Section 5.3.3, large vacancy a-loops migrate in nearly an identical fashion to their equivalent interstitial a-loop counterparts. While the motion of large SIA clusters could conceivably be described as correlated jumps of crowdions, this would not be applicable for the motion of vacancy loops. For this reason, we prefer to quantitatively describe large SIA cluster motion through the kink-pair propagation model to provide consistency between the descriptions of vacancy and interstitial loop migration. For this analysis, we only consider clusters with n > 9 that begin to form dislocation loop character. The migration energies and diffusivity pre-factors can then be described by the following power laws as functions of cluster size:

$$E_m^{SIA}(n) = \begin{cases} 0.046 + \dfrac{0.61}{n^{1.1}}, & \text{BMD19, n} > 9 \\ 0.024 + \dfrac{0.22}{n^{1.8}}, & \text{M07, n} > 9 \end{cases} \quad (5\text{-}10)$$

$$D_0^{SIA}(n) = \begin{cases} 6.6x10^{-3}n^{-0.73}, & \text{BMD19, n} > 9 \\ 1.9x10^{-3}n^{-0.49}, & \text{M07, n} > 9 \end{cases} \quad (5\text{-}11)$$

5.3.3 Vacancy cluster mobility

We first analyze the mobility of small vacancy clusters by plotting their total diffusivity as a function of inverse temperature in Fig. 5-15(a). As was done for SIA clusters, the migration parameters are provided in Table 3 corresponding to total diffusion (using the specified n_d), basal-plane diffusion (n = 2), and diffusion along the c-axis (n = 1). Data could not be provided for small vacancy clusters using either the M07 #3 or M07 #2 interatomic potentials. When implementing the M07 #3 potential, vacancy clusters rapidly dissociate into single vacancies due to the uncharacteristically low predicted vacancy cluster binding energies. While the M07 #2 potential provides a better prediction of the stability of small vacancy clusters, these clusters were predicted to be immobile at all simulation temperatures. Conversely, the BMD19 potential predicted that small vacancies were not only stable at temperatures below ~1000 K, but also exhibited appreciable mobility. Migration characteristics of small vacancy clusters varied greatly depending on their specific configuration. For example, the di-vacancy (stable until ~800 K) diffuses more rapidly than a single vacancy; the tri-vacancy, on the other hand, is considerably more sluggish and is characterized by a large migration energy. The single vacancy, di-vacancy, and tri-vacancy

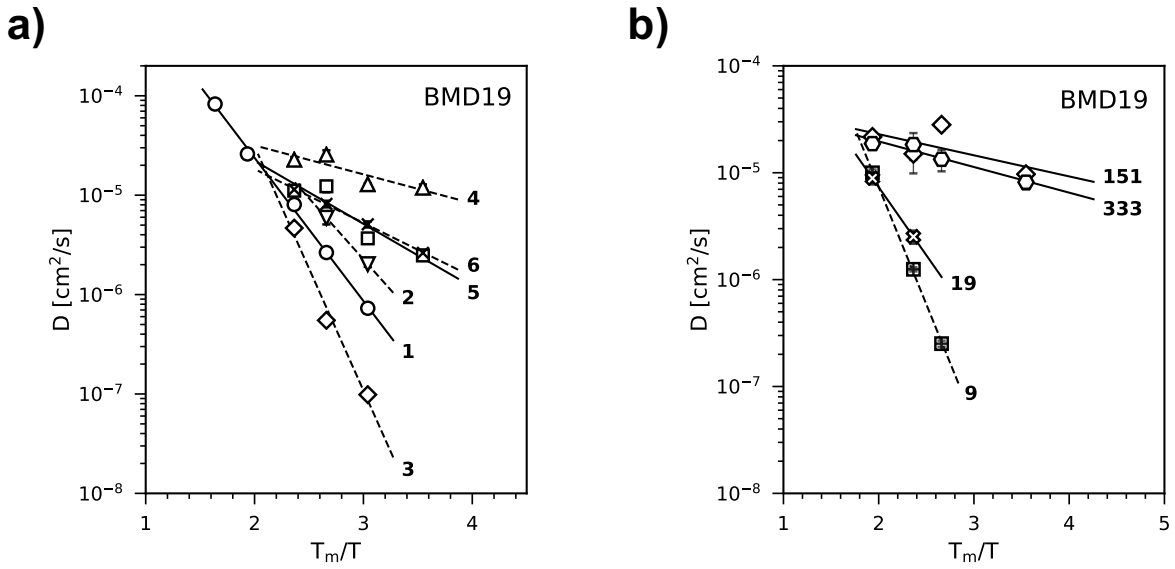

Fig. 5-15. Total diffusivities are plotted as a function of T_m/T for a) small vacancy clusters and b) large vacancy clusters. The data in these plots were collected with the BMD19 potential. [159]

all migrate in three dimensions. A 4-vacancy cluster, however, consists of two vacancies on each of two neighboring basal planes and exhibits almost exclusive two-dimensional migration within the basal plane. The atomic configuration on each of these two basal planes can be thought of as one atom sharing three lattice sites, and in-plane migration can occur rapidly through the correlated replacement of that atom with a neighboring lattice atom. On the other hand, a 5-vacancy cluster shares a similar structure, but with a fifth vacancy on a third basal plane. This configuration migrates rapidly in 1-D along the c-axis. These two cluster sizes are considered special cases, since vacancy clusters with n > 5 again migrate in three-dimensions.

The anisotropy ratios of diffusion are plotted in Fig. 5-16 for clusters with n < 7. Note that the n = 4 vacancy cluster data cannot be shown due to the large magnitude of its anisotropy ratio. In general, small vacancy clusters are characterized by low anisotropy ratios, indicating a preference for diffusion along the c-axis at low temperatures, and only moderately anisotropic migration behavior at higher temperatures. These clusters are also highly mobile and are capable of rapidly migrating to various sinks. It is notable that the diffusion of small vacancy clusters is considerably less anisotropic than the monovacancy, and therefore the clustering of these defects may play a critical role in microstructural evolution, particularly in the growth of basal-plane c-loops.

The total diffusivity as a function of inverse temperature for larger vacancy clusters ($n \geq 9$) is plotted for the BMD19 potential in Fig. 5-15(b). It is clear that there are three size regimes when considering vacancy cluster migration characteristics: small vacancy clusters ($n < 9$), medium vacancy clusters ($9 < n < \sim 151$), and large vacancy clusters ($n \geq \sim 151$). While most small clusters were found to be quite mobile, medium-sized clusters are sluggish in comparison. We attempted to collect migration data for n = 36, n = 55, and n = 91 vacancy clusters, but the diffusion of these clusters were too sluggish to collect adequate data in 50 ns. It was initially surprising, then, to find that n = 151 and n = 333 vacancy clusters were highly mobile even at the lowest attempted simulation temperature of T = 700 K. In fact, the migration patterns and calculated parameters are nearly identical to SIA clusters of the same size. Large SIA and vacancy clusters both form similar perfect dislocation loop geometries with identical Burgers vectors of $\vec{b} = \frac{1}{3}\langle 11\bar{2}0\rangle$. Vacancy a-loops containing n = 151 and n = 333 vacancies are characterized by migration energies of E_m = 0.071 eV and E_m = 0.053 eV, respectively (Table 5-3); in comparison, interstitial a-loops with n = 121 and n = 333 were characterized by migrations energies of E_m = 0.039 eV and E_m = 0.053 eV, respectively (Table 5-2). The diffusivity pre-factors were similarly comparable (only a factor of two lower for vacancy loops). This would therefore imply that interstitial and vacancy a-loops migrate via the same mechanism. Such a conclusion would give credibility to the concept that dislocation loops migrate primarily via a kink-pair propagation mechanism [169-172]. The migration energy, then, would be correlated to the kink-pair nucleation energy which would conceivably be comparable between interstitial and vacancy a-loops. In this model, the diffusivity pre-factor is correlated to the dislocation loop perimeter length (the distance necessary for a kink-pair to propagate), and the lower pre-factor magnitudes for vacancy a-loops could be partially correlated to their greater ellipticity factors. It is interesting that

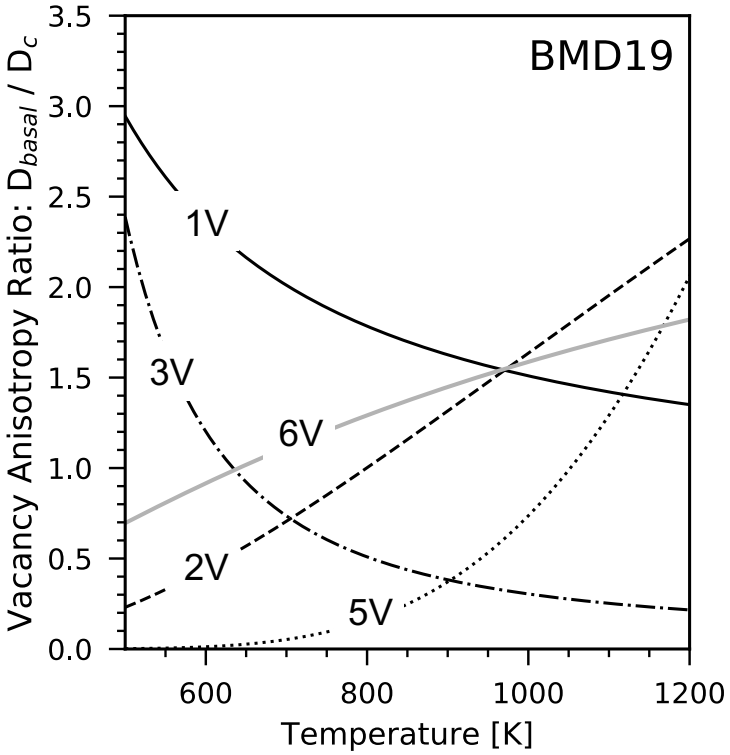

Fig. 5-16. Anisotropy ratios as calculated with Eq. (5-9) are plotted versus temperature for small vacancy defects as predicted by the BMD19 potential. [159]

Table 5-3. Diffusivity pre-factors and migration energies are given to characterize total diffusion (using n = n_d), basal diffusion (n = 2), and diffusion along the c-axis (n = 1) for vacancy clusters of various sizes. [159]

Cluster Size (n_v)	BMD19 Potential (vacancy clusters)						
	n_d	D_0 (cm^2 s^{-1})			E_m (eV)		
		D_0^{total}	D_0^{basal}	D_0^c	E_m^{total}	E_m^{basal}	E_m^c
1	3	0.018	0.016	0.022	0.61	0.59	0.67
2	3	0.011	0.027	2.3×10^{-3}	0.52	0.58	0.41
3	3	2.5	0.49	12.7	1.0	0.94	1.12
4	3	1.2×10^{-3}	2.5×10^{-4}	4.5×10^{-3}	0.12	0.16	0.58
5	3	4.1×10^{-4}	0.20	5.7×10^{-3}	0.27	0.81	0.29
6	3	2.2×10^{-4}	3.2×10^{-4}	9.1×10^{-5}	0.23	0.25	0.18
9	3	0.18	0.15	0.42	0.93	0.90	1.0
19	3	2.6×10^{-3}	4.1×10^{-3}	5.8×10^{-3}	0.54	0.56	0.44
36 - 91	–	–	–	–	–	–	–
151	1 (a)	4.23×10^{-5}	–	–	0.071	–	–
333	1 (a)	4.15×10^{-5}	–	–	0.053	–	–

despite the high mobility of both interstitial and vacancy a-loops, these defects remain on the order of ~5nm with high number densities rather than approaching network dislocation densities [20]. It is possible that solute or impurity interaction with these dislocation loops could impede their mobilities and prevent rapid clustering.

5.4 Discussion: Implications for microstructural evolution in irradiated α-zirconium

There are several key differences between BMD19 and M07 #3 potentials that are expected to affect predictions of defect cluster transport in irradiated α-zirconium. Single SIAs and small SIA clusters exhibit an enhanced affinity for basal-plane configurations with the BMD19 potential. As such, the predicted diffusion of these defects with the BMD19 potential is considerably more anisotropic than the M07 #3 potential indicates. As a unique consequence of the hcp crystal structure, the migration behavior of all SIA clusters will result in almost exclusively 2-D mass transport in the zirconium bulk. Thus, the capture of SIA defects will be biased towards sinks oriented perpendicular to the *a*-axes (such as prismatic *a*-loops) rather than sinks along the *c*-axis (such as basal *c*-loops).

The M07 #3 potential predicts that small vacancy clusters are thermally unstable while the #2 potential indicates that they are stably bound but entirely immobile at all simulation temperatures. In contrast, the BMD19 potential predicts that small vacancy clusters are both stable and surprisingly mobile at temperatures below ~800 – 1000 K. The diffusional anisotropy ratios of these small vacancy clusters are low, indicating either quasi-isotropic migration, or preferential migration along the c-axis depending on the cluster configuration and temperature. These small vacancy clusters would thus either migrate to all sinks unbiasedly, or preferentially migrate towards sinks oriented perpendicular to the *c*-axis (such as basal c-loops). This observation could have profound implications for microstructural evolution and the role of defect cluster mobilities. While the anisotropy of monovacancies does not support the concept of a "diffusional anisotropy difference" between point defects, the difference between the anisotropies of SIA and vacancy *cluster* diffusion could instead support such a conclusion. If the predictions of the BMD19 potential are correct, then it is necessary to include defect cluster mobilities in any mesoscale approach to accurately model microstructural evolution under irradiation.

Another known issue with the M07 #3 potential is the fact that the high-energy BB stacking structure of basal vacancy platelets is considered a local energy minimum rather than a local energy maximum, resulting in the abnormal stability of the BB stacking fault [37]. This is evident when attempting to anneal basal platelets with the M07 #3 potential, as the BB stacking remains stable despite a 500 ps anneal at 600 K. Higher temperature annealing or the direct application of a shearing displacement are required in order to introduce a I_1 basal fault. Conversely, the BMD19 potential readily forms faulted basal structures during a 600 K anneal. It must be stressed again, however, that the formation energies of faulted basal loops must not be considered quantitatively accurate due to the uncharacteristically low

basal stacking fault energy of the BMD19 potential [78]. This has a few consequences: 1) the BMD19 potential should not be used to parameterize expressions for the formation energy of faulted c-loop defects and 2) caution must be taken when discussing the relative stability of prismatic and faulted basal vacancy defects when using this potential. Future interatomic potentials should maintain the stability of vacancy loop configurations relative to void formation in α-zirconium, but must also accurately predict basal stacking fault energies in order to capture the relative formation energy of perfect a-loops with respect to faulted c-loops.

The recent analysis by Christiaen *et al.* [84] indicated that *c*-loops may not form from the continuous aggregation of vacancies, but rather from the transformation of pyramidal pre-cursor structures above some critical size. Regardless of whether or not a *c*-loop forms directly through the absorption of vacancies or through the transformation of this pyramidal pre-cursor structure, the obvious question remains: why do *c*-loops become apparent at high fluence? MD simulations of displacement cascade events have clearly demonstrated that the most common forms of vacancy defects will be monovacancies and small vacancy clusters with $n < 20$ [9-12]. While the direct formation of larger clusters, such as pyramidal *c*-loop pre-cursors, is certainly possible with more energetic PKAs, their direct nucleation would still be considered a comparatively rare occurrence. The BMD19 potential demonstrates an energetic preference for prismatic PPI configurations for small vacancy clusters (Fig. 5-6). It is conceivable, then, that the growth of these small PPI vacancy clusters through the absorption of additional vacancies will eventually result in the formation of perfect prismatic a-loops, consistent with the abundance of these defects in low-fluence irradiated microstructure. If, alternatively, small basal-plane vacancy clusters directly form within a displacement cascade, they will initially consist of a high-energy BB stacking structure. This BB stacking might then act as a nucleation barrier for the formation of larger basal structures, such as pyramidal *c*-loop pre-cursors. It is possible that the high-fluence incubation period for the nucleation of *c*-loops is related to the fluence-dependent availability of solute such as Fe or Cr in the matrix to stabilize these high-energy defects, and allow their growth into pyramidal or *c*-loop structures [55].

Another explanation for the delay in *c*-loop growth may be related to the structure of the pyramidal pre-cursor itself. We have demonstrated that SIA clusters migrate preferentially within the basal plane while vacancy clusters migrate preferentially along the *c*-axis, or quasi-isotropically depending on the cluster size and temperature (Fig. 5-14 and Fig. 5-16). The implication of this observation is that the faulted pyramidal pre-cursor, which has six pyramidal-plane faces, would act as a biased sink for SIA cluster absorption rather than vacancy cluster absorption. This is in contrast to faulted basal *c*-loops, which are expected to act as biased sinks for vacancy cluster absorption. In this framework, the pyramidal pre-cursor structure may actually impede the nucleation of *c*-loops. Interestingly, the analysis of Christensen *et al.* demonstrated that hydrogen may in fact restrict the collapse of a basal platelet, and correspondingly, restrict the formation of basal stacking fault pyramids [66]. The un-collapsed basal platelet would then have a reduced cross-section for SIA capture, and one role of hydrogen may be to encourage the growth of planar *c*-loops, which have a greater bias for vacancy cluster absorption.

In systems without hydrogen, the high-fluence incubation period for *c*-loop nucleation may be related to the fluence-dependent ordering of vacancy a-loops on parallel basal sheets. Harte *et al.* have recently highlighted the fact that *c*-loop positions may be anti-correlated with *a*-loops within these ordered basal sheets [20]. While the authors hypothesized that a-loops may directly transform into vacancy c-loops, an alternate explanation could be related to SIA self-shielding. Because vacancy a-loops align along the basal-trace, any vacancy defect within this ordered basal sheet would have a reduced incoming flux of SIAs. Thus, it is possible that pyramidal pre-cursor structures, which normally would act as biased sinks for SIA defects, would then be able to grow and eventually transform into basal c-loops. The continued growth of c-loops may then result in the absorption of nearby vacancy a-loops as the c-loops grows to the order of 100 nm or larger. Because the formation energy per vacancy decreases with loop size, a single vacancy c-loop would have less energy than several prismatic a-loops. For example, consider the formation energy expressions of vacancy a-loops and c-loops given in Fig. 5-9(b) for the M07 #3 potential (which more accurately depicts basal stacking fault energies). A 5,000-vacancy c-loop would have a formation energy of ~1747 eV while five vacancy a-loops with 1,000 vacancies would have a collective formation energy of ~2,097 eV. Thermodynamically, the system would reduce its energy by growing a single large c-loop rather than several small a-loops. Due to the faulted nature of c-loops, however, the energy of the stacking fault component increases as a function of R^2 and the energetic benefit of growing a larger c-loop would begin to diminish unless solute or impurities act to reduce their stacking fault energy [55]. Future research is required to determine the likelihood of these possible scenarios associated with the formation of vacancy c-loops.

5.5 Summary and Conclusions

Predictions of the preferred defect cluster configuration and diffusion behavior were assessed and compared between the M07 and BMD19 potentials. Both potentials indicated that small SIA clusters preferentially form configurations within a single basal plane. Conversely, large SIA clusters form perfect dislocation loops with PPI habit planes and a Burgers vector of $\vec{\boldsymbol{b}} = \frac{1}{3}\langle 11\bar{2}0\rangle$. For the case of vacancy clusters, both the M07 #2 and #3 potentials predict that 3-dimensional cavities, rather than planar structures, are the lowest energy configuration despite the known lack of void formation in irradiated zirconium. In contrast, the BMD19 potential predicts that PPI planar configurations are lowest in energy, consistent with the abundance of prismatic a-loops in low-fluence irradiated zirconium. Small basal defects are lowest in energy when they form a basal-extrinsic faulted pyramid configuration; above a size of ~1.65 nm (n > 91 vacancies), faulted basal c-loops become the most stable configuration. It must be stressed, however, that the BMD19 potential considerably underpredicts basal stacking fault energies, and therefore artificially predicts lower formation energies for faulted basal c-loops. Caution should be taken when drawing quantitative conclusions concerning the stability of vacancy clusters, particularly relative to prismatic vacancy a-loops, when using this potential.

The diffusion of single vacancies and interstitials are equivalently anisotropic, with a clear preference for basal-plane diffusion, when implementing the BMD19 potential. Additionally, small SIA clusters are almost entirely restricted to diffusion within a single basal plane (2-D migration); migration energies increase monotonically with increasing cluster size between $2 < n < 9$. The M07 #3 potential conversely predicts that small SIA clusters can temporarily assume metastable configurations to migrate rapidly in three dimensions. Thus, the anisotropy of diffusion of small SIA clusters is much greater for the BMD19 potential than it is for the M07 #3 potential. Both potentials predict that SIA clusters with $n \geq 19$ migrate rapidly in 1-D with a nearly constant migration energy regardless of cluster size. These values are $\sim$0.046 eV and $\sim$0.027 eV for the BMD19 and M07 #3 potentials, respectively, and may be related to the kink-pair nucleation energy in α-zirconium.

The M07 #3 potential predicts complete thermal instability of small vacancy clusters while the M07 #2 potential indicates that these clusters are stable but remain entirely immobile for all temperatures up to the maximum value of T = 1100 K considered here. In contrast to this behavior, the BMD19 potential predicts that small vacancy clusters are thermally stable and migrate with appreciable mobility along the c-axis, or quasi-isotropically depending on the cluster configuration. This has significant implications for the role of small vacancy clusters in the stabilization of faulted basal c-loop growth, and highlights the importance in the difference of diffusional anisotropies of defect clusters rather than point defects. Incorporating defect cluster mobilities is likely a critical component for mesoscale codes to accurately predict microstructural evolution in irradiated zirconium. Additionally, the BMD19 potential predicts that large vacancy a-loops with $n \geq 151$ migrate rapidly in 1-D in an analogous manner to interstitial a-loops. The migration energies are nearly equivalent, and this supports the theory that dislocation loops migrate via a kink-pair propagation mechanism. Ultimately, the BMD19 potential provides invaluable knowledge into defect cluster configurations and mobilities that will greatly improve the predictive capabilities of mesoscale codes.

5.6 Implementation of results in the CD model

The work in this chapter has provided an essential database for CD modeling of α-Zr: cluster binding energies and tabulated diffusivity data for all mobile defects. The binding energies of a monomer i to some cluster n defines the magnitude of the temperature-dependent dissociation rates (Eq. (2-30), Section 2.1.4); lower binding energies correspond to greater dissociation rates. These binding energies are shown in Fig. 5-2 for SIA clusters and in Fig. 5-6 for vacancy clusters. However, for the implementation of a phenomenological binding energy expression, it is more convenient to consider defect formation energies, which are often expressed in a power law of the form given in Eq. (5-8). Once these are known, the binding energies for single SIAs and monovacancies can be calculated, respectively:

$$E_{n,1i}^{b} = E_{1i}^{f} - A(N^{m} - (N-1)^{m}) \quad (5\text{-}12)$$

$$E_{n,1v}^{b} = E_{1v}^{f} - A(N^{m} - (N-1)^{m}) \quad (5\text{-}13)$$

where E_{1i}^{f} and E_{1v}^{f} are the formation energies of a single SIA and monovacancy, respectively. These binding energy expressions can be thought of as the difference in the energy between a cluster of size n and its products after monomer dissociation. Power-law expressions for the formation energies of large defect clusters are provided in Fig. 5-9 and are seen to closely represent the data collected from MD simulations. These expressions do not extrapolate well down to small cluster sizes, for which clusters do not exhibit dislocation loop geometries (Fig. 5-17); separate power-law fits are required for small defect clusters. Therefore, accurate binding energy expressions of the forms given in Eq. (5-12) and Eq. (5-13) should be based on the appropriate power-law fits depending on the cluster size. For SIA clusters, PPI vacancy (a-loop) structures, and basal vacancy (c-loop) structures, the size-dependent power-law fits are:

$$E_{SIA}^{f} = \begin{cases} 2.8N^{0.81}, & 2 \leq n \leq 7 \\ 4.6N^{0.66}, & n > 7 \end{cases} \quad (5\text{-}14)$$

$$E_{V,PPI}^{f} = \begin{cases} 1.9N^{0.84}, & 2 \leq n \leq 18 \\ 3.4N^{0.70}, & n > 18 \end{cases} \quad (5\text{-}15)$$

$$E_{V,basal}^{f} = \begin{cases} 2.5N^{0.78}, & 2 \leq n \leq 177 \\ 3.7N^{0.72}, & n > 177 \end{cases} \quad (5\text{-}16)$$

Mobile defect diffusivities within the basal plane and along the c-axis can be calculated with Eq. (2-3) using the data provided in Table 5-2 for SIA clusters and Table 5-3 for vacancy clusters. As discussed in Section 2.1.2, this diffusivity data is crucial for determining the anisotropy factor (Eq. (2-5)) for mobile defects, which directly modifies the reaction rates for capture by sinks with defined geometries (Eq. (2-9), Section 2.1.3). The work in this chapter has demonstrated that vacancy clusters are considerably less anisotropic than SIA clusters. It is therefore expected that basal c-loops will experience a net flux of vacancy defect capture, and this should drive their rapid growth once they nucleate. This data is crucial to capturing these fundamental mechanisms in the microstructural evolution of α-Zr.

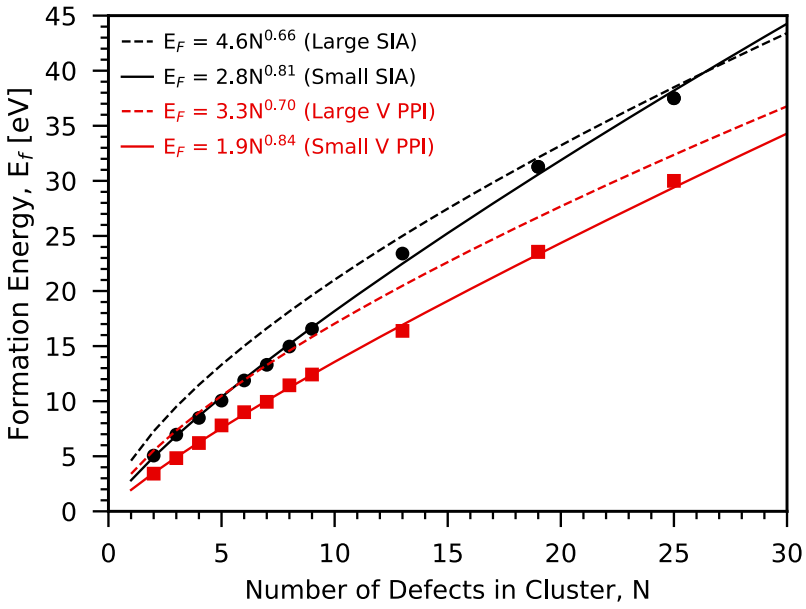

Fig. 5-17. Formation energies for small and large SIA and vacancy defect clusters; markers indicate data obtained from MD simulations while the solid and dashed lines indicate power-law fits for small and large defect clusters, respectively.

Chapter Six:

Dislocation Loop Stress States and Point Defect Capture Radii

In order to effectively model microstructural evolution, there are three broad questions that must be explicitly answered: 1) How many defects form in response to an incident particle flux?; 2) How do these defects transport throughout the lattice?; and 3) At what rate do these mobile defects interact with existing microstructure? The first of these questions was discussed in Chapter Four, for which volumetric defect generation rates were calculated based on tabulated displacement cascade data. The diffusivity of mobile defects, along with their anisotropy of migration, were investigated in Chapter Five. Thus, the only missing data to model dislocation loop capture rates are the capture radii for mobile defects. As described in Section 2.1.3, the capture of defects at dislocation loops is calculated based on spherical kinetics for small loop sizes, but transitions to toroidal kinetics as the loop size increases. There are two defining characteristics for the toroidal capture volume of a dislocation loop: the outer radius (which is based on the size of the loop) and the inner radius (which is equal to the capture radius for mobile defects). The transition parameter, α_{ij} (Eq. (2-22)), smoothly transitions between spherical and toroidal reaction kinetics based on the relative size of the outer and inner loop radii. Additionally, the capture radius directly affects the magnitude of the toroidal interaction rate constant. Thus, it is imperative to calculate accurate values for the capture radii of defects in order to sufficiently calculate dislocation loop capture rates.

Typically, the capture radii of a dislocation loop is assumed to be some multiple of the loop Burgers vector [98], but there is no differentiation between the capture of SIA or vacancy defects. While this method may provide different capture radii for loops with differing Burgers vectors, there is no difference between the capture radii of interstitial and vacancy a-loops, which both share the same Burgers vector; there is no quantifiable distinction between the reaction rates of these two loop types. As such, the differences in the capture rates of mobile defects depends entirely on the diffusivity and concentration of the mobile species. In a MFRT or CD framework, it would then be impossible to model the co-existence of interstitial and vacancy a-loops, as both of these loops would experience a net flux of either vacancies or interstitials. This would result in the growth of one type of a-loop and the shrinkage of the opposite type. It is for this reason that vacancy a-loops are reported to not grow [99] or are simply ignored [100-102] in most modeling attempts. Any model that cannot adequately exhibit simultaneous growth of vacancy and interstitial a-loops is not

physically representing known irradiated Zr microstructure, and cannot provide useful predictions for microstructure evolution.

It is possible that vacancy a-loop ordering is necessary to reduce the incoming SIA flux through self-shielding by neighboring a-loops, although this will require extensive modeling and analysis to evaluate the elastic interactions. Vacancy loops are known to band onto parallel basal sheets in both pure and alloyed Zr [13, 17, 20, 26]. A similar self-shielding phenomenon has been postulated to promote the formation of void and bubble lattices in many metals [22, 24]. However, there are some Zr alloys for which vacancy a-loop banding is weak or non-existent [26-28], and yet a co-existence of interstitial and vacancy type a-loops is still observed. Self-shielding alone cannot fully explain this phenomenon. It is also now known that SIA clusters in Zr migrate with considerable anisotropy within the basal plane ([159], Chapter Five) and would therefore preferentially interact with prismatic a-loops which lie perpendicular to the predominant SIA flux direction [46]. Theoretically, this should result in a net flux of interstitials to vacancy a-loops and mitigate their growth. It is then perplexing to consider that vacancy a-loops account for at least half of visible microstructure in irradiated α-Zr, with sizes comparable to or larger than interstitial a-loops [13, 16-18, 45, 173]. Although, it should be noted that some finesse is required to determine loop character.

One possibility to explain this behavior could stem from a difference in the defect capture rates of interstitial and vacancy a-loops. Modeling the capture of defects by dislocation loops is a computationally expensive task requiring millions of atoms, and as such can only be performed with molecular statics (MS) simulations. To our knowledge, this has yet to be attempted in literature for dislocation loops in α-Zr. A similar work has, however, been performed to investigate the capture of point defects to small cavities in α-Fe [174]. It was found that the effective capture radii between voids and SIAs were notably larger than between voids and vacancies, resulting in biased capture of mobile SIA defects. This bias was found to persist for over-pressurized bubbles, but the magnitude of the bias was greatly reduced due to the compressive strain field acting against SIA capture. The inherent bias for small cavities could have a significant effect on vacancy cluster growth [175, 176], although most models neglect any differences in the capture distances for SIA and vacancy defects [177-180].

It is not unreasonable to assume that differences in the point defect capture tendencies of dislocation loops may exist, and that the capture distances may be related to the strain field surrounding such defects. Any bias in the capture of migrating defects could have notable effects on the reaction rates and may be one of the key drivers for the unique irradiated microstructure in α-Zr. In this work, we perform MS calculations with the modern BMD19 potential [78] to quantify the capture distances of point defects to interstitial a-loops, vacancy a-loops, and basal c-loops. Defect capture is calculated radial to the loop, as well as perpendicular to the loop face. Any correlations between defect capture behavior and the stress states of the loops in these two directions will be discussed, and the potential for biased capture of defects will be assessed.

6.1 Modeling Method

MD simulations were performed as implemented in the Large-Scale Atomic /Molecular Massively parallel Simulator (LAMMPS) code [157]. The modern BMD19 interatomic Zr-Zr potential [78] was selected due to its improved predictions of defect properties compared to the M07 [70] and A95 [69] potentials. Unlike previous Zr-Zr potentials, the BMD19 potential accurately predicts the basal-octahedral site as the preferred configuration for single SIAs [75], has close agreement with defect formation energies calculated by *ab-initio* methods [78], and accurately predicts that vacancy loops are thermodynamically preferred to spherical cavities in α-Zr [159]. The largest drawback of this potential is its severe underprediction of basal stacking fault energies [78, 159]. Because the work performed here is not attempting to address or compare the absolute energies of basal c-loops, this drawback will not affect our results. All energy minimizations were performed with the Polak-Ribiere version of the conjugate gradient algorithm with a relative energy tolerance of 10^{-12} and a force tolerance of 10^{-12} (eV/Å). Periodic boundary conditions were implemented for all simulations. The USER-OMP and USER-INTEL acceleration packages were integrated into LAMMPS to minimize computational time. All atomic positions were observed in the OVITO software [158]. Dislocation loop structures were visualized with common neighbor analysis (CNA) [163].

Interstitial and vacancy a-loops are known to form on or near $\{10\bar{1}0\}$ PPI habit planes with perfect $\vec{b} = 1/3\,\langle 11\bar{2}0\rangle$ Burgers vector at large sizes [13-18]; vacancy c-loops instead form on (0001) basal planes with a Burgers vector of either $\vec{b} = 1/2\,[0001]$ (corresponding to basal extrinsic faulting) or $\vec{b} = 1/6 < 20\bar{2}3 >$ (corresponding to basal I1 intrinsic faulting) [13, 32, 33, 37]. For this work, interstitial loops were formed by inserting parallel basal-crowdions in a disk of radius R on a PPI habit plane (i.e. the lowest energy configuration identified by MS calculations [159]). A unit cell of this structure is visualized in Fig. 5-1. Energy-minimizations were performed before and after dislocation loops were inserted into the simulation box. Due to the significant strain field imposed by SIA defects, these loops did not require annealing to reach their equilibrium configurations. To construct vacancy a-loops, atoms were removed from a double "corrugated" layer in a disk of radius R on a PPI habit plane (which is lower in energy than a single-layer prismatic structure [82, 159]). Basal c-loops, on the other hand, are lowest in energy in single-layer configurations [159] and, as such, were constructucted by removing atoms from a disk of radius R from a single (0001) basal plane. Following the removal of atoms, the box was first energy-minimized and then ramped up to 573 K over 30 ps using an NPT (constant atom, pressure, and temperature) ensemble. The defect clusters were held at temperature for 200 ps before ramping down to 0 K over 30 ps and then performing a final energy minimization to calculate system energetics. Dislocation loop radii of 0.65, 1.2, 2.0, 3.0, and 5.0 nm were considered; this corresponds to approximate cluster sizes of 19, 55, 151, 333, and 955 defects. The simulation box size was set proportional to the loop radius: 8R x 8R x 8R (ranging from ~40,000 atoms for R = 0.65 nm to ~2.8 million atoms for R = 5.0 nm).

The binding energies of point defects to the minimized supercells of annealed defect structures were calculated by placing a single vacancy or SIA in the vicinity of the defect and performing an energy minimization. Single interstitials were placed in basal octahedral positions, as this is the preferred configuration predicted by the BMD19 potential and recent DFT studies [75, 78]. Once minimized, the binding energies were calculated by Eqs. (6-1 and (6-2 for vacancies and interstitials, respectively:

$$E_v^b = E_{v,bulk}^f - \left[\left(E(N-1) + E_{Zr}^{coh}\right) - E(N)\right] \quad (6\text{-}1)$$

$$E_i^b = E_{i,bulk}^f - \left[E(N+1) - \left(E(N) + E_{Zr}^{coh}\right)\right] \quad (6\text{-}2)$$

where $E(N)$, $E(N-1)$, and $E(N+1)$ are the total system energies for a system with N, N-1, or N+1 atoms, $E_{v,bulk}^F$ and $E_{i,bulk}^F$ are the bulk formation energies of a single interstitial (2.94 eV) or vacancy (2.03 eV), and E_{Zr}^{coh} is the cohesive energy of a single Zr atom (6.432 eV at 0K) as calculated with the BMD19 potential. The positions of atoms in and around the defect clusters were used to determine insertion coordinates for vacancies and interstitials. Sampling the entire volume around the larger loops, however, would require a significant number of minimizations for each loop. Therefore, a cross-sectional region containing the face of the loop was considered. The region was three atom layers thick in the direction normal to the loop face, and spanned twice its diameter in the directions parallel to the loop face to determine properties as a function of radial distance from the loop center (Fig. 6-1(b)). A similar cross-sectional slice rotated 90° such that it intersects the loop center (Fig. 6-1(c)) was considered to analyze properties perpendicular to the loop face. The radial and perpendicular interaction volumes for defect capture are visually illustrated in Fig. 6-2.

Once atom positions radial or perpendicular to the loop were determined via the cross-sectional selection, average values for the local atomic stress as well as point defect binding energies could be determined. For properties radial to the loop face, average values were calculated by binning atoms into 1.5 Å elliptical bins that radiated from the loop center. The bins were given ellipticity factors that matched the ellipticity of the current loop being analyzed. As such, properties are averaged as a function of radial distance along the major axis from the loop center. For perpendicular properties, “line scans” were performed with 2.5 Å perpendicular bins along the direction normal to the loop face. The line scan analysis was performed at the center and periphery of the loop. The point defect capture radii could then be calculated in one of two ways. The spontaneous capture radius is defined as the distance from the loop at which the point defect binding energy falls to one-half of its maximum value [174]. The thermal criterion capture radius is defined as the distance from the loop at which the binding energy falls below $\frac{3}{2}k_bT$ (and can no longer thermally escape drift towards the sink) [174]. This value is 0.074 eV at 573 K. Capture radii calculated with both of these methods will be compared for the capture of point defects to various dislocation loops in α-Zr.

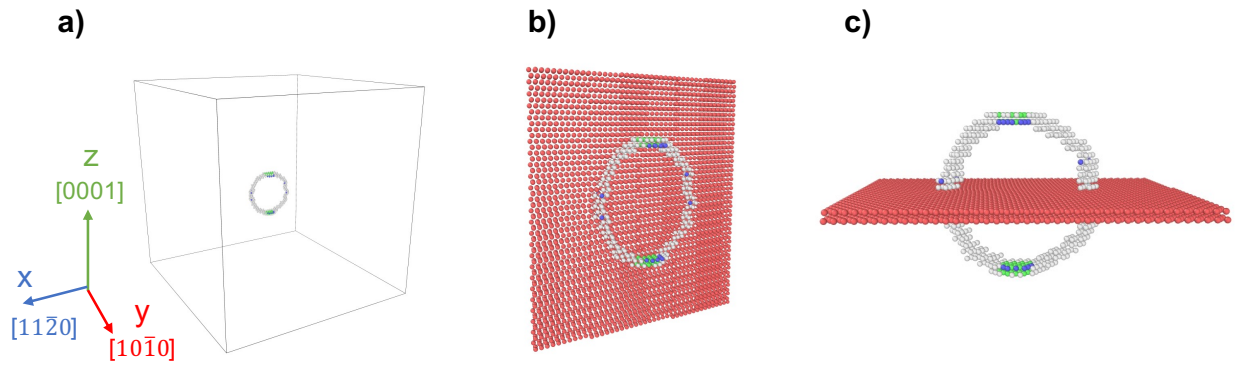

Fig. 6-1. a) simulation box containing an interstitial a-loop visualized through CNA analysis (grey atoms are "unknown" structure, green atoms are FCC crystal structure). Cross-sections of atoms are taken through the b) the face of the loop (radial capture) or c) perpendicular to the loop.

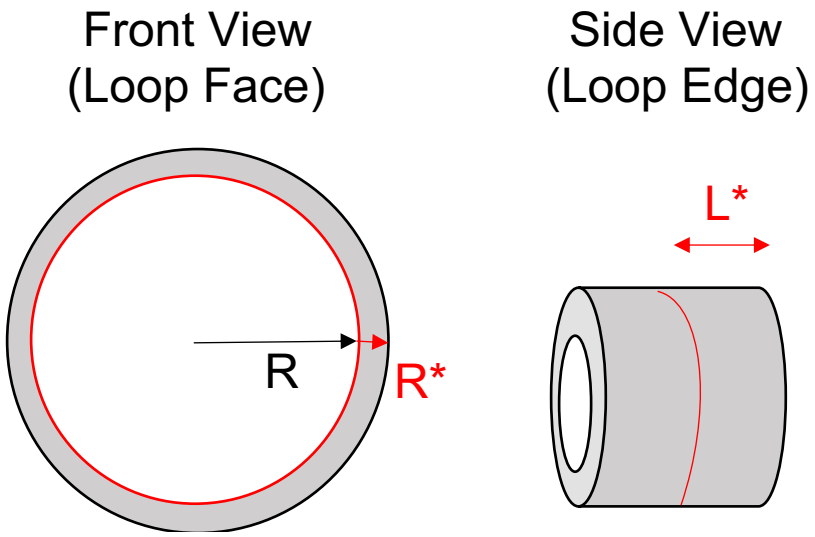

Fig. 6-2. The radial capture radius, R*, defines the interaction volume radial from the periphery of the loop. The perpendicular capture distance, L*, defines the interaction volume normal to the loop face.

6.2 Stress states surrounding dislocation loops

The stress tensors for each atom were calculated in LAMMPS in units of pressure*volume and converted into GPa through the division of the per-atom volume. The atomic stress is represented as average hydrostatic stress colormaps in Fig. 6-3. Tensile and compressive stresses are positive (blue) and negative (red), respectively. Vacancy a-loops exhibit tensile stresses along their loop face (with particularly strong tensile stresses when approaching the inner periphery of the loop), but this behavior reverses beyond the loop periphery; a weak compressive radial stress is exerted on the surrounding bulk. Normal to the loop face, a long range tensile stress extends into the bulk along the primary a-axis direction that intersects the loop. TEM investigation of irradiated Zr shows that vacancy a-loops tend to order on parallel basal sheets with increasing fluence [17, 20, 26]. However, within these basal sheets, the orientations of vacancy a-loops are seemingly random [17]. This is qualitatively consistent with the stress state analysis given here; vacancy a-loops should re-orient such that their tensile strain fields do not overlap.

Interstitial a-loops (Fig. 6-3(c,d)) share similar stress state trends, but with the opposing sign, as vacancy a-loops. These loops exhibit compressive stress along their faces but exert a radial tensile stress on the surrounding matrix; a compressive stress field extends normal to the loop face. Because interstitial and vacancy a-loops grow simultaneously and co-exist in the structure, it is unsurprising to find that the complementary stress states result in irradiation growth strain saturation at moderate fluence [3, 4]. Basal c-loops (Fig. 6-3(e,f)), on the other hand, share similar stress behavior with vacancy a-loops, but with a 90° rotation. Weak compressive stresses are exerted radially from the c-loop periphery (along the *a* directions) while a long-range tensile stress is exerted normal to the loop face (along the *c* direction). This is consistent with breakaway irradiation growth behavior which results in a-axis expansion and c-axis contraction of single crystalline Zr [3, 4].

In order to assess the magnitude of the atomic stresses, atoms were binned into 1.5 Å radial bins from the center of the loop, and 2.5 Å perpendicular bins from the periphery of the loop to calculate averaged stress states (Fig. 6-4). For vacancy loops, the magnitude of radial tensile stresses along the loop face decreases with increasing loop size; conversely, the radial compressive stress exerted beyond the periphery increases with loop size. Considering normal stresses perpendicular to the loop face, the long-range tensile stress slightly increases in magnitude as loop sizes increase. These general trends are similar for interstitial a-loops, but with the reverse sign. As evidenced by a reduced SIA bias to capture by over-pressurized bubbles when compared to cavities of equal size, a local compressive stress is expected to act as a barrier for SIA capture while promoting vacancy capture [174]. The potential impact of dislocation loop stress states on point defect capture, and any biases that may arise, will be addressed in the following section.

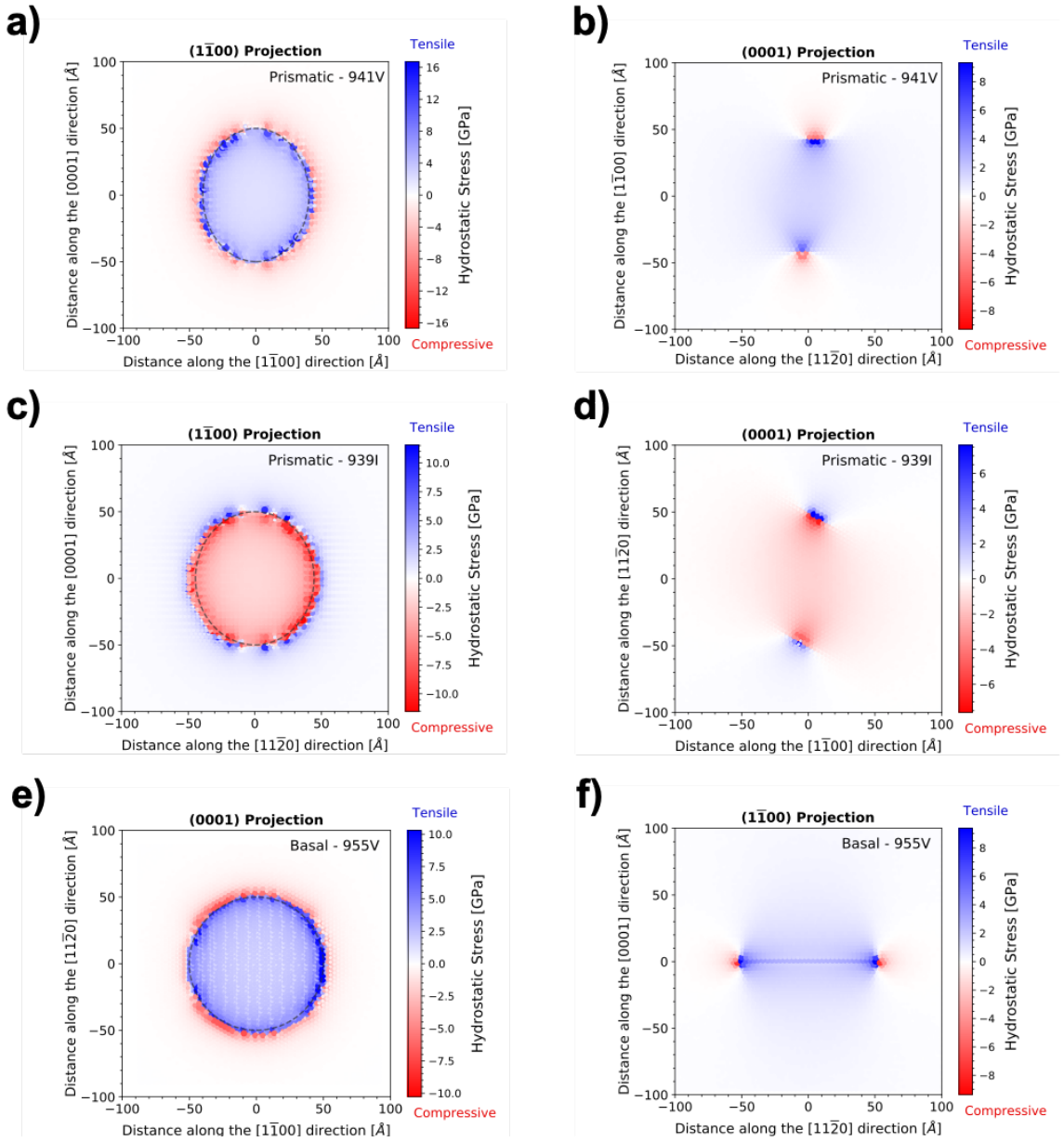

Fig. 6-3. Hydrostatic stress heatmaps for vacancy a-loops (a,b), interstitial a-loops (c,d), and vacancy c-loops (e,f). (11$\bar{2}$0) projections in the first column demonstrate stress radial to the loop center while (0001) projections in the second column demonstrate stresses normal to the loop face.

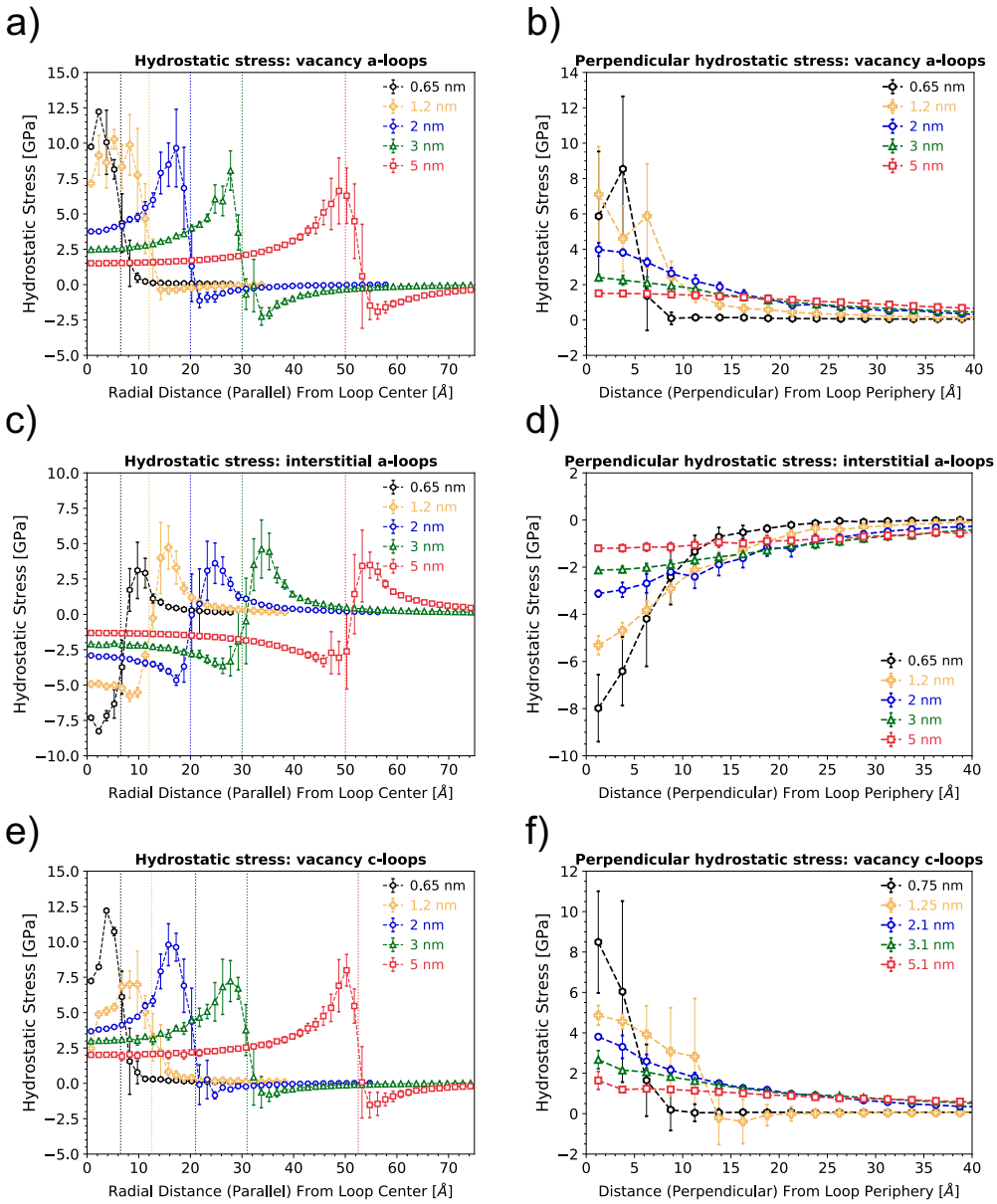

Fig. 6-4. Average values for the hydrostatic atomic stress is plotted in 1.5 Å radial bins (a, c, e) and 2.5 Å perpendicular bins (b, d, f) for vacancy a-loops (first row), interstitial a-loops (middle row), and vacancy c-loops (bottom row). Positive stresses are tensile. Dotted lines indicate the position of the loop periphery (a,c,e)

6.3 Calculating point defect capture radii

6.3.1 Binding energy maps

Point defect absorption at sinks such as dislocation loops is driven by either a reduction in the local formation enthalpy of the defect, or the removal of the defect from the system. Considering Fig. 5-5, the formation energy per defect for interstitial and vacancy loops decreases with loop size. For example, the formation energy per vacancy in a 941V prismatic a-loop is ~0.4 eV while the bulk formation energy for a single vacancy is predicted to be 2.03 eV by the BMD19 potential [78]. Thus, there is a significant potential energy well for a migrating bulk vacancy to be captured by the loop. The same argument could be made for a single interstitial (with a bulk formation energy of 2.94 eV) being captured by a 939I prismatic a-loop for which the formation energy per interstitial is ~0.5 eV [159]. The potential energy gradient causes drift of the point defect towards the loop with its eventual capture. Likewise, there is a significant drive for loops to capture and annihilate defects of the opposing type (i.e. a single interstitial annihilating through capture by a vacancy loop).

When considering defect capture by dislocation loops in a CD modeling framework, large dislocation loops are characterized by toroidal reaction volumes [105, 113, 114]. Functional solutions for the sink strength relating to toroidal reaction volumes are only valid when the loop outer radius notably exceeds the inner radius [112]. Thus, the reaction rates for defect capture at loops must be smoothly transitioned between spherical and toroidal capture volumes, with a mixed regime at intermediate loop sizes. The necessity for this treatment is made clear with the binding energy maps for single SIA capture to vacancy (V) loops with sizes n = 19V, 151V, and 941V in Fig. 6-5. For the 19V, 151V, and 941V loops, the capture volume for a single SIA can be approximated as spherical, mixed, and toroidal, respectively. This capture behavior can be understood by considering that there is an atomic mis-match between the dislocation loop and the surrounding matrix at the loop periphery (an extra or missing plane of atoms for interstitial and vacancy loops, respectively); at the center of these loops, the hcp crystal structure is restored, although it is characterized by a slightly compressed lattice parameter for interstitial loops and a slightly extended lattice parameter for vacancy loops [79, 91, 159]. Thus, migrating defects are preferentially captured at the loop periphery rather than the loop center, and the capture distance can be considered the inner radius of the toroidal capture volume, which is notably exceeded by the loop radius for large dislocation loops (Fig. 6-5(c)).

This capture behavior is reflected in the point defect binding energy maps in Fig. 6-6 (plotted in 1.5 Å radial bins from the loop center). Monovacancy capture energies to vacancy a-loops, interstitial a-loops, and basal c-loops are plotted in Fig. 6-6(a, c, e); single interstitial capture energies to these three loops, respectively, are plotted in Fig. 6-6(b, d, f). Consider first the capture of the same type of defect to a dislocation loop (i.e. an interstitial to an interstitial loop). The general trend is that, as the loop size increases, the capture energy for the defect increases. This is consistent with the thermodynamic argument that

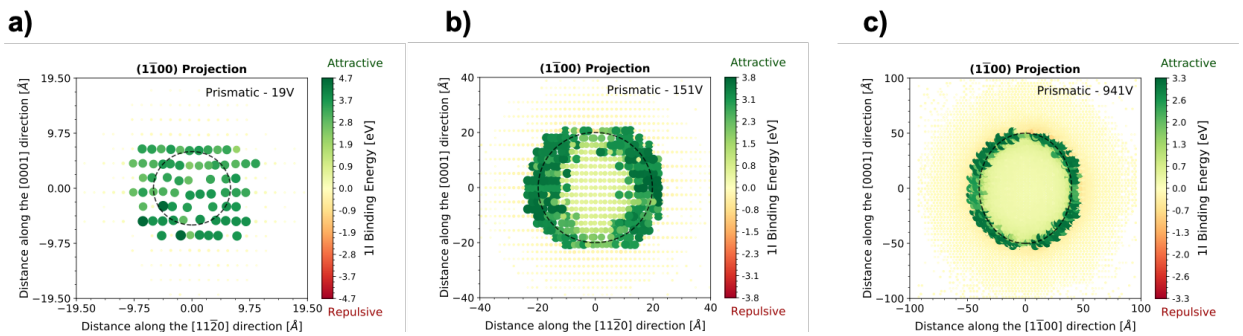

Fig. 6-5. Single interstitial binding energy maps to vacancy loops with a) 19 vacancies (R = 0.65 nm), b) 151 vacancies (R = 2 nm), and 3) 941 vacancies (R = 5 nm).

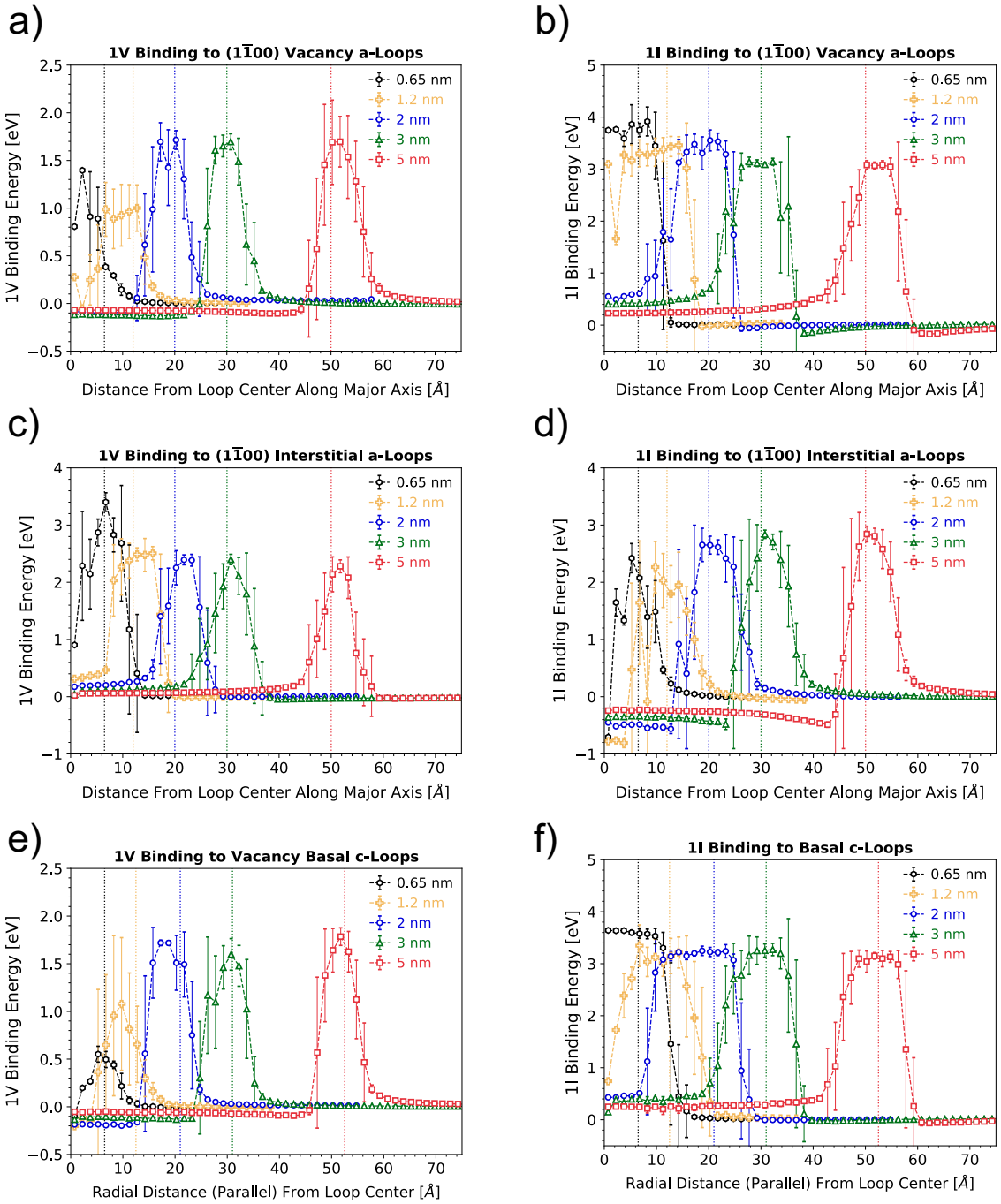

Fig. 6-6. Average values in 1.5 Å radial bins for the binding energies of single vacancies (a, c, e) and single interstitials (b, d, f) for a,b) vacancy a-loops c,d) interstitial a-loops and e,f) vacancy c-loops. Positive binding energies are attractive. Dotted lines indicate the position of the loop periphery (a,c,e)

there exists a deeper potential energy well for capture at larger loops. The opposite is true for defect annihilation at dislocation loops (Fig. 6-6(b, c, f)). As the loop size increases, the capture energy decreases. The annihilation of an interstitial at a vacancy loop can be thought of as the recombination of a Frenkel pair. In this case, the capture energy is large due to the large formation energy of the bulk SIA, but the capture energy decreases with loop size because the annihilating vacancy has a lower effective formation energy. Due to the disparity in bulk formation energies for single SIAs and vacancies, single SIAs always observe higher capture energies towards vacancy loops. Interstitial loops are biased towards vacancy capture at small sizes but this behavior reverses for larger loop sizes. It is interesting to note the uncharacteristically low binding energy of single vacancies to small (< 1.2 nm) basal vacancy clusters (Fig. 6-6(e)). This is especially true when comparing to the vacancy capture energies to small prismatic vacancy clusters. If competing nucleating prismatic and basal structures observe disparate vacancy capture capabilities, this may help explain the low-fluence abundance of prismatic a-loops in irradiated α-Zr.

The capture energies of point defects perpendicular (rather than radial) to the loop periphery are plotted in Fig. 6-7. Appreciable binding is shown by single SIAs to vacancy a-loops and c-loops up to distances as large as ~10 Å (Fig. 6-7(b)). Similar, albeit shorter-range, capture behavior is seen for single vacancies. This implies that long-range interactions with point defects is most likely mediated by the gradient of a stress field, and that interstitials are more susceptible to local alterations of the stress field. It is interesting that the capture distances radial from the loop and perpendicular to the loop are not necessarily equal, particularly for small defect clusters. This discrepancy will be further detailed in following sections, for which the radial and perpendicular capture radii will be quantified.

6.3.2 Spontaneous capture radii of point defects

We first analyze the spontaneous capture of point defects at dislocation loops. This analysis method denotes a threshold energy to detect defect capture; in this work, spontaneous capture is assumed to occur until the binding energy falls to half of its maximum value, as suggested by Kohnert et al. [174]. The distance at which this occurs is considered the spontaneous capture radius, and these values have been tabulated for point defect capture by vacancy a-loops, interstitial a-loops, and basal c-loops in Table 6-1. Considering this analysis method, single SIAs have greater radial capture distances than monovacancies to vacancy loops of all sizes. The potential energy well is deeper for SIAs, and therefore the gradient is steeper, driving longer-range capture of SIAs than vacancies. The radial capture radii, R*, of SIAs to vacancy loops demonstrates that the depth of the potential energy well dominates over stress state when considering spontaneous point defect capture. Vacancy loops exert short-range radial compressive stresses on the matrix (Fig. 6-3(a,e)) that should inhibit SIA capture and promote vacancy capture. As will be discussed in the following section, this stress state has a greater effect on thermal drift, rather than spontaneous, capture of point defects. Similar to the preferential SIA capture by vacancy loops,

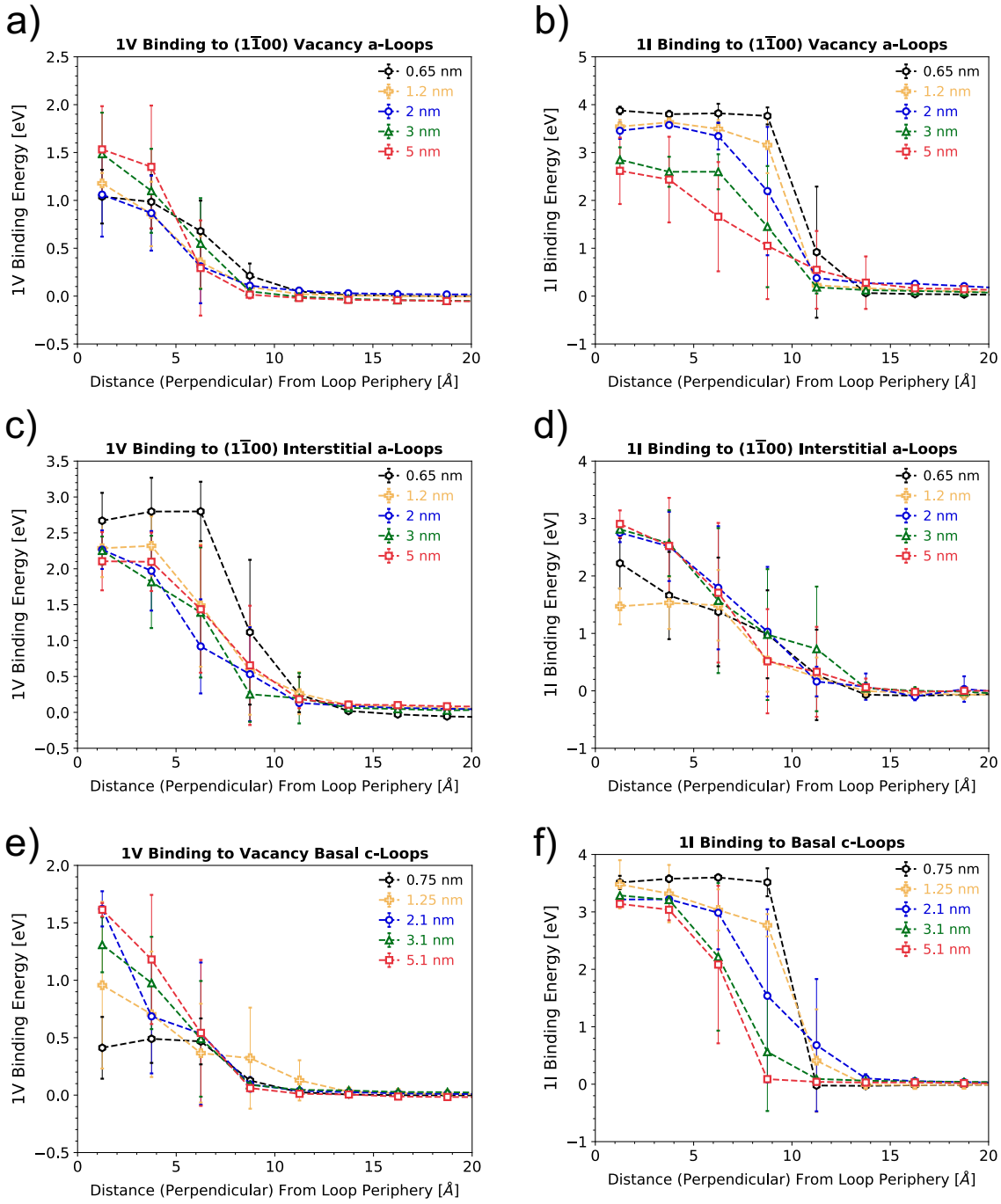

Fig. 6-7. Average values in 2.5 Å perpendicular bins for the binding energies of single vacancies (a, c, e) and single interstitials (b, d, f) for a,b) vacancy a-loops c,d) interstitial a-loops and e,f) vacancy c-loops. Positive binding energies are attractive.

Table 6-1. Spontaneous defect capture distances in the directions radial to (**R***) and normal to (**L***) the loops. Radii are determined by the "half-max" criteria, indicating the distance at which the capture energy of the point defect drops off to one-half of the maximum value.

Loop Radius (Å)	**Effective radial capture radius, R* (spontaneous criteria) (Å)**					
	Prismatic Vacancy a-loop		Prismatic Interstitial a-loop		Basal Vacancy c-loop	
	1I	1V	1I	1V	1I	1V
6.5	4.5	0	3.8	4.4	5.0	2.0
12	4.7	2.2	5.2	5.5	5.4	1.0
20	4.8	2.9	6.0	5.3	4.8	2.1
30	5.8	3.4	6.0	4.9	5.6	3.3
50	6.9	5.9	5.9	4.5	6.6	4.4

Loop Radius (Å)	**Effective perpendicular capture radius, R* (spontaneous criteria) (Å)**					
	Prismatic Vacancy a-loop		Prismatic Interstitial a-loop		Basal Vacancy c-loop	
	1I	1V	1I	1V	1I	1V
6.5	10.4	7.1	7.9	8.3	10.0	7.9
12	9.9	5.1	8.1	7.2	9.8	5.4
20	9.3	5.3	7.6	5.7	8.6	3.4
30	8.8	5.4	6.9	6.8	7.1	5.4
50	7.7	5.1	6.8	7.5	6.9	5.2

monovacancies are captured at greater distances by small interstitial loops. Conversely, large interstitial loops have a greater capture radius for single SIAs than monovacancies. This can be understood by considering that larger SIA loops exhibit reduced formation energies per SIA, and thus offer a lower-energy state for migrating SIAs.

A comparison of the radial capture radii and perpendicular capture radii in Table 6-1 show that the capture distances are not symmetrical about the dislocation loop core. The capture distances perpendicular to the loop periphery are consistently larger than the radial capture distances. However, the same trends for preferential SIA or vacancy capture are still true when considering these perpendicular radii. Incorporating these values would increase the effective capture volume of dislocation loops, particularly for small loops for which these capture distances notably exceed the cluster radius.

6.3.3 Thermal drift capture radii of point defects

The thermal drift analysis method is based on the concept that an interaction gradient between a defect and any given sink promotes defect drift towards that sink [174]. This effective capture radius is considered to be the distance at which the interaction energy falls below $\frac{3}{2}k_bT$. At lower temperatures, it becomes increasingly difficult for a defect to thermally migrate against the interaction gradient, and the capture distance becomes much greater than those calculated with the spontaneous method, as can be seen in a comparison of Table 6-1 (spontaneous) and Table 6-2 (thermal drift analyzed at 573 K). First consider the radial point defect capture distances for vacancy a-loops. When using the spontaneous capture analysis, SIAs are preferentially captured by vacancy a-loops of all sizes; using the thermal drift criteria, however, monovacancies now exhibit greater capture distances to vacancy a-loops above a size of R∼1.2 nm (55V). The opposite effect is true for interstitial a-loops. Using the thermal drift criteria, these loops preferentially capture single SIA defects rather than monovacancies. These observations for the radial capture distances seem to be correlated with the radial stress states exerted by vacancy and interstitial a-loops, respectively. Vacancy a-loops exert a short-range compressive stress on the surrounding matrix in the directions radial to the loop periphery (Fig. 6-3(a), Fig. 6-4(a)), and the magnitude of the compressive stress increases with loop size. This is qualitatively consistent with the point defect capture tendencies of vacancy a-loops. The opposite capture behavior occurs for interstitial a-loops, and this is consistent with the short-range tensile stresses exerted radial to the loop peripheries.

It is interesting to note the point defect capture tendencies in Table 6-2 for basal c-loops. For small sizes, where c-loop precursors take the form of faulted basal pyramids [84, 159], single SIAs are preferentially captured over monovacancies. It is not until a faulted basal c-loop is fully formed on a single basal plane that vacancies observe preferential capture. The biased SIA capture of c-loop precursors could act as a delaying mechanism for c-loop growth, which may account for the fact that these defects are not observed until high fluence [13, 33].

Table 6-2. Thermal drift defect capture distances as determined by the k_bT criteria in the directions radial to (**R***) and normal to (**L***) the loops. At 573K, k_bT is ~0.050 eV. **R*** and **L*** represent the distances at which a point defect can no longer thermally escape drift towards the loop.

Loop Radius (Å)	**Effective radial capture radius, R* (thermal drift criteria, 573K) (Å)**					
	Prismatic Vacancy a-loop		Prismatic Interstitial a-loop		Basal Vacancy c-loop	
	1I	1V	1I	1V	1I	1V
6.5	6.3	4.8	9.5	6.6	9.2	3.5
12	5.7	5.4	10.1	6.9	11.1	4.5
20	5.2	10.1	15.6	7.7	7.2	5.8
30	6.4	9.5	18.9	6.7	7.1	7.3
50	8.0	14.1	21.8	7.7	8.3	10.6
Loop Radius (Å)	**Effective perpendicular capture radius, R* (thermal drift criteria, 573K) (Å)**					
	Prismatic Vacancy a-loop		Prismatic Interstitial a-loop		Basal Vacancy c-loop	
	1I	1V	1I	1V	1I	1V
6.5	14.4	10.2	11.9	12.4	10.2	9.6
12	24.8	9.3	12.2	19.6	12.4	12.2
20	29.3	10.9	13.1	17.7	15.7	9.7
30	32.0	7.7	12.7	14.8	14.8	10.0
50	34.6	11.6	13.1	15.3	15.2	10.4

The effect of the loop stress state appears to affect the perpendicular capture of dislocation loops more than the radial capture (Table 6-2). This is perhaps unsurprising considering the long-range tensile and compressive stresses that extend normal to the habit plane of vacancy loops (Fig. 6-3(b,f), Fig. 6-4(b,f)) and interstitial loops (Fig. 6-3(d), Fig. 6-4(d)), respectively. This then drives long-range normal capture of single SIAs to vacancy a-loops and monovacancies to interstitial a-loops. This effect is particularly true for SIA capture at vacancy a-loops, the opposite behavior as was described for the radial capture distances. Considering this phenomenon, the spatial ordering of vacancy a-loops likely has a impact on the net flux of captured defects. Bands of vacancy a-loops on basal planes, as has been noted in pure Zr [17] and alloyed Zr [20, 26], would cause an overlap of the predominant SIA capture volumes for these loops. Growth of vacancy a-loops in these bands could be driven by the fact that the radial capture volumes remain unimpeded above and below the ordered basal sheets, and these radial capture volumes prefer vacancy capture over interstitial capture. Thus there may be a net bias for vacancy capture within these ordered bands. Harte et al. have reported that c-loop positions are anti-correlated with a-loops within the basal bands; it is possible that a-loop banding is necessary to reduce the incoming SIA flux to c-loop precursors, which are biased for SIA capture, and facilitates the growth of basal c-loops. This hypothesis would be consistent with the fact that there are higher c-loop number densities in Zr alloys that exhibit strong vacancy a-loop banding when compared to those with weak vacancy a-loop banding [20, 26].

When using the thermal drift criteria for calculating capture radii, the resultant capture volumes are sensitive to the operating temperature. At higher temperatures, mobile defects have greater thermal energy to escape the interaction gradient with sinks. Fig. 6-8 demonstrates this temperature dependence for radial point defect capture by dislocation loops with radius R = 5 nm. For the capture of same-type defects (i.e. single SIA capture to SIA a-loops) in Fig. 6-8(a), the calculated interaction distance exhibits a decaying dependence on inverse temperature:

$$r_d^{radial} = \alpha_d \left(\frac{T_m}{T}\right)^{m_d} \quad (6\text{-}3)$$

where T_m is the melting temperature (2128 K). When instead considering the capture of opposing-type defects (i.e. monovacancy capture at SIA a-loops) in Fig. 6-8(b), there is only a weak temperature dependence. This can again be understood based on the stress state overview given in Section 6.2. For the case of SIA a-loops, a tensile stress field is exerted radially from the loop periphery. Migrating single SIAs observe an attractive interaction gradient along this tensile stress field. Thus, temperature plays a greater role on the thermal drift capture of migrating SIAs to SIA a-loops, and vice-versa. The necessary parameters (α_d, m_d) to calculate these temperature-dependent radii are given in Table 6-3 for each loop type and size investigated in this work.

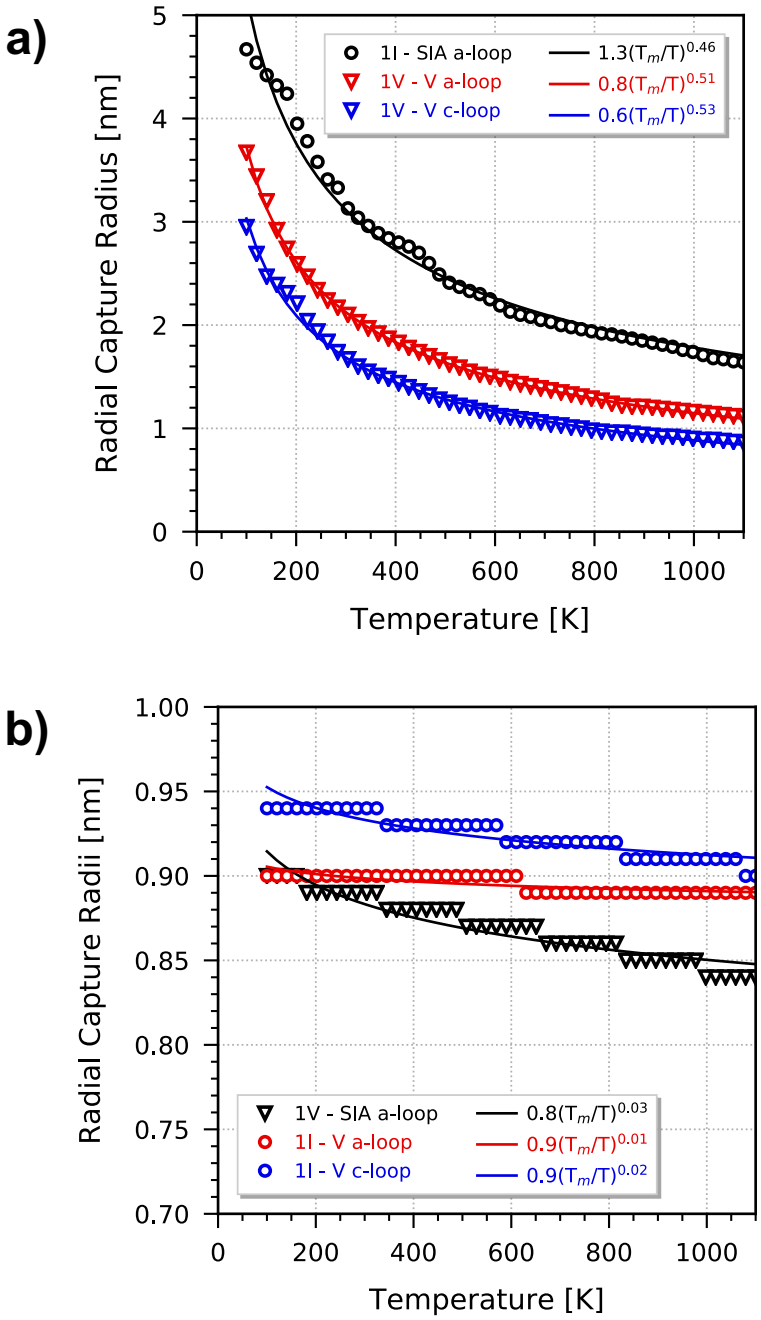

Fig. 6-8. Thermal drift capture radii for single SIA (1I) and monovacancy (1V) capture by SIA a-loops, vacancy a-loops, and vacancy c-loops of size R = 5nm as a function of temperature. Capture radii are shown for the capture of a) same-type defects and b) different-type defects.

Table 6-3. Necessary parameters to calculate thermal drift capture radii (Å) as a function of temperature using Eq. (6-3). For each loop size and type, these parameters are given for single SIA (1I) and single vacancy (1V) capture.

Loop Radius (Å)	α_d **Parameter (Å)**					
	Prismatic Vacancy a-loop		Prismatic Interstitial a-loop		Basal Vacancy c-loop	
	1I	1V	1I	1V	1I	1V
6.5	5.3	3.6	7.5	7.0	6.9	3.0
12	6.5	3.5	9.1	7.6	7.9	3.7
20	6.1	5.2	11.3	8.0	7.6	3.3
30	7.1	6.2	12.3	7.2	7.4	3.7
50	8.9	7.8	12.6	8.3	8.9	5.9
Loop Radius (Å)	m_d **Parameter (unitless)**					
	Prismatic Vacancy a-loop		Prismatic Interstitial a-loop		Basal Vacancy c-loop	
	1I	1V	1I	1V	1I	1V
6.5	0.16	0.33	0.23	0.075	0.29	0.29
12	0.0095	0.47	0.25	0.032	0.19	0.28
20	0.0098	0.56	0.29	0.055	0.062	0.59
30	0.025	0.41	0.37	0.047	0.058	0.64
50	0.0070	0.51	0.46	0.032	0.019	0.53

6.3.4 Net SIA biases to dislocation loops in α-Zr

For a given dislocation loop L, the bias for point defect capture can be written in terms of the loop sink strength for absorption of interstitials (i) and vacancies (v):

$$B_L = \frac{Z_{i,L}}{Z_{v,L}} - 1 \quad (6\text{-}4)$$

The calculation of $Z_{i,L}$ and $Z_{v,L}$ is dependent on the size of the loop. Large dislocation loops can be considered to have toroidal (T) reaction volumes, and an approximation for the sink strength depends on the defect capture radius, r_d [113, 114]:

$$Z^T = \frac{4\pi^2 R_L \rho_L}{\ln(1 + 8R_L/(r_1 + r_d))} \quad (6\text{-}5)$$

where R_L is the loop radius, ρ_L is the loop density, and r_1 is the point defect radius. However, this approximation is only sufficient once the inner radius notably exceeds the loop radius. For small loops (such that the inner radius is equal to or greater than the loop radius), the sink strength is best approximated by a spherical (S) reaction volume:

$$Z^S = 4\pi(r_i + r_j + r_d)\rho_L \quad (6\text{-}6)$$

Dislocation loop sink strengths are smoothly transitioned between spherical and toroidal reaction kinetics, such that the effective sink strength can be calculated by:

$$Z_L = (1 - \alpha_j)Z^T + \alpha_j Z^S \quad (6\text{-}7)$$

$$\alpha_j = \left(1 + \left(\frac{R_L}{3(r_1 + r_d)}\right)^2\right)^{-1} \quad (6\text{-}8)$$

Using the capture radii tabulated in Table 6-1 (spontaneous capture) and Table 6-2 (thermal drift capture at 573K), the net SIA biases for dislocation loops of varying size are plotted in Fig. 6-9(a) for spontaneous capture and Fig. 6-9(b) for thermal drift capture. The effect of the capture radii criterion is significant. When considering spontaneous capture, single SIAs generally have larger interaction volumes. There is a net positive SIA bias for all dislocation loops less than R~15 nm. When considering thermal drift capture, there is an even stronger SIA bias for capture at SIA a-loops. For vacancy a-loops, however, there is now a similarly strong bias for monovacancy, rather than SIA, capture. This phenomenon is quite notable and likely promotes simultaneous SIA and vacancy a-loop growth in irradiated α-Zr. It is common in higher-order modeling to simply assume that SIAs have a ~10 – 20 % bias for capture at all dislocation loops (similar to what is demonstrated with spontaneous capture radii in Fig. 6-9(a)). When using this assumption, CD frameworks

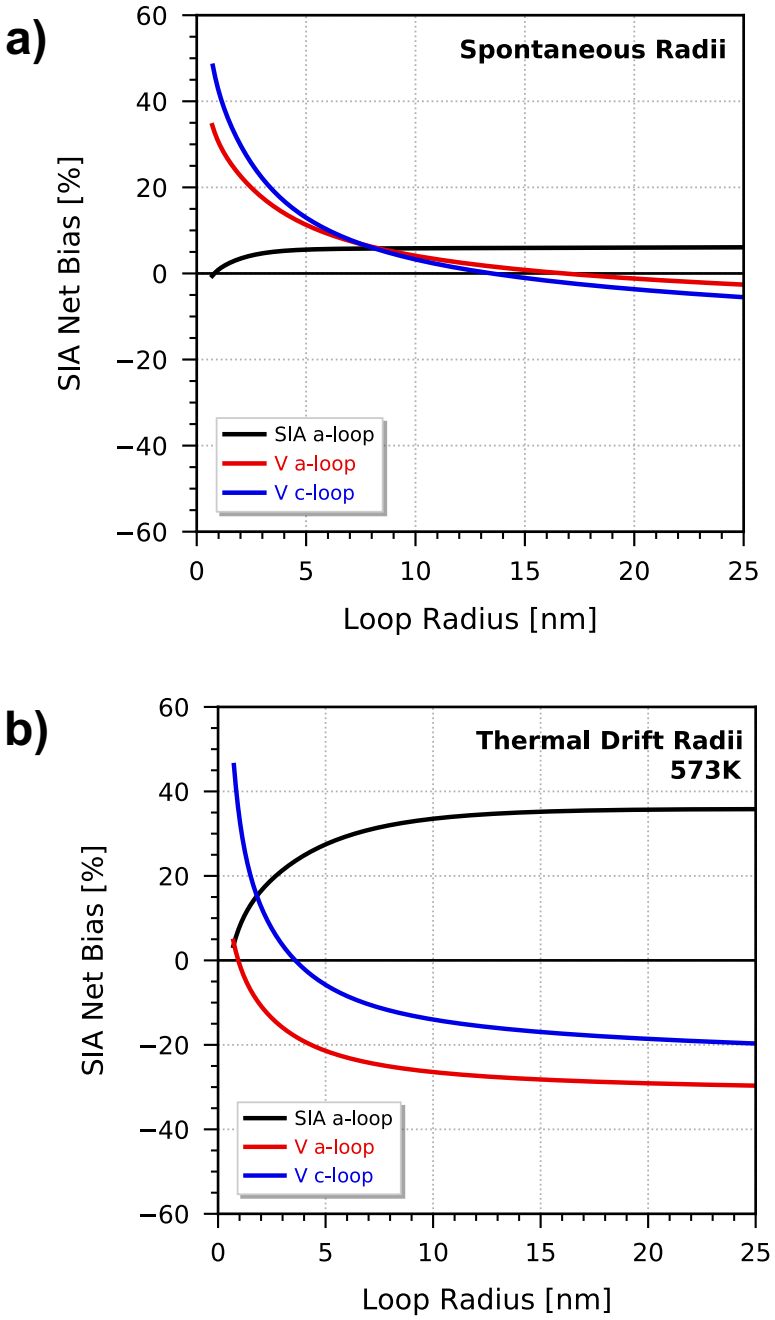

Fig. 6-9. Net SIA biases to SIA a-loops, vacancy a-loops, and vacancy c-loops using a) spontaneous capture radii and b) thermal drift capture radii calculated at 573K.

have been unable to predict the simultaneous growth of interstitial and vacancy a-loops [99-102]. Thermal drift capture radii, which are influenced by the unique stress states for each dislocation loop, provide a physically-relevant and inherent bias for vacancy and interstitial a-loops to preferentially absorb point defects of the same type. This behavior is expected to be reversed when considering capture volumes normal to the loop faces; spatial ordering of vacancy a-loops to overlap these perpendicular capture volumes may be necessary to maintain biased vacancy capture.

It is interesting to note that small c-loops are biased towards SIA capture while large c-loops are biased towards vacancy capture. Preferential SIA absorption by nucleating c-loops could explain why these defects observe delayed growth; once these defects have grown to a size where vacancy biases become relevant, however, their growth is quite rapid. It is crucial to note that the net biases in Fig. 6-9 do not take defect diffusive anisotropy into account, and are derived only from the discrepancy of interaction volumes for point defects. An accurate representation of dislocation interaction rates must consider both these interaction volumes as well as the anisotropy of defect diffusion [46, 159]. For the case presented here, the toroidal sink strength (Eq. (6-5)) would need to be modified by the anisotropic capture efficiency, which will be different for a-loops (which have PPI habit planes) and c-loops (which have basal habit planes). A modification for dislocation loops has been suggested by Saidi et al. [110] based on the original "diffusional anisotropy difference" (DAD) model of Woo [46]. Implementing this defect anisotropy is outside the scope of this article, but is a necessary component for higher-order modeling of microstructure evolution. Because single SIAs and monovacancies migrate with similar anisotropy [159], it is not expected to affect the relative biases shown in Fig. 6-9.

6.4 Summary and conclusions

The stress states and capture of point defects was investigated with the BMD19 potential. Vacancy loops exert short-range radial compressive stresses and long-range tensile normal stresses; the magnitude of the radial compressive stress generally increases with loop size. The same trends are true for interstitial loops, but with opposite stress signs. The spontaneous capture distances of point defects are predominantly related to the depth of the potential energy well, which depends on the magnitude of the defect formation energy in the bulk and its maximum capture energy to the dislocation loops. When analyzing spontaneous defect capture, SIAs observe biased capture to all dislocation loop types. When using the thermal drift analysis method, however, it was found that point defect capture biases were correlated with the stress states surrounding dislocation loops. Monovacancies exhibited biased radial capture to vacancy a-loops while single SIAs observe biased radial capture to interstitial a-loops. This discrepancy in the interaction volumes of point defects provides a physically-relevant and inherent bias that may explain the co-existence of interstitial and vacancy a-loops in irradiated α-Zr. For capture volumes normal to the loop faces, the opposite biases are exhibited. This demonstrates the importance of spatial vacancy a-loop ordering to reduce their incoming SIA flux, and potentially assist in c-loop growth.

Further CD modeling is required to assess the impact of these observations on microstructural evolution.

6.5 Implementation of data into CD model

The implementation of radial defect capture radii, r_d, is quite straightforward in a CD approach. This parameter controls the transition between spherical and toroidal reaction kinetics (Eq. (6-8)) as well as the magnitude of the toroidal reaction rate constant (Eq. (6-5)). Differences in the capture radii would affect the capture tendencies for the various dislocation loops and the resultant biases could drive the unique microstructure we see in irradiated Zr. For interstitial a-loops, vacancy a-loops, and basal c-loops, power-law expressions were fit to the capture radii provided in Table 6-1 (spontaneous capture) and Table 6-2 (thermal drift capture at 573K). The power-law fits are plotted and displayed in Fig. 6-10 for spontaneous defect capture and Fig. 6-11 for thermal drift capture. In order to assess temperature dependence, the thermal drift radii can be calculated at any temperature using the parameters available in Table 6-3 with Eq. (6-3). In Chapter Seven, CD modeling will demonstrate the predicted microstructure evolution behavior when using capture radii calculated with these two methods.

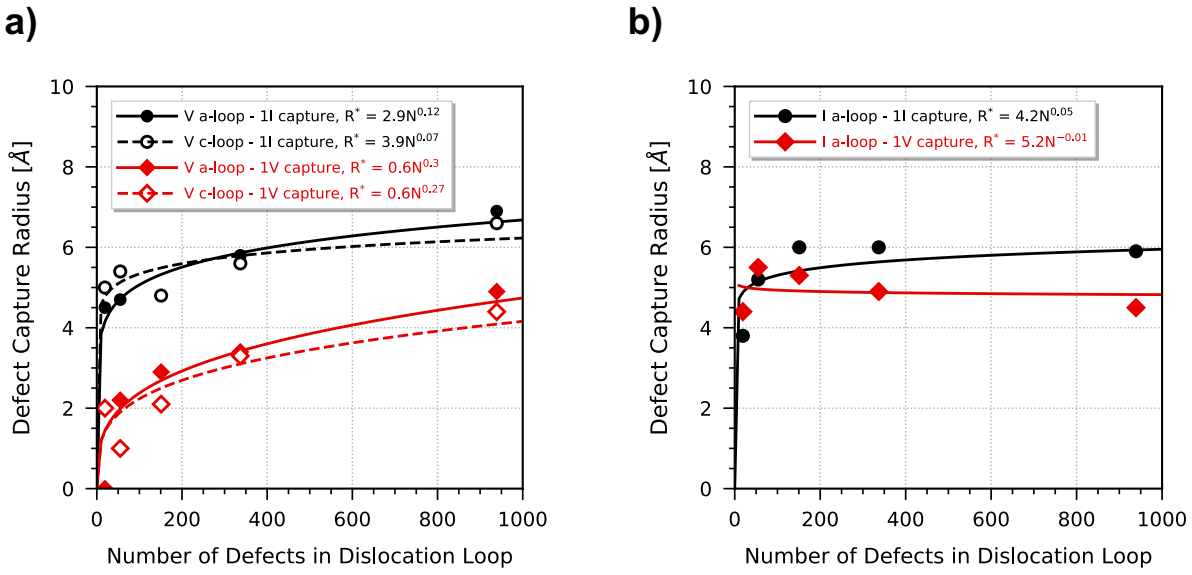

Fig. 6-10. Spontaneous capture radii of single SIAs (1I) and monovacancies (1V) to vacancy a-loops, interstitial a-loops, and basal c-loops. Red lines correspond to 1V capture; black lines correspond to 1I capture.

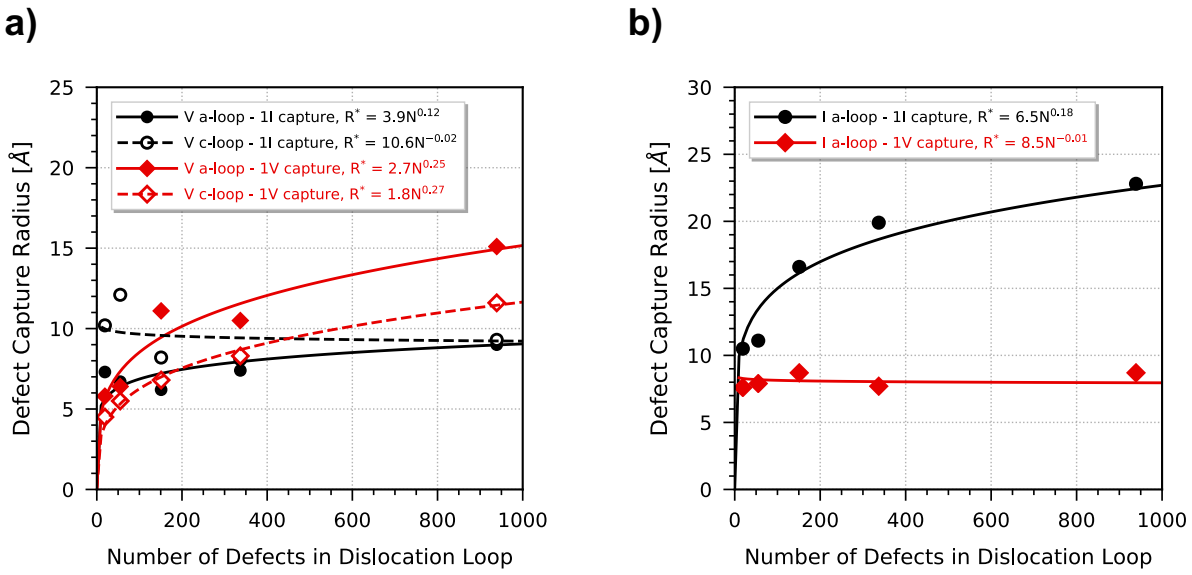

Fig. 6-11. Thermal drift capture radii of single SIAs (1I) and monovacancies (1V) to vacancy a-loops, interstitial a-loops, and basal c-loops. Red lines correspond to 1V capture; black lines correspond to 1I capture.

Chapter Seven:

Cluster Dynamics Modeling of Interstitial and Vacancy a-Loop Co-Existence

The work detailed thus far in this dissertation has provided an essential database of fundamental mechanisms and parameters that govern microstructural evolution under irradiation. Interaction energies of common solute and impurities to c-loops in the nucleation and growth regime have been quantified through *ab initio* calculations (Chapter Three). This data directly informs expressions for c-loop binding energies and mechanistic models for c-loop nucleation. In Chapter Four, volumetric generation rates for defects were derived based on displacement cascade data. The effect of electronic stopping has been noted on total defect production, defect clustering fractions, and defect cluster distributions. After defects are produced from incident irradiation, the resultant microstructure evolves as a consequence of defect transport in the material. Mobility data and inherent anisotropies of diffusion have been tabulated for each of the mobile species in α-Zr in Chapter Five. This database will allow us to adequately implement anisotropic effects on defect interaction rates in a CD framework for point defects and defect clusters. Furthermore, preferred cluster configurations and their binding energies as a function of size are now known. In Chapter Six, the interaction distances of point defects with interstitial a-loops, vacancy a-loops, and vacancy c-loops were assessed in the directions radial and perpendicular to the loop face. It was found that the local stress states surrounding dislocation loops induce an interaction gradient which preferentially attracts defects of the same type as the loop. Thus, an inherent bias emerges which may explain interstitial and vacancy a-loop co-existence.

This wealth of critical data has been lacking in literature, and as such, it is unsurprising to find that recent modeling attempts have relied on a number of arbitrary assumptions to fit to experimental data [96, 97, 99-101]. Only one modeling attempt has managed to predict the growth of vacancy a-loops, but this growth was dependent on strong SIA anisotropy and preferential thin foil orientation [98]. Most models either ignore vacancy a-loops entirely or fail to explain their co-existence with interstitial a-loops in bulk Zr. In this Chapter, we aim to implement a mechanistically-informed CD framework capable of predicting microstructure evolution with minimal assumptions. A detailed overview of the CD model, and a derivation of the equations involved, were provided in Chapter Two. The key equations will be repeated here for convenience. The general ODE that tracks the population of a given cluster *i* balances the gains and losses of the cluster:

$$\frac{dC_i}{dt} = g_i - D_i k_i^2 C_i + \sum_{n+m\to i} k_{n,m}^{+} C_n C_m - \sum_j k_{i,j}^{+} C_i C_j + \sum_{n\to n-i,i} k_{n-i,i}^{-} C_n - \sum_j k_{i,j}^{-} C_i \quad (7\text{-}1)$$

The cluster dynamics code, Xolotl, is used to solve this system of ODEs using the finite difference method and implicit time integration with PETSc [119]. The implementation of each of the terms in Eq. (7-1) will be discussed in the following sections, and related to the specific α-Zr system. In this Chapter, we will build the model to consider vacancy a-loops and interstitial a-loops only; basal clusters will not be incorporated until Chapter Eight. The CD model introduced in this chapter will thus be focused on the low-to-moderate fluence behavior of irradiated α-Zr. Once this has been successfully achieved, the model will be expanded in Chapter Eight to address c-loop nucleation and growth.

7.1 Incorporating our database into the CD model

7.1.1 Description of defect clusters and their properties

Interstitial clusters, denoted as "I_n" for a size of n, are considered mobile in the size range of 1 < n < 5. Small interstitial clusters assume basal-plane configurations and are highly anisotropic, sluggish diffusers. Vacancy clusters, denoted as "V_n", are considered mobile in the size range of 1 < n < 6. Small vacancy clusters assume 3-dimensional configurations and their anisotropy of diffusion varies with configuration. For the selected system temperature, the diffusivity within the basal plane (D_i^a) and along the c-axis (D_i^c) of each cluster are calculated with Eq. (7-2) using the data in Table 5-2 and Table 5-3. Based on these two diffusivity values, a mean diffusivity is calculated ($\overline{D}_i$, Eq. (7-3)) along with the anisotropy factor of diffusion (p, Eq. (7-4)). While MD simulations in pure Zr do indicate that larger defect clusters exhibit rapid 1-D migration, the thermal mobility of these loops are lower than expected in irradiated bcc Fe [181]. Instead, these larger clusters appear to "hop" to produce rapid translations in between long periods of immobility [182-184]. Incorporating this behavior in a CD framework would require a trap-mediated model to account for ballistic detrapping events [182]; for this work, these cluster will be considered immobile, although future models could expand the framework here to include such behavior.

$$D_i(T) = D_0 \exp\frac{-E_m}{k_b T} \quad (7\text{-}2)$$

$$\overline{D}_i = \left(D_i^{a\,2} D_i^c\right)^{\frac{1}{3}} \quad (7\text{-}3)$$

$$p = \left(\frac{D_i^c}{D_i^a}\right)^{\frac{1}{6}} \quad (7\text{-}4)$$

I_n and V_n clusters with n < 13 are assumed to be small enough to calculate their radii through a spherical approximation (Eq. (7-5)). I_n and V_n clusters with n ≥ 13 are considered to be a-type dislocation loops with PPI habit planes; their radii are calculated based on their disk-like shape with Eq. (7-6). Because these dislocation loops have distinct geometries, their capture efficiencies, $P(\lambda)$, for mobile defects must be calculated with Eq. (7-7) [110]. The ellipticity, e, is approximately 0.95 and 0.80 for interstitial and vacancy a-loops, respectively [17]. Elliptical a-loops are extended along the c-axis; the greater the ellipticity, the higher the bias for capture of basal-plane diffusers. Values for $P(\lambda)$ will be the same for loops with equal ellipticity factors, but depends upon the anisotropy factor of diffusion of the mobile defect being captured. The general dependence of $P(\lambda)$ on p is demonstrated in Fig. 2-3.

$$r_n = \left(\frac{3n\Omega}{4\pi}\right)^{\frac{1}{3}} \quad (7\text{-}5)$$

$$r_n^{prism} = \sqrt{\frac{acn}{2\pi}} \quad (7\text{-}6)$$

$$P^{loop}(\lambda) = \frac{p^{-2}\int_0^{\pi/2}\left(1 - f(\Theta) + p^6 f(\Theta)\right)^{\frac{1}{2}}(1 - e^2\,sin^2\,\Theta)^{\frac{1}{2}}\,d\Theta}{a\int_0^{\frac{\pi}{2}}(1 - e^2\,sin^2\,\Theta)^{\frac{1}{2}}\,d\Theta} \quad (7\text{-}7)$$

7.1.2 Defect generation (g_i)

Volumetric defect generation rates are calculated with Eq. (2-2) based on the number of PKAs produced per second with energy E, $\phi(E)$, and the number of defects produced per displacement cascade of energy E, $N_i(E)$. The former quantity is estimated based on the expected Zr PWR energy spectrum produced by typical PWR operating conditions (Fig. 2-1) [106]; the latter quantity is based on the displacement cascade data tabulated in Table 4-4 and Table 4-5 considering electronic stopping. The volumetric generation rates have been plotted in Fig. 4-9 and are directly inputted into the CD model. The dpa rate estimated by SPECTRA PKA is 8.93×10^{-8} dpa/s, and this value is used to convert simulation time into dpa for the plots in this work. The relationship between neutron fluence and dpa is based on the estimation of Carpenter et al. [4]:

$$1.14x10^{25}\ n/m^2\ (E > 1MeV) = 1\ NRT\ dpa \quad (7\text{-}8)$$

7.1.3 Defect absorption at pre-existing dislocation line sinks

Two types of dislocation lines are considered: 1) a-type lines that lie on PPI planes ($\lambda = 0°$) and 2) c-type lines that lie on basal planes ($\lambda = 90°$). The total sink strength for absorption of mobile cluster *i*, k_i^2, is a summation of the sink strengths for these two line types ($k^{a}{}_i^2$ and $k^{c}{}_i^2$, respectively). The line densities for pre-existing a-type and c-type dislocation lines were based on single crystal Zr estimates: 7.25x10^6 cm^{-2} and 2.25x10^6 cm^{-2}, respectively [165]. The elastic bias for absorption, Z_i, is considered to be 1.1 for interstitials and 1.0 for vacancies [46, 98, 99]. Each type of dislocation line have also been assigned an anisotropic capture efficiency for absorption (Eq. (2-4)) based on the anisotropy factor of diffusion for the captured defect *i,* which equals *p* for c-type dislocation lines and p^{-2} for a-type dislocation lines:

$$k_i^2 = k^{a}{}_i^2 + k^{c}{}_i^2 \qquad (7\text{-}9)$$

$$k^{a}{}_i^2 = Z_i \rho_d^a \cdot P(\lambda = 0°) = Z_d^i \rho_d^a \cdot p^{-2} \qquad (7\text{-}10)$$

$$k^{c}{}_i^2 = Z_i \rho_d^c \cdot P(\lambda = 90°) = Z_d^i \rho_d^c \cdot p \qquad (7\text{-}11)$$

7.1.4 Clustering reactions

There are three broad categories of reactions between two clusters *i* and j: 1) reactions that result in cluster growth ($I_i + I_j \rightarrow I_{i+j}$; $V_i + V_j \rightarrow V_{i+j}$); 2) reactions that result in cluster shrinkage ($I_i + V_j \rightarrow I_{i-j}$, $V_i + I_j \rightarrow V_{i-j}$); and 3) reactions that result in cluster annihilation ($I_i + V_j \rightarrow \emptyset$). For clusters with size n < 13, the reaction rate constant is based on a spherical reaction volume defined by the interaction distance, r_{ij}:

$$k_{ij}^+ = 4\pi r_{ij}\left(\overline{D}_i + \overline{D}_j\right) \qquad (7\text{-}12)$$

$$r_{ij} = r_i + r_j + r_{ij}^0 \qquad (7\text{-}13)$$

The value of r_{ij}^0 is set equal to 6.45x10^{-8} cm such that the value of the point defect recombination radius, r_{iv}, equals the commonly implemented value of 1.0x10^{-7} cm [98-101]. Cluster with n ≥ 13 are considered to have dislocation loop geometries, and the reaction rate constant is smoothly transitioned between spherical and toroidal kinetics. The toroidal contribution to the rate constant is multiplied by the anisotropic capture efficiency of the loop (Eq. (7-7)) to account for the loop geometry. For a loop *i* interacting with a mobile defect *j* [113, 114]:

$$k_{ij}^{+}, loops = \left(\left(1-\alpha_{ij}\right)z_{ij}^{T}\cdot P^{loop}(\lambda)+\alpha_{ij}z_{ij}^{S}\right)\left(\overline{D}_i+\overline{D}_j\right) \quad (7\text{-}14)$$

$$\alpha_{ij}=\left(1+\left(\frac{r_i}{3\left(r_j+r_d\right)}\right)^2\right)^{-1} \quad (7\text{-}15)$$

$$z_{ij}^{S}=4\pi(r_i+r_j+r_d) \quad (7\text{-}16)$$

$$z_{ij}^{T}=\frac{4\pi^2 r_i}{\ln(1+8r_i/(r_j+r_d))} \quad (7\text{-}17)$$

The value of the loop capture radius, r_d, can be based on either spontaneous or thermal drift capture. For spontaneous capture radii, discrete values are available in Table 6-1 and power-law fits to extrapolate to all cluster sizes are available in Fig. 6-10. These capture radii are temperature-independent. Conversely, thermal drift radii must be calculated at the selected system temperature using the constants in Table 6-3 with the temperature-dependent expression:

$$r_d^{thermal}=\alpha_d\left(\frac{T_m}{T}\right)^{m_d} \quad (7\text{-}18)$$

where T_m is the melting temperature of Zr (2128K). Once these thermal drift radii have been calculated at the temperature of interest, a power-law expression can be fit to extrapolate to all cluster sizes, as has been demonstrated at 573K in Fig. 6-11.

7.1.5 Cluster dissociation

In this model, we assume that clusters can only emit monomers of the same type ($I_n \rightarrow I_{n-1}+I_1$; $V_n \rightarrow V_{n-1}+V_1$). All clusters I_n and V_n are able to dissociate for n ≥ 2. The reaction rate constant can be calculated as a function of the cluster binding energy, and the rate constant for the reverse reaction ($I_1+I_{n-1} \rightarrow I_n$;):

$$k_{n,1}^{-}=\frac{k_{1,n-1}^{+}}{\Omega}\exp\frac{-E_{n,1}^{b}}{k_b T} \quad (7\text{-}19)$$

The binding energy of a monomer *i* to a cluster of size *n* can be estimated based on the difference in formation energies between the products and reactants. The formation energies for a cluster of size *n* have been fit to relevant power-law expressions:

$$E_{SIA}^{f}=\begin{cases}2.8n^{0.81}, & 2\le n\le 7\\ 4.6n^{0.66}, & n>7\end{cases} \quad (7\text{-}20)$$

$$E_{V,PPI}^{f} = \begin{cases} 1.9n^{0.84}, & 2 \leq n \leq 18 \\ 3.4n^{0.70}, & n > 18 \end{cases} \quad (7\text{-}21)$$

The binding energy is then calculated as:

$$E_{n,i}^{b} = E_{i}^{f} - A(n^{m} - (n-1)^{m}) \quad (7\text{-}22)$$

7.1.6 Overview of assumptions in the model

A considerable database allowing the parameterization of key mechanisms related to defect production, transport, and interaction is now available to inform a CD model; these parameters are summarized in Table 7-1. The primary goal of this work is to directly implement this data when possible in order to reduce assumptions and produce a physically-relevant CD model. Nevertheless, a few simplifying assumptions are made to reduce the complexity of the model for this first iteration. Each of these points can be improved upon in future work by expanding the framework proposed here. The four main assumptions are:

1) Defects are randomly and uniformly distributed (0-D)
2) Dislocation loops are considered immobile
3) Only monomers can be emitted during dissociation events
4) Dislocation line densities do not evolve with fluence

Of these four assumptions, the first is certainly the one which disagrees the most with experiments. Vacancy a-loops are known to align on ordered basal sheets as fluence increases [17, 18, 173]. Such spatial ordering is likely to reduce the incoming SIA flux for defects in these basal bands, and such a phenomenon may be important for breakaway irradiation growth [20, 26]. This work intends to implement foundational physics in a CD framework, and a reduced complexity is preferred as a proof of concept. Xolotl is fully capable of extending systems to 1-, 2-, or 3-D and allows a clear avenue for future work. As for the second assumption, it has been shown experimentally that dislocation loops are far less mobile than MD simulations would imply [159, 182, 184]. Trap-mediated diffusion would need to be accounted for to include this behavior in the model [182]. Assumption three is valid, as the binding energy of larger defects increases rapidly with size (Fig. 5-6). Finally, assumption four is unlikely to have a large effect considering that a-loop and c-loop number densities rapidly dwarf those of dislocation lines [98, 99].

For this article, we specifically attempt to model neutron-irradiated single crystalline Zr in order to compare with the irradiation growth behavior reported by Carpenter et al. [3, 4]. Thus, grain boundary sinks are ignored. Furthermore, there is no alloying content in this current model; future work must consider alloying effects to predict Zr alloy growth behavior.

Table 7-1. CD model parameters to describe microstructural evolution in neutron-irradiated single-crystalline Zr. The tables or figures for which critical parameters can be found are referenced.

Description	Symbol	Value	Source/Reference
Diffusion within the basal plane	D_i^a	Varies based on Eq. (7-2)	Tables 2,3 in [159]
Diffusion along the c-axis	D_i^c	Varies based on Eq. (7-2)	Tables 2,3 in [159]
Anisotropy factor of diffusion	p	Varies based on Eq. (7-4)	[46]
Anisotropic capture efficiency for dislocation lines	$P(\lambda)$	Varies based on Eq. (2-4)	[46]
Anisotropic capture efficiency for dislocation loops	$P^L(\lambda)$	Varies based on Eq. (7-7)	[46, 110]
Loop ellipticity	e	Vacancy a-loops: 0.80 Interstitial a-loops: 0.95	[17]
Atomic volume	Ω	23.4 Å^3	[37]
Volumetric defect generation rate	g_i	Varies for each cluster (Fig. 4-9)	Tables 4,5 in [9]
a-type dislocation line density	ρ_d^a	Single crystal: 7.25x10^6 cm^{-2}	[101, 165]
c-type dislocation line density	ρ_d^c	Single crystal: 2.25x10^6 cm^{-2}	[101, 165]
SIA/dislocation line elastic bias	Z_d^i	1.1	[46, 98]
Vacancy/dislocation line elastic bias	Z_d^v	1.0	[46, 98]
Spontaneous interaction distance for spherical clusters	r_{ij}^0	6.45x10^{-8} cm	Based on r_{iv} in [98-100]
Spontaneous dislocation loop capture radius	r_d	Varies for each cluster (Table 6-1)	Not yet published
Thermal drift dislocation loop capture radius	r_d^{th}	Varies for each cluster (Eq. (7-17), Table 6-3)	Not yet published
Cluster binding energy	$E_{n,i}^b$	Varies for each cluster (Eq. (7-22))	[159]
Dpa rate for neutron irradiation	$-$	8.93x10^{-8} dpa/s	SPECTRA-PKA [106]
Neutron fluence corresponding to 1 dpa of the NRT standard dose	$-$	1.14x10^{25} n/m^2	[4]

7.2 Expected a-loop characteristics from experiments

Table 7-2 summarizes a-loop number densities, mean diameters, and the relative percent of interstitial to vacancy a-loops for a range of temperatures in pure and alloyed Zr. There are quite a few factors that simultaneously affect a-loop characteristics. An increase in irradiation temperature results in loop coarsening, reducing the loop number density and increases the average loop diameter. A similar effect is noted for an increase in the neutron fluence at any given temperature. For example, between a fluence of $3.8x10^{23}$ n/m^{-2} and $1.3x10^{25}$ n/m^{-2} at 573 K (pure Zr), average a-loop diameters increase from 9 nm to 18.6 nm with a corresponding decrease in their number densities. It is therefore necessary to consider the particle fluence when comparing a-loop characteristics in order to drive a fair discussion for trends. When considering the relative fraction of interstitial to vacancy a-loops, it is clear from experiments that there is a greater fraction of interstitial loops at lower temperatures; the reverse is true at higher temperatures. It is unclear why exactly this would be the case, but it may be related to the production bias of mobile defects. At higher temperatures, immobile vacancy clusters would have higher dissociation rates and produce a greater number of mobile vacancy defects, which may drive an enhanced vacancy a-loop growth [39, 41].

Perhaps most interesting is a comparison between the pure Zr and alloyed Zr behavior. The general trend evident from the data in Table 7-2 is that a-loops form with notably smaller diameters and higher number densities in alloyed Zr. It is unclear what mechanism is driving this change in a-loop formation, but two possibilities may include: 1) solute interaction with mobile defects and 2) solute screening of dislocation loop strain fields. *Ab initio* calculations have demonstrated an attractive binding energy of Nb to Zr SIAs [185, 186]. A similar binding behavior has been replicated by MS calculations, resulting in reduced SIA diffusivities in MD simulations [30, 187, 188]. A reduction in defect mobility could be correlated to reduced a-loop sizes in an analogous manner to lower-temperature irradiation conditions. Additionally, APT and EDS analyses indicate a strong tendency for Fe, Cr, Ni, and Sn to segregate to dislocation structures [20, 63]. Similar behavior has been reported with molecular statics calculations of Ni and Fe segregation to a-loops [31, 61]. It is not unreasonable to assume that this behavior could result in strain field screening. As was shown in Chapter Six, long-range capture of defects is directly correlated to the stress imparted on the surrounding matrix, and any alteration of this stress state could change the defect capture behavior of dislocation loops.

A physically-relevant CD model should be able to capture the a-loop characteristic trends discussed in this section. For this work, we focus on the lower-temperature irradiation data for pure Zr in order to reduce the phase space requirements when testing the model. In particular, we attempt to benchmark our model predictions against the two data points at 573K: the low-fluence $3.8x10^{23}$ n/m^{-2} (0.033 dpa) data reported by Jostsons et al. [17] and the high-fluence $1.3x10^{25}$ n/m^{-2} (1.15 dpa) data provided by Gilbert et al. [29]. The a-loop size distribution histograms reported in these two works are

Table 7-2. Experimental data of a-loop characteristics in neutron-irradiated α-Zr.

	Temperature	Neutron fluence	Loop Density	Mean Diameter	Interstitial Loops	Ref.
Pure Zr	573 K	3.8×10^{23} m^{-2}	1.2×10^{22} m^{-3}	9 nm	-	[17]
		1.3×10^{25} m^{-2}	5.0×10^{21} m^{-3}	18.6 nm	-	[29]
	623 K	2.0×10^{23} m^{-2}	8.0×10^{20} m^{-3}	<10 nm	-	[17]
		5.3×10^{23} m^{-2}	2.7×10^{21} m^{-3}	23 nm	47 – 63 %	[17]
	668 K	3.3×10^{23} m^{-2}	7.0×10^{20} m^{-3}	33 nm	23 – 33 %	[17]
		6.4×10^{23} m^{-2}	2.0×10^{20} m^{-3}	65 nm	9 – 33 %	[17]
		18.0×10^{23} m^{-2}	2.0×10^{20} m^{-3}	>62 nm	37 – 55 %	[17]
	673 K	3.3×10^{23} m^{-2}	7.0×10^{20} m^{-3}	33 nm	-	[194]
		1.0×10^{25} m^{-2}	8.5×10^{20} m^{-3}	54 nm	32 %	[16]
		1.2×10^{25} m^{-2}	5.0×10^{20} m^{-3}	50 nm	53 %	[29]
	723 K	1.3×10^{25} m^{-2}	1.0×10^{18} m^{-3}	-	-	[195]
Zircaloy-2	523 K	3.1×10^{24} m^{-2}	2.9×10^{22} m^{-3}	8.6 nm	-	[18]
	553 – 603 K	1.0×10^{25} m^{-2}	1.5×10^{21} m^{-3}	5 nm	-	[20]
	573 K	1.3×10^{25} m^{-2}	1.9×10^{22} m^{-3}	6.5 nm	-	[29]
	615 K	1.0×10^{25} m^{-2}	2.6×10^{22} m^{-3}	8.7 nm	-	[18]
	673 K	1.2×10^{25} m^{-2}	2.8×10^{20} m^{-3}	60 nm	-	[29]
		1.0×10^{25} m^{-2}	6.2×10^{21} m^{-3}	20.1 nm	33 – 45 %	[18]
Zr-2.5Nb	573 K	1.3×10^{25} m^{-2}	-	7.0 nm	-	[29]
	673 K	1.2×10^{25} m^{-2}	-	37 nm	-	[29]

provided in Fig. 7-1(a) and Fig. 7-1(b). At 0.033 dpa, we therefore expect a narrow distribution of a-loops with a mean diameter of 9 nm ($1.2x10^{22}$ m^{-3} density), and at 1.15 dpa, we expect a wide distribution of a-loops with a mean of 18.6 nm ($5x10^{21}$ m^{-3} density).

7.3 Incremental implementation of physics into the CD model

The CD model proposed here incorporates a wide range of robust physics that has often been neglected or simplified. For example, cluster dissociation is ignored in many recent modeling attempts [96, 97, 101] or is only included for di-interstitials [100]. Despite simulating neutron irradiation, most models only consider point defect creation [96, 97, 99, 101] or only consider small SIA cluster formation, but with unreasonably low clustering fractions [100]. Point defect diffusion is often wrongly assumed to be isotropic [96, 97], or only single SIAs are assumed to migrate anisotropically [99-101]. In addition to these unphysical assumptions, these models often used assumed or manually adjusted values for important parameters such as defect diffusivities.

In Section 7.3.1, we will detail the common assumptions and input parameters that have been implemented in recent modeling attempts and apply these to our CD model. Once it is demonstrated that these parameters and assumptions cannot accurately predict known microstructure evolution in irradiated Zr, the robust physics dataset detailed in Table 7-1 will be introduced to the CD model incrementally. As such, the effect of each of the physical parameters will be showcased individually. In Section 7.3.4, the CD model predictions with all of the physics included will be shown. Finally, a key modification to the defect production rates will be outlined in Section 7.3.5 to account for cascade overlap effects. The intent of Section 7.3 is to demonstrate the importance of scale-bridging computational modeling to develop more accurate mechanistic models for microstructural evolution.

7.3.1 Reproducing past literature results using commonly assumed inputs

Common assumptions and input values in past literature include:

1. Only point defects are produced by neutron damage at the NRT standard rate ($G = 10^{-7}$ dpa $s^{-1} = 4.3x10^{15}$ point defects $s^{-1}cm^{-3}$) [98-101].
2. Clusters do not dissociate [96, 97, 101].
3. Defect clusters are immobile [96-99, 101].
4. Single interstitials diffuse with a manually adjusted value of $\overline{D}_i = 10^{-6} cm^2 s^{-1}$ and an assumed anisotropy factor of p = 0.765 [98-101].
5. Monovacancies migrate isotropically with a manually adjusted value of $D_v = 3.0x10^{-17} cm^2 s^{-1}$ [98-101].

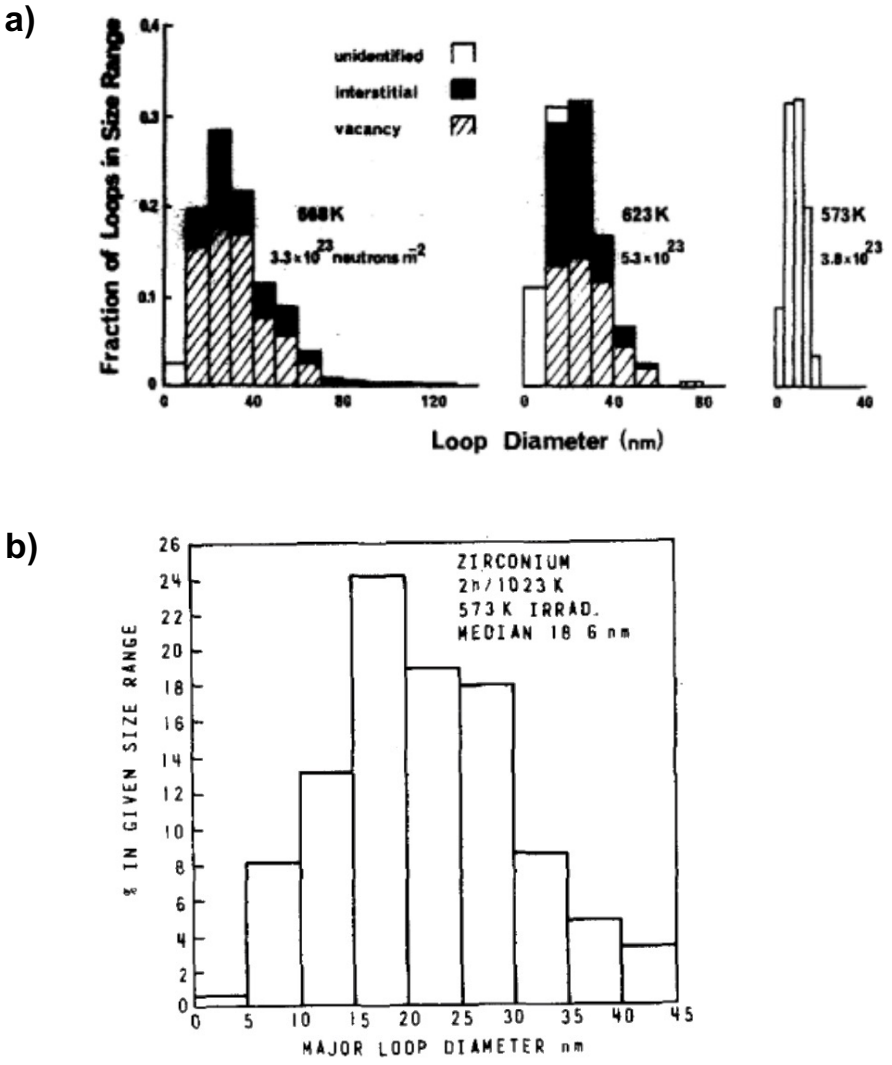

Fig. 7-1. Dislocation a-loop size distribution histograms reported by a) Jostons et al. for a range of temperatures between 573K and 668K [17]; b) Gilbert et al. at 573K [29].

In order to demonstrate how well these assumptions and parameters represent the underlying mechanisms of irradiation damage evolution, we incorporated these values into the CD framework outlined in Section 7.1. We first demonstrate the CD model predictions of damage evolution based on these commonly assumed literature values in Fig. 7-2 (T = 573K). In agreement with past literature [98-101], the point defect concentrations diverge at low fluence and eventually saturate at ~1.0 dpa. The difference in point defect saturation concentrations is driven by the considerable discrepancy in their diffusivities ($\overline{D}_i = 10^{-6} cm^2 s^{-1}$, $D_v = 3.0x10^{-17} cm^2 s^{-1}$). Monovacancies are largely unable to interact with surrounding sinks until their concentrations grow large enough to compensate for the low interaction rates. The effect that this has on dislocation a-loop evolution with fluence is clear in Fig. 7-2(b); that is to say, vacancy a-loops do not nucleate or grow! This behavior has been reported in literature with past CD models [99], and due to the difficulty in simultaneous growing vacancy and interstitial a-loops, vacancy a-loops are ignored in more recent modeling attempts [100-102]. It is known from experiments that vacancy a-loops form in both pure and alloyed Zr, and are even more abundant than interstitial a-loops for many irradiation conditions [13, 14, 17, 18, 29, 34, 173]. It is for this reason that we conclude that these common assumptions and parameter values should not be used in future modeling attempts, as they do not accurately produce a physically-relevant damage evolution profile. In the following sections, we will incrementally introduce the more robust dataset outlined in Table 7-1 to demonstrate the improvements to model predictions.

7.3.2 Effect of defect cluster generation rates based on MD data (g_i)

We first address the common assumption that only point defects are produced from neutron irradiation at the standard NRT rate. It is widely reported from MD simulations that the surviving fraction of the NRT-predicted number of defects is only a small percentage (~15-20%). Applying defect generation at the NRT standard rate corresponds to a sizeable over-estimation in the defect source term. Furthermore, a significant fraction (up to 40 – 60 %) of surviving defects are contained in defect clusters. In fact, even large dislocation loops can directly nucleate from high-energy cascade events [9, 12]. Therefore, the first improvement that we implement to the CD model is incorporating the volumetric defect generation rates presented in Fig. 4-9 [9]. Because the volumetric generation rates are based on MD cascade data, they inherently incorporate the NRT survival fraction of defects as well as defect clustering.

Fig. 7-3 shows the improvements to the defect evolution prediction when incorporating the volumetric generation rates rather than simply assuming point defect generation. With this one change alone, the difference is notable when comparing to Fig. 7-2. There are two main contributors to this behavior: 1) fewer point defects are produced due to in-cascade recombination and defect clustering ($\dot{g}_{1I} = 4.14x10^{14}\text{cm}^{-3}\text{s}^{-1}, \dot{g}_{1V} = 3.0x10^{14}\text{cm}^{-3}\text{s}^{-1}$ compared to $\dot{g}_{NRT} = 4.3x10^{15}\ \text{cm}^{-3}\text{s}^{-1}$) and 2) defect clusters up to a size

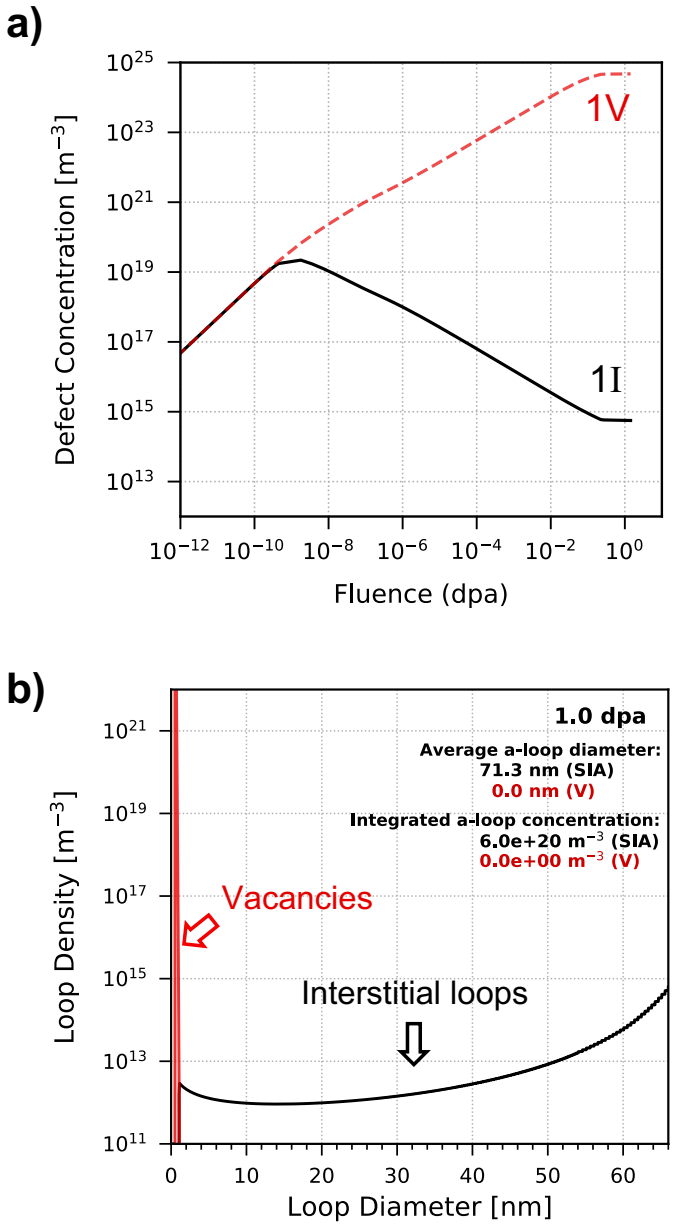

Fig. 7-2. CD model predictions at T = 573K for a) point defect concentrations as a function of fluence and b) vacancy and interstitial a-loop size distributions at 1.0 dpa when incorporating common assumptions and parameter values from literature.

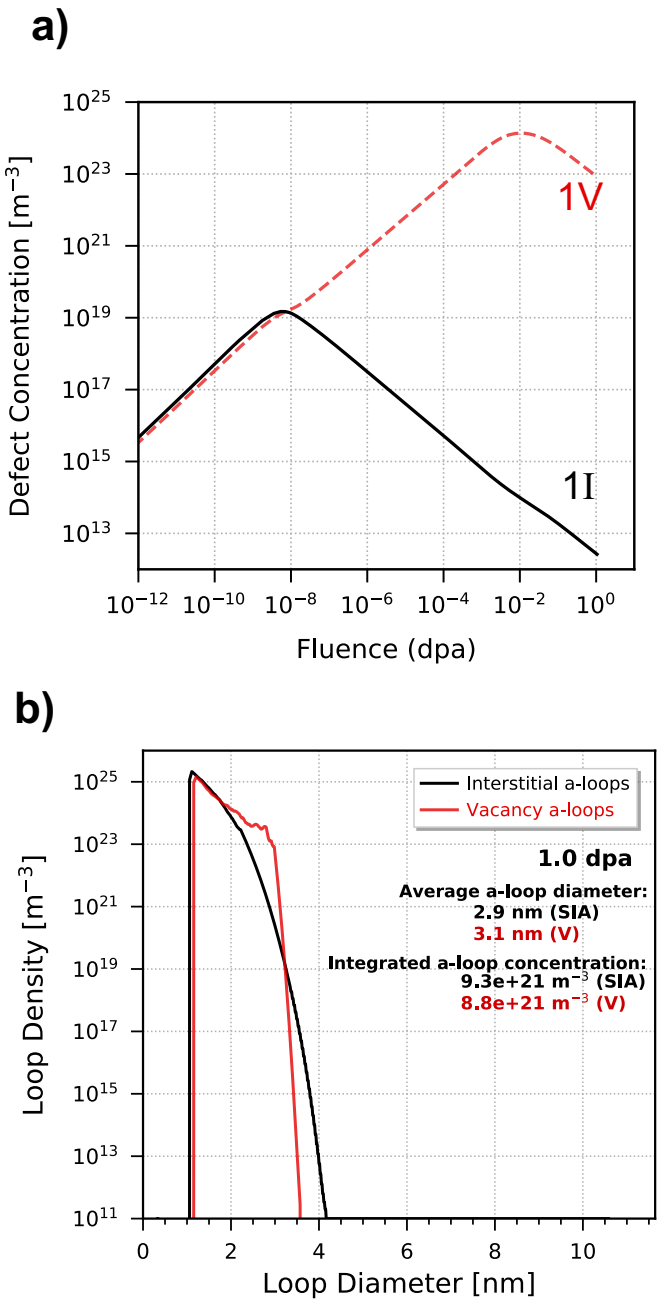

Fig. 7-3. CD model predictions at T = 573K for a) point defect concentrations as a function of fluence and b) vacancy and interstitial a-loop size distributions at 1.0 dpa when incorporating common assumptions and parameter values from literature. The simulation is modified from Fig. 7-2 by using the volumetric defect generation rates calculated with MD displacement cascade data (Fig. 4-9) rather than assuming simple point defect generation at the NRT standard rate.

of 70 defects are directly generated from cascades. These two factors assist in the nucleation of vacancy a-loops and reduce the growth of interstitial a-loops. The total concentration of mobile SIAs is overall reduced due to the higher density of available clusters to interact with.

7.3.3 Comparing dissociation rates for all defect clusters

The magnitude of the dissociation rate constant (Eq. (7-19)) is dependent on two factors: 1) the monomer binding energy to the parent cluster and 2) the forward rate constant for the inverse clustering reaction [105]. The former is calculated with Eq. (7-22) based on molecular statics calculations of defect cluster formation energies with the BMD19 potential (Fig. 5-9) [159]. The forward rate constant is calculated with Eq. (7-12) for spherical clusters and Eq. (7-14) for dislocation loops; both of these expressions depend directly on the diffusivity of the monomer being emitted from the cluster. As the diffusivity of the monomer decreases, the rate of dissociation correspondingly decreases; conceptually, a less mobile monomer is more likely to be re-captured by the cluster from which it was emitted. Thus, the dissociation rate constants have been compared in Fig. 7-4 for two different cases: 1) using the commonly-assumed values for point defect diffusivities in literature (dashed lines) and 2) using the diffusivities calculated through MD simulations with the BMD19 potential (solid lines).

When considering common literature values for point defect diffusivities, the dissociation rate constants for vacancy clusters are several orders of magnitude lower than equivalent interstitial clusters, despite the lower binding energies of vacancy clusters. Conversely, when performing the identical calculation with point defect diffusivities derived from MD simulations (Table 5-2 and Table 5-3), vacancy clusters show notably larger dissociation rates than interstitial clusters. This is now consistent with the concept of the production bias theory which relies on the thermal dissociation of vacancy clusters at higher temperatures to describe key irradiation phenomenon [39, 41]. It is clear that the manually adjusted value for monovacancy diffusion that is often used in modeling attempts is far too low to properly describe damage evolution behavior. The effect of the updated dissociation rates shown in Fig. 7-4 will be demonstrated in the following section with the implementation of MD-based point defect and defect cluster mobilities into the CD model.

7.3.4 Effect of point defect and defect cluster mobility

Defect mobility is incorporated into the CD model based on the parameter datasets in Table 5-2 for interstitials and Table 5-3 for vacancies which were calculated directly from MD simulations with the BMD19 potential [159]. The calculated diffusivities, anisotropy factors, and anisotropic capture efficiencies for interstitial and vacancy a-loops at T = 573K are tabulated in Table 7-3. Both types of point defects migrate with a preference for basal-plane diffusion ($p < 1$). Interstitial clusters are predominantly basal plane diffusers ($p << 1$)

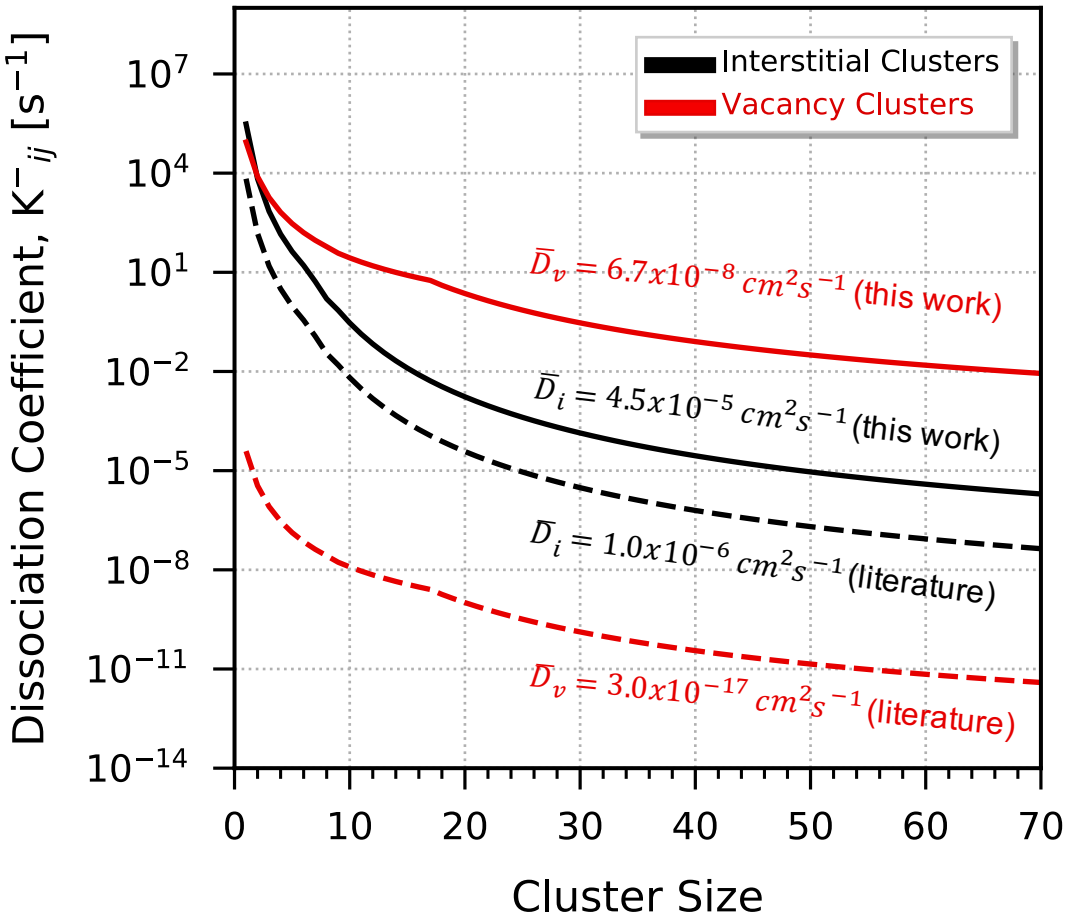

Fig. 7-4. Dissociation rate coefficients at T = 573K for interstitial clusters (black) and vacancy clusters (red) as a function of cluster size. Solid curves are based on calculations with the defect diffusivities in this work (Table 5-2, Table 5-3) while dashed curves consider common diffusivities that have been manually adjusted in literature [98-101].

Table 7-3. Mobile defect diffusivities and anisotropy ratios at T = 573K calculated based on MD data gathered with the BMD19 potential (Table 5-2, Table 5-3). The anisotropic capture efficiency for defect capture at interstitial a-loops, $P^{a,I}(\lambda)$, and vacancy a-loops, $P^{a,V}(\lambda)$, is also listed.

Mobile Species	$\boldsymbol{D^a}$ **(cm² s⁻¹)**	$\boldsymbol{D^c}$ **(cm² s⁻¹)**	$\boldsymbol{\bar{D}}$ **(cm² s⁻¹)**	$\boldsymbol{p}$	$P^{a,I}(\lambda)$	$P^{a,V}(\lambda)$
I_1	$7.8x10^{-5}$	$1.6x10^{-5}$	$4.6x10^{-5}$	0.77	1.3	1.4
I_2	$3.1x10^{-5}$	$4.8x10^{-7}$	$7.7x10^{-6}$	0.50	2.7	3.0
I_3	$2.5x10^{-6}$	$4.8x10^{-9}$	$3.1x10^{-7}$	0.35	5.4	6.1
V_1	$1.1x10^{-7}$	$3.0x10^{-8}$	$7.0x10^{-8}$	0.80	1.2	1.3
V_2	$2.2x10^{-7}$	$5.9x10^{-7}$	$3.1x10^{-7}$	1.17	0.95	0.90
V_3	$2.8x10^{-9}$	$2.0x10^{-9}$	$2.5x10^{-9}$	0.94	1.1	1.1
V_4	$9.9x10^{-6}$	$3.7x10^{-8}$	$1.5x10^{-6}$	0.39	4.3	4.8
V_5	$1.6x10^{-8}$	$1.6x10^{-5}$	$1.6x10^{-7}$	3.18	2.1	1.7
V_6	$2.1x10^{-8}$	$2.4x10^{-6}$	$2.2x10^{-6}$	1.03	1.0	0.98

while vacancy clusters generally migrate quasi-isotropically ($p \sim 1$) or with a preference along the c-axis ($p > 1$) depending on the cluster size. Mobile defects with low anisotropy factors will preferentially interact with prismatic a-loops; the lower the anisotropy factor, the stronger the bias for their capture at a-loops. In addition, vacancy a-loops are more elliptical than interstitial a-loops [17] and this results in an elongation of these loops along the c-axis. As a consequence, mobile defects with low anisotropy factors will have a greater bias for capture at vacancy a-loops than interstitial a-loops, as is seen in Fig. 2-3 and Table 7-3. The behavior described here is expected to play a considerable role in microstructure evolution in α-Zr. Furthermore, MD simulations (as well as *ab initio* calculations [49]) indicate that vacancy diffusion is much faster than has been assumed in previous models [98-101]. This is consistent with the "anomalous self-diffusion" and "facile vacancy migration" that has been coined based on Hood's experimental observations in α-Zr [50].

We first analyze the effect of cluster dissociation and defect mobility on the concentrations of point defects and small defect clusters in Fig. 7-5. The most notable differences are seen for monovacancies and vacancy clusters, for which the average defect concentrations are orders of magnitude lower than what was predicted using literature values for parameters. The reduction in monovacancy concentrations is predominantly driven by enhanced interaction with sinks and defect clusters as a result of the larger diffusivity ($\overline{D}_v = 7.0x10^{-8}$ cm^{-2} s^{-1} compared to $D_v = 3.0x10^{-17}$ cm^{-2} s^{-1} at 573 K). The reduction in vacancy cluster concentrations is driven predominantly by losses due to cluster dissociation rates (Fig. 7-4) which were originally negligible when using commonly assumed values for vacancy diffusivities. Mobile interstitial clusters observe a steady decline in their concentrations as they interact with surrounding sinks.

The effect of defect mobility on the dislocation loop evolution in α-Zr is highlighted in Fig. 7-6 when compared to Fig. 7-3. We now observe considerable interstitial loop growth and notable vacancy loop growth; the number densities of both types of loops are now in the range predicted by experimental data (Table 7-2). While the average loop diameters have also increased, they still fall below experimental predictions for T = 573 K at a dose of 1.15 dpa. For this irradiation condition, Gilbert et al. predict average a-loop diameters of 18.6 nm as seen in Fig. 7-1(b). It is worth noting that the dislocation capture radii are still considered to be zero for this calculation, and variations in this parameter can drive differences in the clustering reaction rates for these loops.

7.3.5 Effect of dislocation loop defect capture radii

The dislocation loop capture radii affects the sharpness of the transition between spherical and toroidal clustering kinetics (Eq. (7-15)) as well as the magnitude of the toroidal reaction rate (Eq. (7-17)). In Chapter Six, loop capture radii were calculated with two different analysis methods: spontaneous capture and thermal drift capture. Considering the spontaneous method, most dislocation loops observed biased capture of interstitials (Fig. 6-9); when considering the thermal drift method, an inherent bias was demonstrated for the

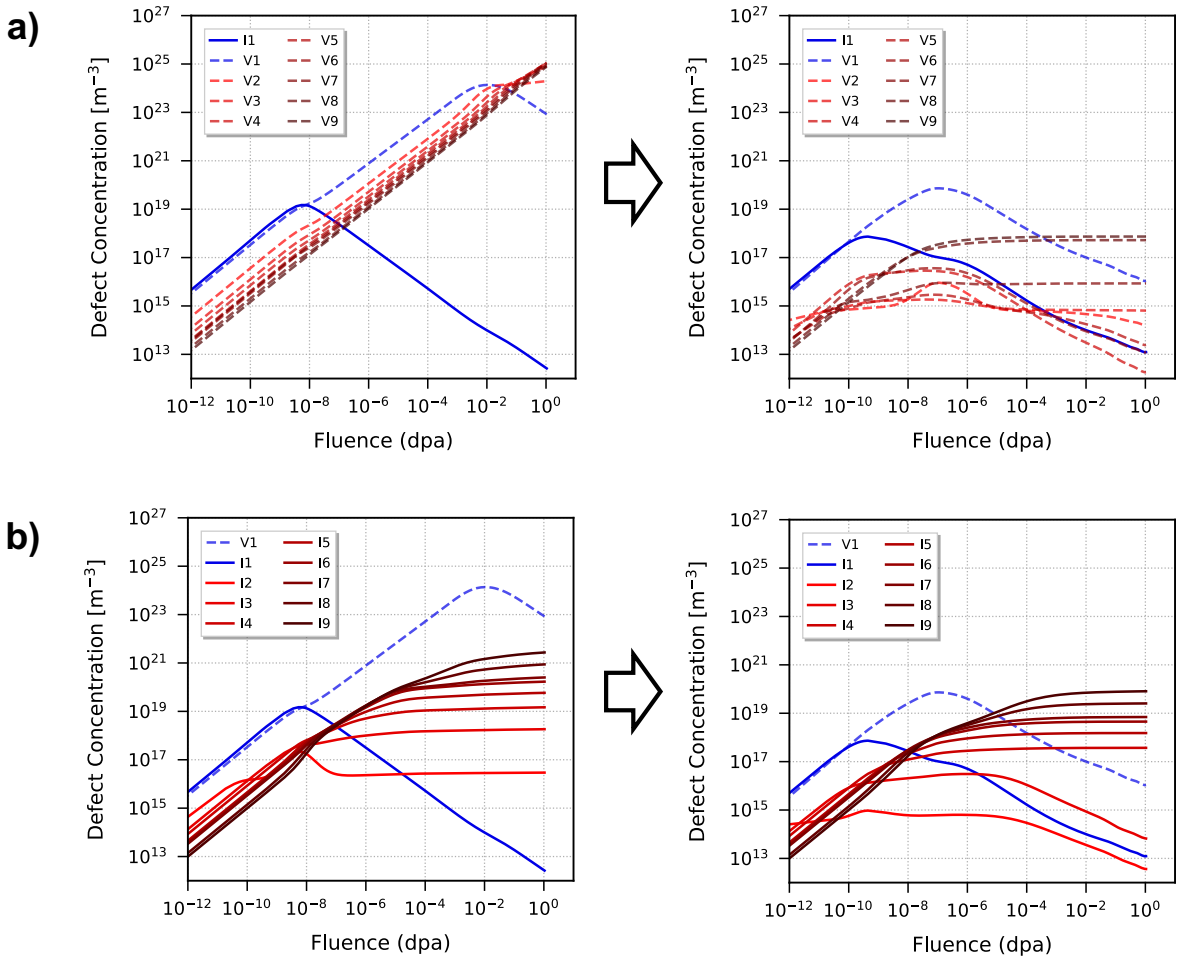

Fig. 7-5. Defect concentrations for a) vacancy and b) interstitial defects in the size range of $1 \leq n \leq 9$ is shown before and after incorporating cluster dissociation for all clusters and MD-based diffusivities at T = 573K.

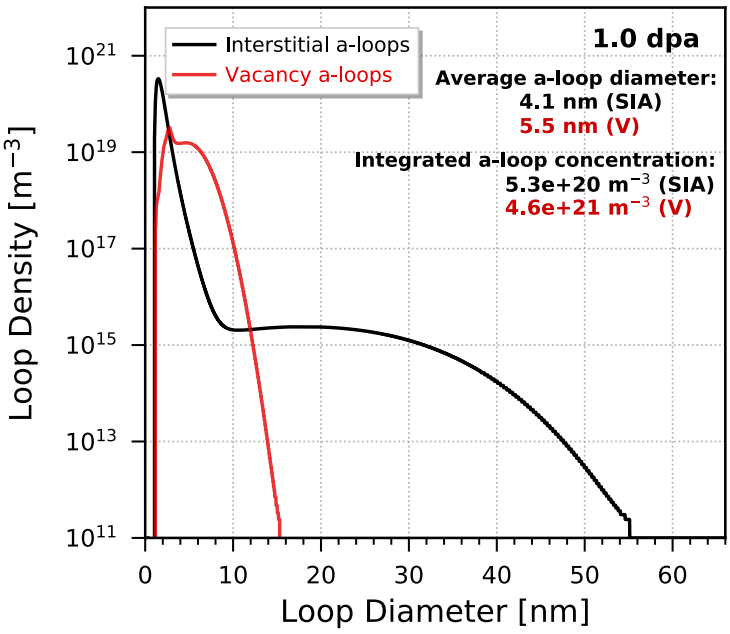

Fig. 7-6. CD model predictions at 573K for the cluster size distribution at 1.0 dpa after incorporating the volumetric defect generation rates, defect mobility, dissociation rates based on the dataset outlined in Table 7-1.

capture of same-type defects at dislocation loops (i.e. vacancy capture at vacancy loops). The effect that capture radii have on point defect reaction rates with interstitial and vacancy a-loops is demonstrated in Fig. 7-7 Interaction rates are compared for calculations that incorporate no capture radii ($r_d = 0$), spontaneous capture radii, and thermal drift capture radii, respectively. For the case with no capture radii, capture rates are simply based on the size of the loop as well as the size and mobility of the captured defect. When incorporating spontaneous radii into the calculation, the consequence is a general increase in the magnitude of the interaction rates due to the enhanced reaction volume. Because the spontaneous capture radii are similar for all dislocation loops for a given point defect, there is a slight bias for point defect capture at vacancy a-loops due to the anisotropic capture efficiency factor, as was discussed in Section 7.3.4. Conversely, thermal drift radii show a greater deviation depending on the type of captured defect and the type of loop. Due to the inherent bias for the capture of same-type defects, interaction rates are higher between single SIAs and interstitial a-loops and vice versa (Fig. 7-7(c)). This is a significant difference in the capture behavior between calculations with spontaneous and thermal drift radii.

The resultant size distribution of dislocation loops using spontaneous and thermal drift capture radii are given in Fig. 7-8(a) and Fig. 7-8(b), respectively. These simulations were performed with the full dataset outlined in Table 7-1. When incorporating spontaneous capture radii, the model predictions are similar to the case with no capture radii (Fig. 7-6). While the reaction rates are all larger in magnitude, the SIA bias for absorption at dislocation loops drives interstitial loop growth. The necessity for a mechanistic bias, then, is quite evident in order to drive simultaneous vacancy loop growth. One potential bias is inherent in the magnitudes of the thermal capture radii for same-type defects, and incorporating these values into the CD model results in the loop distributions seen in Fig. 7-8(b) at 1.0 dpa and T = 573K. For the first time reported in literature, simultaneous growth of interstitial and vacancy a-loops is predicted mechanistically. However, based on the experimental results of Gilbert et al. [29], the resulting a-loop number densities and diameters are still over-predicted.

7.3.6 Accounting for defect production saturation due to cascade overlap effects

The volumetric generation rates for defects (g_i) that were described in Section 7.3.2 and shown in Fig. 4-9 are based on the MD displacement cascade data overviewed in Chapter Four. These cascades are typically run in a pristine simulation box free of any pre-existing defects. As such, the defect generation data is only representative of very low doses for which defect concentrations remain dilute. It has been demonstrated recently in pure W that the reduction in thermal diffusivity saturates at a dose of ~0.1 dpa under continuous 20 MeV self-ion irradiation at room temperature [189]. When calculating the Frenkel Pair density

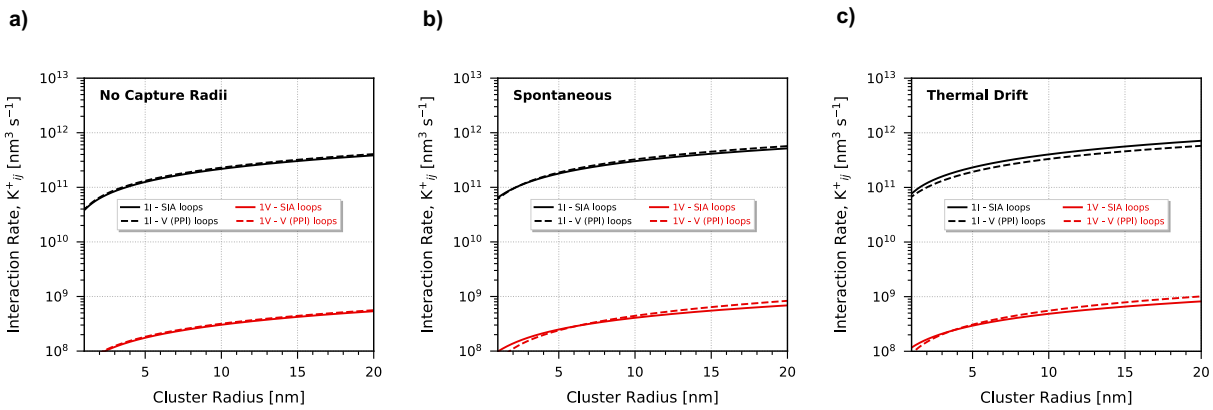

Fig. 7-7. Point defect interaction rates with dislocation loops as a function of the loop radius when calculated using a) no capture radii, b) spontaneous capture radii, and c) thermal drift capture radii.

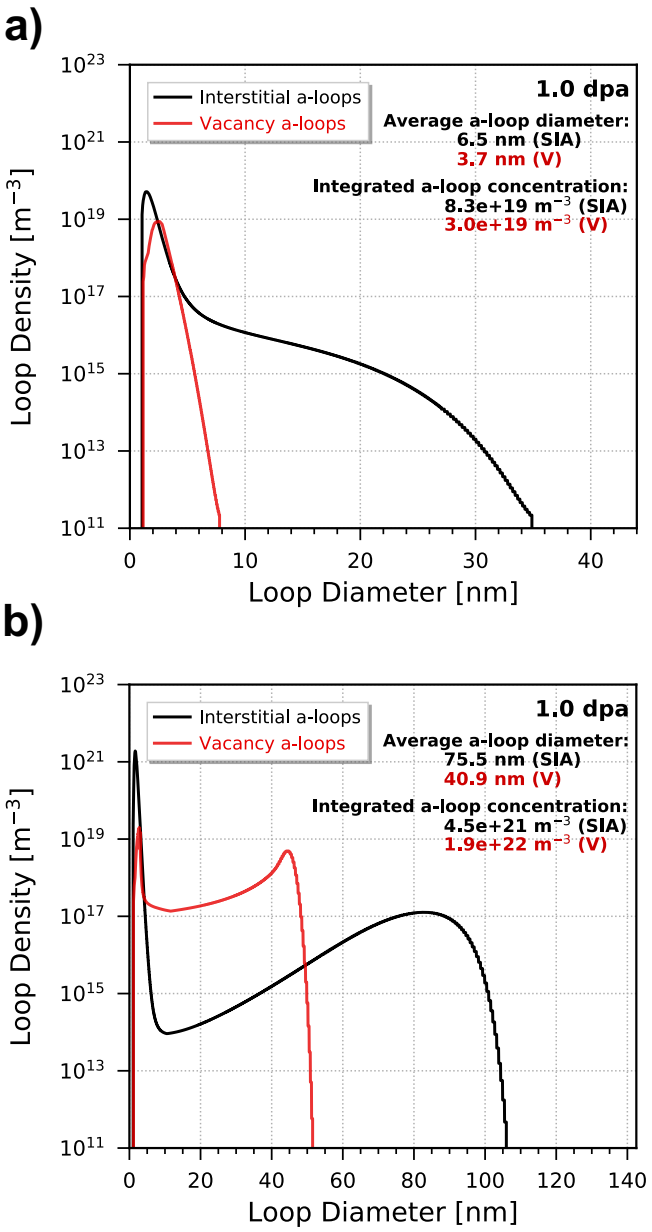

Fig. 7-8. CD model predictions at 573K for the cluster size distribution at 1.0 dpa using the full dataset and framework described in this work. These simulations were run using a) spontaneous capture radii and b) thermal drift capture radii, respectively.

correlated with the reduction in thermal diffusivity, it is clear that the defect fraction deviates from the expected behavior at ~0.005 dpa (Fig. 7-9). Consecutive MD displacement cascades were later performed in a single simulation box of pure W, and defect production was found to saturate when the defect density approached an atomic fraction of 0.004 below a dose of ~0.1 dpa due to cascade overlap effects [190]. In α-Zr, there is experimental evidence that the defect yield begins to saturate at some dose below ~0.1 dpa [191] and sequential displacement cascades predict defect production saturation at ~0.03 dpa [192]. It is therefore plausible to believe that the volumetric generation rates in a CD model should not remain constant as defect concentrations build up, and should instead begin to saturate at low dose.

Ideally, cascade overlap effects should be incorporated into the CD model in such a way that existing defect populations are affected by cascade events. This would require a robust implementation capable of tracking cluster growth or shrinkage, but the data required to adequately inform such an implementation has not yet been reported. As such, we have included cascade overlap effects in a simpler form: a reduction in the volumetric defect generation rates with increasing dose, d. The "effective" generation rates, $\dot{g}^*(d)$, are defined in terms of a cascade efficiency factor, $\eta(d)$, and the original volumetric generation rates, $\dot{g}$:

$$\dot{g}^*(d) = \dot{g} \cdot \eta(d) \quad (7\text{-}23)$$

$$\eta(d) = 1 - \tanh(C \cdot d) \quad (7\text{-}24)$$

The constant C controls the steepness of the hyperbolic curve with increasing dose. Three potential hyperbolic tangent fits are plotted in Fig. 7-10 to demonstrate their effects on microstructural evolution predictions: η_1, η_2, and η_3 which correspond to production saturation at 1.0, 0.1, and 0.01 dpa, respectively. The closest agreement with experimental data is found when implementing the η_2; this is fully consistent with the saturation dose estimated by various experimental and computational reports in literature for pure W and α-Zr [189-191]. As such, the η_2 fit was optimized to provide the best agreement between our CD model prediction of a-loop characteristics and those reported for neutron-irradiated single-crystalline Zr at 573K (Table 7-2). The optimized cascade efficiency curve is plotted in terms of NRT dpa and total defect concentration in Fig. 7-11(a) and Fig. 7-11(b), respectively. Here, total defect concentration is defined as the total number of Frenkel Pair defects, C_{FP}, in the system. The optimized curves for these two conditions are given, respectively:

$$\eta(d) = [1 - \tanh(3.05x10^{-6} \cdot d)\,] + 0.02 \quad (7\text{-}25)$$

$$\eta(C_{FP}) = [1 - \tanh(9.11x10^{-26} \cdot C_{FP})\,] + 0.02 \quad (7\text{-}26)$$

With the incorporation of the full dataset in Table 7-1 and the optimized defect

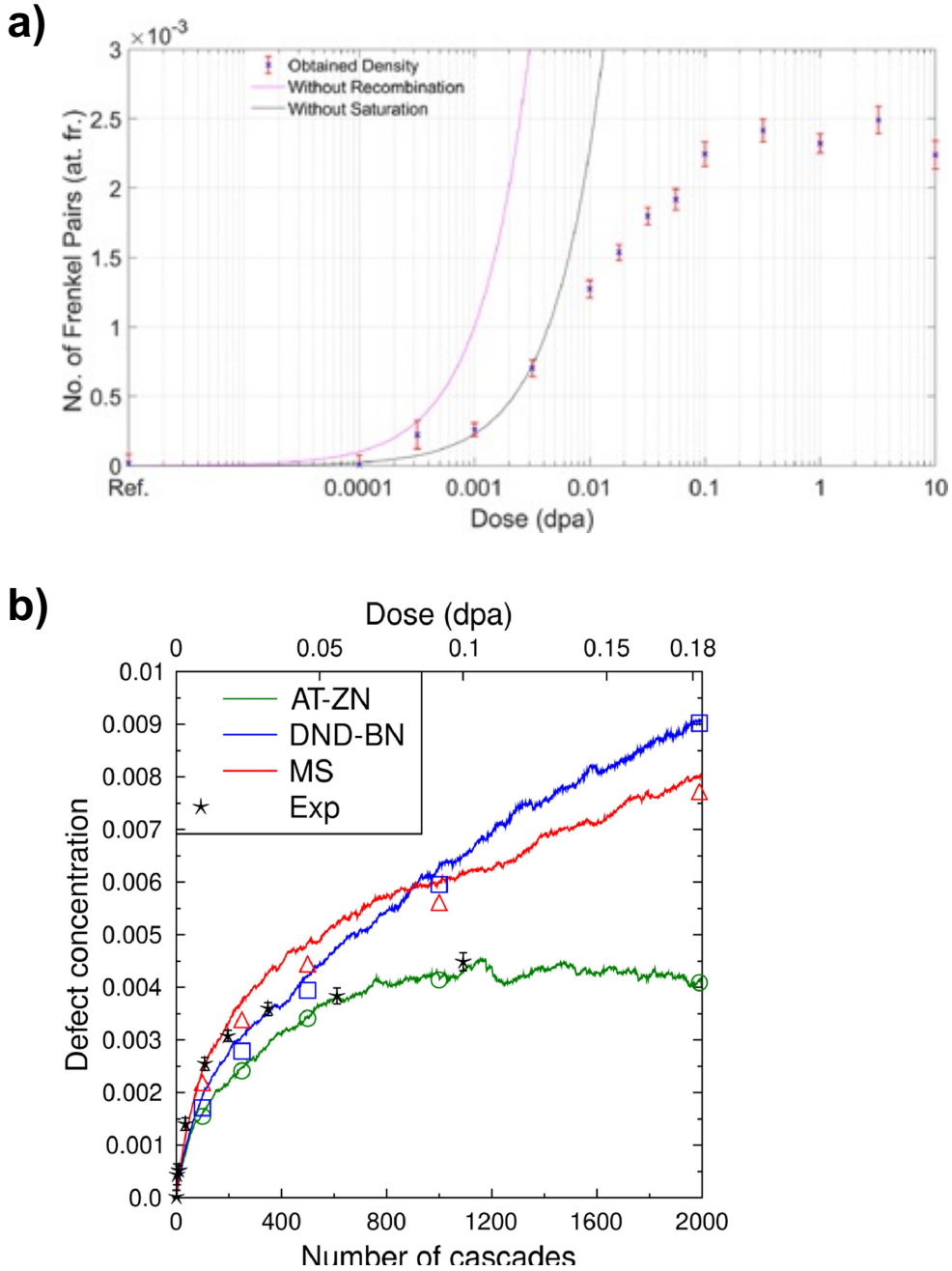

Fig. 7-9. Saturation of produced defects due to cascade overlap effects are predicted by a) thermal diffusivity experiments [189] and b) MD sequential displacement cascade simulations [190].

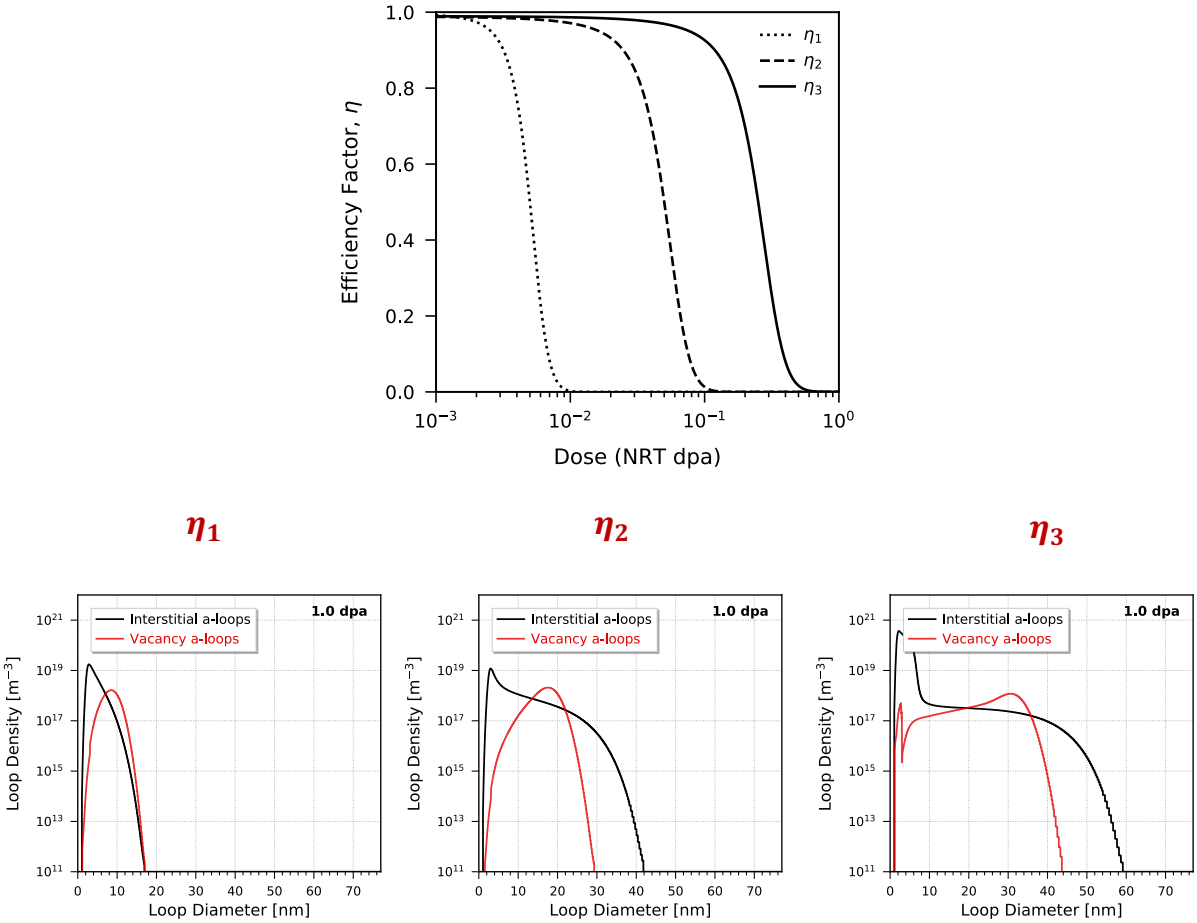

Fig. 7-10. Three representative curves are shown for the cascade efficiency parameter, η, which directly reduces the volumetric defect generation rates as a function of fluence. The resultant defect size distributions at 1.0 dpa are shown.

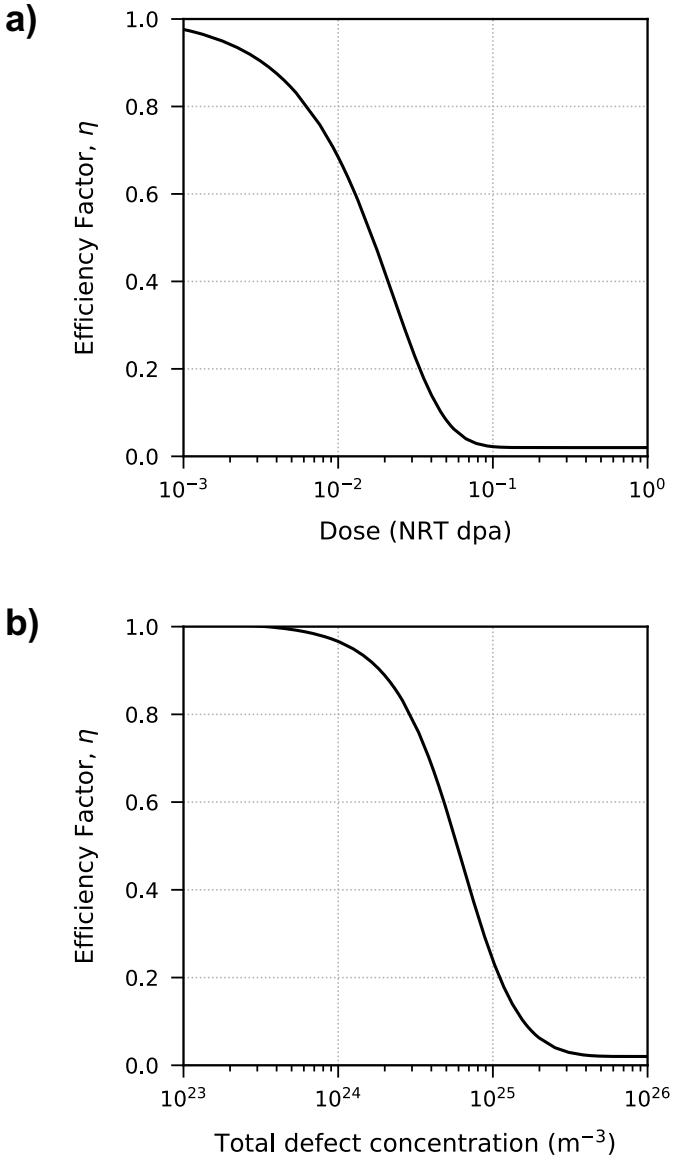

Fig. 7-11. Optimized cascade efficiency factor curve as a function of a) NRT dpa and b) total defect concentration.

generation rates accounting for cascade overlap (Eq. (7-23) and Eq. (7-25)), the dislocation loop distributions are shown in Fig. 7-12(a), Fig. 7-12(b), and Fig. 7-12(c) at 0.033, 1.15, and 3.0 dpa. Corresponding loop size distribution histograms are shown in Fig. 7-12(d), Fig. 7-12(e), and Fig. 7-12(f), respectively. The results at 0.033 dpa offer a direct comparison to the work of Jostsons et al. at 573K for which the average reported a-loop diameter and number density are 9 nm and $1.2x10^{22}$ m^{-3}, respectively [17]. Similarly, the results at 1.15 dpa offer a direct comparison to the work of Gilbert et al. at 573K for which the average reported a-loop diameter and number density are 18.6 nm and $0.5x10^{22}$ m^{-3}, respectively [17]. When considering average loop diameters and size distributions, our CD model agrees remarkably well with these two experimental reports. These doses are generally below the incubation dose for c-loop nucleation, so our model (which currently only considers a-type dislocation loops) should remain valid [13, 32-34]. One oddity of the current model is an over-prediction of a-loop number densities by a factor of ~2.5 at 1.15 dpa. We would expect from the trends observed in Table 7-2 that a-loops should coarsen with increasing neutron fluence and number densities should correspondingly decrease. The CD model proposed here accurately predicts a-loop coarsening, but the number densities only decrease slightly. Otherwise, the implementation of a wide range of informed physics has produced a surprising representation of microstructure evolution in α-Zr. In addition to predicting accurate a-loop size distributions, our CD model generates a near equal number of vacancy and interstitial a-loops. While the relative fraction of interstitial-to-vacancy a-loops is not reported at 573K, the general trend from higher-temperature irradiations suggests that an equal ratio should be expected.

7.4 Recommended future improvements to the CD model

The CD framework and dataset described in this work performs excellently for modeling microstructure evolution in neutron-irradiated pure Zr. There are, however, three critical areas that require future improvement: 1) basal c-loop nucleation and growth, 2) the effect of alloying elements and impurities, and 3) spatial dependence, including possible extension of the model to account for elastic interactions, of the defect cluster populations. The first of these areas for improvement will be addressed in the following chapter. As for the second area, it is clear that the presence of solute/impurities can influence the microstructure evolution behavior. Take for example the differences in a-loop characteristics for pure and alloyed Zr in Table 7-2. Furthermore, breakaway growth behavior appears to be strongly correlated with the solute content of various zirconium alloys [13, 32, 35, 43]. In order to incorporate solute effects into the model, we must first understand how exactly the solute modifies the fundamental mechanisms introduced here. For example, the migration of Fe-V complexes may be facilitated along the c-axis which would alter the anisotropy ratio of diffusion for the affected vacancies [57, 58]. Similarly, Nb binding with SIAs may restrict their migration and reduce their diffusivities [185, 188]. A larger database of lower-length scale data is needed to inform solute-driven mechanisms in

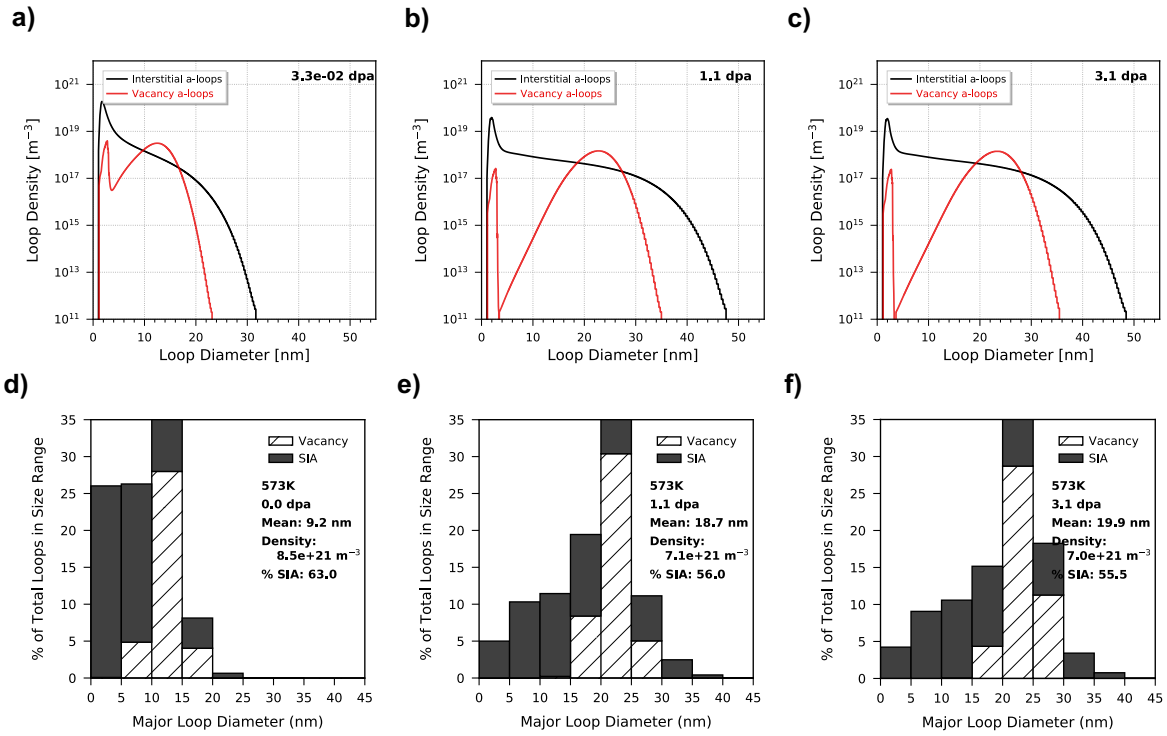

Fig. 7-12. CD model predictions at T = 573K for the cluster size distributions at a) 0.033 dpa, b) 1.15 dpa, and c) 3.0 dpa using the full dataset and framework described in this work. The corresponding loop size distribution histograms are given in d), e), and f) respectively. Cascade overlap effects on defect production saturation is incorporated for these simulations.

a CD approach. While this database is not currently available, future parametric studies with the CD model proposed here could indicate which parameters are the most likely to drive the differences in microstructure evolution in pure versus alloyed Zr.

Regarding the spatial dependence of defect clusters, the current CD model assumes that all clusters are randomly and homogeneously distributed. This obviously does not allow for known microstructure behavior such as vacancy a-loop banding [17, 173]. Incorporating spatial dependence of vacancy loops would have two hypothetical effects: 1) self-screening of SIA capture and 2) enhanced concentration of mobile vacancies within the ordered layers. As shown in Chapter Six, vacancy loops exhibit preferential capture of vacancies radial to the loop periphery. Thus, the biased vacancy capture volume would extend above and below the ordered bands of vacancy a-loops, producing an overall net bias for vacancy drift. Additionally, if vacancy clusters spatially order onto these basal sheets, dissociation events would lead to a local super-saturation of mobile vacancies compared with other areas in bulk Zr. It is possible that some or all of these effects may be responsible for the reported growth of vacancy c-loops within these ordered sheets [20], but future work would be needed to verify these hypotheses.

7.5 Summary and Conclusions

We have proposed a CD framework and outlined a robust dataset that is capable of accurately reproducing experimental a-loop characteristics in neutron-irradiated pure Zr. This includes the simultaneous growth of vacancy and interstitial a-loops in near-equal fractions, an aspect of irradiation microstructure that has never been successfully modeled before. This milestone highlights the strengths of scale-bridging computational modeling as a tool for understanding irradiation damage effects. Lower-length scale simulations have provided the necessary parameters to accurately model: 1) Production of defects from displacement cascades (including recombination and clustering); 2) dissociation rates for all clusters; 3) point defect and defect cluster mobility (including anisotropy); and 4) dislocation capture radii with spontaneous and thermal drift methods. The effect of each of these key aspects were highlighted and compared to literature-assumed values. While the proposed model over-predicts a-loop number densities at high dose, the results are fully consistent with reported a-loop diameters, size distributions, and relative fractions of interstitial-to-vacancy loops for two separate irradiation experiments at low and moderate dose. We recommend that the dataset and framework described here should be used and improved upon in future studies to further our understanding of irradiation effects in α-Zr.

Chapter Eight:

Cluster Dynamics Modeling of c-Loop Nucleation and Growth

While our original model can accurately represent low-to-moderate fluence irradiation (for which a-loops dominate the microstructure), high fluence irradiated microstructure is characterized by a high number density of faulted basal c-loops [6, 13, 32-34]. The nucleation of these faulted defects has been strongly correlated with the onset of breakaway irradiation growth [4, 36].

Despite the key role that these defects play in the growth phenomenon, there is a lack of consensus in the literature to describe why these defects only nucleate at high fluences. There is considerable evidence that solute species can reduce the incubation dose for breakaway irradiation growth, and can accelerate post-breakaway growth strains [13, 34, 35, 45, 54]. The *ab initio* calculations reported in Chapter Three strongly corroborate the hypothesis that solute segregate to nucleating c-loops and reduce their stacking fault energy [55]. However, the exact role of solute interactions and their role in breakaway growth remains ambiguous. For example, Sn reduces irradiation growth strains at low temperatures but increases growth at high temperatures [64]. Fe was originally believed to accelerate growth strains [35] but recent evidence suggests that Fe may suppress growth strains in certain alloys [56]. Other possible alternative factors for c-loop nucleation include helical climb on cold-work induced <c+a> network dislocations [36, 43, 44], vacancy a-loop banding [20], and temperature [33, 42, 44].

While considerable attention has been focused on Zr alloys or cold-worked material, it is important to note that breakaway growth (and, thus, c-loop nucleation) still occurs in single-crystalline high-purity Zr. As such, c-loops should be capable of nucleating without solute-based mechanisms or cold-worked induced microstructure; those factors should simply *accelerate* c-loop nucleation or growth. One recent theory in the literature is that c-loops do not form from the aggregation of vacancies onto a single basal plane as was originally thought [19, 37, 86]. Instead, faulted basal pyramids (FBPs) are hypothesized to act as pre-cursor structures based on large-scale *ab initio* data [84]. These structures consist of faulted basal bases that contain six pyramidal-faulted faces. FBPs have been reported to directly form in displacement cascades with the A95 interatomic potential [85], have nucleated during displacement cascades on existing a-loops with the M07 potential [21], and are predicted to be lower in energy than basal platelets by the BMD19 potential (Fig. 5-6) [159]. Additionally, triangular vacancy platelets have been reported in He-irradiated Zr thin-

foils [87]. It is possible that these metastable structures could facilitate c-loop nucleation directly from displacement cascades.

There have been two recent modeling attempts to include FBPs as pre-cursors to c-loop formation. Li and Ghoniem assumed that all vacancy clustering will form basal defects [100]. While FBPs are not explicitly included in the model, the authors introduced a parameter, Q, which is described as an absorption efficiency for c-loops. To account for the "lower stability" of FBPs, the authors arbitrarily set Q = 0.2 for any basal clusters with a radius below a critical value of 4 nm. Thus, small c-loops have only a 20% absorption efficiency for mobile defects while large c-loops have a 100% absorption efficiency; this mechanism is considered responsible for the delayed growth of c-loops [100]. While this is an interesting theory, the manually adjusted value of 20% for Q is quite low and not supported by lower-length scale data.

Christiaen et al. developed an Object Kinetic Monte Carlo model to predict microstructural evolution in pure Zr [102]. The authors attempt to describe irradiation growth behavior by implementing anisotropic monovacancy diffusion (which is assumed to be more anisotropic than SIA diffusion based on Samolyuk's *ab initio* calculations [49]). A transition probability, p, is introduced with a value between 0 and 1 for cavities to form either vacancy a-loops or FBPs when these clusters reach a size of n = 20. The authors only achieved agreement with experimental growth rates when vacancy a-loops were entirely neglected and all vacancy clusters were assumed to agglomerate into FBPs. Similar to the model of Li and Ghoniem, this approach completely contradicts known irradiation microstructure, for which vacancy a-loops often form in greater quantities than interstitial a-loops [13, 17].

In this chapter, we modify the CD model proposed in Chapter Seven to incorporate the nucleation of FBPs from displacement cascades. The primary goal is to introduce c-loops while still maintaining agreement with vacancy and interstitial a-loop co-existence. Section 8.1 will first detail the necessary modifications to the CD model and Section 8.2 will demonstrate predictions for c-loop nucleation and growth and identify the key driving parameters. Finally, Section 8.3 will cover the future work that we believe is necessary to satisfactorily describe c-loop growth and, thus, breakaway irradiation growth, using the framework that we have developed here.

8.1 Modifications to our CD model to incorporate basal clusters

8.1.1 Description of basal clusters

Basal clusters, denoted as "B_n" for a size of n, are considered to be FBPs for sizes $n < n^b_{transition}$, where $n^b_{transition}$ has been estimated to range from ~91 vacancies based on MS

calculations [159] to ~325 vacancies based on large-scale *ab initio* calculations [84]. The effect of the selected $n^b_{transition}$ parameter will be analyzed in Section 8.2.2. Above this critical transition size, B_n clusters form faulted c-loops with basal habit planes. All B_n clusters are entirely immobile due to their faulted nature. The radius of a disk-like c-loop with n vacancies (which was derived in Section 2.1.3) is given by:

$$r_n^{basal} = a\left(\frac{\sqrt{3}n}{2\pi}\right)^{\frac{1}{2}} \quad (8\text{-}1)$$

where a is one of the hcp lattice parameters (~3.232 Å). The ellipticity factor of basal c-loops is considered to be 1.0 (perfectly circular), as has been demonstrated experimentally by Harte et al. [20]. Conversely, FBPs in this work will be approximated with spherical shapes and capture volumes. Due to their small size and 3-dimensional geometry, this is a valid approximation. It is not appropriate, however, to base their size on the exact expression used for spherical clusters in Section 7.1.1 (Eq. (7-5)). Consider the size of a n = 55 vacancy FBP compared to the size of an equivalent n = 55 vacancy spherical cavity in Fig. 8-1. The spherical cavity is a more compact vacancy cluster with a diameter of 13.4 Å while the FBP is characterized by a base and height of approximately twice this value. An expression was thus derived to approximate an equivalent spherical radius to account for this size discrepancy. Christiaen et al. have reported a full derivation of the volume and surface area for a hexagonal faulted pyramid based on its number of vacancies in α-Zr [84]. The total surface area of a pyramid with n vacancies is found by adding the area of the hexagonal base, S_b, and the area of six pyramidal faces, S_p, which are respectively calculated as:

$$S_b = \frac{\sqrt{3}}{2}a^2 n \quad (8\text{-}2)$$

$$S_p = \frac{a}{2}\sqrt{3a^2 + 4c^2}n \quad (8\text{-}3)$$

where c is one of the hcp lattice parameters (~5.172 Å). In order to estimate an equivalent spherical radius for the faulted pyramid, we set the total surface area of the pyramid equal to that for a sphere ($4\pi r$) and solving for the radius:

$$r^{eq} = \sqrt{\frac{S_b + S_p}{4\pi}} \quad (8\text{-}4)$$

For the example of a 55-vacancy cluster, the equivalent spherical radius calculated with Eq. (8-4) is 11.1 Å; this estimate is much more representative of the size of a FBP (Fig. 8-1). For the rest of this work, FBPs will be approximated as spherical for the purposes of calculating clustering reaction rates.

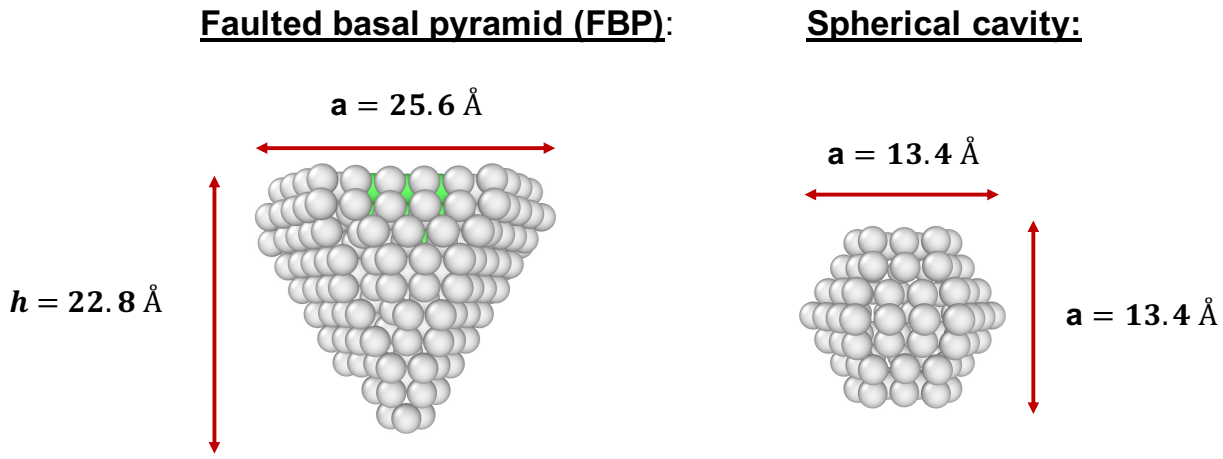

Fig. 8-1. The size of a 55-vacancy cluster is contrasted between FBP and spherical cavity configurations. Atomic positions are visualized via CNA where grey atoms represent "unknown" structure and green atoms represent FCC stacking.

8.1.2 Nucleation of basal clusters

FBPs are assumed to nucleate directly from cascade events, as has been noted with the A95 interatomic potential [85]. To verify this observation, five 40 keV displacement cascades were performed as part of this dissertation using the BMD19 potential [78]. The BMD19 potential was modified to include the ZBL potential at small separation distances. These cascades were performed exactly as described in Section 4.1 of Chapter Four. Once the cascades were fully quenched, the resulting simulation boxes were annealed at 800K for 100 ps using an NPT (constant atoms, pressure, and temperature) ensemble to allow for vacancy clusters to form stable configurations. As seen in Fig. 8-2(a), FBPs were observed to form directly in cascade events. It is interesting to note, however, that vacancy a-loops are fully capable of forming from the same cascade events, as seen in Fig. 8-2(b). FBPs are assumed to only be able to nucleate from vacancy clusters with size n > 19 (the smallest observed cluster to form a FBP configuration [159]). Below this size, basal configurations consist of single-layer vacancy platelets on basal planes, which have a high-energy B-B layer contact in the hcp stacking sequence [37, 55, 82, 159]. This unstable basal configuration acts as a nucleation barrier for FBPs, and thus c-loop, formation. It is for this reason that FBPs are assumed to nucleate only from high-energy displacement cascade events, and do not nucleate due to vacancy agglomeration from clustering events ($V_i + V_j \rightarrow V_{i+j}$).

The volumetric generation rates of FBPs is calculated similarly to what has been done for $I_n$and V_n clusters, as described in Section 2.1.1 and Section 7.1.2. Now, however, the production of vacancy clusters in the size range of 19 < n < 70 is partitioned between B_n (basal) and V_n (prismatic) clusters. We assume that some fraction of the vacancy clusters produced in this size range, Q^b_{nucl}, will form FBP configurations; thus, $(1 - Q^b_{nucl})$ of vacancy clusters in this range will form vacancy a-loops. The volumetric generation rates of FBPs and vacancy a-loops from displacement cascades can then be calculated respectively as:

$$g_i^B = \sum_{40\ eV}^{E_{PKA,max}} Q^b_{nucl} * N_i(E) * \phi(E) \qquad (8\text{-}5)$$

$$g_i^V = \sum_{40\ eV}^{E_{PKA,max}} (1 - Q^b_{nucl}) * N_i(E) * \phi(E) \qquad (8\text{-}6)$$

where $N_i(E)$ is the average number of cluster with size *i* produced from a PKA of energy E and $\phi(E)$ is the number of PKAs produced with energy E per s per volume. Unfortunately, there is no literature regarding the appropriate value of Q^b_{nucl} from displacement cascades in α-Zr. This would require a large number of MD simulations of high-energy cascades to and to subsequently anneal the cascade debris to estimate the fraction of vacancy clusters that produce FBPs, and is certainly a recommended avenue for future work. The effect of the magnitude of this parameter will be demonstrated in Section 8.2.1.

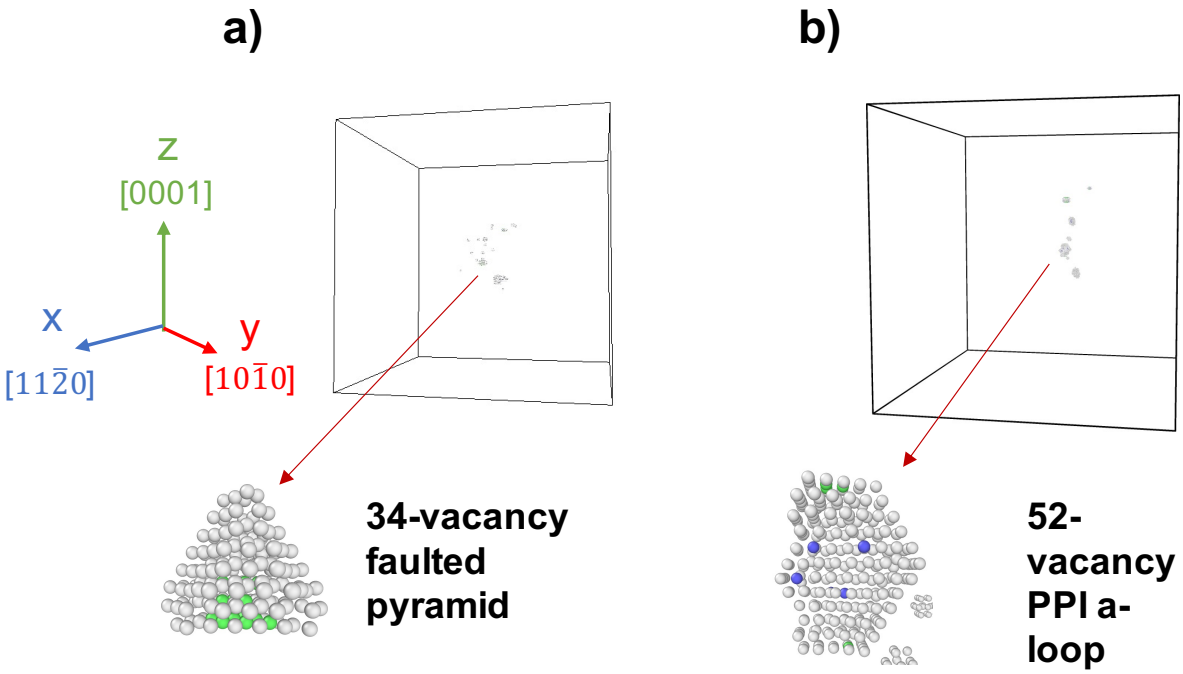

Fig. 8-2. 800K NVT anneals of the damage state resulting from 40 keV displacement cascades with the BMD19 potential produced a) a 34V faulted basal pyramid and b) a 52V vacancy a-loop.

8.1.3 Clustering reactions

There are only three possible clustering reactions with B_n clusters: 1) cluster growth through vacancy absorption ($B_n + V_j \rightarrow B_{n+j}$); 2) cluster shrinkage through interstitial absorption ($B_n + I_j \rightarrow B_{n-j}$); 3) cluster annihilation through interstitial absorption ($B_n + I_j \rightarrow \emptyset$). For B_n with $n < n^b_{transition}$, basal clusters are assumed to have FBP configurations, and their capture volumes are approximated as spherical. As such, the reaction rate constant between basal cluster *i* and a mobile defect *j* is defined as:

$$k^+_{ij} = 4\pi r_{ij} \overline{D}_j \qquad (8\text{-}7)$$

For B_n with $n > n^b_{transition}$, basal clusters form planar c-loop configurations on basal planes. The approach to formulate a reaction rate constant was fully described in Section 2.1.3 and Section 7.1.4; the constant is smoothly transitioned between spherical and toroidal reaction kinetics for a loop *i* interacting with a mobile defect *j*:

$$k^+_{ij}, loops = \left(\left(1 - \alpha_{ij}\right) z^T_{ij} \cdot P^{loop}(\lambda) + \alpha_{ij} z^S_{ij} \right) \overline{D}_j \qquad (8\text{-}8)$$

These calculations are performed exactly as was done for a-loops in Chapter Seven. The difference in reaction rates between a-loops and c-loops stems primarily from the value of $P^{loop}(\lambda)$, the anisotropic capture efficiency for mobile defects. Mobile defects that diffuse predominantly within the basal plane will have higher interaction rates with a-loops than c-loops, as seen in Fig. 2-3. Another parameter which controls the interaction rate is the loop capture radius, r_d. Thermal drift radii were used in this chapter and must be calculated at the selected system temperature using the constants in Table 6-3, as was described in Section 7.1.4.

8.1.4 Cluster dissociation

It is assumed that B_n clusters can only emit vacancy monomers ($B_n \rightarrow B_{n-1} + V_1$). All clusters B_n are able to dissociate for n $\geq$ 19; a 19-vacancy FBP is assumed to produce a monovacancy and a prismatic vacancy cluster ($B_{19} \rightarrow V_{18} + V_1$). The reaction rate constant can be calculated as a function of the cluster binding energy, and the rate constant for the reverse reaction ($V_1 + B_{n-1} \rightarrow B_n$;):

$$k^-_{n,1} = \frac{k^+_{1,n-1}}{\Omega} \exp \frac{-E^b_{n,1}}{k_b T} \qquad (8\text{-}9)$$

The binding energy of a monomer *i* to a cluster of size *n* can be estimated based on the difference in formation energies between the products and reactants:

$$E^b_{n,1v} = E^f_{1v} + E^f_{n-1} - E^f_n \quad (8\text{-}10)$$

The formation energy for a FBP with n vacancies can be estimated by the expression derived by Christiaen et al.:

$$E^f_{FBP}(n) = \Omega\mu\frac{1+v}{1-v}\sqrt{n} + s_p\gamma_p n + s_b\gamma_b n + c_0 \quad (8\text{-}11)$$

where v is the Poisson coefficient, μ is the shear modulus, Ω is a volume factor for the FBP, s_p is the surface factor of pyramidal facets, s_b is the basal surface factor, γ_p is the pyramidal stacking fault energy, γ_b is the intrinsic basal stacking fault energy, and c_0 is a fitting constant [84]. For faulted c-loops, the corresponding formation energy is estimated by the expression derived by Varvenne et al.:

$$E^f_{loop}(n) = \pi R_1^2\gamma n + 2\pi f R_1\overline{K}\sqrt{n}\, ln\left(\frac{R_1\sqrt{n}}{r_c}\right) \quad (8\text{-}12)$$

where R_1 is the radius factor, γ is the loop stacking fault energy (basal extrinsic for loops with less than 200 vacancies, basal intrinsic I_1otherwise), f is a shape factor, r_c is the dislocation core radius, and $\overline{K}$ is an elastic constant [37].

8.1.5 Overview of assumptions and unknowns in the model

The complete dataset of lower-length scale informed parameters is still given in Table 7-1. Similarly, the assumptions presented for the proposed CD model in Section 7.1.6 are still assumed for the work in this chapter. Additionally, we assume that FBPs act as pre-cursor c-loop structures that nucleate in displacement cascades. These assumptions are based on large-scale *ab initio* calculations that predict lower formation energies of FBPs when compared to faulted basal c-loops below some critical size [84]. The existence of FBPs have also been predicted by the A95, M07, and BMD19 interatomic potentials [84, 85, 159]. In particular, FBPs have been reported to form directly in displacement cascades [85], and this has been confirmed with the BMD19 potential in Fig. 8-2. Despite this evidence from lower-length scale simulations, however, we still consider the formation of FBPs to be a cautious assumption, as these defects have not yet been reported in experimental irradiations (with the exception of similar two-dimensional triangular vacancy platelets reported by Liu et al. [87]). The lack of experimental indication for these defects could be related to their small size, and the fact that a-loop number densities rapidly increase, obscuring the identification of these small defects.

The two key parameters which are not fully known are: 1) the critical size of transformation between FBPs and c-loops; 2) the fraction of vacancy clusters that form FBPs in displacement cascades. The former parameter is reported to lie in the range of ~91V [159] < $n^b_{transition}$< ~325V [84]. An appropriate value for the latter parameter is currently

unknown and the data required to inform this parameter is not currently available in literature. Likely estimates for the values of these two parameters will be explored in Section 8.2.2 and Section 8.2.1, respectively.

8.2 Key parameters for c-loop nucleation and growth

Because FBPs are assumed to form during displacement cascades, basal defects are nucleated in the CD model continuously through the volumetric generation term, g_i. Once a FBP has absorbed enough vacancies to reach n > $n^b_{transition}$, it transforms into a faulted basal c-loop. This process has been confirmed with the BMD19 potential by annealing a FBP containing 91 vacancies (the value of $n^b_{transition}$ predicted by the BMD19 potential) for 500 ps at 800 K; the FBP transforms into a basal extrinsic c-loop during this anneal period. The hypothesis that FBPs may act as c-loop precursors appears plausible, but there must be an explanation for the delayed onset of c-loop growth.

Delayed growth could potentially be explained by the capture tendencies of FBPs for migrating defects. The thermal drift radii for FBP capture of interstitial defects is notably larger than that for vacancies (Table 6-2). Due to the approximately spherical geometries of FBPs, the low anisotropy factor of interstitial diffusion does not reduce their interaction rates. Thus, FBPs are strongly biased for interstitial capture (Fig. 6-9). The delayed growth and transformation of FBPs into c-loops could then be driven by any factor that reduces the net incident SIA flux, the SIA bias, or the number density of FBPs. The factor would need to be fluence-dependent such that this effect only occurs above some incubation dose. In the following sections, we will describe the key parameters that affect the population and growth of FBPs based on our CD model predictions. Possible factors that relate to delayed c-loop growth will be considered.

8.2.1 Nucleation probability of faulted basal pyramids in displacement cascades, Q^b_{nucl}

The nucleation of FBPs from displacement cascades is in direct competition with the nucleation of prismatic vacancy a-loops. Estimations of FBP and faulted vacancy a-loop formation energies were calculated with Eq. (8-11) and Eq. (8-12), respectively, and plotted in Fig. 8-3. FBP and vacancy a-loops formation energies are compared for a) small clusters and b) large clusters to demonstrate the switch in stabilities. Markers are given based on molecular statis (MS) data; curves are given based on continuous laws (Eq. (8-11) and Eq. (8-12) for vacancy a-loops and FBPs, respectively).; MS-calculated values as predicted by the BMD19 potential are included as markers. It is clear that FBPs and vacancy a-loops are predicted to have similar

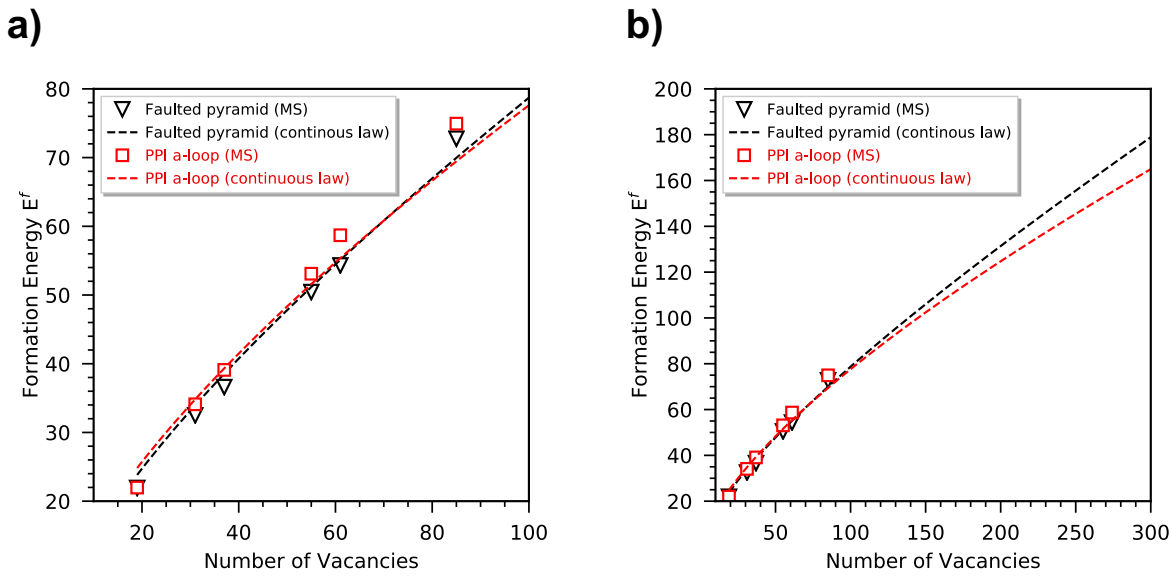

Fig. 8-3. FBP and vacancy a-loops formation energies are compared for a) small clusters and b) large clusters to demonstrate the switch in stabilities. Markers are given based on molecular statis (MS) data; curves are given based on continuous laws (Eq. (8-11) and Eq. (8-12) for vacancy a-loops and FBPs, respectively).

formation energies at small sizes. Based on the continuous expressions, FBPs should have lower energies until n ~ 70 vacancies; this crossover occurs at larger sizes based on MS calculations. Regardless, it is not inconceivable that FBPs could form in relatively large fractions from displacement cascades.

Our CD model predictions for interstitial a-loop, vacancy a-loop, and basal c-loop size distributions at 1.0 dpa with T = 573K are shown in Fig. 8-4 when considering Q^b_{nucl} ranging from 0.1 to 0.5. As a reminder, Q^b_{nucl} is the fraction of vacancy clusters of size 19 < n < 70 that form FBPs in displacement cascades. For these calculations, $n^b_{transition}$ is considered equal to 325 vacancies, the value predicted by large-scale *ab initio* calculations [84]. The general behavior of the c-loop size distribution is striking and drastically different than those for a-loops: as expected for pure Zr, c-loops do not grow within 1.0 dpa of exposure! FBPs nucleate continuously from incident neutron irradiation, but their significant bias for interstitial capture inhibits their growth. The parameter Q^b_{nucl} does not change this behavior. Instead, this parameter controls the nucleation rate of FBPs and, therefore, their saturation density which ranges from 2.2×10^{17} m^{-3} to 1.1×10^{18} m^{-3} for a Q^b_{nucl} value of 0.1 and 0.5, respectively. These densities are approximately two orders of magnitude lower than typical reported c-loop number densities [20], but this is not unsurprising considering the significant influx of SIAs to these defects. It is expected that once conditions change for c-loop growth, their number densities will increase greatly.

8.2.2 Critical transition size of faulted basal pyramids, $n^b_{transition}$

The value for the transition size is estimated to range from n = 91V [159] based on MS calculations to n = 325V [84] based on large-scale *ab initio* calculations. This parameter effectively controls the cluster size range for which FBPs are stable and preferred to planar c-loops. Because FBPs have a strong bias for interstitial capture and c-loops have a strong bias for vacancy capture, the FBP-stable size regime is an important parameter controlling the growth capability of c-loops. This concept is demonstrated in Fig. 8-5 for which dislocation loop size distributions are plotted at 5.0 dpa with $n^b_{transition}$ ranging from 91V to 325V and the FBP nucleation parameter, Q^b, ranging from 0.1 to 0.5. For larger values of $n^b_{transition}$, it is clear that c-loops cannot grow due to the considerable SIA flux incident on FBP pre-cursors. When $n^b_{transition}$ is set equal to 91V, on the other hand, the model predicts a bimodal distribution of basal defects. A large quantity of FBP defects are observed at small sizes due to their continuous nucleation from displacement cascades. Once these defects transform into c-loops they grow rapidly due to the net flux of vacancy defect absorption. The average predicted c-loop diameters reach up to 100 nm at 5.0 dpa, consistent with experimental irradiations [13, 20, 26]. The predicted c-loop number densities are greater for larger magnitudes of the nucleation parameter. It is also worth highlighting that our CD model continues to predict the co-existence of interstitial and vacancy a-loops *in addition* to basal c-loops.

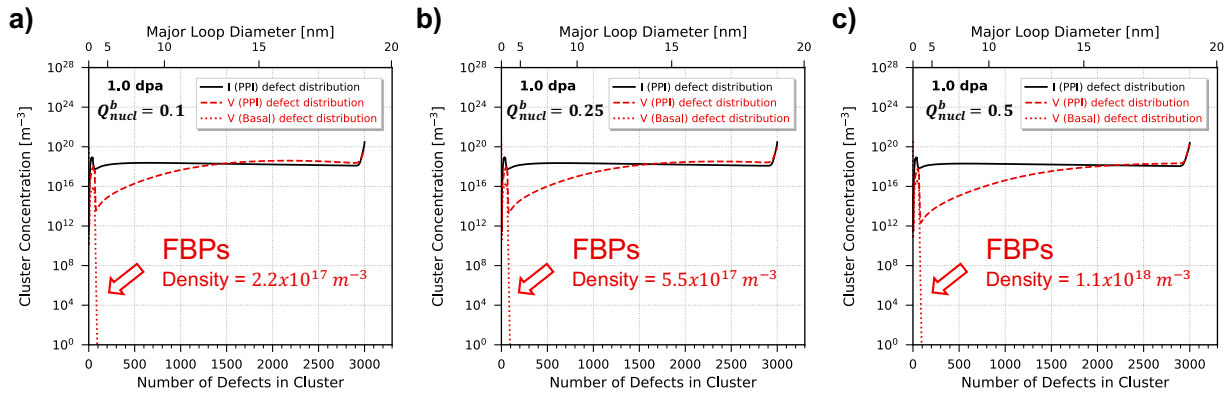

Fig. 8-4. CD model predictions at 1.0 dpa with T = 573K for interstitial a-loop, vacancy a-loop, and basal c-loop size distributions using an $n^b_{transition}$ of 325V and a varying Q^b_{nucl} equal to a) 0.10, b) 0.25, and c) 0.5.

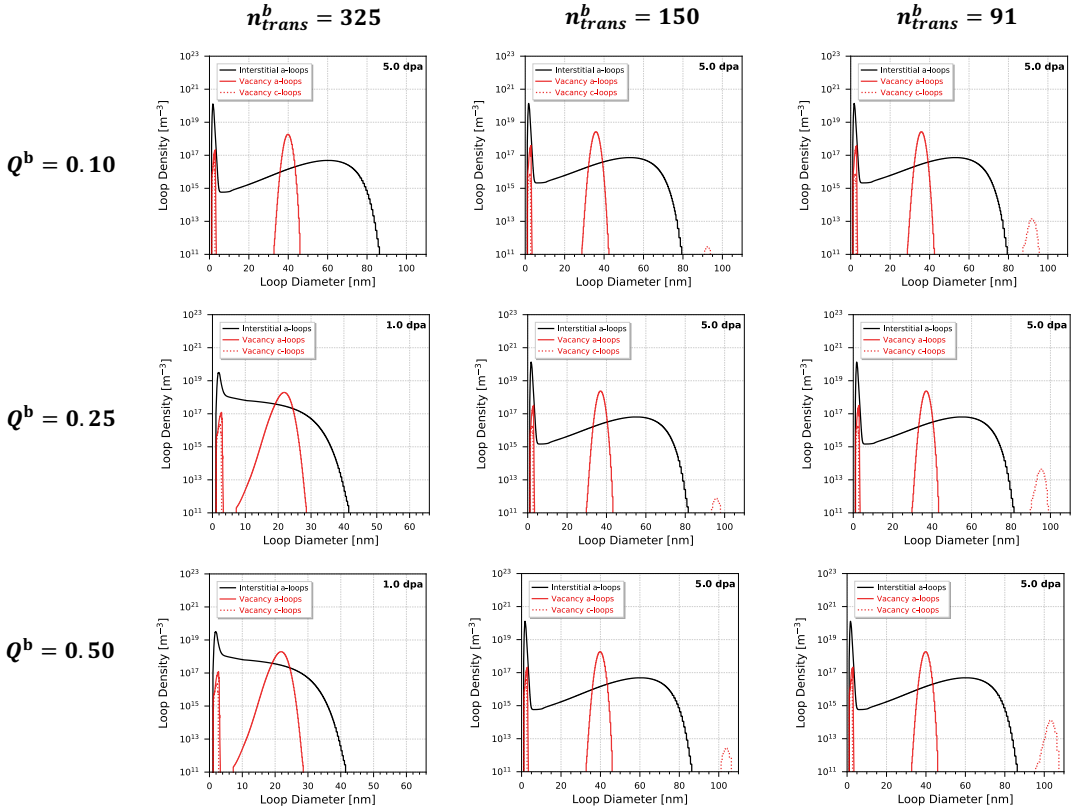

Fig. 8-5. CD model predictions at 5.0 dpa with T = 573K for interstitial a-loop, vacancy a-loop, and basal c-loop size distributions using varying values of Q^b_{nucl} and $n^b_{transition}$.

The results of Fig. 8-5 provide an exciting insight into the growth behavior of c-loops. Based on our CD model predictions, the net SIA bias of FBPs could certainly explain the delayed growth of these defects. This mechanism is relevant in high-purity Zr as well as alloyed Zr. A transition size of $n^b_{transition}$ = 91V appears too small, as this would allow c-loops to grow at all fluences. Rather, the correct transition size likely lies in between this value and the estimate of Christiaen et al. ($n^b_{transition}$ = 325V) [84]. However, it is worth considering the approximate diameter of these defects at the predicted transition sizes as calculated with Eq. (8-4). For a FBP with 91V, the diameter is approximately 2.8 nm; for a FBP with 325V, the diameter is approximately 5.4 nm. Considering that these defects have not yet been resolved by TEM analysis, it is more likely that the transition size lies closer to 91V than 325V.

The rapid growth rate and average c-loop diameter in our model are promising aspects. Rapid c-loop growth, as well as their unique vacancy character, have traditionally been attributed to the difference in anisotropy of point defects by Woo [40, 41, 46]. This theory has recently been disputed based on *ab initio* calculations which demonstrate basal-plane preference for monovacancy diffusion [49]. In fact, both point defects likely migrate with similar anisotropy ratios [159]. At 573 K, the BMD19 potential predicts that single interstitials and vacancies have anisotropy ratios of 0.767 and 0.804, respectively (Table 7-3. While this difference of ~0.04 in the anisotropy factor is not as large as Woo originally predicted, this still results in an approximate 5% bias for monovacancy absorption at basal c-loops. Another form of vacancy bias arises from the larger thermal drift capture radii for vacancy absorption by large c-loops (Table 6-2).

In Chapter Five, it was hypothesized that the rapid growth of c-loops may additionally be attributed to the differences in diffusional anisotropy of mobile defect clusters. This concept is demonstrated in Fig. 8-6 through a comparison of interaction rates with interstitial a-loops, vacancy a-loops, and basal c-loops for mobile defects with a size of $1 < n < 6$. When considering mobile clusters, interstitials have greatly reduced interaction rates with basal c-loops due to their low anisotropy factors of diffusion; vacancy clusters, conversely, have comparable interaction rates between prismatic a-loops and basal c-loops. The reduced capture of interstitial clusters is expected to further assist in c-loop growth.

8.2.3 Solute interaction with basal defects

Certainly, there appears to be a solute-driven mechanism for the stabilization of c-loops, and the resultant incubation dose could be correlated with the ballistic release of solute from intermetallic precipitates under irradiation [32, 35, 45, 55, 60]. One potential effect has been noted in Chapter Three: the reduction in stacking fault energies of basal c-loops due to solute segregation. In the current model, stacking fault energies are incorporated into the formation energy expressions of FBPs (Eq. (8-11)) and basal c-loops (Eq. (8-12)). The binding energies of defect clusters can then be calculated with Eq. (8-10).

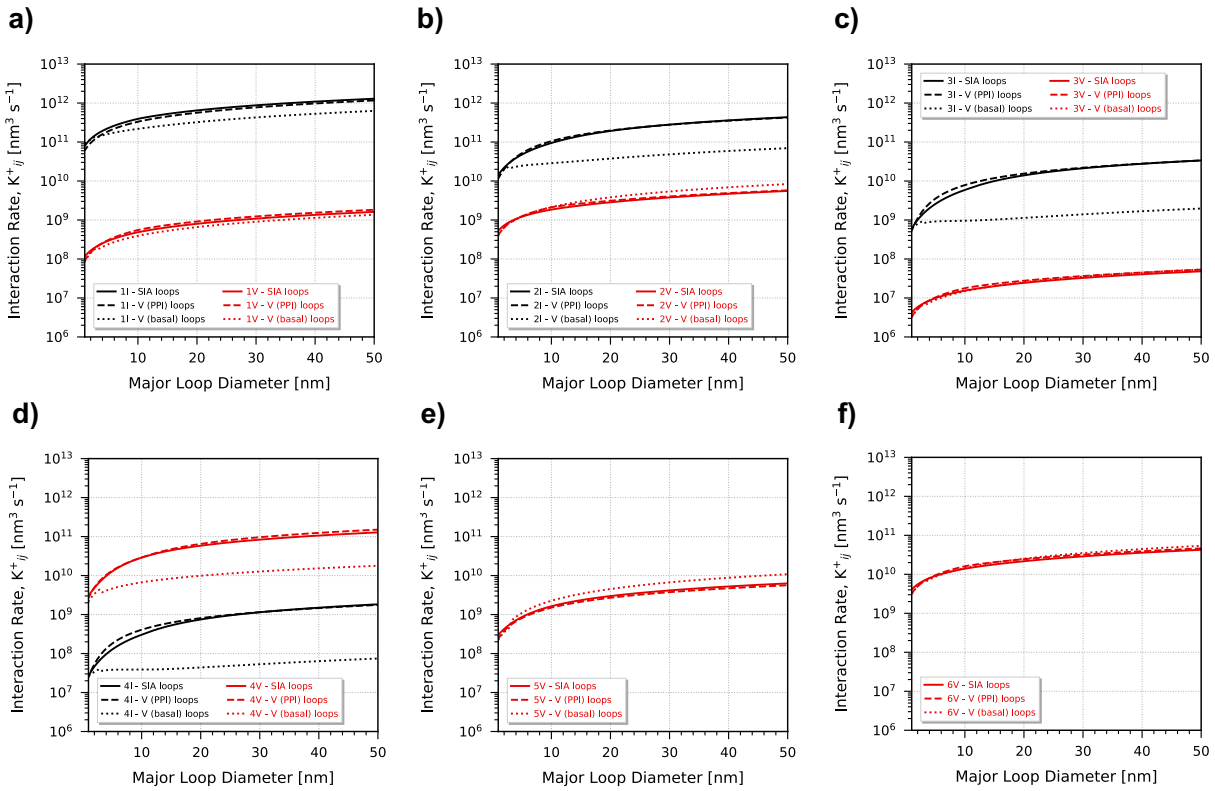

Fig. 8-6. Interaction rates for the capture of a) point defects, b) n = 2 defects, c) n = 3 defects, d) n = 4 defects, e) n = 5 vacancy clusters, and f) n = 6 vacancy clusters with interstitial a-loops (solid lines), vacancy a-loops (dashed lines), and vacancy c-loops (dotted lines). Mobile interstitial capture is indicated by black lines while vacancy capture is indicated with red lines.

For faulted clusters, the total binding energy is reduced due to the increase in stacking fault energy from absorbing an additional defect into a cluster. This is made clear by inserting the parameter values reported in Refs. [84] and [37] for the binding energies of FBPs, basal extrinsic c-loops, and basal intrinsic I_1 c-loops, respectively:

$$E_{n,1v}^{b}(FBP) = 2.03 + 5.35\left[\sqrt{n-1} - \sqrt{n}\right] - 9.08\gamma_E - 19\gamma_p \quad (8\text{-}13)$$

$$E_{n,1v}^{b}(E) = 2.03 + 2.87\left[\sqrt{n-1}\,ln\left(1.50\sqrt{n-1}\right) - \sqrt{n}\,ln\left(1.50\sqrt{n}\right)\right] - 9.08\gamma_E \quad (8\text{-}14)$$

$$E_{n,1v}^{b}(I_1) = 2.03 + 3.02\left[\sqrt{n-1}\,ln\left(1.64\sqrt{n-1}\right) - \sqrt{n}\,ln\left(1.64\sqrt{n}\right)\right] - 9.08\gamma_{I_1} \quad (8\text{-}15)$$

As an upper limit, we can assume that solute segregation reduces stacking fault energies to zero; this was shown to be the case for high-fluence segregation of Fe in Chapter Three. The consequence on c-loop growth behavior is quite striking, as seen in Fig. 8-7. It is important to note that for these simulations the stacking fault energy is set equal to zero from the beginning; to present a more physically-relevant simulation, solute segregation need to be considered as a function of neutron fluence. This would necessitate a time-dependent binding energy and requires a reorganization of the Xolotl code. As such, this is considered necessary future work. Considering this caveat, solute interaction with basal defects is shown to greatly increase c-loop number densities and broaden their size distribution. Two FBP transition sizes were considered: 91 and 325 vacancies. For the case of $n_{transition}^{b}$ = 91V, solute segregation results in two orders of magnitude higher c-loop number densities. For the case of $n_{transition}^{b}$ = 325V, c-loops were originally unable to grow due to the significant SIA bias of FBPs; after implementing solute segregation, c-loops were capable of growing to large sizes and number densities.

Solute segregation is implemented solely as a modification of basal cluster binding energies. As such, the behavior showcased in Fig. 8-7 must be the result of two factors: 1) an increased population of FBPs and 2) enhanced c-loop stability stemming from the reduced dissociation of these defects. This is a promising behavior that lends credibility to the solute-driven enhancement of breakaway irradiation growth strains in Zr alloys when compared to pure Zr [6, 13, 33, 35, 43].

8.2.4 Interstitial absorption at faulted basal pyramids

While it is likely that solute species can *enhance* irradiation growth in Zr alloys through c-loop stabilization, solute interaction cannot be the only factor that induces the onset of c-loop growth. For example, c-loops still observe delayed nucleation in high-purity Zr for which the solute concentration is not large enough to support such a mechanism. One complementary factor that may assist the nucleation of c-loops is a fluence-dependent reduction in the incident SIA flux or SIA bias to FBPs. This could be a consequence of:

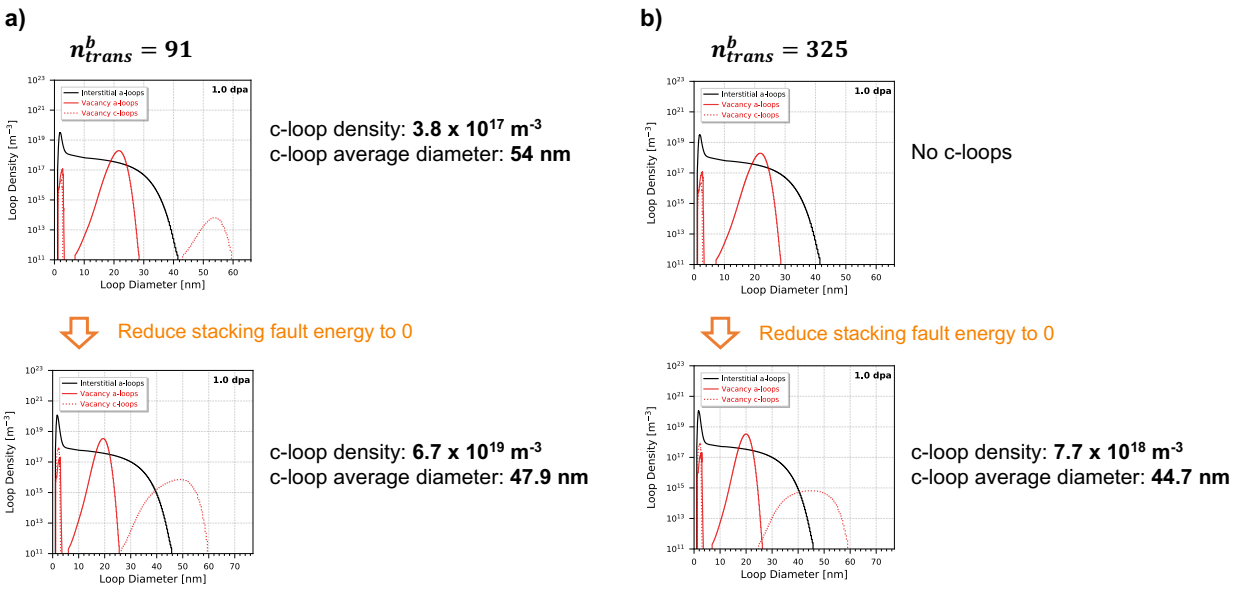

Fig. 8-7. Dislocation loop distributions before and after reducing stacking fault energies to zero (modifying basal cluster binding energies) when considering two FBP transition sizes: a) 91 vacancies and b) 325 vacancies.

1. A reduction of interstitial capture distances to FBPs. This could possibly be related to solute or impurity screening of the tensile strain field surrounding FBPs.
2. A reduction of interstitial diffusivities. Solute interaction with migrating interstitials may reduce their diffusivities, as noted with Nb [30, 188]. However, the impact that this might have on recombination rates would need to be assessed.
3. Spatial ordering of vacancy a-loops. If FBPs form within layers of ordered vacancy a-loops, the SIA capture volume would be self-shielded. Furthermore, a high density of vacancy defects would result in a localized super-saturation of mobile vacancies from dissociation events.

The first of these two factors are clearly alloy-dependent. Any effects of Fe, Cr, or Ni could be delayed in relation to the ballistic dissolution of intermetallic precipitates. It was shown in Chapter Three that Fe and Cr have a particular affinity to nucleating c-loop defects, and their interaction could be a driving force for c-loop growth [55]. The third factor, on the other hand, could pertain to either alloyed or pure Zr. The incubation dose would be related to the time necessary for vacancy a-loop ordering, which has been shown to occur over several dpa (Fig. 1-2) [20]. Any FBPs nucleating within these ordered basal sheets would likely be subjected to a lower SIA flux and a super-saturation of mobile vacancies, both of which would promote c-loop growth. Furthermore, the thermal drift capture volumes of vacancy a-loops favor vacancy capture. These capture volumes would extend above and below the ordered a-loop bands, and may promote preferential drift of vacancies to these ordered structures. This could potentially explain the observations of Harte et al. that c-loops only form within ordered rows of vacancy a-loops [20].

8.3 Recommended future work

In this CD framework, the fraction of vacancy clusters in displacement cascades that form FBPs, Q_{nucl}^{b}, is unknown, but is assumed to range from 0.1 to 0.5. This parameter should be calculated from a much larger database of MD displacement cascade simulations, with subsequent annealing of the cascade debris to allow FBPs to form. From this data, Q_{nucl}^{b} could be estimated and related to the energy of the initial PKA. It is likely that FBPs will only form in higher-energy cascade events (> ~5 – 10 keV) that produce larger vacancy clusters.

In Section 8.2.3, the potential for solute segregation to enhance c-loop growth was demonstrated. In order to physically represent irradiation damage behavior, the fluence-dependent release of solute should be considered to smoothly modify basal cluster binding energies with increasing dose. Another potential effect of solute, or impurities, would be a modification of defect diffusivities due to trapping. The data required to incorporate this behavior is not yet available in literature, but would be necessary to appropriately model microstructure evolution in Zr alloys. It is recommended that MD simulations similar to

those performed in Chapter Five are conducted, but instead of considering pure Zr, the simulation box should contain appropriate amounts of specific solute. By comparing the mean-squared displacement of point defect or defect clusters with and without solute, the effect on the diffusivities can be quantified. Solute interaction may also change the anisotropy factor of diffusion for these defects, which would directly alter their interaction rates with dislocation loops. For example, Fe is believed to cause monovacancies to migrate with a preference for c-axis diffusion rather than basal-plane diffusion, which would increase their absorption rates at c-loops [57, 58].

The current CD model assumes that defects are randomly and homogenously distributed in the bulk. This assumption does not allow our model to consider spatial ordering of vacancy a-loops, which may drive the growth of c-loops at higher doses. Thus, it is recommended to modify this model to incorporate a spatial dependence, including possible extension of the model to account for elastic interactions, of the defect cluster populations. In this way, interstitial and vacancy defects can be appropriately partitioned to relevant sinks, and thus evaluate the extent to which local alterations in mobile defect density could cause differences in the predicted microstructure.

8.4 Summary and conclusions

The CD model proposed in Chapter Seven has been modified to consider the nucleation and growth of basal c-loops. We have considered a recent hypothesis that faulted basal pyramids (FBPs) may act as pre-cursor structures, and are postulated to nucleate directly in displacement cascades. Our CD model accurately predicts that c-loop growth does not occur immediately. Rather, the growth of c-loops is inhibited due to the significant bias for interstitial capture by FBPs. The growth barrier is related to the critical c-loop transition size, which ranges from 91 vacancies to 325 vacancies based on lower-length scale data. The growth of c-loops is likely enhanced by solute segregation which modifies basal cluster binding energies. It is also possible that the delay in c-loop growth coincides with some fluence-dependent factor that reduces the interstitial flux to nucleating FBPs. The incubation dose for breakaway irradiation growth could be related to the spatial ordering of vacancy a-loops; once these loops are aligned, their interstitial capture volumes become overlapped. In alloyed Zr, the incubation dose may be related to the release of elements such as Fe and Cr from intermetallic precipitates.

Regardless of the mechanism, once FBPs have transformed into c-loops, their growth rapidly accelerates due to the net absorption of vacancy defects, consistent with experimental observations. The model proposed here is capable of predicting c-loop growth while maintaining the co-existence of interstitial and vacancy a-loops, an aspect that has never been performed successfully in literature. This work highlights the importance of developing mechanistic models to accurately represent the physics driving defect cluster evolution.

Chapter Nine:

Conclusions and Future Work

In response to high-energy particle irradiation, Zr cladding tubes undergoe an axial expansion and radial contraction that leads to significant rod bowing and restriction of cooling channels. This macroscopic response is ultimately due to an a-axis expansion and c-axis contraction of α-Zr grains, a consequence of its inherently anisotropic hcp crystal structure. Significant interest has been placed on understanding the rapid acceleration of irradiation growth strains at high-fluences. It is well understood that breakaway growth is correlated with the nucleation and growth of faulted vacancy c-loops on basal planes. Unfortunately, the mechanisms responsible for delayed c-loop nucleation remain entirely ambiguous. Several models have been proposed to describe the reported growth behavior. While recent models all claim to predict perfect agreement with reported growth rates, these fits are generally based on manually adjusted parameter values beyond realistic ranges. Furthermore, most models neglect the formation of vacancy a-loops, despite experimental observations that these defects accounting for approximately half of the visible microstructure in irradiated Zr. The goal of this work, then, consisted of two broad categories: 1) to develop a database of key parameters based on lower-length scale calculations and 2) to use this database to inform a mechanistic cluster dynamics (CD) model with minimal assumptions.

Interaction energies of common solute and impurities to c-loops in the nucleation and growth regime have been quantified through *ab initio* calculations (Chapter Three). This data directly informs expressions for c-loop binding energies and mechanistic models for c-loop nucleation. In Chapter Four, volumetric generation rates for defects were derived based on displacement cascade data. The effect of electronic stopping on total defect production, defect clustering fractions, and defect cluster distributions has been determined. After defects are produced from incident irradiation, the resultant microstructure evolves as a consequence of defect transport and reactions in the material. Mobility data and inherent anisotropies of diffusion have been tabulated for each of the mobile species in α-Zr in Chapter Five. This database allowed us to accurately implement anisotropic effects on defect interaction rates in a CD framework. Furthermore, preferred cluster configurations and their binding energies as a function of size have been calculated. In Chapter Six, the interaction distances of point defects with interstitial a-loops, vacancy a-loops, and vacancy c-loops were assessed in the directions radial and perpendicular to the loop face. It was found that the local stress states surrounding dislocation loops induce an interaction gradient which preferentially attracts defects of the same type as the loop. Thus, an inherent bias emerged which may explain interstitial and vacancy a-loop co-existence.

In Chapter Seven, the dataset collected from lower-length scale simulations was incorporated into a CD model. In order to accurately represent microstructural evolution under irradiation, this model considered:

1. Mobile defect diffusivities within the basal plane and along the c-axis
2. Anisotropic capture efficiencies for dislocation lines and loops
3. Volumetric defect generation rates for all relevant defects. These directly considered correlated recombination and clustering within displacement cascades
4. Spontaneous and thermal drift capture radii of dislocation loops for interstitials and vacancies. These affect the smooth transition between spherical and toroidal reaction kinetics, as well as the magnitude of the toroidal reaction rate constant.
5. Monomer emission from cluster dissociation events for all defect clusters

Each of these aspects of the model were based on the lower-length scale dataset developed in this work. The resultant CD model predictions are extremely promising: the simultaneous growth of vacancy and interstitial a-loops in bulk Zr were modeled for the first time in literature. The CD model is capable of predicting accurate a-loop characteristics such as mean diameter, number densities, and relative fractions of interstitial-to-vacancy a-loops with excellent agreement to two separate experimental irradiation studies (one at low dose and one at moderate dose).

Finally, this CD model framework was extended to incorporate the nucleation and growth of faulted basal c-loops. We considered a recent hypothesis that faulted basal pyramids (FBPs) may act as pre-cursor structures to c-loop formation. Nucleation of c-loops occurred as a result of FBP formation directly in displacement cascades. The delay in c-loop growth was attributed to the strong bias for interstitial absorption of FBP structures, as indicated by lower-length scale simulations. As the critical size for transformation between FBP and c-loop structures was decreased, a bimodal distribution of basal defects became apparent. Following the transformation of FBPs into c-loops, their growth accelerates rapidly due to the preferential capture of migrating vacancy defects by basal-plane c-loops. Our model is capable of predicting c-loop growth while maintaining the simultaneous co-existence of interstitial and vacancy a-loops, another milestone which has never been reported in literature.

There are three significant areas recommended for future work: 1) quantifying the nucleation rate of FBPs from displacement cascades; 2) expanding the mechanistic understanding and modeling of the effect of solute and impurities on defect cluster evolution; and 3) considering the spatial organization of vacancy a-loops. The FBP nucleation rate is currently assumed to range between 0.1 and 0.5, but an extensive MD database of displacement cascades (followed by subsequent annealing) would better inform this parameter. As for solute interactions, it is clear that microstructural evolution varies considerably between pure and alloyed Zr. Further understanding of the role of solute and impurities on defect mobility and their capture at sinks is necessary to expand our CD model

to alloyed systems. Finally, a significant SIA capture bias at FBPs is hypothesized to act as the primary driver for delayed c-loop growth. Any factor that reduces the net SIA flux to these defects would thus enhance c-loop growth and encourage breakaway irradiation growth. One such factor could be the spatial ordering of vacancy a-loops which results in self-shielding for SIA capture. Modifying our CD model to include such spatial organization effects would allow a quantification of these effects on microstructural evolution. It is our hope that the work reported here will encourage and inform future work in the field. The coupled projects in this dissertation highlight the importance of scale-bridging computational modeling to solve current and future issues of materials performance in extreme nuclear environments.

List of References

1. R.A. Krishnan, M. K. , Zirconium alloys in nuclear technology, Proc. Indian Acad. Sci. (Engg. Sci.). **4** (1981) 41-56. https://doi.org/https://doi.org/10.1007/BF02843474.
2. W. Gary, *Fundamentals of Radiation Materials Science: Metals and Alloys*. 2nd ed. 2007: Springer. 774 - 781.
3. G.J.C. Carpenter, R.A. Murgatroyd, A. Rogerson, J.F. Watters, Irradiation growth of zirconium single crystals, Journal of Nuclear Materials. **101**(1) (1981) 28-37. https://doi.org/https://doi.org/10.1016/0022-3115(81)90441-4.
4. G.J.C. Carpenter, R.H. Zee, A. Rogerson, Irradiation growth of zirconium single crystals: A review, Journal of Nuclear Materials. **159** (1988) 86-100. https://doi.org/https://doi.org/10.1016/0022-3115(88)90087-6.
5. K. Linga Murty, I. Charit, Texture development and anisotropic deformation of zircaloys, Progress in Nuclear Energy. **48**(4) (2006) 325-359. https://doi.org/https://doi.org/10.1016/j.pnucene.2005.09.011.
6. R. Adamson, M. Griffiths, C. Patterson, Irradiation Growth of Zirconium Alloys: A Review, A.N.T. International (2017). https://doi.org/
7. D.J. Bacon, F. Gao, Y.N. Osetsky, Computer simulation of displacement cascades and the defects they generate in metals, Nuclear Instruments and Methods in Physics Research Section B: Beam Interactions with Materials and Atoms. **153**(1-4) (1999) 87-98. https://doi.org/10.1016/s0168-583x(99)00041-5.
8. D.J. Bacon, Y.N. Osetsky, R. Stoller, R.E. Voskoboinikov, MD description of damage production in displacement cascades in copper and α-iron, Journal of Nuclear Materials. **323**(2-3) (2003) 152-162. https://doi.org/10.1016/j.jnucmat.2003.08.002.
9. J.F. March-Rico, C.M. Mcswain, B.D. Wirth, Quantifying the impact of an electronic drag force on defect production from high-energy displacement cascades in α-zirconium, Journal of Nuclear Materials. **542** (2020) 152539. https://doi.org/10.1016/j.jnucmat.2020.152539.
10. S.J. Wooding, D.J. Bacon, A molecular dynamics study of displacement cascades in α-zirconium, Philosophical Magazine A. **76**(5) (1997) 1033-1051. https://doi.org/10.1080/01418619708200013.
11. S.J. Wooding, L.M. Howe, F. Gao, A.F. Calder, D.J. Bacon, A molecular dynamics study of high-energy displacement cascades in α-zirconium, Journal of Nuclear Materials. **254**(2-3) (1998) 191-204. https://doi.org/10.1016/s0022-3115(97)00365-6.
12. W. Zhou, J. Tian, Q. Feng, J. Zheng, X. Liu, J. Xue, D. Qian, S. Peng, Molecular dynamics simulations of high-energy displacement cascades in hcp-Zr, Journal of Nuclear Materials. **508** (2018) 540-545. https://doi.org/https://doi.org/10.1016/j.jnucmat.2018.06.002.
13. M. Griffiths, A review of microstructure evolution in zirconium alloys during irradiation, Journal of Nuclear Materials. **159** (1988) 190-218. https://doi.org/https://doi.org/10.1016/0022-3115(88)90093-1.
14. M. Griffiths, R.W. Gilbert, V. Fidleris, R.P. Tucker, R.B. Adamson, Neutron damage in zirconium alloys irradiated at 644 to 710 k, Journal of Nuclear Materials. **150**(2) (1987) 159-168. https://doi.org/10.1016/0022-3115(87)90071-7.

15. M. Griffiths, M.H. Loretto, R.E. Smallman, Electron damage in zirconium, Journal of Nuclear Materials. **115**(2-3) (1983) 323-330. https://doi.org/10.1016/0022-3115(83)90323-9.
16. P.M.K.R.G.B.K.F. A Jostsons, *Neutron Irradiation-Induced Defect Structures in Zirconium*
Effects of Radiation on Structural Materials. 1979, West Conshohocken, PA: ASTM International. 61-1979.
17. A. Jostsons, P.M. Kelly, R.G. Blake, The nature of dislocation loops in neutron irradiated zirconium, Journal of Nuclear Materials. **66**(3) (1977) 236-256. https://doi.org/10.1016/0022-3115(77)90113-1.
18. D. Northwood, R.W. Gilbert, L.E. Bahen, P.M. Kelly, R.G. Blake, A. Jostsons, P.K. Madden, D. Faulkner, W. Bell, R.B. Adamson, Characterization of neutron irradiation damage in zirconium alloys — an international "round-robin" experiment, Journal of Nuclear Materials. **79** (1979) 379-394. https://doi.org/10.1016/0022-3115(79)90103-X.
19. C. Varvenne, O. Mackain, L. Proville, E. Clouet, Hydrogen and vacancy clustering in zirconium, Acta Materialia. **102** (2016) 56-69. https://doi.org/https://doi.org/10.1016/j.actamat.2015.09.019.
20. A. Harte, D. Jädernäs, M. Topping, P. Frankel, C.P. Race, J. Romero, L. Hallstadius, E.C. Darby, M. Preuss, The effect of matrix chemistry on dislocation evolution in an irradiated Zr alloy, Acta Materialia. **130** (2017) 69-82. https://doi.org/https://doi.org/10.1016/j.actamat.2017.03.024.
21. C. Dai, P. Saidi, M. Topping, L.K. Béland, Z. Yao, M.R. Daymond, A mechanism for basal vacancy loop formation in zirconium, Scripta Materialia. **172** (2019) 72-76. https://doi.org/10.1016/j.scriptamat.2019.07.006.
22. D.J. Mazey, J.H. Evans, Bubble lattice formation in titanium injected with krypton ions, Journal of Nuclear Materials. **138**(1) (1986) 16-18. https://doi.org/
23. F.W. Clinard, G.F. Hurley, L.W. Hobbs, Neutron irradiation damage in MgO, Al2O3 and MgAl2O4 ceramics, Journal of Nuclear Materials. **108-109** (1982) 655-670. https://doi.org/10.1016/0022-3115(82)90538-4.
24. J.H. Evans, A computer simulation of the two-dimensional SIA diffusion model for void lattice formation, Journal of Nuclear Materials. **132**(2) (1985) 147-155. https://doi.org/10.1016/0022-3115(85)90408-8.
25. N. De Diego, Y.N. Osetsky, D.J. Bacon, Mobility of interstitial clusters in alpha-zirconium. **33**(13) (2002) 783-789. https://doi.org/10.1007/s11661-002-1008-2.
26. E. Francis, R.P. Babu, A. Harte, T.L. Martin, P. Frankel, D. Jädernäs, J. Romero, L. Hallstadius, P.A.J. Bagot, M.P. Moody, M. Preuss, Effect of Nb and Fe on damage evolution in a Zr-alloy during proton and neutron irradiation, Acta Materialia. **165** (2019) 603-614. https://doi.org/10.1016/j.actamat.2018.12.021.
27. V.N. Shishov, *The Evolution of Microstructure and Deformation Stability in Zr-Nb-(Sn,Fe) Alloys under Neutron Irradiation*
Zirconium Production and Technology: The Kroll Medal Papers 1975–2010. 2010, West Conshohocken, PA: ASTM International. 500-2010.

28. V.N. Shishov, Z.E. Ostrovsky, A.V. Obukhov, M.M. Peregud, A.V. Nikulina, V.F. Kon'kov, V.V. Novikov, V.A. Markelov, T.N. Khokhunova, G.P. Kobylyansky, A.E. Novoselov, Structure-Phase State, Corrosion and Irradiation Properties of Zr-Nb-Fe-Sn System Alloys, (2009) 724-+. https://doi.org/
29. R.W. Gilbert, K. Farrell, C.E. Coleman, Damage structure in zirconium alloys neutron irradiated at 573 to 923 k, Journal of Nuclear Materials. **84**(1) (1979) 137-148. https://doi.org/https://doi.org/10.1016/0022-3115(79)90157-0.
30. M. Christensen, W. Wolf, C.M. Freeman, E. Wimmer, R.B. Adamson, L. Hallstadius, P.E. Cantonwine, E.V. Mader, Effect of alloying elements on the properties of Zr and the Zr–H system, Journal of Nuclear Materials. **445**(1-3) (2014) 241-250. https://doi.org/10.1016/j.jnucmat.2013.10.040.
31. C. Dai, P. Saidi, Z. Yao, M.R. Daymond, Atomistic simulations of Ni segregation to irradiation induced dislocation loops in Zr-Ni alloys, Acta Materialia. **140** (2017) 56-66. https://doi.org/https://doi.org/10.1016/j.actamat.2017.08.016.
32. M. Griffiths, R.A. Holt, A. Rogerson, Microstructural aspects of accelerated deformation of Zircaloy nuclear reactor components during service, Journal of Nuclear Materials. **225** (1995) 245-258. https://doi.org/https://doi.org/10.1016/0022-3115(94)00687-3.
33. M. Griffiths, R.W. Gilbert, The formation of c-component defects in zirconium alloys during neutron irradiation, Journal of Nuclear Materials. **150**(2) (1987) 169-181. https://doi.org/10.1016/0022-3115(87)90072-9.
34. R.W.G.V.F. M Griffiths, *Accelerated Irradiation Growth of Zirconium Alloys Zirconium in the Nuclear Industry: Eighth International Symposium*. 1989, West Conshohocken, PA: ASTM International. 677-1989.
35. C.R.M.G.D.G.C.L. Y de Carlan, *Influence of Iron in the Nucleation of ⟨c⟩ Component Dislocation Loops in Irradiated Zircaloy-4 Zirconium in the Nuclear Industry: Eleventh International Symposium*. 1996, West Conshohocken, PA: ASTM International. 653-1996.
36. F.O.J.L.B.D.G.J.M.C.J.P.M.X.F. L. Tournadre, *Impact of Hydrogen Pick-Up and Applied Stress on C-Component Loops: Toward a Better Understanding of the Radiation Induced Growth of Recrystallized Zirconium Alloys Zirconium in the Nuclear Industry: 17th Volume*. 2015, West Conshohocken, PA: ASTM International. 42-2015.
37. C. Varvenne, O. Mackain, E. Clouet, Vacancy clustering in zirconium: An atomic-scale study, Acta Materialia. **78** (2014) 65-77. https://doi.org/10.1016/j.actamat.2014.06.012.
38. M. Christensen, W. Wolf, C. Freeman, E. Wimmer, R.B. Adamson, M. Griffiths, E.V. Mader, Vacancy loops in Breakaway Irradiation Growth of zirconium: Insight from atomistic simulations, Journal of Nuclear Materials. **529** (2020) 151946. https://doi.org/https://doi.org/10.1016/j.jnucmat.2019.151946.
39. R.A. Holt, C.H. Woo, C.K. Chow, Production bias — a potential driving force for irradiation growth, Journal of Nuclear Materials. **205** (1993) 293-300. https://doi.org/https://doi.org/10.1016/0022-3115(93)90092-D.

40. C.H. Woo, Modeling irradiation growth of zirconium and its alloys, Radiation Effects and Defects in Solids. **144**(1-4) (1998) 145-169. https://doi.org/10.1080/10420159808229674.
41. C.H. Woo, B.N. Singh, Production bias due to clustering of point defects in irradiation-induced cascades, Philosophical Magazine A. **65**(4) (1992) 889-912. https://doi.org/10.1080/01418619208205596.
42. V.F.R.B.A. Rp Tucker, *High-Fluence Irradiation Growth of Zirconium Alloys at 644 to 725 K*
Zirconium in the Nuclear Industry. 1984, West Conshohocken, PA: ASTM International. 449-1984.
43. M. Griffiths, D. Gilbon, C. Regnard, C. Lemaignan, HVEM study of the effects of alloying elements and impurities on radiation damage in Zr-alloys, Journal of Nuclear Materials. **205** (1993) 273-283. https://doi.org/https://doi.org/10.1016/0022-3115(93)90090-L.
44. A.R.C.N.C.M.G.E.T.C.H.C.H.W. Ra Holt, *Non-Linear Irradiation Growth of Cold-Worked Zircaloy-2*
Zirconium in the Nuclear Industry: Eleventh International Symposium. 1996, West Conshohocken, PA: ASTM International. 637-1996.
45. M. Griffiths, *Microstructure Evolution in Zr Alloys during Irradiation: Dose, Dose Rate, and Impurity Dependence*
Zirconium Production and Technology: The Kroll Medal Papers 1975–2010. 2010, West Conshohocken, PA: ASTM International. 436-2010.
46. C.H. Woo, Theory of irradiation deformation in non-cubic metals: Effects of anisotropic diffusion, Journal of Nuclear Materials. **159** (1988) 237-256. https://doi.org/10.1016/0022-3115(88)90096-7.
47. C.H. Woo, X. Liu, Atomistic calculation of point-defect diffusion anisotropy and irradiation growth inα-zirconium, Philosophical Magazine. **87**(16) (2007) 2355-2369. https://doi.org/10.1080/14786430601185085.
48. Y.N. Osetsky, D.J. Bacon, N. De Diego, Anisotropy of point defect diffusion in alpha-zirconium, Metallurgical and Materials Transactions A. **33**(3) (2002) 777-782. https://doi.org/10.1007/s11661-002-0144-z.
49. G.D. Samolyuk, A.V. Barashev, S.I. Golubov, Y.N. Osetsky, R.E. Stoller, Analysis of the anisotropy of point defect diffusion in hcp Zr, Acta Materialia. **78** (2014) 173-180. https://doi.org/https://doi.org/10.1016/j.actamat.2014.06.024.
50. G.M. Hood, Point defect diffusion in α-Zr, Journal of Nuclear Materials. **159** (1988) 149-175. https://doi.org/https://doi.org/10.1016/0022-3115(88)90091-8.
51. G.M. Hood, Diffusion in alpha-Zr, HCP and Open Metals, Defects Diffus. Data. **95-98** (1993) 755-774. https://doi.org/https://doi.org/10.4028/www.scientific.net/DDF.95-98.755.
52. M. Griffiths, R.W. Gilbert, C.E. Coleman, Grain boundary sinks in neutron-irradiated Zr and Zr-alloys, Journal of Nuclear Materials. **159** (1988) 405-416. https://doi.org/https://doi.org/10.1016/0022-3115(88)90107-9.
53. H. Rouchette, L. Thuinet, A. Legris, A. Ambard, C. Domain, Influence of shape anisotropy of self-interstitials on dislocation sink efficiencies in Zr: Multiscale

modeling, Physical Review B. **90**(1) (2014). https://doi.org/10.1103/physrevb.90.014104.
54. V. Fidleris, The irradiation creep and growth phenomena, Journal of Nuclear Materials. **159** (1988) 22-42. https://doi.org/10.1016/0022-3115(88)90083-9.
55. J.F. March-Rico, G. Huang, B.D. Wirth, The effect of local chemical environment on the energetics of stacking faults and vacancy platelets in α-zirconium, Journal of Nuclear Materials. **540** (2020) 152339. https://doi.org/10.1016/j.jnucmat.2020.152339.
56. R.A.G.K.J.-H.C.D.G.S.I.T.F.L.H.A.O.S.M. Suresh Yagnik, *Effect of Alloying Elements, Cold Work, and Hydrogen on the Irradiation-Induced Growth Behavior of Zirconium Alloy Variants*
Zirconium in the Nuclear Industry: 18th International Symposium. 2018, West Conshohocken, PA: ASTM International. 795-2018.
57. R.C. Pasianot, R.A. Pérez, V.P. Ramunni, M. Weissmann, Ab initio approach to the effect of Fe on the diffusion in hcp Zr II: The energy barriers, Journal of Nuclear Materials. **392**(1) (2009) 100-104. https://doi.org/https://doi.org/10.1016/j.jnucmat.2009.03.051.
58. R.A. Pérez, M. Weissmann, Ab-initio approach to the effect of Fe on the diffusion in hcp Zr, Journal of Nuclear Materials. **374**(1) (2008) 95-100. https://doi.org/https://doi.org/10.1016/j.jnucmat.2007.07.012.
59. H. Suzuki, Segregation of solute atoms to stacking faults, J. Phys. Soc. Jpn. **17** (1962) 322-325. https://doi.org/https://doi.org/10.1143/JPSJ.17.322.
60. T. Sawabe, T. Sonoda, S. Kitajima. *Distribution of alloying elements in irradiated Zircaloy-2 by atom probe tomography and transmission electron microscopy*. in *Proceedings of 2014 water reactor fuel performance meeting/ top fuel / LWR fuel performance meeting (WRFPM 2014)*. 2014. Japan.
61. C. Dai, F. Long, P. Saidi, L.K. Béland, Z. Yao, M.R. Daymond, Primary damage production in the presence of extended defects and growth of vacancy-type dislocation loops in hcp zirconium, Physical Review Materials. **3**(4) (2019). https://doi.org/10.1103/physrevmaterials.3.043602.
62. P.A. Burr, M.R. Wenman, B. Gault, M.P. Moody, M. Ivermark, M.J.D. Rushton, M. Preuss, L. Edwards, R.W. Grimes, From solid solution to cluster formation of Fe and Cr in α-Zr, Journal of Nuclear Materials. **467** (2015) 320-331. https://doi.org/https://doi.org/10.1016/j.jnucmat.2015.10.001.
63. G. Sundell, M. Thuvander, P. Tejland, M. Dahlbäck, L. Hallstadius, H.-O. Andrén, Redistribution of alloying elements in Zircaloy-2 after in-reactor exposure, Journal of Nuclear Materials. **454**(1-3) (2014) 178-185. https://doi.org/10.1016/j.jnucmat.2014.07.072.
64. R.H. Zee, A. Rogerson, G.J.C. Carpenter, J. Watters, Effect of tin on the irradiation growth of polycrystalline zirconium, Journal of Nuclear Materials. **120**(2) (1984) 223-229. https://doi.org/https://doi.org/10.1016/0022-3115(84)90060-6.
65. S.N. Buckley, S.A. Manthorpe, Dislocation loop nucleation and growth in zirconium-2.5 wt% niobium alloy during 1 MeV electron irradiation, Journal of Nuclear

Materials. **90**(1) (1980) 169-174. https://doi.org/https://doi.org/10.1016/0022-3115(80)90254-8.
66. M. Christensen, W. Wolf, C. Freeman, E. Wimmer, R.B. Adamson, L. Hallstadius, P.E. Cantonwine, E.V. Mader, Diffusion of point defects, nucleation of dislocation loops, and effect of hydrogen in hcp-Zr: Ab initio and classical simulations, Journal of Nuclear Materials. **460** (2015) 82-96. https://doi.org/10.1016/j.jnucmat.2015.02.013.
67. M.J. Norgett, M.T. Robinson, I.M. Torrens, A proposed method of calculating displacement dose rates, Nuclear Engineering and Design. **33**(1) (1975) 50-54. https://doi.org/10.1016/0029-5493(75)90035-7.
68. F. Gao, D.J. Bacon, L.M. Howe, C.B. So, Temperature-dependence of defect creation and clustering by displacement cascades in α-zirconium, Journal of Nuclear Materials. **294**(3) (2001) 288-298. https://doi.org/10.1016/s0022-3115(01)00483-4.
69. G.J. Ackland, S.J. Wooding, D.J. Bacon, Defect, surface and displacement-threshold properties of α-zirconium simulated with a many-body potential, Philosophical Magazine A. **71**(3) (1995) 553-565. https://doi.org/10.1080/01418619508244468.
70. M.I. Mendelev, G.J. Ackland, Development of an interatomic potential for the simulation of phase transformations in zirconium, Philosophical Magazine Letters. **87**(5) (2007) 349-359. https://doi.org/10.1080/09500830701191393.
71. Q.-U.-A. Sahi, Y.-S. Kim, Molecular dynamics simulations of the coupled effects of strain and temperature on displacement cascades in α-zirconium, Nuclear Engineering and Technology. **50**(6) (2018) 907-914. https://doi.org/10.1016/j.net.2018.04.013.
72. Y. Jin, W. Lai, Influence of thermal barrier effect of grain boundaries on bulk cascades in alpha-zirconium revealed by molecular dynamics simulation, Journal of Nuclear Materials. **470** (2016) 97-101. https://doi.org/10.1016/j.jnucmat.2015.12.006.
73. W. Zhou, J. Tian, J. Zheng, J. Xue, S. Peng, Dislocation-enhanced experimental-scale vacancy loop formation in hcp Zirconium in one single collision cascade, Scientific Reports. **6**(1) (2016) 21034. https://doi.org/10.1038/srep21034.
74. C. Dai, L. Balogh, Z. Yao, M.R. Daymond, Atomistic simulations of the formation of <c>-component dislocation loops in α-zirconium, Journal of Nuclear Materials. **478** (2016) 125-134. https://doi.org/10.1016/j.jnucmat.2016.06.002.
75. G.D. Samolyuk, S.I. Golubov, Y.N. Osetsky, R.E. Stoller, Self-interstitial configurations in hcp Zr: a first principles analysis, Philosophical Magazine Letters. **93**(2) (2013) 93-100. https://doi.org/10.1080/09500839.2012.745653.
76. F. Willaime, Ab initio study of self-interstitials in hcp-Zr, Journal of Nuclear Materials. **323**(2-3) (2003) 205-212. https://doi.org/10.1016/j.jnucmat.2003.08.005.
77. C. Domain *, A. Legris, Ab initio atomic-scale determination of point-defect structure in hcp zirconium, Philosophical Magazine. **85**(4-7) (2005) 569-575. https://doi.org/10.1080/14786430412331334625.

78. E. Wimmer, M. Christensen, W. Wolf, W.H. Howland, B. Kammenzind, R.W. Smith, Hydrogen in zirconium: Atomistic simulations of diffusion and interaction with defects using a new embedded atom method potential, Journal of Nuclear Materials. **532** (2020) 152055. https://doi.org/10.1016/j.jnucmat.2020.152055.
79. N. De Diego, Y.N. Osetsky, D.J. Bacon, Structure and properties of vacancy and interstitial clusters in α-zirconium, Journal of Nuclear Materials. **374**(1-2) (2008) 87-94. https://doi.org/10.1016/j.jnucmat.2007.07.011.
80. N. De Diego, A. Serra, D.J. Bacon, Y.N. Osetsky, On the structure and mobility of point defect clusters in alpha-zirconium: a comparison for two interatomic potential models, Modelling and Simulation in Materials Science and Engineering. **19**(3) (2011) 035003. https://doi.org/10.1088/0965-0393/19/3/035003.
81. D. Kulikov, M. Hou, Vacancy dislocation loops in zirconium and their interaction with self-interstitial atoms, Journal of Nuclear Materials. **342**(1) (2005) 131-140. https://doi.org/https://doi.org/10.1016/j.jnucmat.2005.04.004.
82. V.G. Kapinos, Y.N. Osetsky, P.A. Platonov, Computer simulation of vacancy loops and stacking faults in zirconium, Journal of Nuclear Materials. **195**(1) (1992) 83-101. https://doi.org/https://doi.org/10.1016/0022-3115(92)90365-R.
83. G.J.C. Carpenter, Void formation in zirconium under irradiation in the high-voltage electron microscope, Rad. Eff. **19** (1973) 189–190. https://doi.org/10.1080/00337577308232242.
84. B. Christiaen, C. Domain, L. Thuinet, A. Ambard, A. Legris, A new scenario for ‹c› vacancy loop formation in zirconium based on atomic-scale modeling, Acta Materialia. **179** (2019) 93-106. https://doi.org/https://doi.org/10.1016/j.actamat.2019.07.030.
85. R.E. Voskoboinikov, Y.N. Osetsky, D.J. Bacon, Identification and morphology of point defect clusters created in displacement cascades in α-zirconium, Nuclear Instruments and Methods in Physics Research Section B: Beam Interactions with Materials and Atoms. **242**(1-2) (2006) 530-533. https://doi.org/10.1016/j.nimb.2005.08.167.
86. D. Hull, D.J. Bacon, *Introduction to Dislocations*. 5th ed, ed. Butterworth-Heinemann. 2011: Elsevier. 115 - 118.
87. S.-M. Liu, I.J. Beyerlein, W.-Z. Han, Two-dimensional vacancy platelets as precursors for basal dislocation loops in hexagonal zirconium, Nature Communications. **11**(1) (2020). https://doi.org/10.1038/s41467-020-19629-5.
88. B.N. Singh, A. Horsewell, P. Toft, Effects of neutron irradiation on microstructure and mechanical properties of pure iron, Journal of Nuclear Materials. **271-272** (1999) 97-101. https://doi.org/10.1016/s0022-3115(98)00767-3.
89. B.N. Singh, J.H. Evans, Significant differences in defect accumulation behaviour between fcc and bcc crystals under cascade damage conditions, Journal of Nuclear Materials. **226**(3) (1995) 277-285. https://doi.org/10.1016/0022-3115(95)00121-2.
90. H. Wen, C.H. Woo, Temperature dependence and anisotropy of self- and mono-vacancy diffusion in α-Zr, Journal of Nuclear Materials. **420**(1-3) (2012) 362-369. https://doi.org/10.1016/j.jnucmat.2011.10.012.

91. Y.N. Osetsky, D.J. Bacon, A. Serra, Thermally activated glide of small dislocation loops in metals, Philosophical Magazine Letters. **79**(5) (1999) 273-282. https://doi.org/10.1080/095008399177345.
92. Y.N. Osetsky, D.J. Bacon, A. Serra, B.N. Singh, S.I. Golubov, Stability and mobility of defect clusters and dislocation loops in metals, Journal of Nuclear Materials. **276**(1-3) (2000) 65-77. https://doi.org/10.1016/s0022-3115(99)00170-1.
93. Y.N. Osetsky, D.J. Bacon, A. Serra, B.N. Singh, S.I. Golubov, One-dimensional atomic transport by clusters of self-interstitial atoms in iron and copper, Philosophical Magazine. **83**(1) (2003) 61-91. https://doi.org/10.1080/0141861021000016793.
94. G.J.C. Carpenter, D.O. Northwood, The contribution of dislocation loops to radiation growth and creep of Zircaloy - 2, Journal of Nuclear Materials. **56**(3) (1975) 260-266. https://doi.org/10.1016/0022-3115(75)90041-0.
95. R.A. Holt, Mechanisms of irradiation growth of alpha-zirconium alloys, Journal of Nuclear Materials. **159** (1988) 310-338. https://doi.org/https://doi.org/10.1016/0022-3115(88)90099-2.
96. S. Golubov, A. Barashev, R.E. Stoller, B. Singh, Breakthrough in Understanding Radiation Growth of Zirconium, ASTM Special Technical Publication. **1543** (2015) 729-758. https://doi.org/10.1520/STP154320130043.
97. A.V. Barashev, S.I. Golubov, R.E. Stoller, Theoretical investigation of microstructure evolution and deformation of zirconium under neutron irradiation, Journal of Nuclear Materials. **461** (2015) 85-94. https://doi.org/https://doi.org/10.1016/j.jnucmat.2015.02.001.
98. F. Christien, A. Barbu, Effect of self-interstitial diffusion anisotropy in electron-irradiated zirconium: A cluster dynamics modeling, Journal of Nuclear Materials. **346**(2-3) (2005) 272-281. https://doi.org/10.1016/j.jnucmat.2005.06.024.
99. F. Christien, A. Barbu, Cluster Dynamics modelling of irradiation growth of zirconium single crystals, Journal of Nuclear Materials. **393**(1) (2009) 153-161. https://doi.org/https://doi.org/10.1016/j.jnucmat.2009.05.016.
100. Y. Li, N. Ghoniem, Cluster dynamics modeling of irradiation growth in single crystal Zr, Journal of Nuclear Materials. **540** (2020) 152312. https://doi.org/https://doi.org/10.1016/j.jnucmat.2020.152312.
101. S.I. Choi, G.-G. Lee, J. Kwon, J.H. Kim, Modeling of sink-induced irradiation growth of single-crystal and polycrystal zirconiums in nuclear reactors, Journal of Nuclear Materials. **468** (2016) 56-70. https://doi.org/https://doi.org/10.1016/j.jnucmat.2015.11.014.
102. B. Christiaen, C. Domain, L. Thuinet, A. Ambard, A. Legris, Influence of vacancy diffusional anisotropy: Understanding the growth of zirconium alloys under irradiation and their microstructure evolution, Acta Materialia. **195** (2020) 631-644. https://doi.org/10.1016/j.actamat.2020.06.004.
103. K.A. Baseden, J.W. Tye, Introduction to Density Functional Theory: Calculations by Hand on the Helium Atom, Journal of Chemical Education. **91**(12) (2014) 2116-2123. https://doi.org/10.1021/ed5004788.

104. M.E. Tuckerman, G.J. Martyna, Understanding Modern Molecular Dynamics: Techniques and Applications, The Journal of Physical Chemistry B. **104**(2) (2000) 159-178. https://doi.org/10.1021/jp992433y.
105. A.A. Kohnert, B.D. Wirth, L. Capolungo, Modeling microstructural evolution in irradiated materials with cluster dynamics methods: A review, Computational Materials Science. **149** (2018) 442-459. https://doi.org/https://doi.org/10.1016/j.commatsci.2018.02.049.
106. M.R. Gilbert, J.C. Sublet, Differential dpa calculations with SPECTRA-PKA, Journal of Nuclear Materials. **504** (2018) 101-108. https://doi.org/https://doi.org/10.1016/j.jnucmat.2018.03.032.
107. *ASTM E521, Practice for Neutron Radiation Damage Simulation by Charged Particle Irradiation*. Annual Book of ASTM Standards. Vol. 12.02:E521-89. 1995. 8.
108. Y.N.O. A. G. Mikhin, V. G. Kapinos, On the anisotropic migration of point defects in h.c.p. zirconium, Philosophical Magazine A. **70** (1994) 25-33. https://doi.org/10.1080/01418619408242534.
109. M. Griffiths, R.C. Styles, C.H. Woo, F. Phillipp, W. Frank, Study of point defect mobilities in zirconium during electron irradiation in a high-voltage electron microscope, Journal of Nuclear Materials. **208**(3) (1994) 324-334. https://doi.org/https://doi.org/10.1016/0022-3115(94)90342-5.
110. P. Saidi, Z. Wang, Y. Mao, L.K. Béland, Z. Yao, M.R. Daymond, A method for calculation of bias factor in anisotropic mediums, application to α−zirconium, Journal of Nuclear Materials. **528** (2020) 151882. https://doi.org/https://doi.org/10.1016/j.jnucmat.2019.151882.
111. T.R. Waite, Theoretical Treatment of the Kinetics of Diffusion-Limited Reactions, Physical Review. **107**(2) (1957) 463-470. https://doi.org/10.1103/PhysRev.107.463.
112. V. Jansson, L. Malerba, d.b. Andree, C. Becquart, C. Domain, Sink strength calculations of dislocations and loops using OKMC, Journal of Nuclear Materials. **442** (2013) 218-226. https://doi.org/10.1016/j.jnucmat.2013.08.052.
113. A. Seeger, U. Gösele, Steady-state diffusion of point defects to dislocation loops, Physics Letters A. **61**(6) (1977) 423-425. https://doi.org/https://doi.org/10.1016/0375-9601(77)90355-3.
114. A. Kohnert, B. Wirth, Cluster dynamics models of irradiation damage accumulation in ferritic iron. II. Effects of reaction dimensionality, Journal of Applied Physics. **117** (2015) 154306. https://doi.org/10.1063/1.4918316.
115. M. Gaumé, F. Onimus, L. Dupuy, O. Tissot, C. Bachelet, F. Mompiou, Microstructure evolution of recrystallized Zircaloy-4 under charged particles irradiation, Journal of Nuclear Materials. **495** (2017) 516-528. https://doi.org/https://doi.org/10.1016/j.jnucmat.2017.09.004.
116. S. Blondel, D.E. Bernholdt, K.D. Hammond, L. Hu, D. Maroudas, B.D. Wirth, Benchmarks and Tests of a Multidimensional Cluster Dynamics Model of Helium Implantation in Tungsten, Fusion Science and Technology. **71**(1) (2017) 84-92. https://doi.org/10.13182/fst16-109.

117. D.-U. Kim, S. Blondel, D.E. Bernholdt, P. Roth, F. Kong, D. Andersson, M.R. Tonks, B.D. Wirth, Modeling mesoscale fission gas behavior in UO2 by directly coupling the phase field method to spatially resolved cluster dynamics, Materials Theory. **6**(1) (2022). https://doi.org/10.1186/s41313-021-00030-8.
118. *Cluster dynamics code, Xolotl*. [cited 2022 March 9th]; Available from: https://github.com/ORNL-Fusion/xolotl.
119. S. Blondel, D.E. Bernholdt, K.D. Hammond, B.D. Wirth, Continuum-scale modeling of helium bubble bursting under plasma-exposed tungsten surfaces, Nuclear Fusion. **58**(12) (2018) 126034. https://doi.org/10.1088/1741-4326/aae8ef.
120. Q.Q. Shao, L.H. Liu, T.W. Fan, D.W. Yuan, J.H. Chen, Effects of solute concentration on the stacking fault energy in copper alloys at finite temperatures, Journal of Alloys and Compounds. **726** (2017) 601-607. https://doi.org/https://doi.org/10.1016/j.jallcom.2017.07.332.
121. A. Yu, First-principles calculations of stacking fault energy in titanium alloys, SCIREA J. Phs. **1** (2016) 1-10. https://doi.org/
122. W.Y. Wang, S.L. Shang, Y. Wang, Z.-G. Mei, K.A. Darling, L.J. Kecskes, S.N. Mathaudhu, X.D. Hui, Z.-K. Liu, Effects of Alloying Elements on Stacking Fault Energies and Electronic Structures of Binary Mg Alloys: A First-Principles Study, Materials Research Letters. **2**(1) (2014) 29-36. https://doi.org/10.1080/21663831.2013.858085.
123. G. Kresse, J. Furthmuller, Efficiency of ab-initio total energy calculations for metals and semiconductors using a plane-wave basis set, Comput. Mat. Sci. **6** (1996) 15. https://doi.org/
124. G. Kresse, J. Furthmuller, Efficient iterative schemes for *ab initio* total-energy calculations using a plane-wave basis set, Phys. Rev. B. **54** (1996) 11169. https://doi.org/
125. G. Kresse, J. Hafner, *Ab initio* molecular dynamics for liquid metals, Phs. Rev. B. **47** (1993) 558. https://doi.org/
126. G. Kresse, J. Hafner, *Ab initio* molecular-dynamics simulation of the liquid-metal-amorphous-semiconductor transition in germanium, Phys. Rev. B. **49** (1994) 14251. https://doi.org/
127. G. Kresse, D. Joubert, From ultrasoft pseudopotentials to the projector augmented-wave method, Phys. Rev. B. **59** (1999) 1758. https://doi.org/
128. P.E. Blochl, Project augment-wave method, Phys. Rev. B. **50** (1994) 17953. https://doi.org/
129. J.P. Perdew, K. Burke, M. Ernzerhof, Generalized gradient approximation made simple, Phys. Rev. Lett. **77** (1996) 3865-3868. https://doi.org/
130. C. Domain, R. Besson, A. Legris, Atomic-scale ab initio study of the Zr–H system: II. Interaction of H with plane defects and mechanical properties, Acta Materialia. **52**(6) (2004) 1495-1502. https://doi.org/https://doi.org/10.1016/j.actamat.2003.11.031.
131. M. Ghazisaeidi, D.R. Trinkle, Interaction of oxygen interstitials with lattice faults in Ti, Acta Materialia. **76** (2014) 82-86. https://doi.org/https://doi.org/10.1016/j.actamat.2014.05.025.

132. D. Arias, J.P. Abriata, *Binary Alloys Phase Diagram*. 2 ed. 1990, Materials Park, Ohio: ASM International. 1359-1360.
133. P. Nash, C.S. Jayanth, The Ni–Zr (Nickel-Zirconium) system, Bulletin of Alloy Phase Diagrams. **5**(2) (1984) 144-148. https://doi.org/10.1007/bf02868950.
134. Y.H. Jeong, H.G. Kim, T.H. Kim, Effect of β phase, precipitate and Nb-concentration in matrix on corrosion and oxide characteristics of Zr–xNb alloys, Journal of Nuclear Materials. **317**(1) (2003) 1-12. https://doi.org/https://doi.org/10.1016/S0022-3115(02)01676-8.
135. T. Alam, M.K. Khan, M. Pathak, K. Ravi, R. Singh, S.K. Gupta, A review on the clad failure studies, Nuclear Engineering and Design. **241**(9) (2011) 3658-3677. https://doi.org/https://doi.org/10.1016/j.nucengdes.2011.08.009.
136. Z.E. Celiz, M.L. Saumell, R.A. Versaci, P.B. Bozzano, Microstructural Characterization of Excel Zirconium Alloy, Procedia Materials Science. **8** (2015) 442-450. https://doi.org/https://doi.org/10.1016/j.mspro.2015.04.095.
137. G.L.S.A.D.J. S. Valizadeh, auml, dern, auml, M.D. s, auml, E.V.M.G.Z.J.W.L.H. ck, *Effects of Secondary Phase Particle Dissolution on the In-Reactor Performance of BWR Cladding*

Zirconium in the Nuclear Industry: 16th International Symposium. 2012, West Conshohocken, PA: ASTM International. 753-2012.
138. N.N. Greenwood, A. Earnshaw, *Chemistry of the elements*, ed. Butterworth-Heinemann. 1997, Guildoford.
139. L.N. Kantorovich, User-friendly visualization program for ab initio DFT codes VASP, SIESTA, QE, and QUICKSTEP, (1996-2012). https://doi.org/
140. J. Lindhard, M. Scharff, H.E. Schioett, RANGE CONCEPTS AND HEAVY ION RANGES (NOTES ON ATOMIC COLLISIONS, II). **Vol: 33: No. 14** (1963). https://doi.org/Journal Name: Kgl. Danske Videnskab. Selskab. Mat. Fys. Medd.; Journal Volume: Vol: 33: No. 14; Other Information: Orig. Receipt Date: 31-DEC-64.
141. J.F. Ziegler, M.D. Ziegler, J.P. Biersack, SRIM – The stopping and range of ions in matter (2010), Nuclear Instruments and Methods in Physics Research Section B: Beam Interactions with Materials and Atoms. **268**(11) (2010) 1818-1823. https://doi.org/https://doi.org/10.1016/j.nimb.2010.02.091.
142. J.F. Ziegler, J.P. Biersack, *The Stopping and Range of Ions in Matter*. 1985: Springer.
143. J.F. Ziegler, J.P. Biersack, *The Stopping and Range of Ions in Matter*, in *Treatise on Heavy-Ion Science*. 1985, Springer US. p. 93-129.
144. J.P. Biersack, L.G. Haggmark, A Monte Carlo computer program for the transport of energetic ions in amorphous targets, Nuclear Instruments and Methods. **174**(1) (1980) 257-269. https://doi.org/https://doi.org/10.1016/0029-554X(80)90440-1.
145. W.J. Weber, Y. Zhang, Predicting damage production in monoatomic and multi-elemental targets using stopping and range of ions in matter code: Challenges and recommendations, Current Opinion in Solid State and Materials Science. **23**(4) (2019) 100757. https://doi.org/https://doi.org/10.1016/j.cossms.2019.06.001.
146. J. Lindhard, V. Nielsen, M. Scharff, P.V. Thomsen, INTEGRAL EQUATIONS GOVERNING RADIATION EFFECTS. (NOTES ON ATOMIC COLLISIONS, III). **Vol: 33: No. 10** (1963). https://doi.org/Journal Name: Kgl. Danske Videnskab., Selskab. Mat.

Fys. Medd.; Journal Volume: Vol: 33: No. 10; Other Information: Orig. Receipt Date: 31-DEC-63.
147. R.E. Stoller, M.B. Toloczko, G.S. Was, A.G. Certain, S. Dwaraknath, F.A. Garner, On the use of SRIM for computing radiation damage exposure, Nuclear Instruments and Methods in Physics Research Section B: Beam Interactions with Materials and Atoms. **310** (2013) 75-80. https://doi.org/https://doi.org/10.1016/j.nimb.2013.05.008.
148. R.E. Stoller, Primary Radiation Damage Formation, Comprehensive Nuclear Materials. **1.11** (2012) 293-329. https://doi.org/
149. K. Nordlund, Molecular dynamics simulation of ion ranges in the 1–100 keV energy range, Computational Materials Science. **3**(4) (1995) 448-456. https://doi.org/10.1016/0927-0256(94)00085-q.
150. C.P. Race, D.R. Mason, M.W. Finnis, W.M.C. Foulkes, A.P. Horsfield, A.P. Sutton, The treatment of electronic excitations in atomistic models of radiation damage in metals, Reports on Progress in Physics. **73**(11) (2010) 116501. https://doi.org/10.1088/0034-4885/73/11/116501.
151. J. Tian, W. Zhou, Q. Feng, J. Zheng, Molecular dynamics simulations with electronic stopping can reproduce experimental sputtering yields of metals impacted by large cluster ions, Applied Surface Science. **435** (2018) 65-71. https://doi.org/10.1016/j.apsusc.2017.11.080.
152. L. Sandoval, H.M. Urbassek, Influence of electronic stopping on sputtering induced by cluster impact on metallic targets, Physical Review B. **79**(14) (2009). https://doi.org/10.1103/physrevb.79.144115.
153. A.E. Sand, K. Nordlund, On the lower energy limit of electronic stopping in simulated collision cascades in Ni, Pd and Pt, Journal of Nuclear Materials. **456** (2015) 99-105. https://doi.org/https://doi.org/10.1016/j.jnucmat.2014.09.029.
154. A.M. Rutherford, D.M. Duffy, The effect of electron–ion interactions on radiation damage simulations, Journal of Physics: Condensed Matter. **19**(49) (2007) 496201. https://doi.org/10.1088/0953-8984/19/49/496201.
155. D.M. Duffy, A.M. Rutherford, Including the effects of electronic stopping and electron–ion interactions in radiation damage simulations, Journal of Physics: Condensed Matter. **19**(1) (2007) 016207. https://doi.org/10.1088/0953-8984/19/1/016207.
156. A.E. Ismail, J.A. Greathouse, P.S. Crozier, S.M. Foiles, Electron–ion coupling effects on simulations of radiation damage in pyrochlore waste forms, Journal of Physics: Condensed Matter. **22**(22) (2010) 225405. https://doi.org/10.1088/0953-8984/22/22/225405.
157. S. Plimpton, Fast Parallel Algorithms for Short-Range Molecular Dynamics, Journal of Computational Physics. **117**(1) (1995) 1-19. https://doi.org/10.1006/jcph.1995.1039.
158. A. Stukowski, Visualization and analysis of atomistic simulation data with OVITO–the Open Visualization Tool, Modelling and Simulation in Materials Science and Engineering. **18**(1) (2009) 015012. https://doi.org/10.1088/0965-0393/18/1/015012.

159. J.F. March-Rico, B.D. Wirth, Defect cluster configurations and mobilities in α-Zr: A comparison of the BMD19 and M07 interatomic potentials, Journal of Nuclear Materials. **559** (2022) 153441. https://doi.org/https://doi.org/10.1016/j.jnucmat.2021.153441.
160. T.S. Byun, K. Farrell, M. Li, Deformation in metals after low-temperature irradiation: Part II – Irradiation hardening, strain hardening, and stress ratios, Acta Materialia. **56**(5) (2008) 1056-1064. https://doi.org/https://doi.org/10.1016/j.actamat.2007.10.056.
161. A.R. Massih, High-temperature creep and superplasticity in zirconium alloys, Journal of Nuclear Science and Technology. **50**(1) (2013) 21-34. https://doi.org/10.1080/00223131.2013.750054.
162. C. Maxwell, J. Pencer, E. Torres, Atomistic simulation study of clustering and evolution of irradiation-induced defects in zirconium, Journal of Nuclear Materials. **531** (2020) 151979. https://doi.org/https://doi.org/10.1016/j.jnucmat.2019.151979.
163. D. Faken, H. Jónsson, Systematic analysis of local atomic structure combined with 3D computer graphics, Computational Materials Science. **2**(2) (1994) 279-286. https://doi.org/10.1016/0927-0256(94)90109-0.
164. A. Stukowski, K. Albe, Extracting dislocations and non-dislocation crystal defects from atomistic simulation data, Modelling and Simulation in Materials Science and Engineering. **18**(8) (2010) 085001. https://doi.org/10.1088/0965-0393/18/8/085001.
165. A. Rogerson, Irradiation growth in zirconium and its alloys, Journal of Nuclear Materials. **159** (1988) 43-61. https://doi.org/https://doi.org/10.1016/0022-3115(88)90084-0.
166. A. Glensk, B. Grabowski, T. Hickel, J. Neugebauer, Breakdown of the Arrhenius Law in Describing Vacancy Formation Energies: The Importance of Local Anharmonicity Revealed byAb initioThermodynamics, Physical Review X. **4**(1) (2014). https://doi.org/10.1103/physrevx.4.011018.
167. M.W. Guinan, R.N. Stuart, R.J. Borg, Fully dynamic computer simulation of self-interstitial diffusion in tungsten, Physical Review B. **15**(2) (1977) 699-710. https://doi.org/10.1103/physrevb.15.699.
168. S.L. Dudarev, The non-Arrhenius migration of interstitial defects in bcc transition metals, Comptes Rendus Physique. **9**(3-4) (2008) 409-417. https://doi.org/10.1016/j.crhy.2007.09.019.
169. J. Marian, B.D. Wirth, A. Caro, B. Sadigh, G.R. Odette, J.M. Perlado, T. Diaz De La Rubia, Dynamics of self-interstitial cluster migration in pure α-Fe and Fe-Cu alloys, Physical Review B. **65**(14) (2002). https://doi.org/10.1103/physrevb.65.144102.
170. J. Marian, B.D. Wirth, J.M. Perlado, G.R. Odette, T. Diaz De La Rubia, Dynamics of self-interstitial migration in Fe-Cu alloys, Physical Review B. **64**(9) (2001). https://doi.org/10.1103/physrevb.64.094303.
171. N. Soneda, T. Diaz De La Rubia, Migration kinetics of the self-interstitial atom and its clusters in bcc Fe, Philosophical Magazine A. **81**(2) (2001) 331-343. https://doi.org/10.1080/01418610108214307.

172. B.D. Wirth, G.R. Odette, D. Maroudas, G.E. Lucas, Energetics of formation and migration of self-interstitials and self-interstitial clusters in α-iron, Journal of Nuclear Materials. **244**(3) (1997) 185-194. https://doi.org/10.1016/s0022-3115(96)00736-2.
173. P.M. Kelly, R.G. Blake, A. Jostsons, An interpretation of corduroy contrast in neutron irradiated zirconium, Journal of Nuclear Materials. **59**(3) (1976) 307-315. https://doi.org/10.1016/0022-3115(76)90063-5.
174. A.A. Kohnert, M.A. Cusentino, B.D. Wirth, Molecular statics calculations of the biases and point defect capture volumes of small cavities, Journal of Nuclear Materials. **499** (2018) 480-489. https://doi.org/https://doi.org/10.1016/j.jnucmat.2017.12.005.
175. T. Okita, W.G. Wolfer, A critical test of the classical rate theory for void swelling, Journal of Nuclear Materials. **327**(2) (2004) 130-139. https://doi.org/https://doi.org/10.1016/j.jnucmat.2004.01.026.
176. M.F. Wehner, W.G. Wolfer, Vacancy cluster evolution in metals under irradiation, Philosophical Magazine A. **52**(2) (1985) 189-205. https://doi.org/10.1080/01418618508237618.
177. H. Trinkaus, B.N. Singh, S.I. Golubov, Progress in modelling the microstructural evolution in metals under cascade damage conditions, Journal of Nuclear Materials. **283-287** (2000) 89-98. https://doi.org/https://doi.org/10.1016/S0022-3115(00)00332-9.
178. A. Barbu *, C.S. Becquart, J.L. Bocquet, J. Dalla Torre, C. Domain, Comparison between three complementary approaches to simulate ' large ' fluence irradiation: application to electron irradiation of thin foils, Philosophical Magazine. **85**(4-7) (2005) 541-547. https://doi.org/10.1080/14786430412331334616.
179. C. Domain, C.S. Becquart, L. Malerba, Simulation of radiation damage in Fe alloys: an object kinetic Monte Carlo approach, Journal of Nuclear Materials. **335**(1) (2004) 121-145. https://doi.org/https://doi.org/10.1016/j.jnucmat.2004.07.037.
180. C.J. Ortiz, M.J. Caturla, Cascade damage evolution: rate theory versus kinetic Monte Carlo simulations, Journal of Computer-Aided Materials Design. **14**(1) (2007) 171-181. https://doi.org/10.1007/s10820-007-9082-9.
181. K. Arakawa, K. Ono, M. Isshiki, K. Mimura, M. Uchikoshi, H. Mori, Observation of the One-Dimensional Diffusion of Nanometer-Sized Dislocation Loops, Science. **318**(5852) (2007) 956-959. https://doi.org/10.1126/science.1145386.
182. A.A. Kohnert, B.D. Wirth, Cluster dynamics models of irradiation damage accumulation in ferritic iron. I. Trap mediated interstitial cluster diffusion, Journal of Applied Physics. **117**(15) (2015) 154305. https://doi.org/10.1063/1.4918315.
183. Y. Satoh, H. Matsui, Obstacles for one-dimensional migration of interstitial clusters in iron, Philosophical Magazine. **89**(18) (2009) 1489-1504. https://doi.org/10.1080/14786430903008480.
184. T. Hamaoka, Y. Satoh, H. Matsui, One-dimensional motion of interstitial clusters in iron-based binary alloys observed using a high-voltage electron microscope, Journal of Nuclear Materials. **433**(1) (2013) 180-187. https://doi.org/https://doi.org/10.1016/j.jnucmat.2012.09.007.

185. X.K. Xin, W.S. Lai, B.X. Liu, Point defect properties in hcp and bcc Zr with trace solute Nb revealed by ab initio calculations, Journal of Nuclear Materials. **393**(1) (2009) 197-202. https://doi.org/https://doi.org/10.1016/j.jnucmat.2009.06.005.
186. C. Domain, Ab initio modelling of defect properties with substitutional and interstitials elements in steels and Zr alloys, Journal of Nuclear Materials. **351**(1) (2006) 1-19. https://doi.org/https://doi.org/10.1016/j.jnucmat.2006.02.025.
187. M. Tikhonchev, The effect of impurity niobium on diffusion of self-interstitial atom and self-diffusion by interstitial mechanism in zirconium: an atomistic simulation, Materials Research Express. **7**(9) (2020) 096507. https://doi.org/10.1088/2053-1591/abb2cb.
188. M. Tikhonchev, V. Svetukhin, P. Kapustin, Primary radiation damage of Zr-0.5%Nb binary alloy: atomistic simulation by molecular dynamics method, Modelling and Simulation in Materials Science and Engineering. **25**(6) (2017) 065017. https://doi.org/10.1088/1361-651x/aa790f.
189. A. Reza, H. Yu, K. Mizohata, F. Hofmann, Thermal diffusivity degradation and point defect density in self-ion implanted tungsten, Acta Materialia. **193** (2020) 270-279. https://doi.org/https://doi.org/10.1016/j.actamat.2020.03.034.
190. F. Granberg, J. Byggmästar, K. Nordlund, Molecular dynamics simulations of high-dose damage production and defect evolution in tungsten, Journal of Nuclear Materials. **556** (2021) 153158. https://doi.org/https://doi.org/10.1016/j.jnucmat.2021.153158.
191. Y. Idrees, Z. Yao, M.A. Kirk, M.R. Daymond, In situ study of defect accumulation in zirconium under heavy ion irradiation, Journal of Nuclear Materials. **433**(1) (2013) 95-107. https://doi.org/https://doi.org/10.1016/j.jnucmat.2012.09.014.
192. J. Tian, Q. Feng, J. Zheng, X. Liu, W. Zhou, Radiation damage buildup and basal vacancy cluster formation in hcp zirconium: A molecular dynamics study, Journal of Nuclear Materials. **551** (2021) 152920. https://doi.org/10.1016/j.jnucmat.2021.152920.
193. M. Topping, A. Harte, T. Ungár, C.P. Race, S. Dumbill, P. Frankel, M. Preuss, The effect of irradiation temperature on damage structures in proton-irradiated zirconium alloys, Journal of Nuclear Materials. **514** (2019) 358-367. https://doi.org/https://doi.org/10.1016/j.jnucmat.2018.12.006.
194. *7 - Radiation Damage to Zirconium and its Alloys*, in *Materials Science Monographs*, J. Koutský and J. Kočik, Editors. 1994, Elsevier. p. 236-263.
195. A. Jostsons, R.G. Blake, J.G. Napier, P.M. Kelly, K. Farrell, Faulted loops in neutron-irradiated zirconium, Journal of Nuclear Materials. **68**(3) (1977) 267-276. https://doi.org/https://doi.org/10.1016/0022-3115(77)90251-3.

Vita

Jose March-Rico was born and raised in Knoxville, Tennessee. After high school, he was accepted to the University of Tennessee, Knoxville to pursue a career in Nuclear Engineering. After his first year, he decided to pursue a passion for Materials Science and Engineering and eventually received a Bachelor of Science degree in this field. Jose continued his academic career by staying at the University of Tennessee, Knoxville to pursue a Doctor of Philosophy degree in Nuclear Engineering. His research consisted of scale-bridging computational modeling of irradiation effects in alpha-zirconium, applying his passion for materials to nuclear applications. After graduation, he will continue to perform research with a focus on challenges in materials systems. He is overwhelmingly grateful for the help and support from his friends, family, and mentors as he continues down the path of life-long learning.